

Integral-Field Spectroscopy of High-Redshift Galaxies: Implications for Early Galaxy Evolution

DISSERTATION
der Fakultät für Physik
an der Ludwig-Maximilians-Universität München

vorgelegt von
Nicole Paula Heidelies Nesvadba
aus Offenbach am Main

22. Dezember 2005

Integral-Field Spectroscopy of High-Redshift Galaxies: Implications for Early Galaxy Evolution

DISSERTATION
der Fakultät für Physik
an der Ludwig-Maximilians-Universität München

vorgelegt von
Nicole Paula Heidelies Nesvadba
aus Nidderau

22. Dezember 2005

Erstgutachter: Prof. Dr. Reinhard Genzel
Zweitgutachter: Prof. Dr. Ralf Bender
Tag der mündlichen Prüfung: 6. Juni 2006

Zusammenfassung

Vieles deutet darauf hin, dass die aktivste Phase der Galaxienentwicklung schon bei Rotverschiebungen von $z \sim 1$ praktisch abgeschlossen war. Dies gilt insbesondere für sehr massereiche Systeme, die vor allem aus sehr alten Sternen (10 Gyr) bestehen und in denen sehr wenig Gas für weitere Sternentstehung zur Verfügung steht. Auch aktive Galaxienkerne waren im frühen Universum häufiger und zugleich heller. Trotz des reichen Fundus an “fossilen” Daten aus der Milchstraße und benachbarter Systeme ist die direkte Beobachtung von Galaxien bei hoher Rotverschiebung letztlich der einzige Weg, um zu verstehen welche Prozesse unser heutiges Universum maßgeblich geprägt haben. Mit Hilfe von Teleskopen der 8 – 10 m Klasse und neuentwickelten Instrumenten, darunter SPIFFI/SINFONI am VLT, können wir nun individuelle Galaxien bei Rotverschiebungen $z \sim 1 - 3$ (2 – 6 Gyr nach dem Urknall) direkt spektroskopisch untersuchen.

Die Arbeit basiert auf der Analyse spektral und räumlich aufgelöster optischer Emissionslinien, insbesondere $H\alpha$ und $[\text{OIII}]\lambda 5007$, die durch die hohe Rotverschiebung ins nahe Infrarot fallen. SPIFFI/SINFONI ist für solche Untersuchungen besonders geeignet, da es simultan Spektren eines zusammenhängenden, bis zu $8'' \times 8''$ großen Bildfeldes aufnimmt, so dass die interne Kinematik und chemische Gradienten einer Galaxie mit einer einzigen Beobachtung erfasst werden. Galaxien im frühen Universum hatten besonders hohe Sternentstehungsraten ($\sim 10 - 1000 \times$ die der Milchstraße heute) und dadurch helle optische Emissionslinien. Die interne Kinematik folgt aus dem Dopplereffekt, Linienprofil und -breite geben Aufschluss über das Vorhandensein eines AGN, galaktischer “Superwinde” und das Verhältnis von chaotischer zu geordneter Bewegung. Sternentstehungsraten folgen aus der Stärke der Balmer-Linien, insbesondere von $H\alpha$. Charakteristische Linienverhältnisse verraten das Vorhandensein eines AGN, die Quelle der Ionisation, und sie erlauben Schocks von Photoionisation zu unterscheiden, die chemische Zusammensetzung zu bestimmen und Elektrodichten im interstellaren Medium zu messen.

Die vorliegende Arbeit hat den Charakter einer Pilotstudie: Sie umfasst 9 Galaxien, die aufgrund sehr verschiedener Kriterien ausgewählt wurden: aufgrund ihrer Helligkeit bei Wellenlängen im UV- oder Submillimeterbereich oder durch starke Radioemission. Das vielleicht wichtigste Ergebnis ist, dass Gravitation und insbesondere die Dunkle Materie zwar erwartungsgemäß die zentrale Rolle spielt in der frühen Evolution von Galaxien, aber sie ist nicht der einzige maßgebliche Prozess. Sternentstehung und aktive Galaxienkerne (AGN) führen zu hydrodynamischer Rückkopplung, die möglicherweise ein Zeichen von Selbstregulierung bei der Galaxienentstehung ist. Dabei zeigt sich, dass Sternentstehung im frühen Universum ähnliche Auswirkungen auf die Wirtsgalaxie hatte wie heute, AGN allerdings eine möglicherweise deutlich wichtigere Rolle inne hatten.

Ein anderes wichtiges Ergebnis ist die Rotationskurve, die im inneren Kiloparsec einer durch eine Gravitationslinse vergrößerten Galaxie gefunden wurde. Viele Galaxien haben Geschwindigkeitsgradienten von $\sim 100 \text{ km s}^{-1}$, allerdings ist ihre Interpretation als Rotationskurve im allgemeinen nicht eindeutig. Die räumliche Auflösung ist relativ gering, und scheinbar stetige Gradienten könnten auch von nahe beieinander liegenden Galaxienpaaren herrühren, etwa verschmelzenden Galaxien. Galaxienverschmelzungen sind ein wichtiger Bestandteil des “hierarchischen Modells” der Strukturbildung, des momentan gültigen Paradigmas. Daher ist zu erwarten, dass Galaxienverschmelzungen, und damit enge Galaxienpaare, im frühen Universum häufiger waren als heute.

Summary

Several lines of evidence suggest that the most active phase of galaxy evolution, especially in the most massive systems, was largely completed by $z \sim 1$. This results, e.g., from the observation that the most massive galaxies at low redshift have very old stellar populations (~ 10 Gyr) and very little gas to fuel subsequent star formation. Similarly, active galactic nuclei (AGN) were more numerous and brighter in the early universe. Ultimately, the direct observation of high-redshift galaxies will be the only way to understand which processes shaped the universe we see today, in spite of the rich “fossil” data sets we have of the Milky Way and neighboring galaxies. Thanks to the new 8 – 10 m telescope class and novel instrumentation, including SPIFFI/SINFONI on the VLT, individual galaxies at redshifts $z \sim 1 - 3$ (2 – 6 Gyr after the Big Bang) are now within the reach of astronomical spectrographs.

Methodologically, this thesis focuses on the analysis of spectrally and spatially resolved optical emission lines, first of all $H\alpha$ and $[OIII]\lambda 5007$, which are shifted into the near-infrared. SPIFFI / SINFONI is very suited to such a programme, because it records the spectra of a contiguous field of view of up to $8'' \times 8''$. The internal kinematic and chemical gradients within a galaxy can thus be measured in a single observation. Galaxies in the early universe had particularly high star-formation rates, so that many targets are bright optical line emitters. Internal kinematics are measured through the Doppler effect, line profiles and widths indicate the presence of an AGN, galactic “superwinds” and the relationship of chaotic to ordered motion. Star-formation rates are measured from the luminosity of the Balmer lines, especially $H\alpha$. Characteristic line ratios indicate the presence of an AGN, chemical composition, and electron densities in the ISM, and they allow to distinguish shocks and photoionization.

This thesis is a pilot study: It comprises 9 galaxies that fulfill a variety of selection criteria: they are either bright UV or submillimeter emitters, or they are radio-loud. Perhaps the most fundamental result is that gravity (dominated by dark matter) is the main driver of early galaxy evolution, but it is not the only important process. Star formation and AGN cause hydrodynamical feedback processes, which might be a sign of self-regulated galaxy evolution. It is found that star-formation related feedback had similar properties at low and high redshift, but that AGN-driven gas expulsion might have played a major role in the high-redshift evolution of galaxies, that is without low-redshift equivalent. Another important result is the rotation curve we find in the central kiloparsec of a gravitationally lensed UV-selected galaxy. Velocity gradients of $\sim 100 \text{ km s}^{-1}$ have been observed in many high-redshift galaxies, but the interpretation as rotation curves is generally not unique. Given the relatively coarse spatial resolution of high-redshift galaxy data, two nearby galaxies, maybe interacting or undergoing a merger, might blend into one smooth velocity gradient. Galaxy mergers are an important ingredient of the “hierarchical model”, the current paradigm of structure formation, and therefore nearby galaxy pairs were likely more common at high redshift than they are today. The large similarity of the lensed rotation curve with those of nearby galaxies might be a first sign that galaxies evolved inside-out.

Contents

1	Introduction	1
2	Integral field spectroscopy	9
1	The SPIFFI instrument on the VLT	9
2	IFUs – novel tools in extragalactic astrophysics	11
3	Comparing SPIFFI	12
3	Observations and data reduction	15
1	Target selection and observation	15
2	Guest instrument data	18
3	Guaranteed time observations	20
4	Standard star measurements	22
5	Scrutinizing the data reduction	22
6	Extracting line and continuum data	28
7	Error-estimates and instrumental resolution	30
8	Auxiliary data obtained with other instruments	31
4	Properties of high-z galaxies	33
1	Rest-frame optical nebular emission lines	33
2	Evolution of stellar populations	42
3	Galaxy masses	44
4	Dynamical Modelling of high-redshift galaxies	49
5	Exponential disks parameter estimates	50
6	Gravitational lensing	53
5	A merger candidate at $z = 1.3$	57

1	Introduction	57
2	The morphology and spectrum of NIC1143a/b	58
3	Emission line diagnostics and star-formation rates	59
4	NIC1143a/b: Portrait of a merger at intermediate redshift	60
6	Submillimeter selected galaxies	63
1	Introduction	63
2	Comparison with integral-field data of low-redshift ULIRGS	65
3	SMMJ14011+0252	68
4	SMMJ04431+0210	112
7	Small scale dynamics of a $z \sim 3$ LBG	125
1	Introduction: Strong lensing and the 1E0657 arc core	125
2	Evidence that “Arc + Core” is a LBG	127
3	Results and analysis	132
4	Discussion	136
5	Summary and conclusions	142
8	Dynamics of $z \sim 3$ Lyman-break galaxies	147
1	Introduction	147
2	Q0347-383 C5	150
3	Q0201+113 C6	156
4	Q1422+231 D81	161
5	The dynamics of $z \sim 3$ LBGs	167
9	MRC1138-262 and high-z AGN feedback	173
1	Introduction	173
2	Integral-field portrait of a $z = 2.2$ powerful radio galaxy	176
3	Individual sources surrounding MRC1138-262	188
4	The physical characteristics of the outflow	192
5	Driving the outflow in MRC1138-262	198
6	The cosmological significance of AGN-driven feedback	205
7	Conclusions	212
10	Implications for early galaxy evolution: summary	215

1	Central rotation curve of a $z \sim 3.2$ Lyman break galaxy	216
2	The starburst in SMMJ14011+0252	217
3	AGN feedback in the powerful radio galaxy MRC1138-262	218
4	Outlook	219

List of Figures

1	Examples of low redshift galaxies.	2
2	NGC 4038/4039 and NGC 253 at $z = 2$	3
3	“Golden” redshift ranges in the NIR	6
1	SPIFFI raw frames	9
2	Slicer concept.	11
3	MC generated ratio of standard deviation to amplitude in binned data as a function of the number of bins.	13
1	Data-reduction flow-chart	19
2	Sky-subtracted raw-frame (method 1).	23
3	Comparison of data-reduction methods 1 and 2.	24
4	The artificial input spectrum.	25
5	Data-reduction methods 1 and 2: Results.	26
6	Instrumental resolution, calibration functions	32
1	BPT diagrams for a subset of SLOAN	35
2	Densities	36
3	The R_{23} metallicity indicator	37
4	The Calzetti and the galactic extinction law.	40
5	Rotation curve	46
6	Lensing configuration.	54
1	NIC1143a/b continuum and line morphology.	58
2	NIC1143a/b integrated spectra.	59
1	Low- z ULIRGS: $H\alpha$ images	69
2	Low- z ULIRGS: Velocity fields.	70

3	Low-z ULIRGS: Emission line dispersions.	71
4	Low-z ULIRGS: Line ratios	72
5	SMMJ14011+0252 F702W image and labels of components.	73
6	SPIFFI K band continuum and H α line image.	76
7	$J - K$ color map of SMMJ14011+0252	77
8	Spatially resolved line maps in SMMJ14011+0252	78
9	OIII λ 5007/H β map.	79
10	H and K-band spectra of J1n, J1s, and J1c	80
11	BPT diagrams for J1.	81
12	Relationship between $J - K$ color and equivalent width	82
13	SMMJ14011+0252 electron densities.	83
14	Absorption lines in the SMMJ14011+0252 J1 rest-frame UV spectrum.	85
15	Population synthesis fit to the UV spectrum.	86
16	$F702 - J$ color vs. $J - H$ color for SMMJ14011+0252 and A1835.	88
17	Source plane morphologies of SMM14011+0252	89
18	H α +NI spectra in J1.	89
19	Shock diagnostics in SMMJ14011+0252 J1.	90
20	Line ratio / FWHM relationships in J1n and J1s.	91
21	Emission line correlations for NII.	92
22	Emission line correlations for H α	93
23	Dynamical modeling: Velocity map of an exponential disk	96
24	Dynamical modeling: FWHM map of an exponential disk	97
25	Dynamical modeling: Residuals of velocity fit	98
26	χ^2 distribution for a single exp. disks	98
27	Bulge hypothesis: Velocity field.	99
28	Two Components: Velocity field	100
29	J2 H and K-band spectra.	103
30	CO emission in SMMJ14011+0252.	105
31	Continuum and line morphology of SMMJ04431+0210.	113
32	Integrated spectrum of SMMJ04431+0210.	114
33	Spectrum of the nuclear region of SMMJ04431+0210.	115
34	Map of SII emission in SMMJ04431+0210.	116

35	Spectrum of SII emission in SMMJ04431+0210.	116
36	Continuum image and maps of SMMJ04431+0210.	117
37	Density and BPT diagrams of SMMJ04431+0210.	118
38	Narrow line regions in SMMJ04431+0210	119
39	Narrow line regions in SMMJ04431+0210: input, smoothed and rebinned	120
40	Continuum image and maps of SMMJ04431+0210 in the source plane.	121
41	Spatially resolved spectra of SMMJ04431+0210.	124
1	1E0657 arc spectrum and Lyman break filters.	128
2	Rest-frame UV SED of 1E0657 and best fit STARBURST99 model	129
3	Light profile of the core.	131
4	Line image of 1E0657 arc and core.	132
5	K band continuum morphology of 1E0657 arc+core.	133
6	Integrated spectrum of 1E0657 arc and core.	134
7	Oxygen abundance estimated from the integrated spectrum of the arc and the core.	134
8	Spectra of the arc core and knots 1 to 3.	135
9	Spectra extracted from each row of the data cube.	136
10	Velocity curve of E0657 core.	138
11	Velocity curve of 1E0657 and local rotation curves.	139
12	ACS F814W image of the giant arc.	144
13	ACS F814W image of the giant arc, smoothed to the PSF of the FORS R-band image	145
1	Q0347-383 C5 WFPC2-F702W morphology.	150
2	Q0347-383 C5 line image and PSF.	151
3	Q0347-383 C5 WFPC2-F702W image and emission line contours.	152
4	Q0347-383 C5 integrated spectrum.	152
5	Q0347-383 C5 oxygen abundance.	153
6	Q0347-383 C5 spectra of components A and B.	153
7	Kinematic maps of Q0347-383 C5	154
8	WFPC2 F606W image of Q0201+113 C6.	156
9	Integrated spectrum of Q0201+113 C6	157
10	Emission line morphology of Q0201+113 C6.	157
11	WFPC2 F606W image of Q0201+113 C6.	159

12	Q1422+231 D81 integrated spectrum.	161
13	Closeup on the OIII line pair in Q1422+231 D81.	162
14	NIRSPEC spectrum of Q1422+231 D81	163
15	Spatially resolved line emission in Q1422+231D81.	164
16	Velocity map of Q1422+231 D81.	165
17	Velocity curve along the velocity gradient of Q1422+231 D81.	165
18	Q1422+231 D81 χ^2 distribution as function of mass and inclination.	166
19	Velocity-dispersion relationship for $z \sim 3$ LBGs.	168
1	Labeling of substructures.	174
2	H and K band continuum morphology of MRC1138-262	175
3	$H - K$ color image	176
4	Spectra of the inner 6 kpc of MRC1138-262.	177
5	AGN removed integrated K-band spectrum.	178
6	Relative velocities vs. projected radius.	179
7	Velocity map of MRC1138-262.	180
8	zone 1: Integrated spectra.	182
9	Emission line features within zone 2 and correlations.	183
10	zone 2: Integrated spectra.	185
11	Emission line features within zone 2 and correlations.	186
12	zone 3: Integrated spectra.	187
13	Emission line features within zone 3 and correlations.	188
14	OIII and $H\alpha$ morphologies in B3.	189
15	B3: Integrated spectra.	190
16	B3: Velocity shear.	192
17	MRC1138-262 electron density.	196
18	Is MRC1138-262 unique? Comparison with longslit data	206
19	Co-moving QSO number density as a function of redshift.	208

List of Tables

1	SPIFFI filters	10
1	Observations	29
1	The principle optical emission lines.	34
1	Emission lines in NIC1143a/b	61
1	H α relative velocities, line ratios and extinctions	110
2	Emission lines in J2	110
3	Emission lines in J1	110
4	Emission lines in J1c	111
1	Comparison of 1E0657-56 arc core with the Pettini (2001) LBGs.	140
2	Emission lines in 1E0657 arc+ core	143
1	Emission lines in Q0347-383 C5	155
2	Emission lines in Q0201+113 C6	160
3	Q1422+231 D1 emission lines	167
4	Q1422+231 D1 emission lines	167
1	Emission lines in MRC1138-262: zone 1	184
2	Emission lines in MRC1138-262: zone2	185
3	Emission lines in MRC1138-262: zone 3	187

Chapter 1

Introduction

Were the dinosaurs really all green? It might well be that paleontologists will never be able to answer this question conclusively, being limited to fossils that were buried inside rocks for more than 65 Myr. Until a decade ago, cosmologists were in a similar position: Studies of galaxy evolution by necessity used “paleontological” approaches, investigating in detail the low-redshift (preliminary) endpoints of a 14 Gyr long process. Although detailed observations, especially of the properties of the Milky Way and members of the Local Group, could yield some constraints (see Freeman & Bland-Hawthorn 2002, for a recent review), overall, galaxies are just too complex objects to infer their development *a posteriori* – and all evidence thus obtained can only be circumstantial.

This has dramatically changed over the last decade, thanks to the new 10-m-sized telescope class and to new detectors with unprecedented resolution, sensitivity and wavelength coverage. These developments made the early Universe available to direct observations. For cosmologists, watching T-Rex at dinner is no longer a dream.

And this development has not yet come to an end. One of the major improvements of astrophysical instrumentation in the last years was the development of integral-field spectrographs. Because longslit spectrographs (and also masks containing multiple slits) were limited to extract the spectral information only along one direction, but not for a continuous, two-dimensional field, spectroscopy of entire galaxies required repeated observations of the same object and was extremely time-consuming. This has now changed. New instruments, such as the SINFONI integral-field spectrograph SPIFFI, allow to measure the full spectroscopic information of a galaxy with one single observation.

Combining these instruments with telescopes of the 10-m-class (SINFONI is now a facility instrument on VLT-UT4, “YEPUN”) makes them the prime tools for unraveling the properties of galaxies at high-redshift, and hence, to directly probe observationally into the early Universe. This is only possible, because powerful photometric selection criteria have been developed – equally within the past decade – that allow to efficiently find high-redshift galaxies. These exploit almost the entire electromagnetic spectrum, ranging from (rest-frame) X-ray and UV imaging to far-infrared and submillimeter selections into the radio regime. While radio detections have the longest history, starting with the identification of the first quasars in the 1960s, the UV-selection techniques, effectively exploiting the fact that ionizing photons will be absorbed by neutral hydrogen, have only been established in the early 1990s (Steidel et al. 2003, summarizes the results of this survey). Searches based on submillimeter emission are even more recent (e.g. Smail et al. 1997), and are tailored to highly dust-enshrouded systems with extreme star-formation ($\lesssim 1000 M_{\odot} \text{ yr}^{-1}$).

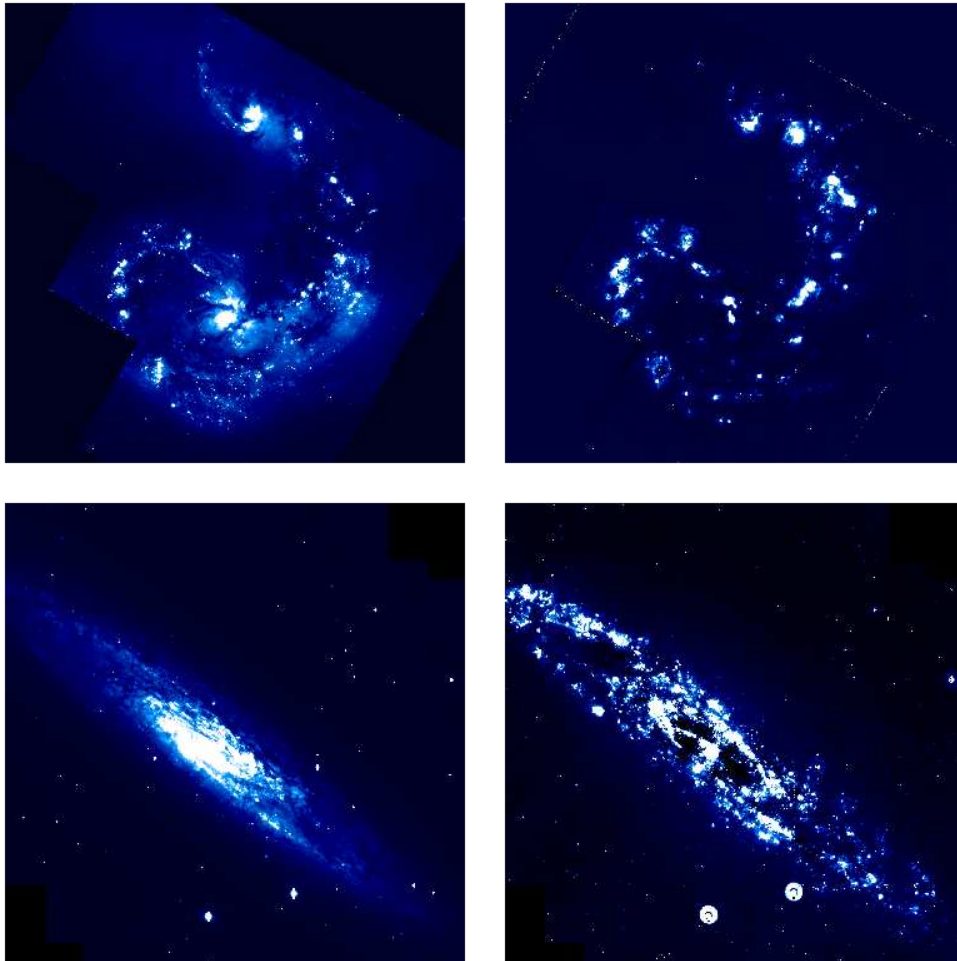


Fig. 1.— *Low-redshift galaxies: NGC 4038/4039 (upper panel) and NGC253 (lower panel). The left panel shows the V band (for NGC 4038/4039) and R (for NGC253) band continua, respectively. H α morphologies are given in the right panel. The data were kindly provided by S. Mengel (NGC4038/4039) and M. Lehnert (NGC 253).*

With all these selection criteria high-redshift galaxies can be identified, but to investigate their properties, detailed follow-up studies are indispensable, and must ideally cover large spectral regions. The infrared wavebands, and namely the near-infrared, play a crucial role in these follow-up studies. At redshifts of $z > 1.5$ (corresponding to ~ 9 Gyrs before our time), the bright rest-frame emission lines are shifted into the near-infrared wavebands. In order to benefit from the long tradition of optical observations in extragalactic astrophysics, and to be able to directly compare galaxies in the early Universe with those seen today, the best-suited wavelength range is therefore the near-infrared. This is even more true, as these direct studies of galaxy evolution come at a high price: The large distance and cosmological surface brightness dimming make high-redshift galaxies very small (effective radii are $r_e \lesssim 1''$) and faint ($m_K \sim 20$ mag and fainter). To illustrate these effects, two low-redshift galaxies are shown in Fig. 1, the Antennae merger NGC4038/4039 and the starburst galaxy NGC253. Fig. 2 shows the same galaxies with their appearance if the spatial resolution and signal-to-noise were like those of high-redshift studies. Where detailed structures cannot be discerned, spectroscopic and photometric analyses become more important, and allow by analogy to infer the physical behavior of the high-redshift sources.

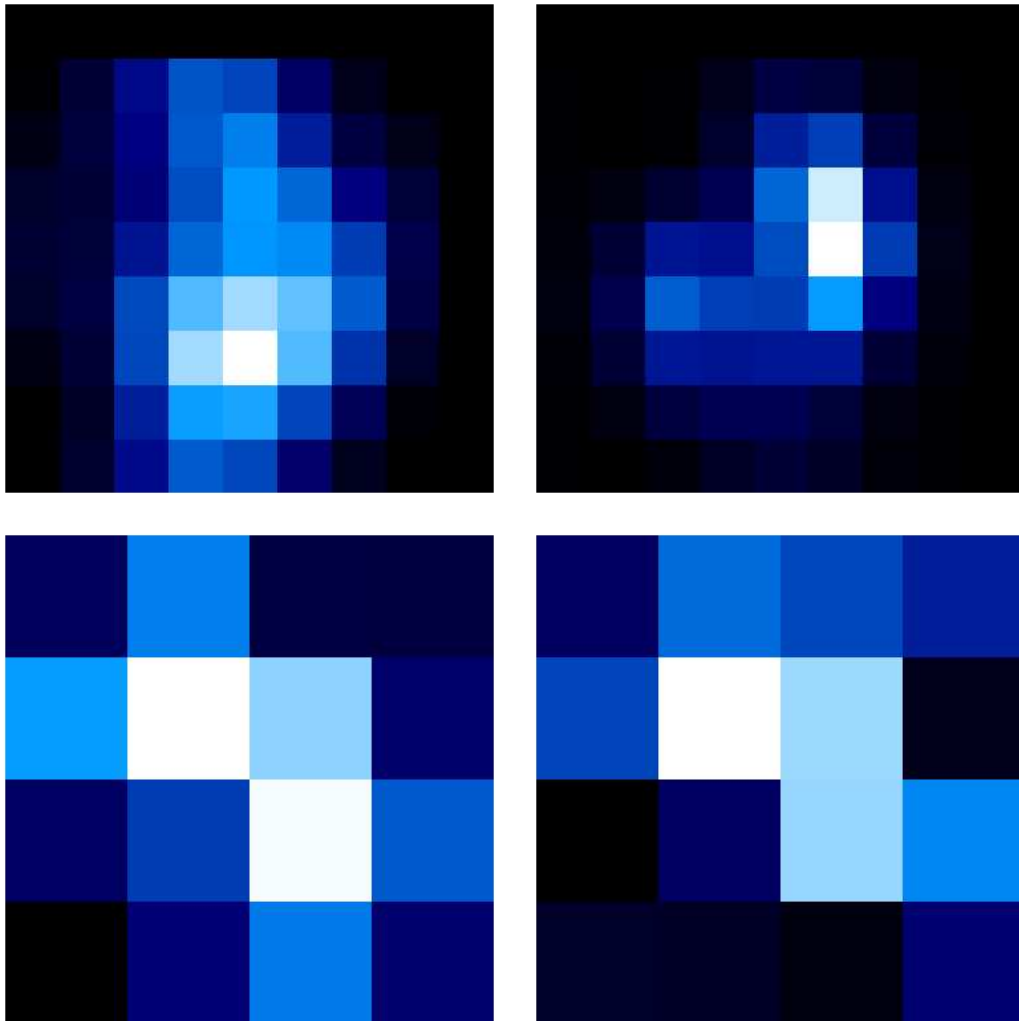


Fig. 2.— *The galaxies shown in Fig. 1 illustrating the typical pixel scales and spatial resolution (2 kpc pix^{-1}) and signal to noise ($S/N = 10$ for the brightest emission) of high-redshift galaxies.*

However, the results are clearly worth the effort. Initial photometric studies already showed that the phenomenology linked with galaxy formation must have been much richer in the past (e.g. Ellis et al. 1996). Both the cosmic star-formation rate (Madau et al. 1996; Giavalisco et al. 2004) and nuclear activity in galaxies (e.g., Pei 1995) reached their maximum at redshifts $z = 2 - 3$ and have been steadily declining during the past 10 Billion years. These redshifts are nearly optimal for spectroscopy in the near-infrared bands. This is illustrated in Fig. 3. The blue, red, and green bands indicate the redshift ranges for which the prime emission lines fall into the near-infrared atmospheric windows. The detailed analysis of these lines allows to infer the physical and chemical properties of the galaxies, such as the ionizing source, gas densities, and chemical enrichment. The kinematics imprinted on the spectrum yield the main dynamical drivers and set constraints on the mass and history of mass assembly.

Not only has observational technology fundamentally improved in the last decade, but also the precision of computer simulations which set the theoretical framework to deduce the formation of cosmic structure from first principles. They describe the build-up of cosmic filaments and galaxy clusters down to the scale of massive individual galaxies for different evolutionary scenarios. The

current paradigm is the Λ CDM (“Cold Dark Matter”) Universe. The presence of dark matter has been suspected as a consequence of detailed dynamical studies of galaxies and galaxy clusters for about half a century (for an early account see Zwicky 1952). The fact that it must be cold, i.e. nonrelativistic, follows from studies of the cosmic microwave background (e.g., Spergel et al. 2003). The dark energy Λ , eventually, plays the most mysterious part in present-day cosmology, but its basic phenomenology can be included in the models. When cosmological parameters are important for this thesis, the model chosen is the dark-energy dominated post-WMAP flat Λ CDM model with (dark) energy density $\Omega_\Lambda = 0.7$, matter density $\Omega_M = 0.3$, and $z = 0$ Hubble parameter $H_0 = 70 \text{ km s}^{-1} \text{ Mpc}^{-1}$.

All these findings are consistent with the picture of a hierarchically forming Universe, where smaller structures merge to form the big mass concentrations observed today. In this picture, dark matter “halos” are the main kinematic drivers of the mass assembly, and only on size scales of individual galaxies and below, baryons have an impact on structure formation.

The hierarchical model is a non-linear description of mass assembly, and it is therefore counter-intuitive in some respects. Maybe the most striking example is the apparent “anti-hierarchical” growth of the most massive galaxies. The most massive galaxies at low redshift appear “old, red and dead” – they are dominated by old ($\sim 10^{10}$ yrs) stellar populations, have little gas content, and form stars at very low rates. The age of the stellar populations indicates that their formation redshifts must be $z \gtrsim 1 - 2$. They have high metallicities¹, which indicates that they must have been evolving rapidly at high redshift. The tight correlation between the mass and the metallicity of galaxies has recently been confirmed by Tremonti et al. (2004) based on 53000 galaxies from the SLOAN survey.

However, the “anti-hierarchical growth” is only in contradiction to the hierarchical model, if the model is understood as a pure “bottom-up” assembly. This static view however is naive, because it neglects that the density perturbations during the recombination era (which are the “seeds” of large scale structure) were scale-free. The shorter collapse times of bigger overdensities will make the most massive objects evolve quickest. Smaller clumps cannot catch up, but will evolve at a slower pace. Since their number density will be depleted by accretion onto higher mass systems, and replenished by growth of smaller structure into concentrations of their size, overall the hierarchical model predicts a scenario, where the mass spectrum at a given redshift depends on a dynamical equilibrium between mass scales rather than a naive “bottom-up” assembly of structure. However, this implies that a galaxy of given mass observed in the local Universe will have a different evolution than a galaxy with equal mass observed at higher redshift.

The investigation of mass assembly is seriously hindered by the fact that the underlying driver – the dark matter – is not directly observable at high redshift. Even at low redshift, measuring its exact distribution, e.g. in galaxy clusters, is extremely challenging, and still lacks a thorough, model-independent approach. Most mass estimates for high-redshift galaxies are stellar masses, based on luminosities, hence they do not take dark matter into account and are prone to large systematic uncertainties. Dynamical mass estimates are clearly superior, but difficult to obtain for large galaxy samples, and due to the observational limitations of high-redshift studies, it is only now becoming possible to measure dynamical masses with some accuracy.

Therefore models of structure formation try to incorporate the impact of a given (dark matter) halo on the (baryonic) galaxy or galaxies that reside within. This is complicated by the presence of the baryons themselves. Whereas large-scale structure formation is solely based on gravity,

¹i.e. they are rich in elements other than the primordial hydrogen and helium.

(M)HD effects come into play at the mass scale of individual galaxies ($\log M/M_\odot \lesssim 13$) which will influence the behavior of the baryons by the means of cooling, loss of angular momentum and especially large-scale feedback.

These processes in the baryonic sector are complex with a large number of degrees of freedom and they are rather poorly understood. This is where the current generation of structure formation models fails and where specific observational constraints are needed. The processes are often parameterized in simple recipes or efficiencies, which might not be very satisfying from a physical point of view. However, this approach helps to tie the models more strongly to the observations which are therefore indispensable.

The main feedback process that is currently incorporated in the models is related to star-formation. When stars are formed in a galaxy with rates per unit area $\Sigma_* \gtrsim 0.1 M_\odot \text{ yr}^{-1} \text{ kpc}^{-2}$ then they will inevitably lead to large-scale gas outflows (Heckman 2003). Many of the observed high-redshift galaxies known today easily surpass this limit. The mechanism behind the starburst driven feedback involves the ejecta of supernovae and young stars, which after thermalization will form an overpressurized (factors $\sim 10^3 - 10^4$) bubble expanding along the largest pressure gradient in the ISM of the host (Heckman et al. 1990). For disk galaxies, this is approximately along the disk normal. The wind reaches velocities of several thousand km s^{-1} (Heckman 2003), but most optical line emission comes from gas clouds within the wind that are partially ionized and accelerated. Terminal velocities of these clouds are up to typically $\sim 300 \text{ km s}^{-1}$. The typical energy release of $\sim 10^{59}$ ergs for a typical ($\equiv L^*$) galaxy (Lehnert & Heckman 1996b) appears sufficient to unbind substantial gas fractions from comparably shallow potential wells, but not from massive galaxies.

Starburst-driven winds are a common feature of high-redshift galaxies, but indicators are often too subtle to allow a detailed analysis of the wind properties. This is also the case for most targets of this sample, where characteristic blue flux excesses (“blue wings”) are found, which are indicative of outflowing gas. In one case, however, which is the $z = 2.6$ galaxy SMMJ14011+0252 J1, the data allow to probe deeper into the wind properties. This is the first time that a galactic wind at high redshift is directly compared with starburst-driven winds in the local Universe. Another process that has only very recently been recognized by the modelers (e.g., Di Matteo et al. 2005) is AGN feedback. Active galactic nuclei are the most luminous objects in the Universe and are most likely powered by the release of gravitational energy in the highly relativistic surroundings of supermassive black holes (SMBHs, $\log M/M_\odot \sim 6 - 9$; Kauffmann & Haehnelt 2000). The masses of supermassive black holes (measured through stellar velocity dispersions in the cores of a small sample of nearby galaxies) appear to be tightly related to the bulge mass of their host (“M- σ relationship”; Ferrarese & Merritt 2000; Gebhardt et al. 2000). This might indicate a tight evolutionary link between a galaxy and its central supermassive black hole. In addition, the near ubiquity of non-luminous SMBHs in nearby galaxies (Yu & Tremaine 2002) indicates that they are a fairly general component of galaxies, and not very exotic objects as was initially thought.

That AGN have an impact on their host is well established (e.g. Tadhunter 1991). However, whether this impact is local (e.g. along the often very well collimated radio jets²) or has more general consequences for the gaseous component of the host, is still not conclusively determined for a representative sample of AGN. This thesis includes a first step towards establishing AGN feedback as the dominant mechanism by which the evolution of the most massive galaxies is regulated. The spatially-resolved kinematics of the host galaxy of a $z \sim 2.2$ AGN (MRC1138-262, Chapter 9)

²Back-to-back AGN ejecta of thin, relativistic, synchrotron-emitting plasma often reaching beyond the host galaxy on size scales of up to several Mpc.

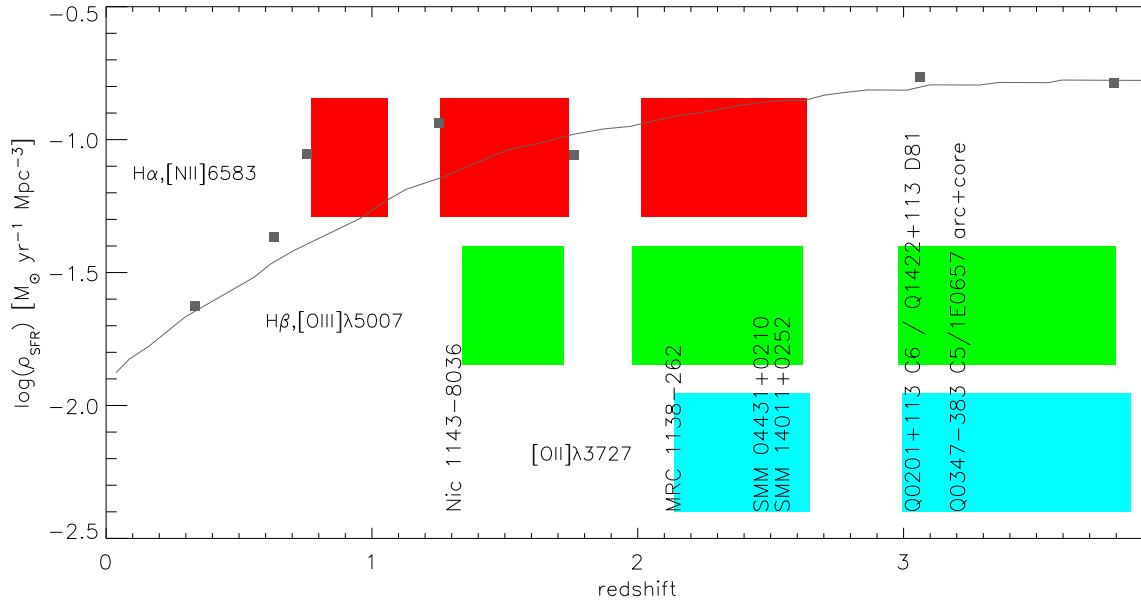


Fig. 3.— ‘Golden redshift ranges’ for ground-based NIR spectroscopy of high redshift galaxies. The gray dots (line) indicate the dust-corrected measured (modelled) star-formation rate densities taken from Giavalisco et al. (2004). Vertical labels indicate the redshifts of targets studied in this thesis.

clearly shows that the overall gas dynamics within the interstellar medium are dominated by the feedback from the central AGN.

High-redshift galaxies have often very distorted morphologies, not reminiscent of the well expressed Hubble types seen at low redshift (Giavalisco 2002). It is not easy, however, to determine the cause of this morphological shift. Many photometric studies (especially the early ones) used rest-frame UV photometry, and it is known that at these wavelengths, many galaxies appear clumpy and irregular, because emission is dominated by individual star-forming regions, and dust extinction is very high. Today, more and more researchers favor the view that these peculiar morphologies might be intrinsic, because the irregularities persist also at observed optical wavelengths, which are less sensitive to extinction (for a $z = 2$ galaxy, the near-infrared atmospheric windows reach to rest-frame wavelengths $\lambda_{rest} \sim 8000\text{\AA}$). Moreover, cosmological surface brightness dimming will make it difficult to identify the more regular underlying large-scale emission of a galaxy, irrespective of redshift, so that only the brightest regions (e.g., giant star-forming regions, AGN or nuclear starbursts) can be observed (see Fig. 2).

Are these morphologies due to merging galaxies? A positive answer to this question based on photometry alone cannot be unique. Irregular morphologies might also arise from the collapse of large self-gravitating gaseous disks, leading to fragmentation and star-formation within separated bright knots (Immeli et al. 2004). The expected morphology of these objects – ultimately galaxies forming from primordial cold gas – resembles a merger, but the characteristic velocity field of the disk would be preserved. By studying the spatially resolved kinematics of these sources (velocities and line widths) and their chemical evolution, these scenarios can – in principle – be distinguished. Observational constraints, however, and especially the coarse spatial resolution due to the seeing, make this distinction in practice a very subtle task.

In a hierarchically forming Universe, mergers obviously play a crucial role. However, growth

by accretion of cold gas must also occur, and gauging the relative impact of these modes is among the major tasks of observational cosmology. In this thesis, it is tried to find the simplest model to consistently explain the overall properties of each individual galaxy, by simultaneously using all available photometric and kinematic data. Additional constraints, e.g. the evolutionary history of the source, are used when available. By comparing individual sources with simple dynamical models, e.g. rotating exponential disks, it is tried to find the simplest scenario to describe the data, taking explicitly into account the limited spectral and spatial resolution, low signal-to-noise ratios, and the impact of irregular morphologies on the measured kinematic patterns.

This is the first systematic study of the properties of high redshift galaxies using an integral-field spectrograph in the near-infrared. As such, it does not focus on one well-constrained aspect of the internal structure and dynamics of high-redshift galaxies but attempts to accurately describe the intrinsic properties of different types of objects and selected with different criteria. Nonetheless, the number of objects is small, and reflects the observational challenges of the high-redshift Universe. Exposure times of several hours were needed for each of the 8 objects in this study.

This thesis does not aim at conclusively elucidating any detailed question of high-redshift extragalactic astrophysics, but it does contribute to a number of open questions, each of which is worth a more detailed investigation of statistically more robust samples. However, any of these studies would be a thesis in itself. This work therefore truly has the character of a pilot study, and illustrates the large potential that near-infrared integral-field spectroscopy has to understand the processes that shaped the Universe we see today.

Chapter 2

Integral field spectroscopy

1. The SPIFFI instrument on the VLT

This work is based on integral field spectroscopic data taken with the “SPectrograph for Imaging of Faint FIelds”, SPIFFI, which was developed and built at MPE (Eisenhauer et al. 2000). As part of the larger “SPectrograph for INtegral Faint Field Imaging” SINFONI (Eisenhauer et al. 2003), which upon completion will comprise an adaptive optics module including a laser guide star,

SPIFFI has now become a facility instrument in the Cassegrain focus of the Yepun telescope (UT4) of the Very Large Telescope (VLT). The VLT is a complex of four similar 8.2-meter telescopes on top of the Cerro Paranal in the Chilean Atacama desert operated by the European Southern Observatory ESO, allowing astronomical observations of the Southern sky (declinations below $\sim 30^\circ$).

Most of the present data were taken in an early SPIFFI Guest Instrument (GI) run between February and April 2003, using UT2-Kueyen. Additional data sets were obtained during guaranteed time observations (GTO) in 2004/2005, with an upgraded version of SPIFFI. The GI instrument used a smaller detector and had no adaptive optics, but otherwise did not strongly differ from the final layout. All observations are described in Chapter 3 and summarized in Table 1 of that chapter. For instrumental characteristics that depend on detector type, specifications will be given for both designs.

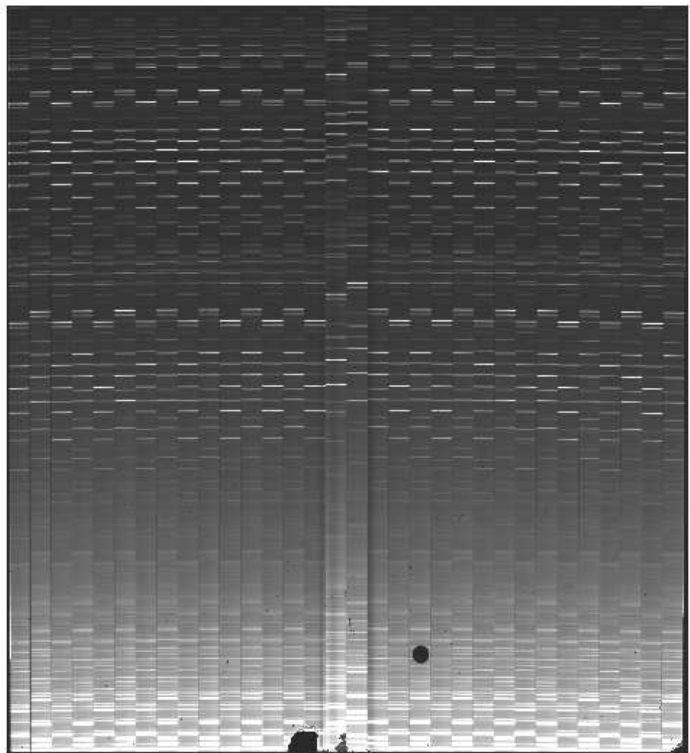


Fig. 1.— *Co-added (unregistered) SPIFFI raw frames of 4 hours of data of Q0347-383 C5. The pseudoslit is along the abscissa, the ordinate yields the spectral information of each individual spatial pixel.*

The heart of the SPIFFI instrument is an image slicer consisting of two stacks of 32 narrow mirrors which are placed such that they dissect the field of view into 32 stripes, each (for the purposes presented here) is $0.25''$ wide and $8''$ long. These are then reassembled end-to-end to form a continuous “pseudo-longslit”. The basic principle is illustrated in Fig. 2. The image of the pseudoslit is then led to a conventional grism and projected onto a 2048×2048 pixel detector array (1024×1024 pixels for the GI instrument). Fig. 1 shows an example of the resulting raw frame: The pseudoslit is lined up along the abscissa, spectral information is along the ordinate. The bright features are telluric night sky lines, originating from OH line emission in the atmosphere. The spectral shift inbetween neighboring slitlets serves to reduce scattering in the presence of bright spectral features (especially the unavoidable night-sky-lines). The slicer also re-arranges the order of slitlets, to further minimize correlations between adjacent regions of the sky.

The offline data reduction will then reassemble the raw data to form a three-dimensional data cube, with two spatial and one spectral direction. Hence for each spatial element, the spectral information is readily accessible. The details of these computations, together with the special requirements of astronomical data reduction in the near infrared, are addressed in Chapter 3.

SPIFFI allows to simultaneously obtain separate spectra for 64×32 spatial elements (32×32 pixels in the GI configuration). A pre-optics in front of the image slicer allows to choose different pixel scales, to meet different requirements with respect to spatial resolution and signal-to-noise, e.g. for diffraction-limited adaptive optics (AO) observations or in the seeing-limited mode, where atmospheric turbulence deteriorates the spatial resolution. The low surface-brightness of the sources is of concern for the observation of high-redshift galaxies. Larger spatial bins are beneficial because they collect each more photons and minimize photon-noise. In addition, adaptive optics was not yet available for these observations, therefore the largest pixel scale of $0.25''$ was chosen for this analysis, resulting in a field-of-view of $8'' \times 8''$. This is well suited to the size of the seeing disk under the best ever obtained conditions at Paranal ($\sim 0.2''$), and subsamples it even under good ($\gtrsim 0.5''$) conditions. High-redshift galaxies have typical sizes of a few seconds of arc, hence the field-of-view in the $0.25''$ mode has a reasonably good size to simultaneously obtain data from the whole source.

SPIFFI has four filters in the near-infrared wavebands J, H, H+K and K, to block 2nd order spectra. For those which are relevant for this work (J,H and K), central wavelengths and bandwidths are given in Table 1.

Table 1:: SPIFFI / SINFONI filters

Filter (1)	λ_c (2)	$\Delta(\lambda)$ (3)	R(GI) (4)	R(GTO) (5)
J	$1.25\mu\text{m}$	$0.15\mu\text{m}$	1600	2000
H	$1.65\mu\text{m}$	$0.20\mu\text{m}$	2000	3000
K	$2.20\mu\text{m}$	$0.25\mu\text{m}$	2400	4000

Column (1) – Filter band. Column (2) – central wavelength. Column (3) – Bandwidth. (4) – Spectral resolution during the GI observations ($R=\lambda/\Delta\lambda$). (5) – Approximate spectral resolution of the facility instrument.

To minimize thermal backgrounds originating from the instrument itself, SPIFFI is cooled with liquid nitrogen to a temperature of ~ 80 K.

2. Integral field units – novel tools in extragalactic astrophysics

The classical instruments for spectroscopic studies of extragalactic objects are longslit spectrographs. Only very recently, integral-field spectroscopic instruments have joined the pool of ready-to-use tools in extragalactic astrophysics.

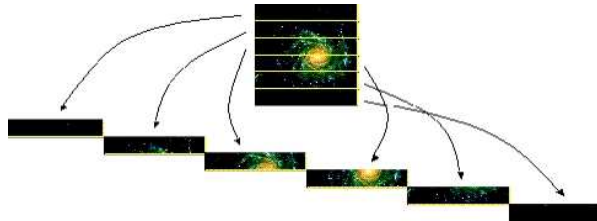


Fig. 2.— *Basic principle of the SPIFFI image slicer (illustration taken from the SPIFFI/SINFONI website).*

Multi-object spectrographs use masks consisting of a number of slits, but leave the basic principle of slit spectroscopy unaltered. They are therefore not suitable to spatially resolve the spectral information from continuous regions of the sky along more than one direction. Other instrumental designs have been developed exploiting e.g., optical fibers to guide the light from different locations in the field of view to the grating, or imaging scanning through the waveband with very narrow, tunable filters to recover the spectral information (Fabry-Perot imaging).

Compared to the conventional longslit spectroscopy and imaging, integral-field units are in an intermediate position. This leads to a number of very obvious, but also to some rather subtle advantages. For studying the evolution and kinematics of high-redshift galaxies, these are especially:

- Spatially resolved, spectroscopic data are obtained simultaneously for the whole galaxy. In longslit spectroscopy, spectra can only be taken along one direction.
- Galaxy rotation leads to velocity gradients along preferred kinematic axes. These naturally coincide with the morphological major axis for virialized spiral galaxies, but this is not necessarily the case for galaxies with irregular morphology or for galaxies undergoing mergers. Especially in case of galaxies in formation, coincident morphological and kinematic axes cannot a priori be assumed. Hence it is a major limitation to define the direction of main interest *before* the observation, as must be done when using longslits. The same holds for objects with inherently complex kinematics, e.g. interactions between radio jets and host galaxies in powerful radio-galaxies (see Chapter 9).
- Images of line emission are obtained irrespective of redshift for all lines that fall within the band, in one single observation and without specially tailored filter sets. This allows to study very conveniently the morphology of the line emitting regions and compare line strengths in different regions, e.g. to measure differences in extinction or ionization.
- Spectroscopic and morphological data are obtained at the same telescope pointing with a most accurate alignment, which only depends on robust distortion corrections within individual cubes.
- Spectroscopic and morphological information are obtained simultaneously. Unavoidable uncertainties in e.g. equivalent widths, due to varying weather conditions and air masses in subsequent observations (as must be done classically), can be ruled out.

- Continuum imaging can be obtained from clipping emission lines, allowing fine-tuning of the spectral region. This is very important for high-redshift objects, because emission lines are at arbitrary observed wavelengths, which cannot all be accounted for with dedicated filter sets.
- In longslit spectra, slit-losses occur if the galaxy is not well placed on the slit, or if its spatial extent exceeds the slit width. This is particularly limiting the precision of spectrophotometry, when the seeing disk exceeds the slit width. The seeing will cause parts of the emission to be blurred off the slit. On the other hand, with an integral-field unit, the spectral flux can easily be obtained by combining all spectra of the source within the full field-of-view.
- Adaptive optics is not of direct concern for this work. Nonetheless, for the sake of completeness, it should also be mentioned that AO does help to increase the signal-to-noise by sampling the full PSF (assuming a perfect Strehl-ratio).

Disadvantages, on the other hand, are few. SPIFFI reaches (or surpasses) the sensitivity and spectral resolution of longslit spectrographs in the near infrared, and therefore has a similar performance. However, its rather complex design increases instrumental polarizations and makes it unlikely that similar instruments will soon be available for spectropolarimetric studies. However, such studies are not very frequent. Especially for high redshift galaxies, the faintness of the sources makes spectropolarimetry in the near-infrared impossible with present-day instrumentation, except for very rare cases, and requires extreme observing times (several nights).

The main limitations as compared with conventional imaging are the relatively small field-of-view and (at least in the $0.25''$ pixel scale) coarse spatial resolution. In some cases, and especially for very faint targets, the small field-of-view might make it difficult to ensure accurate telescope pointing and alignment of individual frames. As will be shown in Chapter 6, the combination of integral-field observations with conventional, deep near-infrared imaging can therefore be very powerful for thorough studies of the physical environment in high-redshift galaxies.

3. Comparing SPIFFI's spectroscopic performance with longslit spectrographs

This is the first systematic study of high-redshift galaxies using a near-infrared integral field device. It is therefore of major interest to investigate SPIFFI's spectroscopic performance as compared to the more standard longslit spectrographs.

Two of the sources in this sample (Q1422+231 D81 and Q0347-383 C5) have previously been observed with other near-infrared spectrographs. Since it can be ruled out that the integrated flux of galaxies varies over timescales of years, by comparing observations of similar objects, it is possible to *in vivo* compare the sensitivity of SPIFFI with that of other instruments. This is in some sense complementary to the more theoretical approach based on calibration data, as e.g. used in exposure time calculators. Here, source-specific aspects as e.g. slit-losses are automatically taken into account.

The two comparisons are carried out in a similar way: Signal-to-noise values (S/N) are estimated from the published (i.e., printed) spectra, and compared with those of the SPIFFI data. However, for such spectra the S/N are usually not given explicitly, and must be estimated from the spectra themselves in the respective publication.

In a statistical sense, the standard deviation of a Gaussian distribution can be estimated from the largest deviations in the sample, and is a function of sample size. The quantitative relationship

follows from a simple Monte Carlo simulation. This was done by modelling the average standard deviation and amplitude as a function of sample size (i.e., number of spectral bins). For each size step, 30000 realizations were computed and averaged. Statistical fluctuations are $\sim 0.6\%$. The result is shown graphically in Fig. 3. Depending on the number of spectral bins that are compared, the correction factor to measure the standard deviation from the amplitude within the spectral region can directly be read off the ordinate. However, the estimate is only approximately correct, as only one single realization of the statistical distribution is actually measured in the data. Nonetheless, it is a quantitatively defined estimate and in the present case, the uncertainties introduced by the method will not exceed those that are inherent to the spectrum (e.g., deviations from Gaussian noise, especially due to night-sky-line residuals).

A number of observational differences must be taken into account, which are not related to the performance of the spectrograph. The VLT and Keck telescope have different sizes, 8.2 m (for both UT2 (i.e., GI data) and UT4 (GTO data)), and 10 m, respectively. Different total exposure times can easily be accounted for, exploiting that the signal-to-noise ratio increases with time as $S/N \propto \sqrt{t}$. The influence of the Earth’s atmosphere (seeing and transparency), on the contrary, is difficult to state precisely.

More quantitatively, this translates into two corrections to be applied for differences in the exposure time and inbetween telescopes, which are

$$SNR_{spif} = \sqrt{\frac{t_{spif}}{t_{inst}}} \frac{D_{VLT}}{D_{inst}} SNR_{comp}, \quad (2.1)$$

with t_{inst} , D_{inst} being the exposure time and the telescope aperture of the comparison instrument, and t_{spif} , D_{spif} being the exposure time and telescope size in use with SPIFFI. Since the lines are typically resolved, the signal-to-noise is estimated by setting $SNR = f_{line}/(rms_{cont} fwhm_{line})$, with the line flux f_{line} , noise in a sideband rms_{cont} (with or without continuum flux, depending on the source), and FWHM of the line, $fwhm_{line}$.

The goal of this comparison is to investigate which of the instruments is most suited to observing such targets, and not to identify the most sensitive detector or highest throughput. Therefore, pixel sizes and spectral binning are not taken into account, because the performance on a given object is compared. All data sets have, e.g., seeing-limited spatial resolution and typically resolve the lines of high-redshift galaxies spectrally with $R \sim 2000 - 4000$, the actual value depending on the instrument and the wavelength and redshift of individual lines and targets.

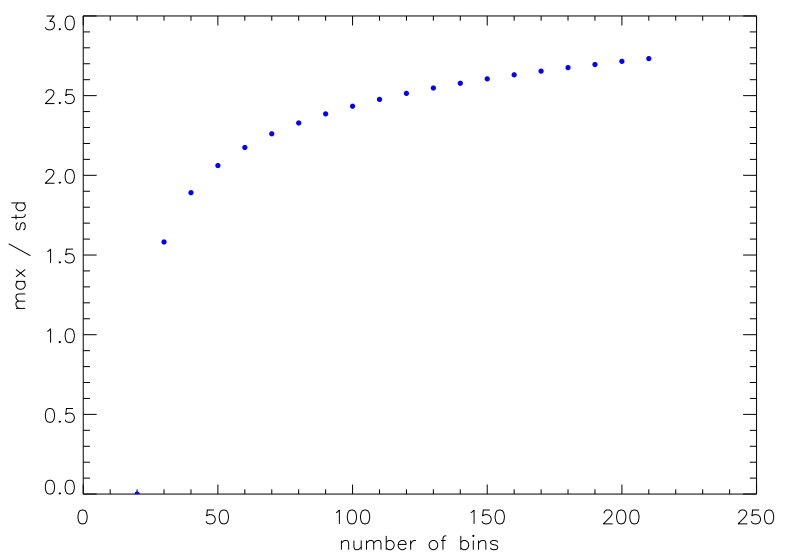


Fig. 3.— Monte Carlo generated ratio between standard deviation and amplitude for Gaussian distributed noise as function of the number of bins. Strictly speaking, these values are valid only for a statistical sample.

3.1. Q0347-383 C5 – Comparing ISAAC with SINFONI (2nd engineering array)

Q0347-383 C5 has published spectra taken with ISAAC on UT-1 of the VLT. (Pettini et al. 2001) Estimating the signal-to-noise value over ~ 50 bins that are not affected by night-sky-lines, and applying a correction of 2.1 to translate the amplitude into the standard deviation (see Fig. 3) yields approximately $S/N = 10.5$ for $[\text{OIII}]\lambda 5007$. This estimate uses the line flux, as the emission line appears spectrally resolved. Its width is $FWHM \sim 4$ pixels, the core ~ 150 counts. The flux enclosed within a Gaussian with these parameters then yields the S/N .

In the integrated SINFONI spectrum of Q0347-383 C5, smoothed to approximate the ISAAC resolution, $[\text{OIII}]\lambda 5007$ has $S/N = 29.96$. Taking into account that the total ISAAC exposure time was 18000 s, and that of SINFONI was 14400 s, the sensitivity of SINFONI is ~ 3.2 times higher. Further instrumental differences are not considered, as UT1 and UT4 are almost similar (neglecting possible differences in the reflectivity of the telescopes), and the impact of the weather conditions is hard to quantify. This simple comparison can also not distinguish whether the large sensitivity difference is dominated by the intrinsic sensitivity of each instrument, or from observational constraints, especially slit losses in the longslit spectra. However, the latter seems not very likely, as the source extent ($\sim 0.3''$ effective radius) is well below the $1''$ slit width of the spectrograph.

3.2. Q1422+231 D81 – Comparing NIRSPEC with SPIFFI-GI

Q1422+231 D81 has published spectra taken with NIRSPEC on Keck 2 (Pettini et al. 2001). Following the same procedure as outlined for Q0347-383 C5 in the previous section yields an estimated $S/N = 20.5$ for the $[\text{OIII}]\lambda 5007$ line. This accounts for the integrated line flux, because the line appears spectrally resolved in the printed spectrum. From the SPIFFI data $S/N = 27.9$ is measured for the integrated spectrum of Q1422+231 D81. The NIRSPEC data have an integrated exposure time of $t_{NIR} = 6300$ s as compared to $t_{SPI} = 7200$ s with SPIFFI. Using equation 2.1 then yields a $SNR_{spif} = 32.6$ if observations had taken place under circumstances similar to those of the NIRSPEC data taking. This is a factor 1.6 better than the signal-to-noise ratio achieved in the NIRSPEC run.

Chapter 3

Observations and data reduction

1. Target selection and observation

This thesis focuses on the rest-frame optical emission line properties of a small sample of galaxies selected through a large set of methods. By selecting galaxies with a broad range of properties, the diverse set of physical processes is investigated that are likely to influence the evolution of galaxies such as merging and feedback from an active galactic nucleus (AGN). The galaxies were chosen to have redshifts where the important optical diagnostic lines fall into one of the near-infrared windows of the J, H and/or K bands – namely they must lie between $z \sim 1.5 - 3.5$ (see Fig. 3 of Chapter 1). It is both important to study galaxies with a wide range of selection methods and through the measurement and analysis of their optical emission lines. Given the large number of physical processes that might influence or control galaxy evolution, it is important to study classes of objects exhibiting a range of phenomenologies. Astrophysically, this means that the targets were selected with a variety of techniques, such as by their submillimeter flux, emission lines, or UV continuum emission, or by their radio luminosity, to identify galaxies hosting a powerful AGN. In addition, selecting high-redshift galaxies with redshifts such that the optical diagnostic lines are in the near-infrared atmospheric windows means they are studied with the same techniques and analyses that are used to investigate local galaxies. This allows a direct comparison of galaxies at low and high redshift. Moreover, studying galaxies in the rest-frame optical as opposed to the rest-frame UV means that even heavily obscured galaxies can be included with some confidence, and that it is possible to investigate their intrinsic properties instead of being overwhelmed by the high and variable extinction.

Besides some very significant astrophysical advantages to studying galaxies in the near-infrared (NIR), there are also some practical advantages. The smearing of the image, due to turbulence in the Earth’s atmosphere (“seeing”), is strongly wavelength-dependent (with coherence lengths $\propto \lambda^{6/5}$; Lena et al. 1998), so that the loss of spatial resolution due to the turbulent blurring is comparably small in the NIR compared to optical wavebands. Given that typical sizes of even the most extended high-redshift galaxies do not exceed a few seconds of arc, this is clearly a significant advantage. SPIFFI’s coarsest pixel scale is $0.25''$, well below the typical FWHM of the seeing disk ($\gtrsim 0.5''$). Hence, apart from observations using adaptive optics, the spatial resolution is limited by the seeing.

Unfortunately, there are several difficulties in observing high redshift galaxies generally and in the infrared in particular, especially given the goal to obtain spatially extended information. This implies reaching the lowest possible surface brightnesses ($\mathcal{O}(10^{-16}) \text{ W m}^{-2} \mu\text{m}^{-1} \square'$). Due

to their large distances their integrated fluxes will be low. High redshift galaxies are difficult to resolve. This is both because there may be intrinsic size evolution (e.g., Bouwens et al. 2004) and cosmological surface-brightness dimming ($J_z/J_{z=0} \propto (1+z)^4$). As stated previously, the important diagnostic optical emission lines fall at wavelengths between 1 and $2.5\mu\text{m}$. Near-infrared detectors have historically had some significant limitations compared to optical detectors. Detector cosmetic quality is sometimes not good, with significant numbers of hot and dark pixels which can make data reduction especially difficult for faint objects. They also have had high read noise and dark current which limited their sensitivities (i.e., they are not background limited) between the OH lines and at moderate and high spectral resolutions and small projected pixel scales. The noise of the arrays is compounded by the atmosphere, which at near-infrared wavelengths is not very benevolent, the strong OH night sky lines can vary on timescales of a few minutes. This limits the integration times to 5 – 10 minutes and thus it is sometimes not possible to over-come the readnoise of the array with long integration times and limiting the performance of the instrument. Besides the emission lines, the transmission is variable, significant over large fractions of the near-infrared, and limits the observations to 3 near-infrared wavebands (J-, H-, and K-bands due to wavelength-dependent absorption of CO_2 and H_2O). In addition, for wavelengths beyond ~ 2.2 to $2.4\mu\text{m}$, thermal background emission becomes a significant source of noise. How significant depends on the altitude of the observatory (the emissivity of the atmosphere), the emissivity of the telescope structure and mirror, and the temperature, thermal homogeneity, and baffling of the instrument.

There are techniques which can mitigate against the brightness and variability of the night sky emission in the near-infrared. Rest-frame optical emission line fluxes of high-redshift galaxies are $\mathcal{O}(10^{-16})\text{ W m}^{-2}\mu\text{m}^{-1}$, a factor ~ 100 fainter than the night-sky emission. As a consequence, observations are differential, requiring a robust (and nearly instantaneous, due to the time variability) estimate of the night sky emission, to subtract the telluric signal (“night sky subtraction”). This can either be carried out by taking separate “sky frames” or (if the instrument has a sufficiently uniform response all across the field-of-view) by using the regions within the field of view that are devoid of object emission. Both approaches have been used for this work.

Observing faint sources, such as high-redshift galaxies, requires total integration times of several hours, even with 8-m-class telescopes and the most sensitive near-infrared detectors available today. This is even more a constraint, when one aims at spatially-resolved observations, as is the case here. Hence, a sequence of individual exposures (typically 4 – 8) will be taken and reduced separately, and in a final step, all of the individual sequences will be combined to yield the final, high-sensitivity, data set. For most of the high-redshift sources signal-to-noise ratios in the single frames are near $S/N = 1$, so that the source cannot be discerned. As a result, good pointing stability of the telescope, and excellent mechanical stability of the instrument (within fractions of an arcsec, depending on the pixel scale), are mandatory to allow to “blindly” combine these frames. Because the absolute pointing precision is not sufficient, a nearby (within $120''$ of the target), comparably bright star ($K = 15$ mag at least) is used for the absolute telescope positioning. After the star’s position within the field of view is known, the telescope can be offset accurately to the target of interest.

Ideally, the telescope pointing will not be identical for all individual frames. Spatial “dithering” (i.e., offsets by a few pixels between individual exposures) allows for the mitigation of static pixel-to-pixel variations across the detector or illumination differences within the field-of-view. In addition, combining total exposures from individual frames with shorter exposure times will provide a good means to identify cosmic rays or temporally variable pixels. For this work, sequences of 4 – 8 individual exposures (“templates”) were typically taken with predefined dither patterns. If longer exposures were necessary (as was usually the case) then these templates were executed repeatedly.

To optimize the alignment inbetween different templates, it is necessary to blindly co-add all frames taken within the same template, and then derive a template-to-template offset by cross-correlating the images (either the image plane of the collapsed cubes, the continuum image or the line image, depending on the characteristics of the source). This is because templates were not necessarily executed sequentially and may have been executed on different nights. Thus the same pointing could not be guaranteed between templates.

In the GI data, the overall pointing stability was not sufficient to allow blind registration of subsequent on-off pairs at different dither positions. Luckily the dither pattern was such that two subsequent on-source frames were obtained without offsetting the telescope. In all sources, the line emission was bright enough to allow cross-correlation of the combined line images of these two frames, or, in some cases, to orient on bright foreground sources. Observing dates and total exposure times for the objects studied in this work are summarized in Table 1.

Most of the data included in this thesis were taken by the SPIFFI team during the commissioning and an early “guest instrument” run in spring 2003, using the UT1 of the ESO-Very Large Telescope on Paranal. As described in Chapter 2, SPIFFI was then brought back to Garching, optimized, furnished with a new (but still equipped with an engineering-grade) detector, and permanently installed on UT-4 of the VLT in summer 2004. In early 2005, this second engineering grade array was replaced by a new, science grade detector.

In spite of these changes, the overall data reduction strategy remained mostly the same, although with each subsequent array, reduction became somewhat simplified by the improving cosmetic quality. In many steps, reduction of SPIFFI data does not greatly differ from the established reduction schemes used for near-infrared longslit data. It therefore follows the widely used IRAF longslit reduction package (Tody 1993), and was extended by R. Davies in 2003 to meet the special requirements of an integral-field device. However, this initial approach was mainly meant to provide a quick reduction scheme for initial inspection of the data, and not so much for a detailed analysis, so that a few adaptations were necessary afterwards. These improvements included enhancing the robustness of the wavelength calibration, and avoiding a few artifacts introduced by the reduction algorithm. Those changes did improve the quality of the reduction, as will be shown explicitly on the example of an artificial “toy galaxy” (with *a priori* known spectral and spatial properties) in Section 5. To illustrate the differences between the old and the new approach, the initial reduction scheme will be quickly described in that context.

A C-based package has been finalized in the meantime, and is, e.g., the basis of the ESO calibration pipeline (Abuter et al. 2005). However, it was not yet available at the time when most of the data for this thesis were reduced, and cannot be used to reduce GI data. For consistency, the GTO data included into this thesis were reduced with the same algorithms as the GI data, with some modifications where necessary. No detailed comparison was tried between the data reduction method used here and the package of Abuter et al. (2005), because the GTO data do not form the backbone of this thesis. However, a quick (eyeballed) comparison of data of $z \sim 2$ BX galaxies reduced with either method in another context than this thesis, does not indicate strongly different performances or systematic differences between the two approaches.

As a first step, the data reduction algorithms will be described that were used for this work. Section 2 gives an overview of the scheme developed to reduce the GI data, and Section 3 will describe the changes that were necessary for the GTO instrument.

2. Guest instrument data

SPIFFI commissioning and guest instrument (GI) runs were carried out between February and April 2003 on UT1 of the ESO VLT. Due to the overlapping with the instrument’s commissioning, observations were done by the SPIFFI instrument commissioning team.

Although SPIFFI uses a technique which is still novel in combination with the 10-m-telescope class – image slicing – to obtain spatially-resolved spectra of a contiguous field of view, data reduction schemes can be developed that are very similar to those commonly used for longslit spectroscopy. Any use of already available packages will have to be extended, however, to account for the uniqueness of the instrument. The basic algorithm, that was used to reduce the GI data and hence the main part of the data used for this work, is illustrated in the middle column of Fig. 1.

Dark subtraction

The initial step is to remove the dark current from the individual exposures. As part of the day-time calibration plan, exposures are taken with the same duration as used during the night and with one of the filter wheels in the “closed position”. Since the filter wheels are in thermal equilibrium with the cryostat, which itself is at a low enough temperature to not emit significantly in the near-infrared, the detector is not exposed to any light. Matching integration times with the object exposures is obviously important to provide an accurate estimate of the dark current but also because the number of “bad pixels” depends on integration time. Subsequently, in the data reduction process, these bad pixels need to be accounted for as to not add noise or to be mistaken for signal in the finally reduced frames.

Flat fielding

After the dark current is removed, it is necessary to correct for large-scale variations across the field-of-view. In this step, the data are “flat fielded”. Flat field calibration frames are taken during daylight with the instrument set in exactly the same configuration as for the object frames and are made by observing a uniformly illuminated surface. This surface can either be the lamp-illuminated dome of the VLT or an integrating sphere observed within the AO module. During the period when most of the data presented in this thesis were taken, only the illuminated dome was available for taking the flat field calibration frames. Residuals in the illumination pattern of this “flat” image are used to scale the response in each region of the detector accordingly for all individual frames.

Bad pixel correction

To account for static “bad pixels”, i.e., pixels with anomalous response (identified in either the dark frames or in the flat-fields), a bad pixel correction is applied, replacing the “bad” values by the averaged values of the 26 neighboring pixels in the three-dimensional data cube (which for this use is temporarily reconstructed at this step and then re-transformed into the original raw-frame).

Wavelength calibration

The individual frames are then wavelength-calibrated. To account for some spectral flexure between the frames, the frames are rectified and wavelength-calibrated using both arc-lamp spectra (taken during day-time calibrations) and the measured OH lines in each frame¹. Two columns are clipped on either end of each slitlet to avoid overlapping flux between slitlets that lie adjacent and thus improve the accuracy of the calibration, which is generally $\sim 1 \text{ \AA}$ in the GI data or within $\sim 20\%$ of one spectral pixel. In later data, they amount to 0.1-0.2 \AA . To rectify the frames, the algorithm collapses the spectra within each slitlet, assuming they are exactly 32 pixels long. Although this is not strictly correct, it is of sufficient precision for the GI data. (With the final design and

¹This method relies on the IRAF tasks “identify” and “reidentify” and “fitcoords”.

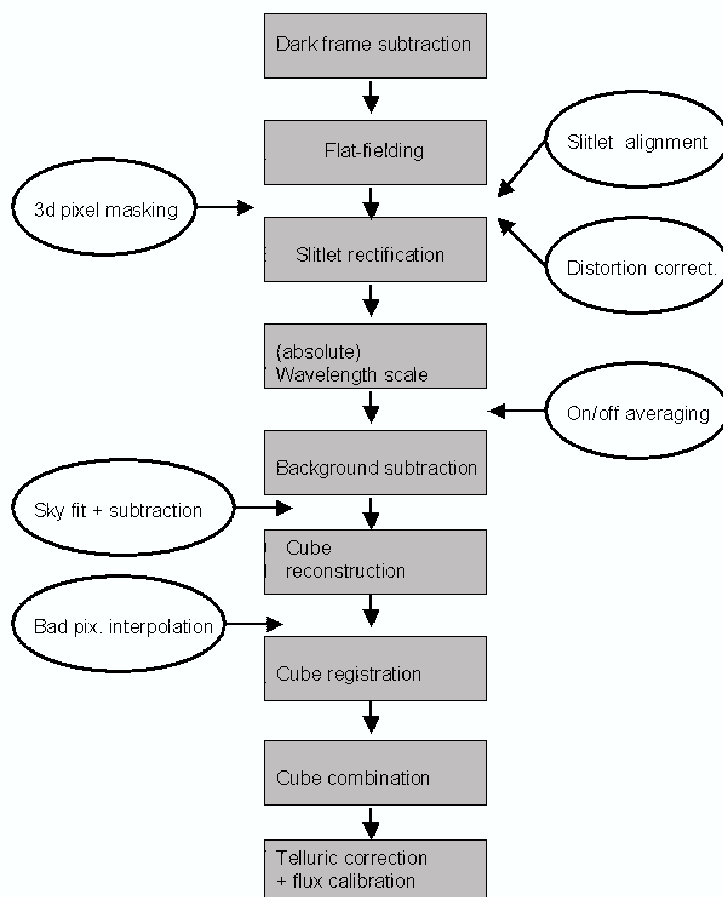


Fig. 1.— *Flow-chart of the various IRAF-based SPIFFI data reduction algorithms. Gray-shaded boxes indicate steps common to both approaches. Ovals in the left column name steps that are only in the original scheme, ovals in the right column those that were introduced with the updated method developed for this thesis.*

the larger detectors, however, an additional step is required to determine slitlet-lengths, which will be described in section 3.) Arc-lamp spectra are used to define the absolute wavelengths of the night sky lines measured in the frames. The algorithm then calculates individual dispersion solutions in each slitlet by fitting Legendre polynomials. Shifts between slitlets are determined by cross-correlating the night-sky lines.

Night sky subtraction

To mitigate against variations in the night sky emission, which are strongly wavelength-dependent, each sky frame was normalized to the average of the object frame separately for each wavelength. If bright sources were within the field-of-view, they were explicitly masked before calculating the average, applying a sigma-clipping algorithm. In the following, the empty “sky”-frames were subtracted from the according “on-source” frames. In spite of the normalization of the background frame, some OH lines show strong residuals in the sky-subtracted frames, leading to spikes that exceed the signal strength by far. They were corrected by averaging over neighboring spectral pixels, when a pixel differs strongly ($>20\sigma$) from the average of the surrounding spectral pixels, and has a wavelength close to that of a strong OH line. Thus the strong OH emission lines are clipped. (The better quality of the science grade array installed in the winter of 2005 made better sky-subtraction possible, so that for the data taken with the new array this step was not necessary.)

Cube reconstruction

The three dimensional data cubes were then constructed from the raw frames, assuming that each spatial row of the field was exactly 32 pixels long, and allowing only integer pixel shifts. Although this is not strictly correct, spatial resolution was slightly reduced. However, this method avoided loss of signal-to-noise due to resampling the data.

The cubes were then spatially aligned by cross-correlating the collapsed spectra. Again, maximum signal-to-noise was retained using only integer pixel shifts between the individual data cubes used in constructing the final data set with the total integration time. Depending on the individual source, either line- or continuum-images were used for cross-correlation, or the full data cubes. When combining the cubes deviant pixels were clipped.

3. Guaranteed time observations

Additional data were taken during early guaranteed time observations (GTO) in November and December 2004 and March and April 2005. In the 2004/05 runs, data were only taken in the K band. Individual and total integral times are summarized in Table 1.

Typical source diameters do not exceed a few seconds of arc, so that they occupy only a small area within the field of view. By adopting a dither pattern such that the source falls into distinct quadrants of the field of view, pairs of subsequent frames can be used for background subtraction. SPIFFI’s 2nd engineering- and science-grade detectors have a very uniform sensitivity across the entire field of view, which coupled with SINFONi’s uniformity of field, variations in the illumination can be neglected relative to the total sky background. Both properties are crucial for this method, because the background subtraction is done using different areas within the field of view (and thus different regions of the detector). As a benefit, overheads are obviously greatly reduced. Instead of requiring ~ 2.5 hours of telescope time for an hour on-source as in the GI run, in the GTO observations an hour on-source data were taken in ~ 1.25 hours (neglecting the time required to observe spectroscopic standard stars which can be done during twilight).

The differences between the SPIFFI GTO and GI instrument required some changes in the data

reduction scheme, although the overall strategy did not change. The most important change was in the size of the science grade array compared to the two engineering grade arrays. The science grade array is a 2048^2 device compared to 1024^2 for both engineering grade arrays. This factor of 2 better sampling with the new camera optics build for the larger array means that each slitlet doubled in the number of pixels and the spectrum is no longer under-sampled in the spectral direction. The slitlets are slightly shorter than 64 pixels. Although the difference is marginal for each slitlet (~ 0.3 pixels), this difference is systematic and, if not corrected for, sums to a difference of nearly 20 pixels in the last row of spatial pixels. It therefore cannot be neglected.

The SPIFFI calibration plan foresees dedicated day-time calibrations to determine the exact slitlet length with the aid of an artificial point source, however, it can also be measured directly from the data. Since the slitlet length does not vary within one night, the dark-pixel corrected and flat-fielded (unregistered) raw frames of all faint sources taken within one night are combined into an average raw-frame with good signal-to-noise ratio. Signal-to-noise ratios of the high-redshift galaxies are typically close to unity in the single frames. Therefore for the purpose of this calibration, the on-source frames can be considered as “empty”. Residuals of the sources will not appear in the average frame, because they fall onto different regions of the detector, due to the spatial dithering, and are suppressed rather than enhanced. The raw-frame shown in Fig. 1 of Chapter 2 was obtained in this way.

The algorithm assumes an initial slitlet length of 64 pixels. The central column of two adjacent slitlets in the raw frame is then taken as a reference, and in between these two midpoints, the position of the flux maximum (i.e. the night sky line) along the spectral axis is measured. The column is assigned to the slitlet where the spectral position is in better agreement with the central column. To avoid loss of signal-to-noise due to resampling, the length of each slitlet is assumed to be 63 pixels, if the cumulative difference is below 0.5 pixels, and 64 pixels, if it exceeds half a pixel. To ease later data reconstruction steps, these slitlets are mapped into a frame with 64 pixels per slitlet, leaving the last pixel empty when necessary.

The larger physical detector size also increases the image distortion, which originates from the projection of the intrinsically curved image onto a flat surface. This distortion is obvious in Fig. 1 of Chapter 2, and must be accounted for in the wavelength calibration. Especially, it makes the rectification of the spectra more difficult, as explained above for the GI instrument. Therefore an auxiliary procedure had to be introduced: The curvature is again measured from the averaged combined frame of all faint sources. The position of several strong night sky lines is measured column by column in the raw frame, and the measured difference between the columns is used as a zeroth-order curvature correction. The same offsets are used for the data and for the reference (lamp) frame which is used for the wavelength calibration in a similar way as in the GO scheme to obtain the absolute wavelength scale.

In the GTO data, frames taken within one template are generally registered according to the offsets determined during data taking and written into the header. Typical signal-to-noise ratios are large enough to optimize the registration of subsequent templates (especially those taken in different nights) by cross-correlating the line images. This is necessary, because, in spite of using blind offsets from the measured positions of acquisition stars, the pointing stability will lead to small (1-2 pixels) variations of the source position.

4. Standard star measurements

Like in all ground-based data, the wavelength dependent transmissivity of the Earth’s atmosphere leaves its imprint in the SPIFFI/SINFONI data. Although in principle, theoretical models of the atmosphere exist, it is best to correct for atmospheric effects by directly measuring a (sufficiently well known) spectrum of an astronomical object near the time of observation, and under similar conditions. Practically, most commonly used are early-type stars (O to A type, approximated by a black body with the according temperature) or solar analogs (approximated by a solar spectrum), which are observed at the time of observing, and are at similar air masses ² and coordinates near the target of interest. Stars of this type are used because either they are devoid of many strong absorption features from their atmosphere or in the case of the solar-analogues or roughly A0-type stars, have a high signal to noise template spectrum (Sun or Vega) readily available that can be used to remove the intrinsic atmospheric absorption lines. After dividing this “standard star” spectrum by the template spectrum (and accounting for prominent stellar absorption features, e.g. Br γ absorption), this spectrum yields not only the atmospheric absorption, but also the instrumental response function. Since SPIFFI oversamples the seeing disk, the correction procedure uses the integrated stellar spectra. This telluric correction was applied to the final, combined cubes. For the GI data, one standard star measurement was done per object and night. During the GTO data taking, standards were observed for each template (typically one star per hour), to be more sensitive to varying weather conditions. When flux variations did not exceed a few percent, the stars were averaged to improve the data quality, otherwise they were weighted according to the relative observing times before extracting the calibration information.

Stars are also used for absolute flux calibration. For the observations presented here, the same stars were used as in the telluric correction. Since the magnitude of the star and the transmission curves of the filters are known, the total count-rate collected from the star can be translated into the total flux, which then yields the calibration factor for the data. Different exposure times must be accounted for by another scaling factor.

The size of the seeing disk, and hence the spatial resolution of the data, were also estimated using the standard stars (complemented by dedicated PSF calibrators in the GTO data taking). Since stars are intrinsically point sources, the measured FWHM in right ascension and declination directly yield the FWHM of the seeing disk. To derive the overall seeing relevant for the final, combined cubes, the data were again weighted according to the fractional observing time of the data before averaging. Estimates of the seeing for the individual targets are listed in Table 1.

5. Scrutinizing the data reduction algorithms using a toy galaxy

5.1. Motivation

The data reduction algorithm described above is based on, but not similar, to the initial, IRAF-based software package, which was mainly a quick, early attempt to do a rough reduction of the early GI data. A few artifacts were evident, and originated from transforming the classical (two-dimensional) longslit-routines into a three-dimensional scheme, such as a wavelength-dependent background over-subtraction in slitlets containing bright line emission, which in the data cube essentially lead to “dark spots” in the image plane and “phantom absorption lines” in the spectra

²Air masses are given by the zenith angle z as $\sec(z)$

(see Fig. 3). The motivation to develop a new algorithm was to avoid such artefacts, while retaining a similar, or obtaining even a better, sensitivity.

High-redshift galaxies are also much fainter than the sky and telescope background. It is therefore crucial to have a thorough understanding of possible systematics introduced by the reduction algorithm, even if they are small relative to the total signal in each raw frame (or would not strongly affect high signal-to-noise data). To interpret the data in a most robust way, it is therefore an advantage to have a simple algorithm, whose behavior can be traced relatively easily and step-by-step.

Any data-reduction method will have some impact on the appearance of the data (and be it that it enhances signal-to-noise in just the way that is wanted), which might be too subtle to be *a priori* aware of. Adding a “toy galaxy” with an artificially produced spectrum to the raw frames, and reducing it just like the real data, allows to compare input and output in an independent way and to obtain a robust estimate of the systematic uncertainties introduced by the data reduction chain.

In the remainder of this section, the data reduction scheme that was introduced in the context of this thesis will be compared with the initial approach. In both versions, the initial steps are similar. Namely, these are:

1. Dark frame subtraction
2. Flat-fielding
3. A rough interpolation to account for strongly deviating pixels in the reconstructed cubes *before* sky subtraction
4. Wavelength calibration through cross-correlation and rectification of the slitlets.

These very basic steps are unlikely to strongly influence the signal, because they apply to the non sky-subtracted frames, which are dominated by the night sky emission. The galaxy spectra are very localized within the cube, with the exact position varying between individual frames. Hence it appears unlikely that imperfections in the flat-fielding or dark subtraction will have a large impact on the resulting combined data set.

Subsequent to these steps, however, the two methods diverge (see also Fig. 1). In the following, the initial method will be referred to as “method 1”, and the updated scheme as “method 2”, which is discussed in detail in Section 2.

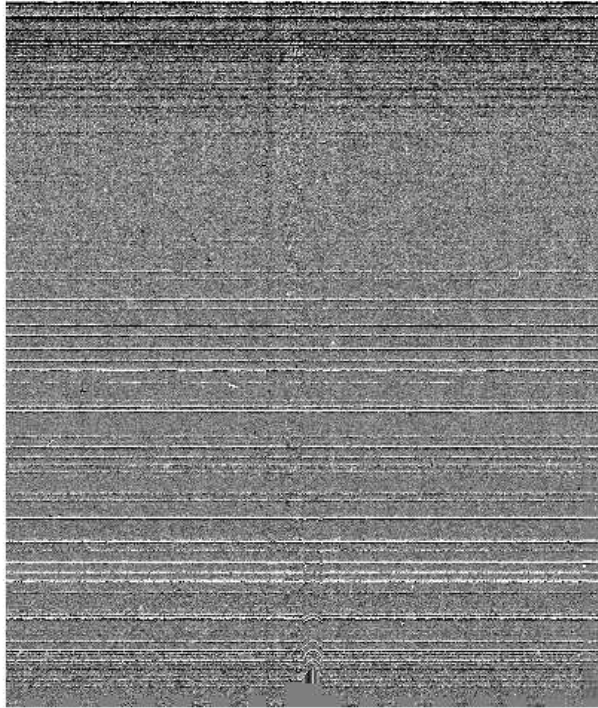


Fig. 2.— *Sky subtracted raw-frame reduced with method 1. Night sky line residuals appear as bright vertical lines across the detector. The characteristic slitlet pattern is lost because this frame is already wavelength-calibrated and rectified.*

5.2. Method 1 – the initial IRAF 3D-package

In method 1, empty sky frames are subtracted from the on-source frames without any correction. Because of undersampling of night-sky lines, and the time variations of the night sky, this results in a rather poor suppression of night sky lines, with residuals varying for different slitlets (c.f. Fig. 2). To minimize the residuals *after sky-subtraction*, a second order Legendre polynomial is fitted to each slitlet separately, and subtracted from the data. Because the SPIFFI-GI field of view consists of only 32 pixels in each direction, source emission, and especially emission lines, will lead to slightly, but systematically over-estimated backgrounds in the on-source frames, which ultimately results in artificial “dark spots” surrounding the source in the final cube (see Fig. 3). Since this effect is present in each single exposure, depends on the source-position, and is non-stochastic, it cannot be suppressed by co-adding all frames to the overall exposure.

Subsequently, cubes are constructed by re-ordering the pixels from the raw-frame to the three-dimensional cube. To suppress highly deviant pixels that are observed in the single-exposure cubes, those that differ by $>5\sigma$ from their 3-dimensional surroundings are replaced by the mean of the neighboring 8 pixels. Although this keeps pixels that are highly deviant from affecting the final spectrum it also potentially has a major impact on reducing the signal strength because it will tend to clip the peak of the line emission.

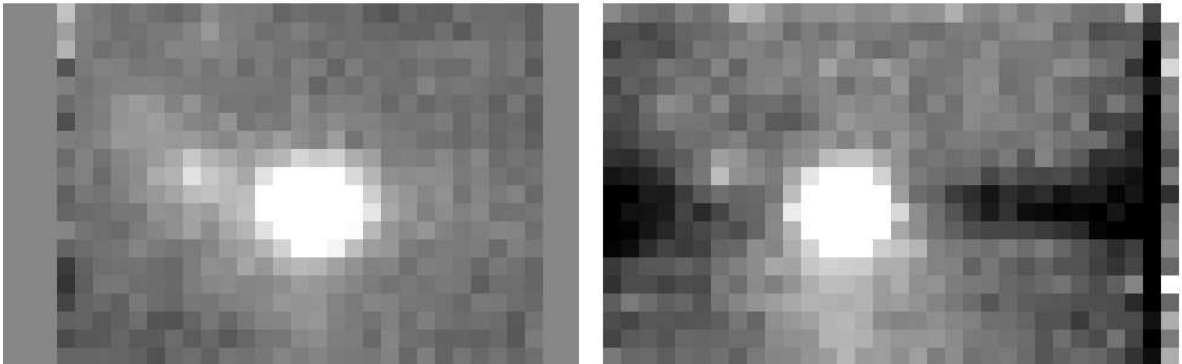


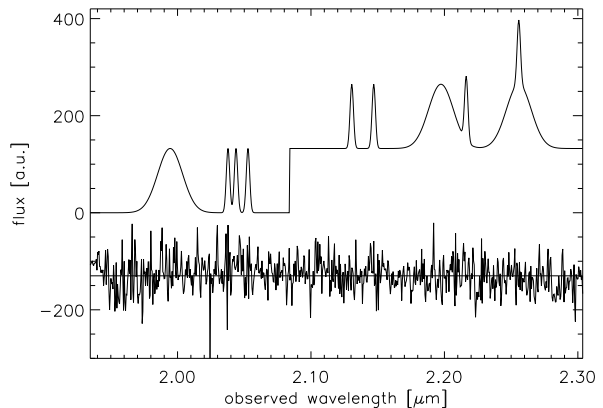
Fig. 3.— *H*-band line-free continuum image of the $z = 2.16$ radio galaxy MRC1138-262, extracted from data cubes that were reduced with method 1 (left panel) and method 2 (right panel). Method 1 produces “dark regions” adjacent to the bright point source, which are due to background over-subtraction.

5.3. The artificial spectrum of the toy galaxy

The SPIFFI data reduction using any method is relatively complicated due to the very nature of forming cubes out of 2-dimensional projections of the data set. With a large number of interpolations and the need to reject highly deviant pixels, there is some danger that flux could be lost or line profile distorted. To test this possibility, an artificial galaxy spectrum was added to a set of real data. These data were then reduced using the methods outlined previously. By measuring the properties of the reduced spectrum compared to that of the artificial input spectrum, the impact of the reduction methods can be quantified. An artificial input spectrum, consisting of “continuum” emission redward from $2.08 \mu\text{m}$ and several emission lines, is added to the measured raw frames of a subsample of 27 frames of the SMMJ14011+252 K-band data set.

The artificial spectrum itself is shown in Fig. 4. Its flux was chosen to be comparable with the signal of SMMJ14011+0252 (Chapter 6).

Since it is essential to recover line properties for a wide variety of situations, both “Broad lines” with a FWHM of 44 pixels were included ($\sim 3000 \text{ km s}^{-1}$), and various “narrow lines” with a typical FWHM of 6 pixels ($\sim 400 \text{ km s}^{-1}$). Considering the SPIFFI resolution of $\sim 150 \text{ km s}^{-1}$, this results in a typical intrinsic (deconvolved) Gaussian width of $\sigma \sim 160 \text{ km s}^{-1}$ for the “narrow lines”. Including features with a range of characteristics allows to investigate the interplay of night sky lines, continuum and broad and narrow line emission all from the same spectrum.



This artificial spectrum is smeared spatially to match the seeing disk ($0.4'' \times 0.6''$) of the actual data set as measured from standard star observations. An IDL-based algorithm was developed to derive the position of the “toy galaxy” in the raw frames from the chosen position in the combined cube, depending on position within the data cube and spatial dithering of the individual frames. The artificial signal was then added to each individual frame, and the frames were reduced according to the two methods.

Fig. 4.— *Artificial spectrum of the toy galaxy (above) and the original sky spectrum. The features of the artificial spectrum are discussed in section 5.3.*

5.4. Results

The reduced spectra are shown in Fig. 5 for reduction schemes 1 and 2. All spectra were extracted from $1.25''$ square apertures (5×5 pixels) which is approximately twice the full width at half maximum. Thus these extractions encompass the majority of the flux from the object.

In the following, “efficiency” ϵ will refer to the ratio of the measured flux to the flux of the input spectrum. To estimate ϵ , scaled versions of the input spectrum were fitted to the fully reduced spectra. Blue lines in Fig. 5 represent the input toy spectra. The lower spectrum in each panel shows the fit residual. For method 1, $\epsilon = 0.7$, i.e. the input signal flux was on average lowered by 30 %, while in method 2, $\epsilon = 0.93$. In either case the average count rate in the final reduced cube was negative because of over-subtraction in the blue part of the spectrum where there was no continuum ($\lambda < 2.08 \mu\text{m}$). For method 2, this over-subtraction was always within one standard deviation per pixel. This illustrates an unresolved issue in the reduction of the SPIFFI integral-field spectra: Although the night-sky subtraction in individual spectral pixels is sufficiently good (i.e., at or within 1σ) marginal overall systematic problems lead to residual over- or undersubtraction of the background. This over- or under-subtraction is most prominent when summing up while collapsing spectral areas within the cube. The presence of strong night sky lines (which are generally difficult to suppress) further complicates the situation, because the statistical background estimate will be more uncertain. This can be a problem when using SPIFFI data to estimate broad band magnitudes for example. This ability is important to retain in that it allows to estimate “line free” magnitudes for objects with high emission line equivalent widths and practically can save telescope time by

precluding having to take a broad band image of a source.

If the sky background is fitted with a function varying across the spatial planes (and/or spectral planes, as e.g. linear functions allowing for a slope or Legendre polynomials), then the background over-subtraction will be difficult to reconstruct (and correct for) after. If however a simple average is subtracted, that was obtained from each separate spectral plane (or from within each slitlet, leading to a slightly more complicated correction algorithm), then this can be easily reconstructed later on because it will lead to a constant offset across all images extracted from the data cube. Therefore, if the source is small enough to leave empty sky within the data cube, this offset can be measured in each individual image extracted over arbitrary spectral areas in the cube, and directly be corrected for.

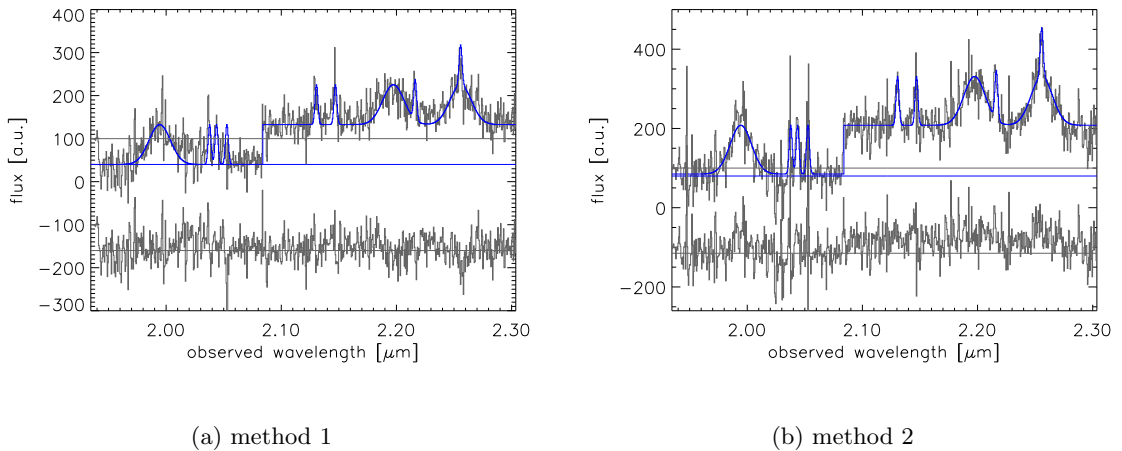


Fig. 5.— *The data cubes obtained from the fully reduced artificial spectrum using the two methods. In each panel, the upper spectrum (dark gray line) shows the reduced cube. The blue line indicates the rescaled input spectrum used in the fit. Lower panels show the fit residuals. Horizontal lines illustrate the shifts between the spectra. The shift of the residual is arbitrary, however, the offset between the black and blue horizontal lines in the upper spectra are a consequence of the background over-subtraction.*

Continuum

The continuum was chosen to set in at $\lambda = 2.0847$, and its measured position is $\lambda = 2.084$, ~ 1.5 pixels to the blue, in each reduced version. This is within the spectral resolution. The scaling factors obtained for the two methods (see above) apply also to the continuum. No obvious impact of the data reduction scheme on the continuum shape was found with either method.

Narrow lines

Narrow lines were added with and without overlapping night sky lines, and with and without underlying continuum. This was to test the interplay of narrow lines with both the night sky lines and the continuum strength. It was aimed to investigate the overall influence of telluric spectral features on the line measurement, and not to set limits on line fluxes that can be detected relative to the strengths of night sky lines. Therefore a uniform amplitude was chosen for all lines (20 counts) and width (6 pixels or $\sim 400 \text{ km s}^{-1}$). Where lines were blended with night sky lines, residuals of intermediate strength were used.

With one exception, all lines were detected. Only when the line was entirely blended with a night sky line, and no continuum was present, method 1 did not lead to a line detection. Inter-

estingly, the according night sky line is fully suppressed in the original data cube. This illustrates that successful night sky line suppression does depend on the presence of a signal if method 2 is applied and does not scale directly with exposure time.

On average, the wavelengths of the reconstructed lines were blueshifted by $0.00066 \pm 0.00040 \mu\text{m}$, with method 1, and by $0.00044 \pm 0.00030 \mu\text{m}$ with method 2, probably due to the finite bin size of the spectral pixels. This offset is entirely consistent with no offset using either method. Method 1 tends to underestimate the line widths, albeit not at a significant level – measured FWHMs are on average $31 \pm 33\%$ lower than the input values. Method 2 over-estimates the FWHMs on average by $5.0 \pm 34\%$, again not significant. In either case, the widths of emission lines which coincide with night sky lines are not accurately recovered; the line width is under-estimated by $>50\%$ in all but one case, where for method 2, the width is over-estimated by 37% . For comparison, and to provide an impression of the intrinsic noise of the data cube after sky subtraction, the line width is recovered within $<2.5\%$ of the input value when the model spectrum is added to the final data cube. This shows that the presence of strong night sky lines contaminating the line emission severely limits the ability to recover accurate line parameters. It is also found that this is more subtle than one might naively expect. Not only will night sky lines hamper our ability to measure kinematics, but that using a measurement of the residual noise in the final cube as a basis of estimating the likely error in the line parameters will significantly under-estimate the true systematic uncertainty.

Integrated fluxes are on average underestimated by a factor 2 (0.5 ± 0.18) in method 1. Also when no night sky lines are present, the integrated flux is lowered by $>40\%$. With method 2, $\sim 1/4$ of the integrated flux (0.25 ± 0.34) is missed, albeit with a large scatter, which is mainly due to the missing flux in case of blending with night sky lines. In the absence of night sky lines, the flux is recovered with an accuracy of better than 20% . Errors, estimated by simply adding the artificial spectrum to the final data cube, the comparison spectrum, are $<4\%$ for all narrow lines. In principle, these limitations also apply when measuring the flux standards. However, given that for the flux calibration the shape of the curve is more relevant than the fluctuations, the accuracy of the flux calibration depends mainly on the signal-to-noise ratio and not so much on the ability to subtract the night sky lines. This may suggest that flux calibration data should be interpolated to remove the night sky lines using only regions where the night sky is dominated by continuum.

Broad lines

Broad lines were added both to the continuum and the continuum free part of the spectrum. In addition, narrow lines were added at the center and at the red wing of the broad line. The scatter of the wavelengths in the comparison spectrum yields the uncertainty of the measurement itself, in contrast to the two cases, where the artificial signal was reduced together with the data cube. The broad lines in the reduced data are blueshifted by on average $0.8 \pm 0.07\%$ in method 1, and $0.38 \pm 0.03\%$ in method 2. The widths of the broad lines are generally over-estimated by $40 \pm 34\%$ with method 1, and $23 \pm 20\%$ with method 2. Line fluxes can only crudely be determined, although on average they show good agreement with the input values: With method 1, the broad line flux is underestimated by on average $6 \pm 37\%$, with method 2 it is overestimated by $16 \pm 12\%$. Given the small number of broad lines, however, mean values are only of limited significance. However, the scatter is assumed to be representative and is generally consistent with good estimates of the input parameters of the broad lines.

Signal-to-noise ratio

Given all the possible sources of systematic uncertainty identified through this exercise, it is important to ask: What about simple estimates of the signal-to-noise? While such a question may seem naive at best and ridiculous at worst, most of the time, only final data cubes can be used to estimate the significance of a line or continuum detection. So how reliable is a simple estimate using

the final reduced data cube? The lower spectra in each of the panels in Fig. 5 shows the spectra based on the different reduction schemes, with the scaled artificial spectra removed. The residuals depend on the reduction method (see e.g., the residuals at $\lambda \sim 2.15\mu\text{m}$), and also on the presence of a signal (e.g., the feature at $\lambda \sim 2.05\mu\text{m}$ or at the continuum 'break' at $\lambda \sim 2.08\mu\text{m}$). Strictly speaking, this means that a correct signal-to-noise ratio can only be measured *in situ*, but cannot be determined from nearby off-source (or "off-line") spectra, both spectrally or spatially. However, the deviations from the unmanipulated data are small when reducing the data using method 2. (The exception is the continuum free narrow line emission that is fully confused with a night sky line at $\lambda \sim 2.05\mu\text{m}$). In all other cases, the signal-to-noise ratio will only be marginally affected, when estimating, e.g., the strength of a night sky line residual.

5.5. Consequences and conclusions

Generally speaking, this study shows that data reduction methods should be preferred which do not correct for residuals, but rather avoid them. In addition, 'local' corrections (e.g., averaging over neighboring pixels in either the two dimensional spectrum or in the cube) bear the risk of increasing the noise while perhaps decreasing the signal and thus overall decreasing the signal-to-noise of the final cube. If counts from adjacent pixels are averaged, then this should be done *before* sky subtraction, so that the presence of the source (which is typically very faint when high redshift galaxies are observed) will not affect the background estimate. Otherwise the small field of view will be dominated by the source for all but the faintest sources, and over-subtraction of the night sky will alter the characteristics of the spectra ("dark spots" neighboring the source within image rows). Nonetheless, the simplest, lowest order correction functions should be used (like the average in method 2 rather than the Legendre polynomial in method 1), to ensure that the resulting background oversubtraction can be very easily recovered in the final data set. Imaging data are constructed by extracting along the spectral axis of the data cube. Therefore, even when the spectra are insignificantly, but systematically over-subtracted, this will lead to an obvious negative region or overall background in the resulting image. Nonetheless, with either method, the presence of bright sources within the field of view, and especially in the same slitlets as the source (e.g., foreground stars) should be avoided if possible.

Overall, data reduction method 2 leads to a better representation of the input (artificial) data. The original spectrum could almost entirely be recovered (scaling factor 0.93) from the reduced cube, whereas in method 1, only 70 % of the input flux is measured. This has consequences especially for the measurement of broad lines, that are hard to discern in Fig. 5. Although the data reduction introduces a small scatter of the observed line positions, the additional uncertainties are negligible. More worrisome are the changes in line width and fluxes, especially in the presence of night sky lines and for broad lines if using method 1. A flat, featureless continuum is well recovered with both reduction methods (including the position of strong spectral breaks).

6. Extracting line and continuum data

The SPIFFI data cube contains the full spectral information for a contiguous $8'' \times 8''$ field of view (using the relevant $0.25''$ pixel scale). From these data, separate line and continuum images were extracted using the following schemes:

Table 1:: Observations

Source (1)	band (2)	$t_{exp,tot}$ (3)	$t_{exp,sg}$ (4)	date (5)	seeing (6)
SMM14011-0252	J	4800	300	March 26, April 4, 2003	$0.6'' \times 0.4''$
	H	7200	300	March 25, 27 and 28, 2003	
	K	27600	600	Feb 8, 9, 11 and 12, 2003, March 23 and 25, 2003, April 4 and 5, 2003	
SMM04431+0210	K	15600	600	Feb 9,12, 2003, Mar 23,24,25,28,2003	$0.7'' \times 0.45''$
MRC 1138-262	H	6600	300	April 9th, 2003	$0.6'' \times 0.4''$
	K	8400	600	April 7th, 8th, 2003	
1E0657-56 arc+core	K	11400	600	April 5, 6, 7, 9 and 10, 2003	$0.6'' \times 0.4''$
NIC1143-8043	H	9300	300	March 27, April 4, 5, 10, 11, 2003	$0.92'' \times 0.76''$
Q0347-383 C5	K	14400	600	Dec 20, 2004	$0.55'' \times 0.49''$
Q0201+113 C6	K	3600	600	Dec 21, 2004	$0.75'' \times 0.79''$
Q1422+231 D81	K		600	April 7th, 8th, 9th, 11th 2003	$0.67'' \times 0.43''$

Column (1) – Source name. Column (2) – Obs. band. Column (3) – Total on-source observing time in seconds. (4) – Individual exposure time per frame in seconds. (5) – Observing date (6) – Seeing of the co-added cubes (FWHM). Observations in 2003 were carried out with the GI instrument, in 2004 with the final layout.

Continuum images:

Obtaining continuum images is not only complicated by emission lines originating from the target, which would be clipped easily, but also by the presence of numerous night sky lines, that cannot be perfectly suppressed. Their higher brightness compared to the sky background leads to (in absolute numbers) intrinsically larger scatter in the sky-subtracted data, and in many cases perceptible residuals are dominant even in combined cubes of several hours exposure time.

To minimize the impact of such (spectrally) localized features, polynomials (typically of order 5) are fitted to each individual spatial pixel within the full SPIFFI spectral range, clipping deviant spectral bins. The fitted spectra that fall within the “classical” band widths (i.e. 1.17-1.33 μm in J, 1.49-1.78 μm in H and 2.03-2.37 μm in K) are then collapsed to yield continuum images that are reasonably unaffected from lines. Using SPIFFI’s full spectral bandpass for the fit, and collapsing only over wavelengths within the (smaller) “classical” bandpasses, serves two causes: Continuum magnitudes are directly comparable with those obtained, e.g., through near-infrared broad-band imaging. Measured magnitudes can readily be used without taking into account SED-dependent corrections. In addition, the fit is more robust against features near the band edges, which could have a major impact, if the fitted spectra were restricted only to wavelengths within these bandpasses.

Line images:

Continuum emission was estimated on a (spatial) pixel-by-pixel base in a similar manner as for the continuum images. However, instead of retaining the continuum and clipping the lines, the spectral region around the emission line (typically ~ 2 FWHMs) is retained, and all other spectral bins are clipped. The continuum underneath the line is derived from the polynomial fit and subtracted.

The cube is then collapsed to yield the line image.

7. Error-estimates and instrumental resolution

The long total integration times with large numbers of separate integrations often spanning days or weeks result in changing conditions (weather, relative telescope pointings, source on different parts of the detector, etc.). Together with the relatively low signal-to-noise of observations of high redshift galaxies, these result in systematic effects, that can dominate the overall error budget. Estimating systematic effects is notoriously difficult, a rather detailed error assignment, at least on some “archetypal” data are therefore of great use to investigate the relative impact of statistical and systematic uncertainties.

Statistical errors are derived in the most direct way, i.e., by constructing Monte Carlo simulations for each line, using the line characteristics (signal-to-noise ratio and width of the final spectrum), and assuming that the detector and sky noise follow a Gaussian distribution. Ten thousand Monte Carlo events are simulated for each separate observed line and – thanks to the rather mature state of today’s computing hardware and according computing speed – all error estimates given in this thesis are based on the distribution of the measured compared to the input line characteristics. In light of the previous discussion, it may seem odd to assume simple Gaussian noise and to use the noise estimates from the data cube directly. Unfortunately, the previous analysis indicates caution in interpreting data strong affected by night sky lines. For data that are not confused with night sky lines, it is appropriate to make this assumption. Therefore, the approach here is to mostly use data far enough away from individual night sky lines and simply point out when there may be a problem. This is due to the difficulty in estimating the actual impact case by case.

This work is mainly concerned with estimates of the dynamical properties of galaxies such as their velocity dispersions and gradients. Measurements of this type depend crucially on the accuracy with which wavelengths can be measured and on the stability of these values between separate integrations and its reproducibility due to the large range of dates over-which the data may be taken. To estimate the scatter of the kinematic line parameters, K-band GI data frames of SMM14011+0252 were used, which span a comparably large range in observing dates, weather conditions, and telescope elevations (i.e., “air masses”). Several spectra from different regions in the field of view were compared, originating from data cubes taken in 4 nights in April 2003. Apart from an obvious dependence of the flux estimates from the weather conditions (including the seeing), variations between nights were negligible compared to the scatter within frames, and the intrinsic wavelength-dependence of the spectral resolution. Uncertainties on the estimated line positions have essentially no influence, uncertainties are $\sim 9 \text{ km s}^{-1}$ for the line widths and $\sim 6\%$ for the flux. These values were added quadratically to the Monte Carlo errors. Similar results were found for the H-band.

The same data sets were also used to directly measure the spectral resolution, which can be done easily because the widths of the telluric OH lines are known to have widths that are well below SPIFFI’s spectral resolution; the instrumental resolution determines the line width, which can be given as a linear function of wavelength:

$$\text{FWHM(K)} = 274.5 - 60.7 * \lambda[\mu\text{m}],$$

(with the FWHM given in km s^{-1}) for the full resolution spectra. If the spectra were smoothed

over 3 pixels before the fit (see Fig. 7), the best fit is

$$\text{FWHM(K)} = 438.6 - 102.6 * \lambda[\mu\text{m}],$$

In the GI data, an average line width of $145 \pm 15 \text{ km s}^{-1}$ was found, and $220 \pm 20 \text{ km s}^{-1}$, if the spectra were smoothed over 3 pixels. In the H band a similar analysis was done using night sky lines in the sky frames of NIC1143-8036a/b, originating from 3 nights in March and April, 2003. All air masses were near 1.8. Average line widths found to be:

$$\text{FWHM(H)} = 335.6 - 109.1 * \lambda[\mu\text{m}],$$

(with the FWHM given in km s^{-1}) for the full resolution spectra. If the spectra were smoothed over 3 pixels before the fit (see Fig. 7), a linear fit can be stated as:

$$\text{FWMH(H, sm3)} = 470.6 - 150.4 * \lambda[\mu\text{m}],$$

Since the scatter spans nearly the full range of the fitted function within the H band, for most purposes it is sufficient to use the average line widths instead. They are $\langle \text{FWHM(H)} \rangle = 155.8 \pm 14 \text{ km s}^{-1}$ for the full resolution data, and $\langle \text{FWMH(H, sm3)} \rangle = 223.5 \pm 16 \text{ km s}^{-1}$ if the data are smoothed over 3 pixels.

Since also K-band data of the GTO instrument was used for this thesis, a similar analysis was carried out to derive the according spectral resolution. Resulting distributions and linear fits are shown in Fig. 7. Fitting functions are:

$$\text{FWHM(K, GTO)} = 177.6 - 35.0 * \lambda[\mu\text{m}],$$

for the full-resolution data. If again the spectra are smoothed over 3 pixels, the resolutions are given by the relationship

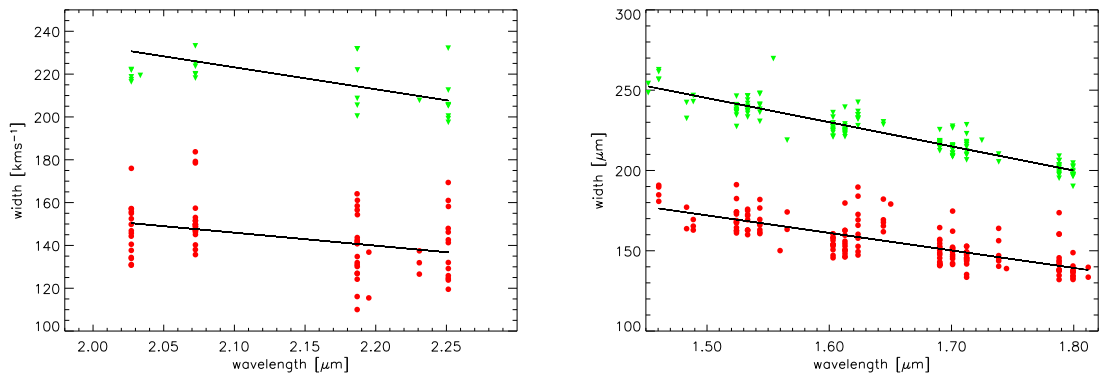
$$\text{FWHM(K, GTO)} = 255.6 - 56.1 * \lambda[\mu\text{m}],$$

Average resolutions are $102.7 \pm 8.3 \text{ km s}^{-1}$ if no smoothing is applied, and $135.4 \pm 8.7 \text{ km s}^{-1}$ if the data are smoothed over 3 pixels.

The measured line widths are a convolution of the intrinsic profiles with the instrumental signature. In order to derive the intrinsic line widths of astrophysical objects, the data must be deconvolved. This can be done by quadratically subtracting the instrumental resolution (as measured from fitting the night sky lines) from the measured values.

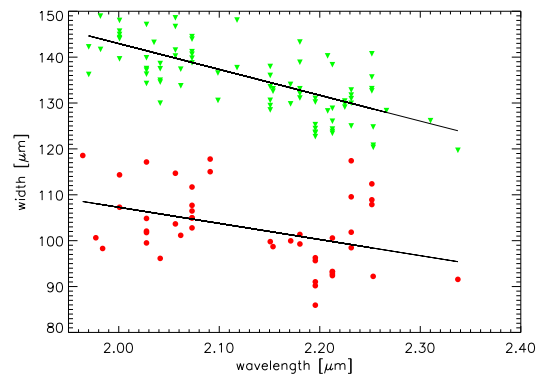
8. Auxiliary data obtained with other instruments

Depending on the individual source, auxiliary data were used (both imaging and spectroscopy), mainly taken with ISAAC on the VLT UT1 and the Wide Field Planetary Camera 2 and ACS on NASA's Hubble Space Telescope. Some of these data were kindly provided by other researchers, who worked on these data sets in another context, some were taken from the archive and reduced for the purpose of this work. The reduction of these data tightly follows the standard recipes given in the corresponding hand books. The origin and characteristics of these data will be indicated specifically in each case in the chapter where they are analyzed.



(a) K band (GI)

(b) H band (GI)



(c) K band (GTO)

Fig. 6.— Measured widths (FWHM) in the SPIFFI-GI K band, determined from night sky lines. Red dots indicate the widths of the data in the cubes with full spectral resolution, green upside-down triangles show line widths obtained after smoothing over 3 spectral bins.

Chapter 4

Tracing the properties of high redshift galaxies

1. Rest-frame optical nebular emission lines

Spectroscopy is the most important tool in astrophysics to reveal the physico-chemical properties of distant sources. Astrophysical spectra yield the redshift and hence – for a given cosmological model and large enough distance – also the distance. The spectral energy distribution (SED) as a function of frequency also holds the key to as distinct properties as mass, chemical composition, temperature and density, kinematics, and the energy source.

For a system in thermodynamic equilibrium (or which can at least with some justification be approximated by assuming a *local* thermodynamic equilibrium (LTE)), the photon wavelength reflects the dominating energy range of the emitting medium, defining the energy range of atomic transitions (at least to zeroth order) by the classical Maxwell-distribution for particle density n :

$$f_0(p) = \frac{n}{\sqrt{(2\pi mkT)^3}} e^{-(p-p_0)^2/2mkT}, \quad (4.1)$$

with the Boltzmann constant k , temperature T , momentum p , average (bulk) momentum p_0 , and particle mass m .

At optical wavelengths, continuum emission and absorption lines mostly originate from stellar atmospheres. In high redshift galaxies and predominantly at rest-frame UV-wavelengths, line absorption by galactic-scale outflows of cold gas, the so called “galactic winds”, is also commonly observed, and typically leads to absorption lines which are blueshifted with respect to the systemic recession (e.g. Pettini et al. 2001). The main stellar source of line emission is ionized low-density gas around massive hot stars with hard enough spectra to emit a sufficient number of photons above the hydrogen ionizing threshold (“HII regions”). This threshold is $E=13.6$ eV, or at a wavelength $\lambda=91.8$ nm (related by $E = hc\lambda^{-1}$, with the Planck constant h and speed of light c). Recombination will then lead to downward-cascading of excited states and to the emission of (among others) optical lines (Balmer series, i.e. dipole transitions to $n = 2$). It is a major cooling process for ionized gas at above $T\sim 10^4$ K, keeping the temperature of HII regions at roughly that value. Other ionizing sources exist and their somewhat different phenomenology is also observed in high-redshift galaxies (such as shocks due to winds or AGN). Identifying the ionizing source is important to correctly interpret the spectra, because emission line diagnostics is often founded on empirical relationships and is valid only for a limited range of source functions.

Due to the low density in HII regions, collisional de-excitation is marginal, so that higher-order transitions with accordingly lower transition rates occur, leading to “forbidden” lines from metastable energy levels. In HII regions, the most important forbidden lines originate from single ionized lines of nitrogen (designated [NII]), sulphur ([SII]), and the single and double ionized oxygen lines [OII], [OIII]). This mixture does not only reflect the typical ionization states in the plasma and reveals whether they are excited by electron scattering or UV photons. It also depends on the enrichment with elements across the periodic table, produced by the stellar nucleosynthetic chains. The most important emission lines, which can be luminous enough for the purpose of high-redshift observations, are summarized in Table 1.

The different mechanisms will especially lead to different characteristic line ratios, and the underlying atomic processes were modeled for large ranges of typical environments in emission line nebulae. Codes available for this purpose are e.g. CLOUDY (Ferland 2004) or MAPPINGS (Kewley et al. 2005). The results of these simulations are given in the literature, e.g. Osterbrock (1989) or Kewley et al. (2001) and provide a robust method to identify the ionizing source. This is frequently done by using BTP-diagrams as shown in Fig. 1, where the relative strength of lines tracing high and low ionizing states are compared. To mitigate against extinction (Section 1.3), the ratios of the diagnostic lines with nearby Balmer lines are used.

The following paragraphs will shortly illustrate the physical basis of astrophysical emission line diagnostics. Detailed discussions are given in a large number of astrophysical text books, especially Osterbrock (1989) and Dopita & Sutherland (2003).

Table 1:: The principle optical emission lines.

line ID	λ_{rest}	z_{max}	use
(1)	(2)	(3)	(4)
[OII]	3726	~ 5.5	density/metallicity
[OII]	3729	~ 5.5	density/metallicity
H β	4861	~ 3.5	SFR/extinction
[OIII]	4959	~ 3.5	
[OIII]	5007	~ 3.5	BPT/metallicity
[OI]	6300	~ 2.5	BPT
[NII]	6548	~ 2.5	
H α	6563	~ 2.5	SFR/extinction
[NII]	6583	~ 2.5	BPT/metallicity
[SII]	6716	~ 2.5	density/BPT
[SII]	6730	~ 2.5	density/BPT

Column (1) – Emission line ID. (2) – Rest-frame wavelength. (3) – Redshift cutoff for the NIR atmospheric windows. (4) – Diagnostics.

1.1. Densities and temperatures

Within ranges of about 100 to 10^5 cm^{-3} , the gas density can be estimated from the ratios $[\text{SII}]\lambda 6716/[\text{SII}]\lambda 6731$ or $[\text{OII}]\lambda 3726/[\text{OII}]\lambda 3729$ (Osterbrock 1989). Some of the sources discussed in this thesis have bright enough emission in these line doublets, so that densities can be determined.

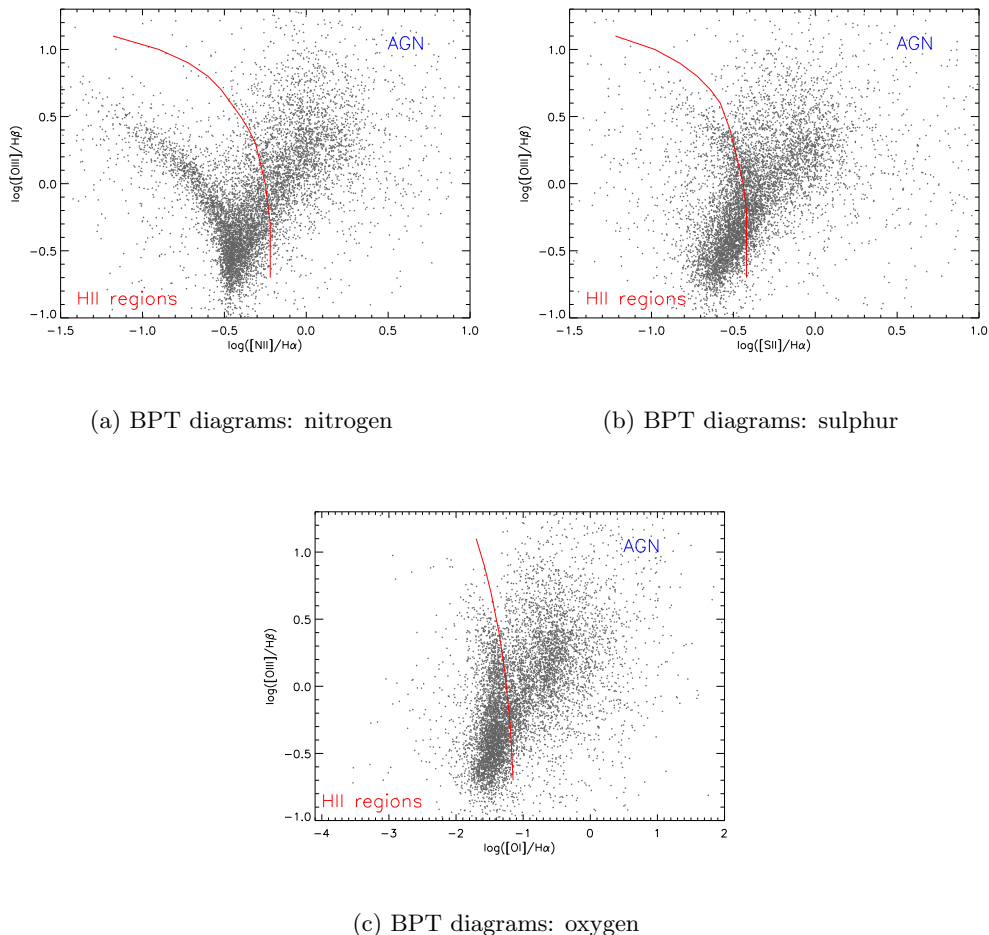


Fig. 1.— *BPT diagrams illustrating emission line diagnostics on the example of a subset of 50000 nearby galaxies publicly available from the SLOAN survey. Red lines indicate modelled dividing lines between AGN and HII-region like ratios taken from Osterbrock (1989).*

The line doublets are emitted from atoms of the same species, ionization, and from upper levels with very similar energy, so that their population does not strongly depend on temperature. If the electron densities in the gas are near the critical values for collisional de-excitation¹, then not all excited states will decay radiatively, but also via collisional channels. Branching fractions are different for the two transitions of the doublet, are set by atomic physics, and depend strongly on density. Thus, in optically thin environments the observed relative line strengths will yield the electron density in the gas. Fig. 2 shows the relationship between electron density and line ratio for the two doublets used in this work.

Due to the large density gradients observed within galaxies, the measurements cannot be representative, but depend on a number of selection effects. Only photo- or otherwise ionized regions will emit the line doublets. In addition, O^+ and S^+ are most abundant in the low-ionization regime. If the ionizing source is too strong, higher ionization states will dominate.

¹i.e., radiative and collisional de-excitation have equal transition probabilities

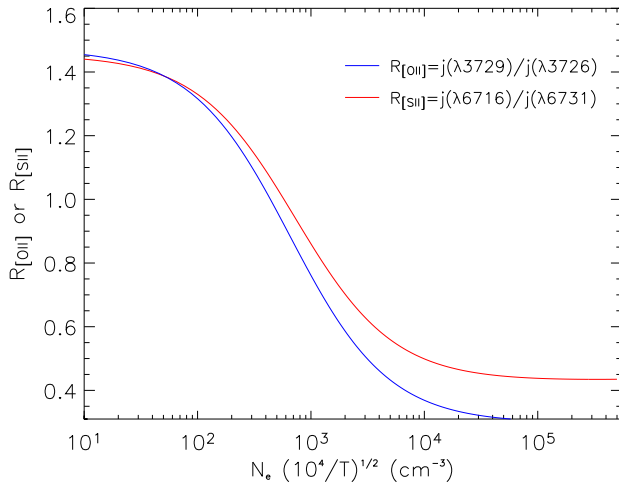


Fig. 2.— *Electron densities as a function of line ratios in the [SII] $\lambda\lambda 6717, 6730$ and [OII] $\lambda\lambda 3726, 3729$ doublets.*

atomic species with the same ionization but *at very different energies* will yield a measure for the temperature, because the population of the levels depends on temperature T ($\propto \exp(\Delta E/kT)$). Most commonly used is [OIII]. Photons are radiated in the $\lambda\lambda 4959, 5007$ doublet if the 1D_2 level is populated directly, or via cascading from the 1S_0 level after emission of a $\lambda 4363$ photon. Other channels are negligible. Branching fractions are set by atomic physics, and can be calculated, so that the relative line strengths of [OIII] $\lambda 4363$ to the doublet [OIII] $\lambda\lambda 4959, 5007$ will then provide a temperature measure.

The [OIII] $\lambda 4363$ line is relatively weak and accordingly difficult to measure in high-redshift galaxies. Therefore in the present sample the temperature cannot be measured directly, so that “typical” values must be assumed where necessary, derived from representative samples at lower redshift. It is fortunate in this context that most HII regions have a rather uniform temperature of $\sim 10^4$ K, so that uncertainties due to the unknown temperature will not dominate the error budget.

1.2. Element enrichment

Except for hydrogen, helium and a few isotopes of light elements, virtually all chemical elements were produced by stellar nucleosynthesis. Hence the chemical composition of a galaxy cannot be an arbitrary mixture of chemical elements, but roughly reflects the branching fractions obtained from the different nucleosynthetic chains. Nonetheless, the processes involved are sufficiently complex so that systematic variations in the element mix are valuable tracers for e.g. star-formation properties of galaxies in the past (e.g. the enhancement of α -elements relative to elements of the iron peak, $[\alpha/Fe]$, Thomas, Greggio, & Bender 1999). However, for many purposes (and especially for high-redshift studies with the according low signal-to-noise data), only the overall “metallicity” can practically be derived, i.e. the relative fraction of elements heavier than helium ² with respect

If the gas is either photoionized by an ionizing continuum or shock-heated, then [SII] emission forms in a region with a thermal pressure of a few $\times 10^{-12}$ n_e dynes cm^{-2} (e.g., Shull & McKee 1979). Most [SII] emission originates from the “partially ionized zone” of the emission line nebulae. For $T_e \approx 10^4$ K this thermal pressure is equivalent to $n_{tot} \approx 3 n_e$. This necessary condition for strong [SII] emission from the partially ionized zone will be used to calculate the mass and other characteristics of the emission line nebula when appropriate.

The method to determine temperatures from the line ratios is closely related to the density measurement: If collisional de-excitation can safely be neglected, the population of energy levels of the same

²“metals” for simplicity

to hydrogen. Although, strictly speaking, the term “metallicity” refers to the iron abundance, it is often used in a somewhat looser sense, and might relate to the relative abundances of other elements as well. Here it will be used as a synonym for “oxygen abundance” ($[O/H]$), which in the case of star-forming high-redshift galaxies is easiest to measure.

Metallicities are a valuable tracer of the integrated evolutionary history of galaxies. In the simplest case (“closed box model”) they increase monotonically as the galaxy evolves (i.e. with increasing number of generations of stars). However, it is known that this closed box model is too easy an approach, because it is at odds with metallicity measurements even in the solar neighborhood (“G dwarf problem”). In addition, both outflows of enriched material can occur (e.g. Lehnert & Heckman 1996a), as well as inflows of primordial gas. Nonetheless, metallicity does show correlations which hint a close relationship with galaxy evolution, e.g. the tight mass-metallicity relation (Tremonti et al. 2004), which indicates either that more massive galaxies have evolved more rapidly in the past than lower-mass systems, or that they are more efficient in retaining their gas content. The relative contributions of both phenomena are subject of current research, especially in the high-redshift regime, where the contribution of past outflows, and the according enrichment of the intergalactic medium (IGM) are studied directly (Adelberger & Steidel 2005).

$[O/H]$ can be measured directly from the emission line fluxes, but also depends on the electron temperature in the HII regions. To break this degeneracy, temperature-sensitive emission line ratios can be used, such as $[OIII]\lambda\lambda 5007, 4363$ (see Sec. 1.1). Unfortunately these involve the faint $\lambda 4363$ line and are therefore difficult to measure for high-redshift galaxies. More promising are therefore empirical metallicity calibrators, i.e. line ratios that are relatively insensitive to density, temperature, or ionization, and whose values were calibrated empirically against the direct measurements for a representative sample of galaxies, generally at low redshift.

One such empirical $[O/H]$ calibrator is R_{23} , defined as the ratio of emission line fluxes

$$R_{23} = \frac{I_{OIII,5007+4959} + I_{OII,3726+3729}}{I_{H\beta}} \quad (4.2)$$

Since it has originally been proposed by Pagel et al. (1979), R_{23} has been exhaustively scrutinized at low redshift, both using the integrated line emission of galaxies, and by comparing separate HII regions within nearby systems. This particularly includes the analysis of Tremonti et al. (2004), who used detailed fits to all available metal absorption lines in the spectra of 53,000 galaxies from the SLOAN Digital Sky Survey, and find that R_{23} serves as an overall good empirical metallicity calibrator. Nonetheless, this comparison confirms the long known shortcoming that R_{23} tends

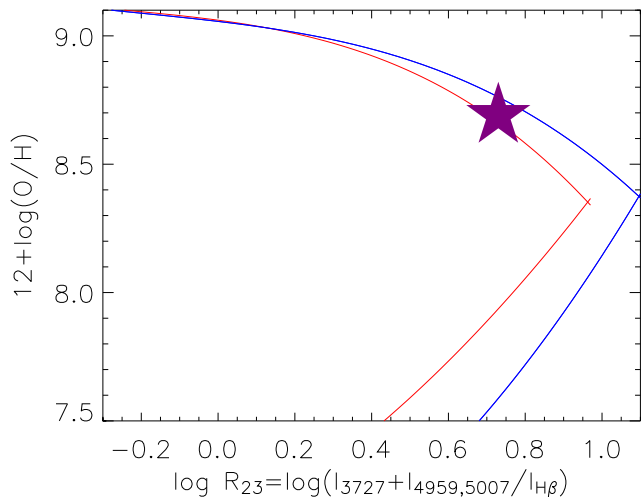


Fig. 3.— Relationship between R_{23} and $[O/H]$ abundance. Red and blue lines indicate the limits for ionization parameters $Q \sim 0$ and $Q \sim 1$, respectively. The purple star indicates the solar oxygen abundance, $[O/H]_{\odot} = 8.69$ (Allende Prieto, Lambert, & Asplund 2001).

to slightly underestimate the true abundances, especially at very high metallicities (several times solar), due to line saturation.

A number of caveats must be considered. R_{23} refers to the *emitted* line fluxes, whereas the *measured* fluxes are inevitably biased by extinction. If both $H\alpha$ and $H\beta$ are measured, then extinction-corrected line fluxes can be calculated using observed line fluxes and the Balmer decrement. The method will be described in Section 1.3.

Another limitation of R_{23} is its sensitivity to ionization, which in principle holds for all empirical calibrators using nebular line emission. This is easy to circumvent, as shown by McGaugh (1991), because the ionization can be measured directly from the relative [OII] to [OIII] line strengths. Another complication is the two-valued shape of the distribution for low metallicity, as seen in Fig. 3. Fortunately though, many high-redshift galaxies seem to fall near the turnover point of the distribution, so that this does not add much uncertainty (e.g. Pettini et al. 2001). If additional metal lines have been observed (in most cases [NII] λ 6583), their fluxes provide an independent metallicity constraint to break this degeneracy. If e.g. [NII]/ $H\alpha$ exceeds a few percent, then the upper, high-metallicity branch of R_{23} applies.

R_{23} allows to derive reliable metallicity estimates based on only 5, and typically 5 of the brightest, emission lines. However all five lines fall within the atmospheric windows only for restricted redshift ranges $z\sim 2$ and $z\sim 3$, and will in any case require observations in multiple bands. This is mostly due to the limited bandpasses of near-infrared spectrographs and the comparably low rest-frame wavelength of the [OII] emission lines. On the contrary, [OIII] and $H\beta$ emission lines have similar enough rest-frame wavelengths so that it is of interest how well metallicities can be derived if a dedicated [OII] measurement is missing ($R_{[OIII]}$ hereafter). Based on a low-redshift dwarf galaxy sample, Kobulnicky et al. (1998) attempt a calibration of [OII]-to-[OIII] line ratios, and find that for low metallicity galaxies, the scatter is substantial, but in many cases not larger than the intrinsic uncertainties in spectroscopic studies of high-redshift galaxies, especially when oxygen abundances are low. For e.g. $R_{[OIII]} \sim 0.6$ their calibration suggests $\log R_{[OII]} = 0.4 \pm 0.15$. Hence in this work, for galaxies where only [OIII] and $H\beta$ were measured, the relationship given by Kobulnicky et al. (1998) will be used.

Alternative metallicity calibrators have been proposed for high redshift studies, especially [NII]/[OIII] and [NII]/ $H\alpha$ (Pettini & Pagel 2004). Because [NII] λ 6583 and $H\alpha$ have very similar rest-frame wavelengths ($\Delta\lambda \sim 20\text{\AA}$), they can serve as a ‘‘poor-man’s’’ metallicity calibrator when no other strong emission lines were observed (e.g. due to limited bandwidth). From a sample of 137 resolved HII regions in nearby galaxies Pettini & Pagel (2004) derive the calibration

$$12 + \log[O/H] = 8.90 + 0.57 \times [NII]/H\alpha \quad (4.3)$$

However, [NII] fluxes can be strongly enhanced in the presence of shock ionization as e.g. caused by starburst-driven winds (e.g. Lehnert & Heckman 1996a) or the hard input-spectra of AGN. Winds are frequently observed in star-forming galaxies at low redshift, and appear to be almost ubiquitous at high-redshift. Nonetheless, [NII]/ $H\alpha$ might provide a representative metallicity measure if the [NII]/ $H\alpha$ ratio is small and AGN can be ruled out for other reasons, as e.g. the case in $z \sim 2$ BX galaxies (Shapley et al. 2004).

To use [NII]/[OIII] is more robust, although Pettini & Pagel (2004) show from low-redshift data that it scatters by factors of ~ 3 . The best-fit calibration function they find is

$$12 + \log[O/H] = 8.73 - 0.32 \times \frac{[OIII]/H\beta}{[NII]/H\alpha} \quad (4.4)$$

For $z \sim 2-3$, $[\text{NII}]/[\text{OIII}]$ is observationally more economical than R_{23} because it allows quantitative metallicity estimates from only 2 – instead of 3 – measurements in different wavebands. On the other hand, for $z \sim 3$ galaxies it cannot be used, because $[\text{NII}]$ is shifted out of the K-band for $z \geq 2.7$. This again makes R_{23} more appealing, because it can directly be measured for redshifts $z \leq 3.7$, and therefore allows to directly compare sources over a considerably larger redshift range without introducing methodological bias.

When possible, this work relies on the well-established R_{23} . (strongly supersolar) metallicities. The fraction of high-redshift galaxies with such large metallicities is probably small. If ionization is properly taken into account and if the appropriate branch of the calibrator can be determined, then its precision is significantly higher than that of $[\text{NII}]/[\text{OIII}]$.

All abundance measurements based on line emission are prone to intrinsic uncertainties, e.g. bias towards the most strongly line emitting regions. Especially for extreme starbursts and very young stellar populations, one can easily imagine that this is problematic, when the age of the burst is near the dynamical timescale. In addition, cosmological aspects might come into play when using locally calibrated relationships for high-redshift sources, such as systematic changes of the ionization, maybe caused by enhanced background radiation. However, to the precision with which high-redshift galaxy spectra are currently available, these limitations are a minor concern. In addition, the main goal is to compare the evolutionary states of galaxies at similar redshift. For these *relative* measurements, uncertainties in the *absolute* calibration, as well as *systematic* cosmological trends are less problematic.

1.3. Extinction

Extinction (i.e. scattering and attenuation) of light by gas or dust particles is a strong function of wavelength. Light is effectively reddened when passing through a cloud or the interstellar (intergalactic) medium, which is most commonly parametrized by the color excess $E(B - V) = A(B) - A(V)$, the difference of attenuations in the B and the V band. $A(\lambda)$ is usually given in magnitudes, and related to the extinction optical depth by $A(\lambda) = \log(e)/0.4 * \tau_{ext,\lambda} \sim 1.086\tau_{ext,\lambda}$.

Any “generic” extinction law can only be a crude approximation, due to the complexity of the microscopic processes involved, which depend e.g. on the dust grain properties. An empirical, nearly linear galactic extinction law has been derived to give the expected extinction as a function of λ^{-1} for optical wavelengths in the Milky Way, so that only the absolute magnitude of extinction along a given line of sight remains as free parameter.

Blindly applying the galactic extinction law to extragalactic systems is a major source of uncertainty. When explicitly measuring, e.g. the extinction in the low-metallicity, gas rich Small Magellanic Cloud dwarf galaxy, significant differences were found. Calzetti (1997) have examined a sample of 25 UV-selected, mostly star-forming galaxies from UV to infrared wavelengths, with the goal to derive an empirical extinction law which is tailored to the properties of star-forming galaxies rather than the Milky Way, and is valid over essentially the full wavelength range where extinction is relevant (UV to near-infrared). Their reddening law is shown in Fig. 4. However, issues remain, e.g. poorly understood discrepancies between the reddening determined from continuum and line emission (Calzetti 1997) These point towards complicated spatial dust distributions, most likely due to dusty cocoons around young stars. Moreover, extinction is of course a major limitation in heavily dust-enshrouded galaxies, and especially for observations of their nuclear regions. At low redshift, this can be overcome by observing at longer wavelength, e.g. in the NIR. At high redshift, unfortunately, this way to circumvent the dust is not possible, due to observational limitations,

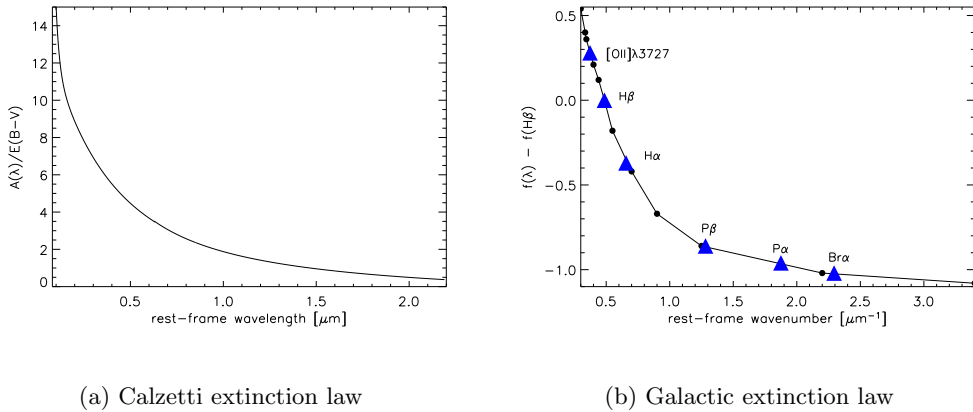


Fig. 4.— *Total-to-selective extinction law according to Calzetti (1997) for a wavelength range from 800 Å to 22000 Å and assuming a uniform dust “screen”.*

most of all the low atmospheric transparency, detector sensitivity, and spatial resolution.

Two-component theoretical models combining separate extinction laws for dust-enshrouded HII regions around massive young stars and for the ambient ISM favor a similar scenario. They were found to be consistent with the observed spectral properties of a few low-redshift galaxies from the UV to infrared wavelengths (Charlot & Fall 2000), including the attenuation of Balmer lines. These models account for the short lifetimes of the cocoons, but still require template extinction laws to take into account the (measured) dust compositions of the individual galaxy.

Since most high-redshift galaxies are actively star-forming, the Calzetti-law is well suited in the high-redshift context. However, the presently available data sets are not sufficient to systematically probe any extinction law for high-redshift galaxies. Systematic differences might arise, e.g. from evolutionary effects, such as different dust properties. Some indications that dust at high redshift might have different properties have been found in high-redshift radio galaxies (Reuland et al. 2004). In the context of this thesis, the Calzetti and the two-component law are used to correct model SEDs for extinction (see also Section 2).

Because extinction of line and continuum emission are found to be different, the extinction of the line emission is measured and corrected for explicitly, using the Galactic extinction law and the observed intensity ratio of the two Balmer lines H α and H β , when both lines are measured (or when limits on the H β flux can be given). Since all studied emission lines are within a rather restricted wavelength range ($\sim 3000 - 7000$ Å), the results obtained with different extinction laws do not greatly differ. The intrinsic Balmer decrement is mildly temperature dependent, but for most applications in this work can be assumed to be $F_{H\alpha}/F_{H\beta} = 2.87$, which is the value for $T = 10^4$ (Osterbrock 1989). If shock-excitation dominates, then temperatures can be higher and the intrinsic Balmer decrement depends on the shock velocity. In cases where this applies, the intrinsic Balmer decrement will explicitly be stated.

In the context of optical line emission, as most relevant for this work, the convention is to give extinction relative to H β . It follows from the galactic extinction law $f_g(\lambda)$ and

$$\frac{F_{H\alpha}}{F_{H\beta}} = \frac{F_{H\alpha_0}}{F_{H\beta_0}} \times 10^{-c(f_g(H\alpha) - f_g(H\beta))}, \quad (4.5)$$

where F_λ and F_{λ_0} denote the extinguished and intrinsic flux at wavelength λ , respectively, and $F_{H\beta}$

and $F_{H\beta_0}$ denote the $H\beta$ fluxes. The logarithmic reddening constant c is found from the measured Balmer decrement $F_{H\alpha}/F_{H\beta}$ by setting

$$c = 2.7 \times \log(F_{H\alpha}/F_{H\beta}) - 1.24 \quad (4.6)$$

The galactic extinction law $f_g(\lambda)$ then yields the extinction corrected line fluxes for $H\alpha$ and all other lines.

Not all galaxies in this sample have $H\alpha$ and $H\beta$ measured. For some targets, meaningful constraints on extinction could be set from fitting the SEDs with population synthesis models (see Section 2). In cases where this is also not possible, a fiducial $A_V \sim 1$ mag is assumed, which is the average extinction in the integrated emission of galaxies at low redshift.

When the light of high redshift galaxies passes through the ISM of the Milky Way, it is already shifted into the infrared so that additional galactic extinction will be very low. Therefore, unlike in the low-redshift regime, the impact of the Galactic ISM on the observed signal is (generally speaking) negligible. The same is the case for sources that are lensed by foreground clusters at intermediate redshift ($z \sim 0.25$). The reddening due to the IGM is much less than the intrinsic reddening within the high-redshift source. Therefore it can equally be neglected.

1.4. Kinematics

The intrinsic kinematics of the targets were derived from the spatially-resolved emission lines in the SPIFFI data. Systematic redshift variations were found within most of the galaxies. They yield intrinsic motions of the source along the line of sight, simply based on the Doppler effect. To calculate velocity shears Δv from wavelength shears, one sets

$$\Delta v = \frac{\lambda - \lambda_0}{\lambda_0}, \quad (4.7)$$

where λ_0 denotes the systemic observed wavelength taken as reference value, and λ the local observed wavelength, which might vary across the source. v is given in units of the speed of light.

The width of the line yields the velocity dispersion $\sigma = \text{FWHM} / 2.355$ ³. The observed line widths often do not greatly exceed the instrumental resolution. To obtain the intrinsic line width $FWHM_{int}$, the lines must therefore be deconvolved using the observed $FWHM_{obs}$ and instrumental resolution $FWHM_{inst}$

$$FWHM_{int} = \sqrt{FWHM_{obs}^2 - FWHM_{inst}^2} \quad (4.8)$$

Generally speaking, the instrumental resolution is not high enough to measure the velocity dispersion due to turbulent motion within individual HII regions (Rix et al. 1997). Therefore the line widths can be assumed to not be dominated by the “micro”physics of individual HII regions, but large-scale gravitational motion for quiescently star-forming, rotating galaxies. Chapter 9 will show that this is not generally true, e.g. for radio galaxies with strong AGN feedback.

³assuming a Gaussian line profile.

1.5. Line profiles

The comparably small signal-to-noise ratios and overall small number of independent spectral resolution elements per emission line lead to line profiles that are approximately Gaussian in the SPIFFI cubes, although intrinsic profiles might have different shapes. An important exception are blue wings, which are observed in some of the galaxies, and which reach terminal (bulk) velocities of a few 100 km s^{-1} . These originate from outflowing gas along the line of sight, which is due to either supernova or AGN-driven feedback.

2. Evolution of stellar populations

Individual stars and emission line nebulae have been resolved only in a small number of nearby galaxies. In all other cases, a galaxy's SED is composed of the emission of numerous heterogeneous objects, e.g. stars, dust and nebulae. In order to disentangle these components, and draw conclusions regarding the global properties of the galaxy, computational packages have been developed, which simulate the integrated emission of complex astrophysical systems, such as star clusters or galaxies. Three such codes have been used in the framework of this thesis:

- STARBURST99 (Leitherer et al. 1999)
- STARS2000 (Sternberg, private communication)
- ISOCHRONE SYNTHESIS (Bruzual & Charlot 2003)

Their basic approaches are similar: All three algorithms use stellar evolutionary tracks and spectral libraries to infer and calibrate the integrated emission of populations of stars with different masses, but within a common evolutionary framework. By assembling a stellar population with a chosen initial mass function (IMF), the integrated emission of the aging population can be studied. In addition, colors can be extracted for different redshifts, and various extinction laws can be fitted, e.g. the Calzetti-law or the prescription by Charlot & Fall (2000) (see Section 1.3). Input parameters include generally the metallicity, extinction and the star-formation history: Was the dominant stellar population created in an instantaneous burst, with a (e.g., exponentially) declining rate, or are stars formed continuously over cosmologically significant time scales ?

Correctly modelling all stages of stellar evolution is a complex task, because short evolutionary stages contribute that are not very well studied, but might have a significant impact to the global emission at certain evolutionary steps (e.g., AGB stars in the near-infrared ; Maraston et al. 2002). In addition, in many cases (and especially when the data cover only optical wavelengths) age, metallicity and extinction are degenerate, which leads to large irreducible uncertainties.

The three applied packages are optimized for different wavebands (e.g., the rest-frame near-infrared for STARS2000) and galaxy types (e.g. actively star-forming, but not too strongly dust-obscured galaxies for STARBURST99). As a result, STARBURST99 allows to model nebular emission in addition to the stellar SED, and optionally includes winds. All three packages provide a wealth of additional information concerning color evolution, line indices, star-formation rates, ionizing photon flux, etc.

On more practical grounds, the packages also differ in computational speed, user-friendliness and specific input parameters (e.g., different built-in extinction prescriptions). However, their results do not drastically differ in most cases (A. Sternberg, private communication), and are

certainly of good enough precision to be – in most cases – mutually interchangeable for high-redshift galaxies. Therefore, all three packages were used in the framework of this thesis.

2.1. Star-formation rates

Only the most massive ($> 8 M_{\odot}$), young stars in a population, namely O and B types, are hot enough to ionize the surrounding hydrogen and form HII regions. These stars evolve rapidly, producing the first supernova explosions a few 10^7 yrs after the onset of star-formation. Typical variability time-scales in star-forming stellar populations can be derived from very basic causality arguments such as dynamical time scales (Lehnert & Heckman 1996a), and are much larger, on order $10^8 - 10^9$ yrs. Therefore the imprints of young, hot stars in galaxy SEDs can be used in a rather direct way to approximate current star-formation rates.

Consequently, UV continuum and line emission is the natural choice to measure the emission of early-type stars, especially at high redshift, when the rest-frame UV emission is shifted into the observationally more convenient optical wavebands, although of course extinction must be corrected for. Naively, namely Ly α line emission would be a prime signature to quantitatively measure the contribution of young stars to the overall SED. However, UV emission, and especially the resonant Ly α line, is very susceptible to optical depth effects, and the spectra of high-redshift galaxies show strong absorption (e.g. Shapley, Steidel, Pettini, & Adelberger 2003). Absorption and scattering of the UV-emission, and even changes in the line profiles, are commonly observed in these sources and may dramatically alter the results. Nonetheless the luminosity of the UV continuum emission, namely emission at wavelengths $\sim 1500 - 2800 \text{ \AA}$, has been calibrated against stellar population models (e.g, Kennicutt 1998), and is widely used to estimate star-formation rates.

In an alternative way, which is much less affected by extinction and radiative transfer and is very relevant for this work, luminosities of the hydrogen Balmer lines are used to probe star-formation rates. Due to the faintness of high-redshift sources, the method is essentially restricted to H α (which falls into the atmospheric windows for $z = 2 - 2.6$) and H β (for $z \lesssim 3.6$).

The luminosity of the Balmer lines is directly related to the number of ionizing photons by the branching fraction of the observed Balmer line with respect to the overall recombination cross section and can in principle be calculated. However, in practice this simple conversion will not yield the correct rates, due to a number of reasons, such as extinction, unknown escape fractions of ionizing photons, energy loss by collisional excitation of metals, etc. Therefore empirical relationships, derived from population synthesis models, and scrutinized with low-redshift galaxy samples, are more reliable. The most frequently used calibration is that of Kennicutt (1998), which is also applied in this work, using extinction-corrected line fluxes when possible. It is given by

$$SFR[M_{\odot} \text{ yr}^{-1}] = L_{H\alpha}[1.3 \times 10^{34} \text{ W}]. \quad (4.9)$$

and is valid for a 1 to $100 M_{\odot}$ Salpeter IMF ⁴(Salpeter 1955), as opposed to the original relationship of Kennicutt (1998), which used different mass cutoffs. As only the high mass stars in the population contribute to the hydrogen ionizing flux, is it obvious that the choice of the IMF, and especially its high-mass cutoff, has a large impact on the derived SFR.

Whereas star-formation rates derived from optical and UV measurements are fairly reliable for

⁴ $dM/M \propto 10^{-2.35}$. Although different relationships are used, overall little scatter in the IMFs of different systems have been observed. Lower and upper mass cutoffs currently are the largest uncertainties.

quiescent star-formation, they obviously break down in the most vigorously and dusty starburst galaxies, especially in infrared-luminous sources (LIRGs and ULIRGs), and in mergers. Extinctions in these systems can reach many magnitudes even in rest-frame near-infrared wavebands, and the areas are optically thick to the Balmer and Lyman series. In these cases, star-formation rates can only be estimated from the far-infrared flux [i.e., from the dust re-processed UV emission, see] (Kennicutt 1998). The faintness and small spatial extent of high-redshift galaxies, however, make this approach also difficult. Although global star-formation rates can be determined from far-infrared observations, exactly localizing the burst within a source from far-infrared and sub-millimeter data is far from being straight-forward (see e.g., the discussion of the CO emission in SMMJ14011+0252, Chapter 6), and observations are time consuming and not always possible with ground-based instruments. In these cases, extrapolations are necessary, which bear additional uncertainties given that they commonly rely on empirical relationships established at low-redshift, and might be susceptible to evolutionary differences, e.g. in the dust properties (Reuland et al. 2004).

3. Galaxy masses

3.1. Dynamical masses of elliptical and disk galaxies

Dynamical mass estimates are the most direct and robust, but also the most laborious way to measure the mass of an extragalactic system. If one wants to also include the non-luminous and the dark matter content of a galaxy, then dynamical mass estimates are even the only direct approach. In this sense, they are also the only robust method to tie the assembly of dark matter halos (as described by theoretical models) to that of the observed galaxies.

Assuming virialized motion around the morphological galaxy center, the dynamics of complex systems can be roughly described by

$$M = v_c^2 \times r_g / G, \quad (4.10)$$

with gravitational constant G , circular velocity, v_c , and gravitational radius $r_g = GM^2/W$ (with mass M and potential energy W).

At low redshift, the formalism to derive the galaxy mass from spatially resolved emission line data takes into account the different dynamical properties of early and late Hubble types. Whereas disk galaxies have large angular momentum and well defined rotation curves⁵, this is not the case for all elliptical and spheroidal galaxies. Velocity shears and line widths observed with good signal-to-noise and spatial resolution allow to derive detailed dynamical models that ultimately yield not only the mass, but also, e.g., dynamical distortions due to past mergers (for a recent review, see Sofue & Rubin 2001).

Strictly speaking, all mass estimates can only yield the mass within the largest radius for which a velocity is measured. The non-Keplerian rotation curves of disk galaxies at large radii show that this is not representative for the total mass of the system. However, it is often sufficient to compare the mass profiles or integrated mass of galaxies within given radii, so that in some respects this is not a major concern. This is especially true for evolutionary studies.

⁵velocity v as function of radius r , $f = v(r)$

Rotationally supported galaxies

A number of avenues exist to derive the masses of disk galaxies. In the most simple form, Equation 4.10 can be used directly, setting r_g equal to the observed radius. The circular velocity v_c generally is different from the intrinsic velocity of a star or line-emitting cloud at a given orbit around a galaxy, due to, e.g., epicyclic⁶ motion or streaming. In extragalactic systems these lead to line broadening, because velocities are obtained from integrating over large areas. v_c also depends on inclination of the disk normal with the line of sight i , as $v_c = v_{obs} \times \sin^{-1}(i)$. The inclination is estimated (assuming axial symmetry of a thin disk) from the observed ratio (a/b) of the minor to major axis $i = \arccos(a/b)$. This relationship holds strictly only for infinitely thin disks, and will lead to underestimates of the true inclination, especially for dynamically hot⁷ systems and for galaxies that are seen nearly edge-on. Moreover, the final spatial resolution will tend to lower the measured velocity v_{obs} , especially for small targets with few independent resolution elements. Additional uncertainty comes from cosmological surface brightness dimming, due to which the observed velocity of faint targets will be biased towards the brightest patches. In a disk with smooth radial density profile, this will lead to an underestimate of the true circular velocity at a given radius, except for (at least partial) flat rotation curves. In addition, massive patches might alter the rotation curve (Elmegreen et al. 2005, estimate photometric masses of few $\times 10^8 M_\odot$ in the bright patches of some of their high-redshift “clump cluster” galaxies, which are $\mathcal{O}(0.1)$ of the total galaxy mass.).

In principle, this approach also involves a spherical mass distribution within the radius r . Lequeux (1983) have shown, however, that the relationship is approximately correct for most mass distributions⁸ without introducing major errors. Namely, they find that

$$M(r) = \frac{(0.6 - 1.0)rv^2}{G}, \quad (4.11)$$

with circular velocity v and gravitational constant G . If the kinematic data across the disk is well sampled, then the mass can directly be inferred from fitting the data with a mass model. This thesis adopts the simplest model which are exponential disks, where the surface density Σ declines with radius as

$$\Sigma(R) = \Sigma_0 e^{-R/R_d}, \quad (4.12)$$

with central surface density Σ_0 , and radius R given in units of the disk scale length R_d . The exponential decline of surface mass density with radius follows from the similar decline in surface brightness, which is observed in many disk galaxies at low redshift (Freeman 1970) and has lately also been directly observed with high-resolution imaging at high redshift (Ravindranath et al. 2004; Elmegreen et al. 2005). Accordingly, mass-to-light ratios are required to be roughly constant for all radii. This is of course not strictly correct, especially for large radii, where the dark matter content dominates. However, since cosmological surface brightness dimming makes it difficult to even securely identify the turnover radius in high-redshift galaxies with current observations, the contribution of dark mass is for the time being very difficult to address quantitatively. Ultimately, however, comparing the radial luminosity and dynamical mass profiles of high-redshift galaxies, and decomposing the contribution of luminous and dark matter as a function of radius, will be very interesting.

⁶peculiar motion with respect to the local standard of rest.

⁷large peculiar motions as compared to the bulk rotation

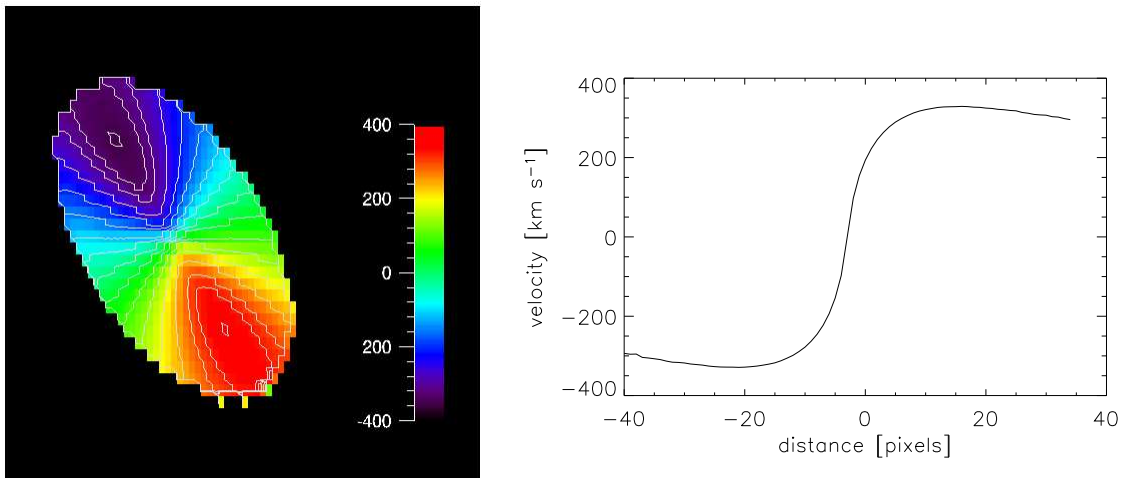
⁸Generally, these are composed of varying contributions of a spherical and a disk component, and a – mainly dark – halo

Following Binney & Tremaine (1987), the circular speed $v_c(R)$ of an exponential disk is given by

$$v_c^2(R) = R \frac{\partial \Phi}{\partial R} = 4\pi G \Sigma_0 y^2 [I_0(y)K_0(y) - I_1(y)K_1(y)], \quad (4.13)$$

with $y = R/(2R_d)$, gravitational constant G and the modified Bessel functions of first and second kind. The velocity field of an exponential disk is shown in Fig. 5. Contours show lines of constant velocity, and their characteristic shape lead to the commonly used name “spider diagram”. However, the properties of this field might be illustrated more directly by the one-dimensional rotation curve along the kinematic major axis shown in the right panel of Fig. 5. v_c rises almost linearly over radii of \sim a disk scale length. This inner part of the rotation curve is frequently referred to as “solid-body rotation”, although this name might be misleading, because the shape might originate from observational constraints⁹ rather than the intrinsic mass distribution. At larger radii, the rotation curve reaches its “turnover points” and flattens. v_c is typically measured from the rotation curve at $2.2R_d$, if the surface brightness is high enough to trace the emission far enough out.

In an undisturbed, rotationally supported, self-gravitating exponential disk also the line widths are predicted, which depend on the disk inclination, mass, and disk height. An isolated exponential disk will typically have larger line widths in the center, where the surface mass densities are higher, than at larger radii, where surface mass densities are lower.



(a) Velocity map

(b) Rotation curve

Fig. 5.— Velocity field and rotation curve of an exponential disk with $5 \times 10^{10} M_\odot$ mass and $1''$ characteristic radius. The colors in the map indicate velocities relative to the center and are given in km s^{-1} . Contours connect points of similar relative velocity and have the shape of the typical “spider diagram”.

Unfortunately, the small spatial extent and faintness of high redshift galaxies are a major hindrance in deriving well-sampled rotation curves well beyond the turnover points. Nonetheless, crude dynamical models have been fitted to some of the galaxies in this thesis, explicitly accounting for the seeing, coarse spatial sampling and – if applicable – distortions from gravitational lensing.

⁹e.g. beam smearing or extinction / absence of line emitters

In one case, evidence for turnover points has been found (see Chapter 7). The parameters derived from the dynamical model are biased by the small number of individual spatial resolution elements and low signal-to-noise ratios. The impact of these uncertainties will be discussed on the example of Lyman-Break galaxies in Chapter 8.

In cases where the size or the galaxy or signal-to-noise ratio do not allow well constrained dynamical fits, the mass will approximately be derived from setting $v_{obs} = 1/2 \times \Delta v_{max}$, where Δv_{max} is the maximum velocity shear measured within the source, and the radius is taken to be half the observed source extent.

If only line width measurements are available, then the mass of the rotating disk can be estimated from the observed radius r and the velocity dispersion $\sigma_{obs} = \text{FWHM} / \sqrt{2 \ln(2)}$

$$M(r) = \frac{(\sigma_{obs}/f_{stat})^2 r}{G} \quad (4.14)$$

where G denotes the gravitational constant and σ_{obs} the observed velocity dispersion. $f_{stat} = 0.6$ is a statistical correction factor, to account for the unknown inclination and apparent flattening of the velocity profile due to the seeing (Rix et al. 1997). It also takes into account systematic differences between line widths obtained from optical emission lines and HI, which is the most reliable tracer for galaxy kinematics – if it can be observed. The inclination correction is necessary in this case, because this approach assumes that the velocity dispersion is dominated by the rotational shear along the line of sight, which is true for typical rotationally supported disk galaxies, if they are not nearly face on. Strictly speaking, such a correction is valid only when deriving the mean mass of a statistical sample of randomly oriented sources. If used for individual galaxies, it corresponds to the assumption that this source has average inclination.

Pressure supported early-type galaxies

In the low-redshift universe, giant early-type galaxies appear to be gas-poor and not dominated by rotation about the center, but by triaxial distributions of orbits. They are gas-poor, so emission lines are generally not available to estimate their intrinsic velocity field, but stellar absorption lines must be used. The virial theorem can also be used to derive mass estimates for these systems, which is approximately

$$M(r) = \frac{c \sigma^2 r_e}{G}, \quad (4.15)$$

where σ^2 is the stellar velocity dispersion, r_e the effective radius of the galaxy, and G the gravitational constant. c is a constant depending on the density profile of the galaxy, $c \approx 2$ for an isothermal sphere. More realistic are estimates of c which take the empirical fundamental plane of early type galaxies¹⁰ into account. E.g., Bender et al. (1992) find $c \approx 4 - 7$ from dynamical modelling of about 100 low-redshift galaxies, with an average of ≈ 5 . This thesis adopts $c = 5$. Since these appear to be triaxial systems, inclination does not need to be corrected for.

¹⁰Central surface brightness μ_c , velocity dispersion σ and half-light radius r_e of early type galaxies are strongly mutually correlated so that ellipticals fall onto a narrow “plane” in the corresponding three-dimensional space.

3.2. The kinematic tracers

Direct measurement of stellar photospheric lines might be the most reliable kinematic tracer, but it involves high signal-to-noise continuum observations and is therefore not generally feasible for high-redshift galaxies. However, galaxies in the early universe were comparably rich in gas (e.g., submillimeter galaxies have gas fractions of ~ 0.4 in mass Tacconi et al. 2005) and photoionizing radiation of massive young stars as a result of the higher star-formation rate densities at high redshift (Giavalisco et al. 2004), so that typically the kinematics of the ISM are measured instead.

“The” classical kinematic tracer for galactic (gaseous) disks is neutral hydrogen, HI, as shown especially by the studies of the large scale gravitational potential of the Milky Way (Binney & Merrifield 1998). However, only a relatively small number of galaxies has had their HI velocity fields measured, and especially for high-redshift galaxies, studies of the rest-frame 21cm hyperfine structure emission will not be within the reach of radio telescopes before the “Square Kilometer Array” SKA will be fully operational, and probably not before ~ 2020 (according to the SKA website, <http://www.skatelescope.org>).

In the meantime, other kinematic tracers must be found. Often used at low redshift are H α for the more extended emission, and CO to the central regions, where H α rotation curves cannot be well spatially resolved. H α is found in nearby galaxies to form a diffuse envelope around the HI disk, which could serve as an adequate replacement. However, studies of high-redshift galaxies are limited by cosmological surface brightness dimming which make it impossible to detect this faint diffuse H α line emission. H α is however a promising kinematic tracer for high-redshift galaxies, because it is also emitted from the HII regions surrounding massive young stars. If H α cannot be used, e.g. because it does not fall within the atmospheric windows for a given redshift, then other bright nebular emission lines are used, e.g. [OII] λ 3237 or [OIII] λ 5007. Pettini et al. (2001) compare the redshift of [OIII] λ 5007 with that of photospheric rest-frame UV absorption lines in a small sample of $z \sim 3$ Lyman-break galaxies, and do not find systematic differences.

CO emission lines have been found for a number of dusty high-redshift galaxies, and particularly in submillimeter-bright sources (e.g. Greve et al. 2005; Neri et al. 2003). Generally speaking, these CO emitters are spatially not resolved, and their morphology and orientation is unconstrained, so that dynamical masses can only be rough estimates. However, it is not clear yet how many galaxies of the overall high-redshift population are bright CO line emitters. CO emission in submillimeter galaxies has been observed, but observations of many other galaxy populations (e.g., Lyman-break galaxies with a few rare exceptions) failed. Another, maybe more general caveat is that low metallicity (i.e., little evolved) galaxies will probably not yet have formed sufficient CO molecular gas to be bright emitters.

3.3. Limits of high-redshift mass estimates

Strictly speaking, it is not clear which approach – assuming rotationally or pressure-supported systems – is correct to deduce dynamical masses at high redshift. At low redshift, it is known that all disk galaxies rotate, and bulk rotation has also been observed in a large number of early-type galaxies, except for the most massive systems, which might form a distinct class with peculiar evolutionary histories (e.g. Faber et al. 1997). Mass estimates based on the two scenarios differ by factors of a few, which – given the large observational uncertainties – might be acceptable for the time being.

Another caveat is the assumption that the kinematic fields arise from *virialized* motion. Al-

though this finds observational justification at low redshift, it is rather bold to claim that the same is true for all stages of galaxy evolution. This is not only due to the fact that isolated forming galaxies might be non-virialized. If the hierarchical model is correct, then galaxy mergers must have been much more frequent in the early Universe than they are today. The virial assumption obviously also breaks down in merging systems, when tidal stirring and dynamical friction alter the gravitational potentials within the components. Dynamical mass estimates in these systems are accordingly difficult or even impossible to give. Not all merging systems will be easily identified at high redshift, due to limited spatial resolution. Relative velocities of the two components are often similar to those observed in rotating disks.

One way to estimate whether the virial assumption is justified for a given high-redshift galaxy is by comparing the contribution of random versus bulk motion in the galaxy, approximately given by the ratio of velocity dispersion σ and shear v , v/σ . In the disturbed large-scale gravitational potential of merging galaxies, random motions will dominate the kinematics. Hence v/σ will be smaller than in unperturbed systems.

The by far largest uncertainty comes from the poorly constrained geometry of the sources. High-redshift galaxies suffer from cosmological surface brightness dimming ($I_z/I_{z=0} \propto (1+z)^{-4}$) corresponding to comparably shallow isophotal cuts, so that only the brightest (and presumably rather central) parts of galaxies can be observed, but they cannot be traced out to large radii. In addition, the appearance is dominated by bright, irregular clumps, making it difficult to uniquely discriminate between mergers and isolated galaxies with irregular morphology.

Extinction is another caveat, which is most severe at rest-frame UV wavelengths, but especially in dust-enshrouded systems also persists through most of the rest-frame optical range. On the other hand, rest-frame infrared observations are observationally very challenging (e.g., $2.2 \mu\text{m}$ (K-band) at rest-frame corresponds to $6.6 \mu\text{m}$ at $z=2$) and are restricted to space missions (e.g., SPITZER). High-redshift galaxies are too faint and small to allow rest-frame NIR morphological studies with the current generation of instruments.

Fortunately, blue (especially UV selected) high-redshift galaxies appear largely unaffected from drastic morphological changes across the observationally accessible wavebands (e.g. Giavalisco 2002). In addition, the SED fitting including SPITZER rest-frame NIR luminosities of Lyman-break galaxies (see Chapter 8) of Barmby et al. (2004) indicate that UV selected high-redshift galaxies do not have dominating underlying “hidden” old populations that would be missed in studies at shorter wavelengths. This adds credence that the morphology of blue high-redshift galaxies as currently observable is not strongly altered by dust extinction or low-luminosity old stellar populations dominating the gravitational potential. However, for red, and especially dust-enshrouded galaxies (e.g., DRGs and submillimeter galaxies) this might lead to non-negligible effects.

4. Dynamical Modelling of high-redshift galaxies

Spectroscopy along only one direction does not allow to constrain the appropriate dynamical model for an accurate mass estimate without a prior, and especially if the kinematic major axis cannot be defined *a priori*. This can only be done using the integral-field kinematics, i.e. the velocity and width maps. Due to the faintness and small spatial extent of high-redshift galaxies, this is however possible only for a subsample of the population. Another benefit of detailed modelling is that it allows to control systematic effects, that arise, e.g., from the small number of independent (or mildly correlated) data points that typically can be resolved. Finally, the full two-dimensional pattern is accounted for to extract the kinematic parameters (e.g. mass, and disk inclination) from

data-sets that have rather modest signal-to-noise ratios.

This work uses the computational package DYSMAL, kindly provided by R. Davis, which was adopted and extended for the use of high-redshift galaxies. The surface mass densities are calculated for input mass models (Gaussian distributions, power laws or exponential disks) in concentric rings about the galaxy center. The velocities are then calculated in each coordinate of the ring.

In the context of this thesis, the model velocity fields are manipulated to match the actual SINFONI data. With this aim,

- observed sizes and pixel scale are adopted to be representative for the high-redshift sample,
- noise is added by amounts that are similar to the noise observed,
- spectra are extracted from apertures of several adjacent pixels (typically 3×3 pixels),
- the spectra are smoothed over 3 pixels along the spectral axis,
- the anisotropic pixel size of SINFONI is adopted by averaging over two adjacent rows,
- the non-circular SINFONI seeing disk is adopted.

The next section will describe how the models are fitted to the data, how the goodness of fit is estimated, and the presence of systematic residuals is examined. The subsequent sections will outline more generically, how observational constraints will influence the data taken of galaxies with the global properties of high redshift galaxies.

5. Parameter Estimates for Exponential Disks from Observed Kinematic Maps

The main goal of the fitting is to verify whether the exponential disk hypothesis can give an appropriate description of the data and to deduce an accurate mass estimate. Therefore, whenever possible, it is tried to constrain a maximum number of structural parameters in an independent way. Imaging data, preferably high-resolution HST imaging is very helpful to constrain the inclination and (luminous) size of a disk.

The free parameters of an exponential disk are the radius, scale length, inclination and tilt angle, disk height and mass. Radius, inclination and tilt angle can therefore be constrained independently from the kinematics. Disk heights are not directly observable in high redshift galaxies, therefore a fiducial $q_0 = 0.2$, as found for low-redshift disk galaxies, is assumed. To estimate the disk scale length, the one-dimensional velocity curve along the velocity gradient is searched for the characteristic “turnovers”. If these are found, then their position indicates the scale lengths. This is however, only the case for one source. In other cases, the observed radius is used as lower limit to the disk scale length. If all these constraints can be set, the mass remains as the only free parameter. Otherwise multi-dimensional fits are necessary.

5.1. Mass estimates

To simplify the reasoning, in the following it will be assumed that all parameters except the mass can be fitted independent of the velocity field. Extending the method to multi-dimensional

fitting only enlarges the required grid of models, but does not alter the approach in a fundamental way.

To estimate the best-fit mass, the χ^2 s as function of measured velocity $y(i)$, the corresponding r.m.s. uncertainty σ_y and expected velocity $f(i)$,

$$\chi^2 = \sum \frac{(y(i) - f(i))^2}{\sigma_y^2} \quad (4.16)$$

are calculated (and mapped) across the velocity field. The minimal χ^2 is then used to identify the best fit mass in an appropriate range for typically 10 - 20 mass assumptions. The map of individual χ^2 can be used to decide qualitatively, whether the fits are good overall representations of the data, or vary strongly across the source. In addition, residual maps are produced, also to identify systematic residuals.

5.2. Goodness of fit

The most obvious way to estimate the “goodness of fit” is undoubtedly by using the reduced $\chi^2 = \chi^2/n(d.o.f.)$ directly. This requires that the number of degrees of freedom $n(d.o.f.)$ can robustly be estimated. However, this is difficult in this case because the spectra are correlated by the seeing. Because the χ^2 fit probability (and hence the χ^2 goodness-of-fit estimator) depends on the number of degrees of freedom in a crucial way, it cannot be applied to also yield the “goodness of fit”. Therefore another approach will be used, namely the “run test”, which examines whether the scatter about the median of a distribution is random or whether trends are present that hint systematic discrepancies.

When fitting velocity maps, this means that the map of fit residuals will be searched for areas where the velocities were systematically over or underestimated, and to quantify how significantly this deviates from random scatter.

The expected number r and r.m.s. scatter where the residual changes its sign is (Barlow 1989)

$$r = 1 + \frac{2N_A N_B}{N}, \quad \text{number of “runs”} \quad (4.17)$$

$$r.m.s. = \sqrt{\frac{2N_A N_B (2N_A N_B - N)}{N^2 (N - 1)}}, \quad \text{stat. uncertainty} \quad (4.18)$$

where N_A and N_B indicate the number of data points with positive and negative residuals, respectively, and $N = N_A + N_B$.

Because the run test is one-dimensional, the velocities are given as function of radius from the geometric center¹¹ of the line emitting region, in agreement with a partly covered exponential disk. It should be emphasized that by construction, model and data will have the same spatial resolution, so that adjacent pixels are equally correlated in the data and the model, and correlations cannot explain differences between the expected and observed numbers of runs.

¹¹midpoint with respect to the geometry within some isophotal cut

5.3. Dynamic vs. stellar (photometric) masses

To estimate the *stellar* mass of a galaxy, population synthesis models (Section 2) can be used. Since the models yield the total flux of a given stellar population in a given waveband, the relationship between observed and modelled luminosity directly yields the mass scaling. However, the accuracy of this method obviously depends on how well a given model represents the real galaxy (see Section 2), i.e. on a good estimate of the mass-to-light ratios (M/L). In practice, this approach is limited by degeneracies between age, extinction, and metallicities, that even in multi-color photometry are hard to overcome. Related uncertainties are a factor ~ 2 (e.g. Berta et al. 2004).

In addition, non-luminous matter and especially dark matter are not included. This obviously adds substantial systematic uncertainty and is also the reason why stellar masses are of rather limited use to investigate the mass assembly history of dark matter in the universe. At low redshift, gas fractions are typically low, so that not to include them in the mass estimate will only add a small bias. This is not necessarily true at high redshift, when galaxies were richer in gas. Hence photometric masses can only yield lower limits on the overall mass content of a galaxy, even if the data allow to correctly model the intrinsic SED. Nonetheless, photometric masses are widely used, especially in the high-redshift regime, because they are observationally economical and comparably easy to obtain for large samples of galaxies, and for sources that are too faint for spectroscopy.

As a rough surrogate for detailed modelling, when only order-of-magnitude mass estimates are needed, absolute (observed) near-infrared magnitudes can be used for the estimate. The near-infrared continuum is only mildly affected by variations in the mass-to-light ratio due to episodes of enhanced star-formation, and is dominated by the old stellar population. For the local universe, an empirical calibration of the H-band luminosities vs. mass relationship has been given by Zibetti et al. (2002) using a sample of 324 nearby elliptical and dwarf galaxies.

5.4. Estimating gas masses from line fluxes

Following a somewhat similar idea, the luminosity of the Balmer line emission can be used to give an emission-based mass estimate for the gas content in a system. Although the ionized gas only makes up a minor fraction of the total gas mass in a galaxy, its determination can be very important for a more subtle analysis, e.g. to constrain the energetics of galaxy outflows, or to estimate filling factors. The method uses the formalism presented in Osterbrock (1989) to calculate the ionizing radiation from stars.

Since nearly all hydrogen within the Stromgren sphere of an HII region is ionized, and recombination cross sections can be derived from atomic physics, the luminosity \mathcal{L} emitted in a Balmer line of frequency ν and with an effective recombination coefficient α_{eff} is proportional to the total number of ionized hydrogen atoms within a volume V :

$$n_p n_e = \frac{\mathcal{L}}{h\nu\alpha_{eff}V}, \quad (4.19)$$

where n_p and n_e denote the number densities of protons and electrons, respectively, and h Planck's constant. If the electron density n_e can be measured or estimated, then $V n_p m_p$ (where m_p is the proton mass) will yield the total hydrogen mass within the nebula, which in turn approximates the total gas mass.

Observationally, H α is the most important line in this thesis to estimate gas masses. Using

equation 4.19 and numerical values taken from Osterbrock (1989), the ionized gas mass in units of M_\odot can be derived from the measured $H\alpha$ luminosity by setting

$$M_H = 9.73 \times 10^8 L_{H\alpha,43} n_{e,100}^{-1} M_\odot, \quad (4.20)$$

where luminosity is measured in units of 10^{43} ergs s^{-1} , and electron density in units of 100 cm^{-3} .

6. Gravitational lensing

Light deflection by large masses was historically one of the key predictions of general relativity (GR), and had an important role in establishing GR as an accepted physical theory. Soon after publication of the Einstein equations in 1915, Arthur Stanley Eddington confirmed that indeed the light of stars passing near the sun during the total eclipse of 1919 was deflected by precisely the amount that was derived from Einstein's equations.

For the study of high-redshift galaxies, light deflection by the gravitational potential of massive ($10^{15} M_\odot$) galaxy clusters at intermediate redshift ($z \sim 0.2 - 0.4$) serves as a “natural telescope” to enhance the emission of faint galaxies and enlarge their image. Some of the sources in the present sample are such lensed galaxies, therefore a rough overview about the principle of lensing seems appropriate. The description follows Binney & Merrifield (1998) and Fort & Mellier (1994).

Effectively, the gravitational potential Φ causes the vacuum to have a refractive index n , whose value is given by GR to be

$$n = 1 + \frac{2\Phi}{c^2}, \quad (4.21)$$

with the speed of light c . Fig. 6 sketches the simplest scenario, in which source, lense and observer are coplanar and the lense is point-like. The deflection angle ξ is determined by GR to be

$$\xi(x_\perp) = -\frac{4}{c^2} \nabla_\perp \Phi_2(x) \quad (4.22)$$

where Φ_2 is the gravitational potential integrated along the line of sight. In case of a point-like lense, this simplifies to

$$\xi = \frac{4GM}{c^2 x_\perp}, \quad (4.23)$$

with impact parameter x_\perp . Fig. 6 also illustrates that for all radii up to a critical impact parameter R_{crit} the image of the background source will reach the observer. This radius defines the boundary between the strong ($D_L < R_{crit}$) and the weak ($D_L > R_{crit}$) lensing regime, and for a point-like lense is given by

$$R_{crit} = \sqrt{\frac{4GM}{c^2}} \sqrt{\frac{D_{SL} D_L}{D_{SL} + D_L}} \quad (4.24)$$

It is generally referred to as Einstein-ring. Background-sources that are seen at the Einstein-radius or within are not only strongly magnified (factors 10 and more), but also strongly distorted, and are seen as gravitational “arcs”. In the special case of Fig. 6, and if the spatial resolution is sufficient, a source seen at the Einstein-radius would appear as bright ring centered around the lense. This example illustrates that the magnification by gravitational lenses is not isotropic, but along certain magnification axes, which can lead to strong geometric distortions.

Obviously, a galaxy cluster is not well described by a simple point-like potential, although the basic features are preserved, especially the distinction between strong and weak (or median)

lensing. In the simplest case, the overall potential of the lensing cluster is described by spherical or elliptical isothermal spheres (SIS) (Binney & Tremaine 1987) or somewhat more complex NFW mass profiles (Navarro et al. 1997). One complication arises from the dominating contribution of dark matter in the cluster, which cannot be directly observed, and which in the general case will not be evenly distributed, but forms “subclumps”. It is obvious a strong limitation that all currently used models of cluster lenses are *a priori* model dependent. Non-parametric approaches are being developed, but are not yet in a very mature stage (e.g., Diego et al. 2005).

Generally speaking, cluster potentials are highly non-linear, therefore the lense does not focus the full emission onto one point, but onto caustic sheets. One consequence in case of strong lensing is the appearance of multiple images (“arcs”) of one single source. Instead of one single Einstein-radius, in the more general case of a smooth elliptical potential, two “critical lines” are formed, where arcs can form. Multiple critical lines are of course also observed in more irregular, clumpy potentials.

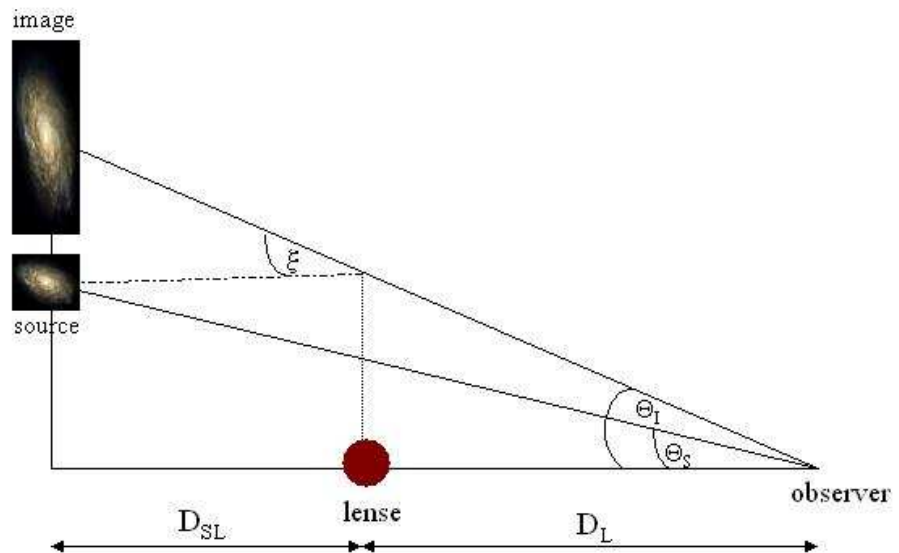


Fig. 6.— Schematic drawing illustrating the gravitational magnification of a high-redshift galaxy by a foreground lense.

The somewhat imprecise term of “magnification” might be misleading, because the intrinsic surface brightness of the source is actually preserved. It is merely the geometric magnification of the image, which leads to a brighter integrated flux. As a consequence, quantities given per unit area (e.g., star-formation rates per square-parsec) will not be subject to the considerable uncertainties that are usually introduced by the lensing, and that even the most careful lensing model can only crudely account for. Spatial extents and derived quantities (e.g. dynamical masses) can only be rough estimates, especially for gravitational arcs. As a benefit, however, gravitational lenses are

achromatic, therefore analyses of the source colors, such as population synthesis modelling, will not be affected by the lensing. This also holds for comparison of quantities derived from the flux at vastly different wavebands, e.g. star-formation rates found from the far-infrared and from UV wavelengths.

However, especially for very strongly lensed objects, which are, generally speaking, not spatially resolved perpendicular to the magnification axis, also color-based analyses are not easily interpreted. Intrinsically small parts within the galaxy will be most strongly magnified so that inhomogeneities within the source can determine the overall appearance. It is known from nearby galaxies, that gradients, e.g. in color or metallicity, within the same galaxy are rather frequent. At high redshift, the faintness of the sources and their small spatial extent make it impossible to study gradients within unlensed sources. Therefore the properties of lensed and unlensed high-redshift sources can only very cautiously be compared. Nonetheless, they are a valuable tool for studying high redshift galaxies, simply because they allow to access size scales that could otherwise not be reached. Some observational constraints can be given, e.g. on velocity shears or line widths, which are in many ways complementary to the information extracted from the overall high-redshift population.

Detailed investigations of gravitational lenses also allow to set constraints as to the distribution and homogeneity of dark matter within the lense, and to infer information about the large-scale geometry of the universe. However, for this work, they merely serve as a tool to magnify the background galaxies. The sample includes 3 gravitationally lensed sources: SMM14011+0252, SMM04431+0210 and 1E0657-56 arc core with magnification factors of 5, ~ 10 and 20, respectively. Especially the analysis of SMM14011 and 1E0657 will illustrate that gravitational lensing plays an ambiguous role in the study of high-redshift galaxies.

Chapter 5

NIC J1143-8036a/b:

A merger candidate at $z=1.3$

1. Introduction

As discussed in section 1, mergers play a crucial role in the hierarchical model of structure formation. However, strong cosmological surface brightness dimming and increasingly large distances make discovering merging pairs of galaxies at high redshift very challenging. Only systems with two or more bright, high star-formation rate (generally massive) components can be expected to be discovered in any complete way. Interestingly, emission line surveys can minimize the impact of some of these limitations by being more sensitive to emission line equivalent width (EQW) than to continuum magnitude (although astrophysically, line emission is ultimately limited by a maximum possible EQW which then translates into a general continuum magnitude limit).

One such survey that is both sensitive and at high angular resolution was a “parallel” survey in the H band with NICMOS on board the HST performed by McCarthy et al. (1999). Using NICMOS in slit-less grism mode, they discovered a sample of 33 emission-line galaxies at redshifts between $z=0.75$ and $z=1.9$, reaching 3σ continuum limits between $H = 20$ and $H = 22$ in various fields, and a median F160W magnitude of 20.4.

Among the morphologically most peculiar objects in the NICMOS survey is NICJ1143-8036a/b, which appears as a close (projected separation of only one arcsec) pair of compact, distinct sources. These two sources have $H = 21.4$ and 20.5 for components a and b, respectively. Although their resolution was not high enough to spectrally resolve the $H\alpha$ and [NII] emission lines, McCarthy et al. (1999) derived star-formation rates of $7 M_{\odot} \text{ yr}^{-1}$ (component a), and $12 M_{\odot} \text{ yr}^{-1}$ (component b), correcting for a fiducial [NII]-to- $H\alpha$ ratio of $[\text{NII}]/H\alpha = 0.3$. The morphology is very suggestive to view this source to be a galaxy merger candidate, with redshifts of $z = 1.35$ and $z = 1.36$ for component a and b, respectively. The NICMOS spectra have very low spectral resolution ($R \sim 200$), which makes kinematic measurements highly uncertain. The measured velocity offset of the two components is $\sim 1300 \text{ km s}^{-1}$, which is curiously high for a gravitationally bound system.

The overall properties, even with the uncertainties, are intriguing, because only few good merger candidates are known at these redshifts, moreover, candidates that were found serendipitously, and are hence unbiased by the selection techniques often used to identify galaxies in the “redshift desert”. Investigating the properties of this merger candidate with SPIFFI seemed therefore appropriate. Thanks to the data reduction scheme presented in Chapter 3, it is now possible to

extract meaningful limits on the internal kinematics and emission line ratios from the SPIFFI data cubes, which proved to be difficult in an earlier analysis of the same data set (Schegerer 2004). The overall goal is to determine whether or not this is really a merger, over what time scale it is likely to merge, and to measure each components characteristics like star-formation rate and possibly their metallicities.

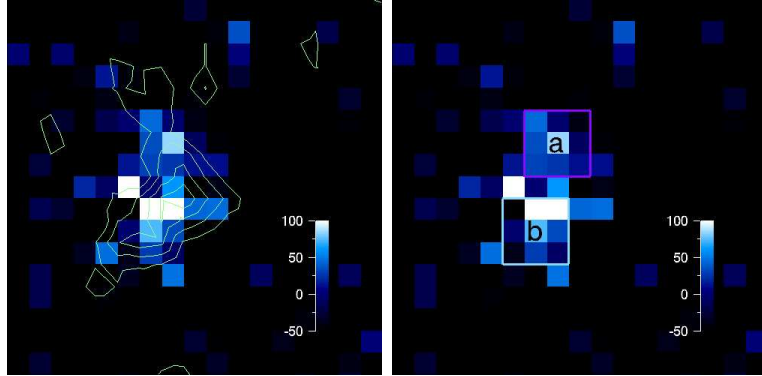


Fig. 1.— *left: Line free H band continuum image of NIC1143a/b, with the contours showing the $H\alpha$ line emission. Contours are given for 2 to 6σ , the colorbar yields the flux in units of $10^{-16} \text{ W m}^{-2} \mu\text{m}^{-2} \text{ arcsec}^{-2}$. right: Light blue boxes show the most likely location of the two sources in the continuum image. In both images north is up, east to the left.*

2. The morphology and spectrum of NIC1143a/b

The H band line-free continuum image¹ is shown in Fig. 1. Overall, the source appears elongated in east-west, which mostly reflects the asymmetry in the SPIFFI PSF. It appears marginally resolved in the data set, although seeing and the relatively coarse sampling relative to the source size make it challenging to separate the components. Each component appears unresolved in our data and the pair is separated by $\sim 1''$. The southern source, b, is the brighter of the two. The morphology of the source is consistent with that found by McCarthy et al. (1999).

Overlaid on the continuum image in Fig. 1 are contours representing the spatial distribution of $H\alpha$ line emission (smoothed over 3 pixels in both spatial and the spectral direction to approximately match the spatial and spectral resolutions). The line emission peaks on the southern source, one pixel north-west from its (apparent) center, and coincides with the strongest continuum emission. Overall, the highest surface brightness line emission follows the continuum distribution for both sources, with the lower surface brightness line emitting material being perhaps marginally more extended.

Spectra were extracted (summed over) from within the regions marked a and b in Fig. 1 and smoothed over 3 pixels in spectral direction, again, to approximately match the instrumental resolution, which was measured from the width of night sky lines to be $224 \pm 16 \text{ km s}^{-1}$ for smoothed data (see Section 7). They are shown in Fig. 2 and Table 1 summarizes the properties of the emission lines in NIC1134a/b. The lines have an intrinsic full width at half-maximum (FWHM) of (a) $206 \pm 14 \text{ km s}^{-1}$ for $H\alpha$ and [NII], and (b) $344 \pm 31 \text{ km s}^{-1}$. The low signal-to-noise ratio of the [NII] line in component a makes it difficult to derive an independent width. Therefore the

¹Section 6 of Chapter 4 describes how continuum and line images are extracted from the data cube.

measured $H\alpha$ value is adopted, which results in a line ratio of $[NII]/H\alpha = 0.17$. In component b, $[NII]$ is not detected and, again assuming that both $H\alpha$ and $[NII]$ have the same width, the resulting 3σ -limit is $[NII]/H\alpha < 0.09$. The redshifts of components a and b are $z = 1.334 \pm 0.0001$ and $z = 1.3334 \pm 0.0009$, respectively, indicating a velocity offset of $128 \pm 30 \text{ km s}^{-1}$ between the two components. This is in agreement with a previous analysis of the SPIFFI data (Schegerer 2004), but much lower than the result of McCarthy et al. (1999), who measured a velocity gradient of $\sim 1300 \text{ km s}^{-1}$, more than 30σ higher.

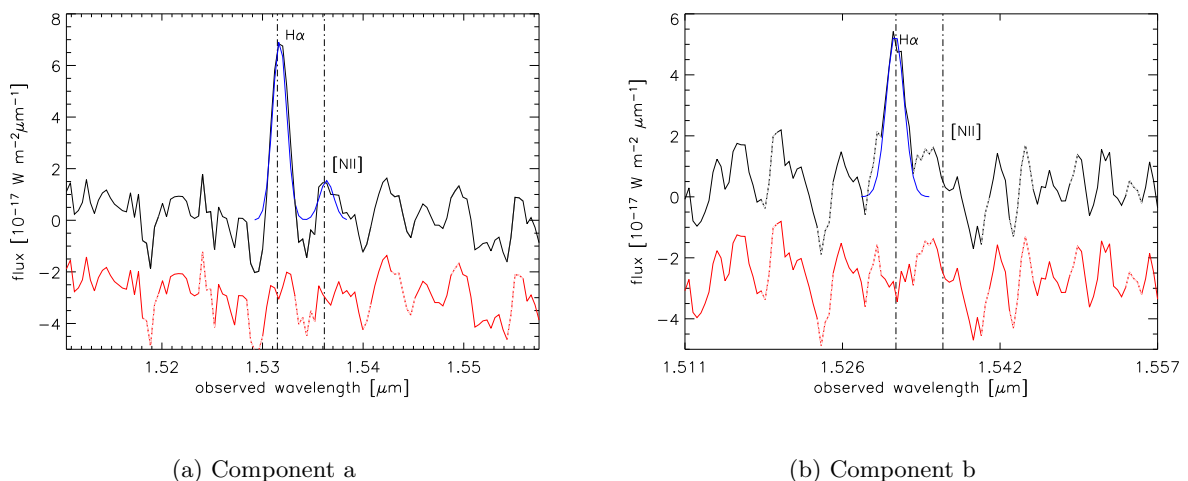


Fig. 2.— Spectra of NIC1143a/b. Dotted lines indicate the position of night sky line residuals. Vertical dot-dashed lines yield the position of the redshifted emission lines. Blue lines show the best Gaussian fits for $H\alpha$ and $[NII]\lambda 6583$ (source a) at $z_{H\alpha}$, and $H\alpha$ emission (source b). Fit residuals (lower line) are given in red and are shifted arbitrarily along the ordinate.

As already discussed by McCarthy et al. (1999), the NICMOS data are low resolution ($R = 150$) and since they are slit-less spectra, are difficult to wavelength calibrate accurately. Thus all of these discrepancies are entirely understandable and in fact this was the reason to follow-up these sources with SPIFFI in the first place. In addition, although the SPIFFI data do not suffer from these specific problems, they could be subject to large systematic errors, which are hard to quantify, due to the blending with the night sky line, especially in the H-band where the OH night sky lines are highly variable. However, as shown in Fig. 2, the $H\alpha$ and $[NII]\lambda 6583$ emission lines are not strongly affected by strong night sky lines.

3. Emission line diagnostics and star-formation rates

As outlined in Section 1.2, metallicity estimates based solely on $[NII]/H\alpha$ can only be rough estimates, as the $[NII]/H\alpha$ ratio may be dramatically altered by non-stellar excitation, and will lead to severe overestimates, i.e. in the presence of galactic winds or AGN. In addition, the $[NII]/H\alpha$ ratio saturates at metallicities above \sim solar (Pettini & Pagel 2004). However, these caveates are minimized in this case, because both the present sources have relatively low $[NII]/H\alpha$, suggesting that photoionized HII regions are the main contributor to the optical line emission.

Thus, using Equation 4.3, abundance estimates are $12 + \log [O/H] = 8.5$ (or 0.2 dex below solar) for component a and (using the upper limit to $[NII]$ to obtain an upper limit to the metallicity) $12 +$

$\log [O/H]=8.3$ (0.4 dex below solar) for source b. The inherently large absolute uncertainty of the calibrator (0.2 dex) is of concern only for the absolute abundance estimate (which can nonetheless crudely be constrained to be subsolar), but not for the relative measurement, establishing distinct abundance ratios in the two components.

Since the SPIFFI data are also flux calibrated, star-formation rates can be deduced following the method described in Section 2.1 of Chapter 4. In NIC1143a/b, the star-formation rates are found to be about $10 M_{\odot}\text{yr}^{-1}$ in each component. Since this value is estimated from non-extinction corrected data, this result should be considered a lower limit. If the typical extinction measured in low-redshift galaxies ($A_V \sim 1$ mag) applies to NIC1143a/b, then the intrinsic $H\alpha$ line fluxes are likely a factor ~ 2.5 higher, indicating star-formation rates of $\sim 20 - 30 M_{\odot} \text{yr}^{-1}$ in each component.

4. NIC1143a/b: Portrait of a merger at intermediate redshift

The SPIFFI results on NIC1143a/b now paint a reasonably clear picture as to the nature of this source. While it is difficult based solely on morphology in both the SPIFFI and the NICMOS data to safely say that these are two individual galaxies, there are a number of strong lines of evidence to suggest that they are indeed two galaxies: The velocity widths ($200 - 300 \text{ km s}^{-1}$) of both a and b are large and different and the $[\text{NII}]/H\alpha$ ratios of the a and b are also different. This implies that both are separate galaxies. To see such different ionization states and abundances on a scale of 9 kpc would be difficult to understand. Moreover, unless in the unlikely state that these two galaxies are orbiting in the plane of the sky while each of their individual rotation axes are also in the plane of the sky, the velocity widths of a and b exceed their relative velocities. If one were to hypothesize that the velocity offset represents rotation and the widths of the lines in a and b represent the dispersion in a disk, such a configuration is not stable and certainly cannot maintain such a structure. Again, the kinematics suggest that these are two independent galaxies.

Models of interacting/merging galaxies have shown that when the relative velocities of the interacting galaxies is less than or of-order of their internal velocities, dissipation and loss of orbital angular momentum is very efficient and a merger takes place in several orbital time scales. While it is difficult to directly estimate an orbital time scale of NIC1143a/b, assuming a circular orbit with a diameter given by the projected separation of a and b (about 9 kpc) and a relative velocity exactly as measured, yields an orbital time of about 2×10^8 yrs. Statistically speaking, the orbital velocity is likely to be about a factor of 2 higher than measured, as is the likely true separation, and so this estimate is uncertain at about a factor of 4 for a random sample of orbital orientations and viewing angles. In spite of this uncertainty, the kinematics and close projected separation suggests that NIC1143a and b will merge in less than a few 100 Myrs.

As a result, the measured relative velocities of a and b likely represent non-circular velocities, so that the shear cannot be used to estimate a total dynamical mass for the system. The line widths, however, are narrow enough to appear dominated by the kinematics in the individual galaxies and therefore do provide a rough estimate of the mass in each individual component. Measured velocity dispersions are $\sigma = 150 \text{ km s}^{-1}$ and 90 km s^{-1} for b and a, respectively. If each is rotationally supported then Equation 4.14 applies. Assuming that that rotation is dominating the observed line widths and that the half-light radii of each is $0.2''$ (2 kpc; the resolution of the NICMOS data from McCarthy et al. 1999):

$$M = 1 - 3 \times 10^{10} M_{\odot}, \quad (5.1)$$

Of course, the true deprojected velocity is $V_{measured}/\cos i$, with the unknown inclination angle i .

Again, for a statistically random sample, the final masses are likely to be a factor of a few higher.

Alternatively, for a sphere of uniform density, using Equation 4.15, the masses are:

$$M = 2 - 5 \times 10^{10} M_{\odot}. \quad (5.2)$$

Both components show low, but different abundance ratios, indicating that they have different evolutionary histories, but are overall not very strongly evolved.

At $z \sim 1.3$, NIC1143a/b falls in the “redshift desert”, where relatively small numbers of galaxies have been studied in any detail. Steidel et al. (2004) have conducted a survey of “BM” sources within a redshift range encompassing that of NIC1143a/b, but include an analysis of the rest-frame optical emission of only one source close to the redshift of NIC1143a/b (Q1307-BM1163 at $z=1.41$). Perhaps not surprisingly, given the rather modest star-formation rates in NIC1143a/b, its properties over-lap with those of the “BM” galaxies at similar redshifts.

Shapley et al. (2004) have found that “BM” galaxies have modest $H\alpha$ -estimated star-formation rates of a few to a hundred $M_{\odot} \text{ yr}^{-1}$ and metallicities of modestly below up to solar. For Q1307-BM1163 in particular, Steidel et al. (2004) and Shapley et al. (2004) find a star-formation rate of about $20 M_{\odot} \text{ yr}^{-1}$ (for a Kroupa IMF) and a velocity dispersion of 126 km s^{-1} . Q1307-BM1163, from its $[\text{NII}]/H\alpha$ ratio, also has a sub-solar metallicity ($12+\log [O/H] = 8.5$). All of these properties are comparable to those estimated in NIC1143a/b, although with the additional fact that NIC1143a/b is a pair of merging galaxies. Whereas the ensemble of “BM” galaxies reach approximately solar values on average, their lowest metallicities are similar to that in NIC1143a.

Overall, these findings indicate that the $H\alpha$ -selected galaxy pair NIC1143a/b is not very different from the class of “BM/BX” sources at similar redshifts. Based on only one source, it is hard to generalize such a similarity. Multi-band photometry of NIC1143a/b is needed to determine if it fulfills the “BM/BX” criteria. At least its evolutionary state and approximate dynamical mass as determined from its optical emission line properties seems very similar. The present data on NIC1143a/b suggest it is similar to “BM/BX” but may represent a less evolved end of their overall distribution. Perhaps here the short merger time plays a key role in allowing a NIC1143a/b like source to become a typical “BM/BX” source. At this redshift, a merger time scale of 200 – 400 Myrs implies a $\Delta z \lesssim 0.15$. At the end of the merger, models suggest that the metallicity would have increased substantially, perhaps to the solar value, the mass would be approximately doubled, and at least until the gas is exhausted have a star-formation rate a factor of a few higher (Mihos, Richstone, & Bothun 1992) – all characteristics similar to the typical “BM” galaxy.

Table 1:: Emission lines in NIC1143a/b

Source (1)	line (2)	λ_{obs} (3)	redshift (4)	FWHM (5)	$FWHM_{intr}$ (6)	flux (7)
a	$H\alpha$	1.5318 ± 0.0001	1.3340 ± 0.0001	16 ± 2	206 ± 14	1.23 ± 0.11
a	[NII]	1.5364 ± 0.0008	1.3339 ± 0.0009	...	206 ± 122	0.20 ± 0.16
b	$H\alpha$	1.5314 ± 0.0001	1.3334 ± 0.0001	24 ± 2	344 ± 31	1.24 ± 0.133
b	[NII]	< 0.11

Column (1) – Regions as defined in Figure 1. Column (2) – Line ID. Column (3) – Observed wavelengths in μm . Column (4) – Redshift of the line. Column (5) – Full-width at half-maximum measured for $H\alpha$ in \AA . Column (6) – Intrinsic FWHMs corrected for instrumental resolution units of km s^{-1} . Column (7) – Line fluxes in units of $10^{-19} \text{ W m}^{-2}$.

Chapter 6

Submillimeter selected galaxies

1. Introduction

The most actively star-forming galaxies in the local universe are generally heavily dust-enshrouded. As a consequence, they are extraordinarily bright in the far-infrared, but have red rest-frame optical and UV spectral energy distributions suggestive of strong extinction. Most extreme are the ultraluminous infrared galaxies, ULIRGs, which exceed infrared luminosities of $10^{12} L_{\odot}$. When searching for ULIRG analogs at high redshift, the bright infrared emission should be shifted into the submillimeter range, and the brightest of these sources – and especially those that are being magnified by a gravitational lens – are within the sensitivity of present-day (sub)millimeter bolometers.

A substantial population of submillimeter-bright ($> 5\text{mJy}$ at $850\mu\text{m}$) high-redshift galaxies (SMGs) has been identified in the last ~ 5 years, most of them with the Submm Common-User Bolometer Array SCUBA on the James Clerk Maxwell Telescope JCMT in Hawai'i. The sample has been extended by a very similar sample of sources detected with the MAMBO bolometer at the 30 m IRAM telescope. At redshifts $z \sim 2$, these sources have a 400 times higher comoving number density than their low-redshift analogs and appear overall more luminous ($L_{highz}^* \gtrsim 20 \times L_{lowz}^*$) (Blain et al. 2002). The emission of these very dusty high-redshift galaxies accounts for $\gtrsim 50\%$ of the submillimeter background (Blain et al. 1999), unlike in the local universe where individual ULIRGs are nearly equally luminous, but very rare. A few hundred SMGs have been identified so far. However, due to their faintness and obscuration, investigating their intrinsic properties is difficult. The redshifts of about 100 radio-loud SMGs have been measured through rest-frame UV follow-up spectroscopy, and they appear to be strongly peaked around $z \sim 2.2 \pm 0.7$ (Chapman et al. 2005).

In the far-infrared and submillimeter range, SMGs indeed resemble ULIRGs qualitatively, but can be about an order of magnitude more powerful than the typical ULIRG (Greve et al. 2005). Tacconi et al. (2005) have made a detailed comparison based on a sample of 14 SMGs with CO measurements, which also includes SMMJ14011+0252: SMGs and ULIRGs appear to have similar properties including dust temperatures. Both populations have compact CO emitters ($r_e < 2 \pm 0.8$ kpc compared to < 1 kpc for local Ulirgs) and about an order of magnitude higher infrared luminosities ($\mathcal{L}_{SMG} \sim 10^{13.1} L_{\odot}$ compared to $\mathcal{L}_{ULIRG} \sim 10^{12.1} L_{\odot}$, but similar luminosity densities. The gas fractions in SMGs appear also higher ($f_{g,SMG} \sim 0.4$ vs. $f_{g,Ulirg} \sim 0.16$). Tacconi et al. (2005) also emphasize the ambiguity of the often observed double-peaked CO line profiles in about one half of the sample, which might either be due to a rotating disk (rather, a ring-like structure)

or two merging, unresolved or barely resolved, components.

SMGs appear to be highly clustered with a correlation length of $\sim 7 \pm 2 \text{ Mpc}^{-1}$, which is larger than that of LBGs and quasars (Blain et al. 2004). This suggests they are a distinct class of objects rather than a different evolutionary stage of the same underlying population, although not all authors agree that current data are robust enough to make this statement conclusively (see, e.g., Smail et al. 2004). They rather view SMGs as one stage in an evolutionary sequence of the most massive systems, during which star-formation is particularly strong, maybe triggered by a major merger. After being an SMG for about 10^8 years, these galaxies will then become powerful radio galaxies and quasars when the AGN feedback starts to dominate. Prime indications for this interpretation include the $K - z$ relationship¹ that SMGs appear to have in common with high-redshift radio galaxies (Smail et al. 2004). Recently, Dannerbauer et al. (2005) have found an overdensity of H α emitters around the SMG SMMJ14011+0252, indicating that SMGs might be massive objects in the centers of forming galaxy clusters, similar to radio galaxies.

The large extinction within these objects makes it difficult to identify their counterparts at observed optical wavelengths. Even in near-infrared wavebands, they are comparably red. Frayer et al. (2004) find on average $J - K = 2.6 \pm 0.6$, with the brighter sources (K brighter than 19 mag) appearing bluer ($J - K \sim 2$) than the fainter ones ($J - K \gtrsim 3$). Color dichotomies within the SMG population (Smail et al. 2002) might indicate the presence of at least two distinct subclasses. SMGs appear relatively large compared with other populations at similar redshift: Frayer et al. (2004) find sizes of $0.5 - 2.1''$ from near-infrared imaging, Smail et al. (2004) have measured a median size of $2.3 \pm 0.2''$ in a sample of 78 SMGs and 18 OFRGs².

Consensus has been reached that SMGs are rather massive objects, a few times more massive than the optically selected $z \sim 2$ BM/BX galaxies (Tacconi et al. 2005). Their bolometric luminosities are $\mathcal{L}_{bol} \gtrsim 10^{12} L_{\odot}$ and stellar masses are typically $M_{stellar} \sim 3 \times 10^{10} M_{\odot}$ (Smail et al. 2004). SMGs apparently contain substantial gas masses, CO line luminosities indicate $\sim 2 \times 10^{10} M_{\odot}$ in gas. This measurement has recently been refined by Tacconi et al. (2005), who find average gas fractions of about 40%. More direct evidence that SMGs are massive comes from dynamical estimates. About one half of the known SMGs have companions. Swinbank et al. (2004) have obtained near-infrared spectra of 7 of these galaxies, and find an average dynamical mass of $1.5 \pm 0.9 \times 10^{11} M_{\odot}$ from the velocity offsets and distances between the components. Line widths in the Swinbank et al. (2004) sample indicate dynamical masses of $1 - 2 \times 10^{11} M_{\odot}$ and dynamical time-scales of $10 - 20$ Myrs. Among the most striking properties of SMGs are the large CO line widths found in many sources, some of them showing double peaked line profiles. Currently it cannot be distinguished conclusively whether these originate from disk rotation or are dominated by a merging galaxies (Greve et al. 2005; Tacconi et al. 2005). However, if the motion is approximately virialized, then in either case, even with the uncertainties in the relative geometries and orbital projection velocities, the measurements provide a good indication of the mass scale of these galaxies over radii of a few kpc or less. Since the gas is both susceptible to disassociation in strong shocks and is highly dissipative, it is likely that this molecular gas traces the inner gravitational potential with its kinematics. However, being highly dissipative, the molecular gas can also collect in the overlap regions of disks or in the separate nuclei of merging galaxies. Such gas may therefore reflect velocities that are gravitationally driven, but are not correlated directly or an accurate measure of the enclosed gravitational potential (Colina et al. 2005).

¹Absolute K-band magnitude and redshift of powerful radio galaxies are correlated, indicating evolutionary trends (De Breuck et al. 2002).

²“Optically Faint Radio Galaxies” with similar near-infrared properties but different far-infrared emission.

SMGs appear to be dominated by rather young stellar populations (Smail et al. 2004, find average ages of 450 ± 80 Myrs) and rather moderate extinction for highly dust-enshrouded systems: $A_V = 1.7$. The SED of SMMJ14011+0252 is consistent with a $1 - 2 \times 10^8$ yr old population (Tecza et al. 2004, see also the next sections of this thesis). Their morphologies are generally disturbed – Smail et al. (2002); Chapman et al. (2003) classify only $\sim 15\%$ as regular. These morphologies might either be intrinsically disturbed (e.g., due to an on-going major merger) or originate from strong variations in the dust distribution, leading to complex morphologies by selectively obscuring large regions of the galaxy relative to others. Clumpy dust distributions are also indicated by the surprisingly bright Ly α emission in some SMGs, that is in apparent contradiction to the large extinction within the sources (Chapman et al. 2004) which should be effective in destroying both ionizing photons and the Ly α emission itself due to high neutral H scattering optical depths. However, a patchy irregular dust distribution could possibly allow a fraction of the intrinsic number of Ly α photons to escape, perhaps helping resolve this paradox. Another possibility is that the Ly α emission comes from a satellite object in the halo of the submm galaxy. Perhaps such objects are less evolved, more metal poor, and relatively dust poor, allowing for bright Ly α emission. Of course such objects would be fortuitously close in redshift to allow for a proper redshift determination of the submm source (cf. Greve et al. 2005).

From rest-frame optical observations of ~ 25 SMGs, Swinbank et al. (2004) conclude that about 40% of all SMGs are dominated by AGN emission, the rest by the starburst. Those which do not have an optically evident AGN have a H α line width of $\text{FWHM} = 400 \pm 70 \text{ km s}^{-1}$, larger than that of rest-frame UV selected populations at these redshifts, but perhaps not as broad as the widths found in the CO gas (e.g. Tacconi et al. 2005). The average spatial extent of the H α emission is $4 - 16 \text{ kpc}$ (in diameter) and significantly differs from the CO distribution ($\text{FWHM} < 0.5 \pm 0.2 \text{ kpc}$ Tacconi et al. 2005). H α equivalent widths vary strongly within their sample, and are on average $75 \pm 25 \text{ \AA}$ (similar to local galaxies of extremely high infrared luminosities). Equivalent widths of AGN tend to be higher as compared to starburst-dominated sources, but the scatter is large.

Included in this thesis sample are two SCUBA detected SMGs, SMMJ14011+0252 at $z = 2.565$ and SMMJ04431+0210 at $z = 2.509$. Both sources are gravitationally lensed by moderate amounts ($\mathcal{M} \sim 3 - 5$ and $\mathcal{M} \sim 4$, respectively), but have very different intrinsic properties, both at rest-frame optical and mm wavelengths. In this sense, this pair may be representative of the diversity within the general population.

2. Comparison with integral-field data of low-redshift ULIRGS

2.1. Low-redshift sample and method

Given the similarity of $z \sim 2$ SMGs and low-redshift ULIRGS, it is of major interest to investigate how low-redshift ULIRGS would appear if they were at high redshift. Although rest-frame optical studies of low-redshift ULIRGS with IFUs are relatively rare, they do exist, and maybe the largest sample presently available is that of Colina et al. (2005). They used the INTEGRAL IFU on the 4.2 m William-Herschel telescope to obtain data sets of 8 ULIRGS at redshifts $z \lesssim 0.1$. Luis Colina kindly provided parts of his data set for the present analysis, namely the H α intensity, velocity and dispersion maps, and maps of the [NII]/H α ratios of six targets: IRAS08572+3915, IRAS12112+0305, IRAS14348-1447, IRAS15205+3542, IRAS15250+3609, and IRAS17205-0014.

Since the extracted maps were provided, and not the original cubes, the comparison can only be approximate, because it will make a difference, whether, e.g. the line ratios extracted

from the high-resolution and signal-to-noise data sets have their resolution lowered after extraction of the spectra or before (mathematically, this corresponds essentially to the difference between summing before or after interpolating and convolving). However, the spread in the individual source properties is considerable, especially for a population which is as complex as are ULIRGs, so that this inconsistency will not be the largest source of uncertainty.

Size scales and fluxes in the “redshifted” sample were calculated for $z = 2$. A surface brightness cutoff of 3×10^{-18} ergs s⁻¹ cm⁻¹ pix⁻¹ was assumed, to account for cosmological surface brightness dimming, which will make the fainter regions of high-redshift galaxies difficult to observe. Using the ESO exposure time calculator³ for SINFONI indicates that this cutoff flux corresponds to a total integration time of about 18 hrs with a 0.25'' pixel scale, an observed wavelength of $\lambda_{obs} = 2.2\mu\text{m}$, signal-to-noise ratio per pixel $S/N = 5$ and line widths of $FWHM = 20 \text{ \AA}$.

Two sets of observational constraints were applied, namely a 0.25'' pixel scale and 0.5'' seeing, and 0.1'' pixel scale and 0.3'' seeing, respectively. These correspond roughly to the typical observing conditions with SPIFFI/SINFONI in the seeing-limited and AO-assisted mode, respectively. (In fact, the 0.5'' seeing-limited resolution is somewhat optimistic.) At $z = 2$, an arcsec corresponds to a projected physical distance of ~ 8 kpc.

To obtain “high-redshift” intensity maps, the Colina et al. (2005) H α maps were rebinned to the appropriate scales and convolved with the seeing disks. Pixels with flux fainter than the 3×10^{-18} ergs s⁻¹ cm⁻¹ pix⁻¹ cutoff was set to zero, and Gaussian noise was added, corresponding to a signal-to-noise ratio in the brightest pixel of $S/N_{max} = 15$. Again, this is in a sense a “best possible data” scenario rather than typical, especially for the rather faint SMGs.

To “redshift” the kinematic and line ratio maps, the direct convolution with the seeing disk would obviously yield wrong results. Therefore the maps were intensity-weighted with the seeing-disk convolved H α maps (again, respecting the 3×10^{-18} ergs s⁻¹ cm⁻¹ pix⁻¹ cutoff) before adding noise that corresponds to uncertainties of 10 km s⁻¹ in the velocity and dispersion (so that the uncertainties on FWHM are ~ 25 km s⁻¹). For the [NII]/H α ratios, an absolute uncertainty of 0.05 in the ratios was assumed.

Two targets were too faint to be even detected at high redshift: IRAS17205-0014 and IRAS 15250+3509. Since this study aims more at comparing morphologies and kinematics of the ULIRGs, and SMGs appear to be “scaled-up” ULIRGs (Tacconi et al. 2005), the flux of these targets was scaled up by factors of 5. This has no physical justification other than that the results are visually similar to the data often observed in high-redshift galaxies. Unfortunately, the NIR continuum maps were not available.

2.2. Results

Fig. 1 shows the H α intensity maps of the 6 Colina et al. (2005) ULIRGs that were available to this comparison. The left column shows the unmanipulated data sets, the “high-z” sample assuming seeing-limited conditions is shown in the middle, and the right column yields the simulated AO-sample.

Maybe the most striking result is that none of the upper three targets, which appear as isolated (although not very regular) galaxies in the low-redshift data, are spatially resolved with

³see <http://www.eso.org/observing/etc>

the seeing-limited observations. Spatially extended are only the targets which consist of more than one component, with typical sizes of $r \sim 1 - 2''$.

The composite targets, which are clearly spatially resolved at low redshift, appear like isolated, extended galaxies in the seeing-limited sample. In the AO data sets, the pairs in IRAS0857+3915 (with a relative projected distance $D \sim 6$ kpc) and IRAS14348-1447 ($D \sim 9$ kpc) are seen as two individual unresolved blobs, although their PSFs do have some overlap. In IRAS12112+0305 ($D \sim 5$ kpc), the H α emitting gas is not concentrated in the two nuclei, but forms a long-stretched ridge inbetween the components. Although the projected distances in IRAS12112+0305 and IRAS0857+3915 are very similar, IRAS12112+0305 seems more tidally disturbed, maybe indicating stronger interactions between the two components, which could have caused the H α bright ridge between the galaxies. This ridge is spatially resolved, but the line emission from the fainter of the two nuclei is too faint to be observed in the high- z data observations.

The velocity maps are shown in Fig. 2. Again, the left column indicates the low-redshift data, the simulated, redshifted data sets under non-AO conditions are shown in the middle, and the right column shows the AO simulation. Dynamic ranges are the same for each galaxy in all three scenarios, to illustrate the loss in dynamic range due to the loss of spatial resolution. However, this effect cannot be modelled accurately, because the absolute values will not be well represented when redshifted the extracted data sets. The contours yield the H α flux to ease orientation and comparison between the different maps of each galaxy.

Due to the limited spatial resolution, the composite sources appear to have an intrinsic velocity gradient in the high redshift data, which is difficult to distinguish from disk rotation. However, note that the intrinsic rotation of the larger component of IRAS0857+3915 is seen in the AO-like data, but not the non-AO like data sets. Since IRAS14348+1447 is resolved into two components in the AO-like data set, this source would also be identified as a composed of two components in the AO-like scenario. IRAS17208-0014, which Colina et al. (2005) identify as their only candidate for disk rotation, is spatially not resolved in the simulated high- z data sets.

Fig. 3 shows the redshifted dispersion maps with the same order as above. H α contours are given to show orientation. Again, all three panels have the same dynamic range for the individual galaxies, to illustrate how the spatial resolution and lower signal-to-noise influences the measurements. The dispersions vary over areas smaller than the spatial resolution elements in most galaxies, thus smoothing dispersion variations and lowering the full dynamic range. However, dispersions near the nuclei of composite sources do show the same trends, and in these cases, the absolute values are approximately as in the low-redshift data sets for the AO-like simulation. Interestingly, the off-nuclear high-dispersion region in the tidally-disturbed, single-nucleus IRAS15206+3342 (Colina et al. 2005) is seen in both high-redshift scenarios, although the source is spatially not resolved.

Puech et al. (2005) report that they have found more regular dispersion maps in parts of their sample of galaxies at intermediate redshift ($z \sim 0.6 - 1$), as would be expected from rotating disk galaxies for an illustration (see the Section on the modelled exponential disk galaxies, Section 4 of Chapter 4). Their observational conditions are relatively similar to this comparison. None of the ULIRGs with two components shows similar behaviour, but the measured dispersion maps trace the difference in the velocity dispersions in each component. This alludes to an interesting possibility to discriminate between isolated galaxies and sources with multiple components smeared by the seeing.

Finally, Luis Colina also kindly provided the [NII]/H α ratio maps of his data sets. The high-redshift algorithm assumes uncertainties of 0.05 in the ratio as an “optimistic-but-achievable” estimate. Again, the dynamic range is fixed separately for each ULIRG under all three observing

scenarios. The spatial resolution and noise tend to lower the variability of the line ratios within the sources. Line ratios in the two components of the composite sources, however, are only marginally changed. Off-nuclear regions with large [NII]/H α ratios, probably indicating outflows in the low-redshift data sets, have too low surface brightness and do not have the necessary spatial extent to be robustly detected in the high redshift data.

2.3. Conclusions

Integral-field optical emission line data of low-redshift ULIRGs kindly provided by Luis Colina was “redshifted”, i.e., data quality was deteriorated to the spatial resolution, binning, surface brightness detection limits and signal-to-noise values typical for high-redshift observations. Namely, these comprise the H α intensity maps, velocity and dispersion fields, and spatial distributions of [NII]/H α line ratios. Two scenarios are considered, a “non-AO-like” case with a spatial resolution of FWHM= 0.5” and 0.25” pixel scale, and an “AO-like” case with spatial resolution of FWHM= 0.3” and 0.1” pixel scale.

The comparison illustrates the challenges of observations of the intrinsic properties of high-redshift galaxies. Due to the limited spatial resolution and signal-to-noise ratios, disturbed kinematics are difficult to distinguished from large-scale rotation, and features on smaller scales, but crucial to a correct interpretation of the data, will be lost. In addition, the dynamic range of the data will be lowered by the tight observational constraints. Interestingly, and although such a comparison can only be anecdotal given the complexity of ULIRGs, dispersions seem to be less affected than, e.g., velocities. Especially sources consisting of two components nearly have their intrinsic dispersions and line ratios preserved in the AO and non-AO high redshift scenarios.

3. SMMJ14011+0252

3.1. Introduction

SMMJ14011+0252 is the best-studied individual submillimeter-selected galaxy. Observations range from X-rays to radio wavelengths, and deep longslit spectroscopy has previously been taken in the rest-frame UV and optical range. At a redshift of $z = 2.565$ ⁴, all relevant optical emission lines fall within the atmospheric windows, namely [OII] $\lambda\lambda$ 3726,3729 at $\lambda_{obs} = 1.38$ (J band), H β and [OIII] $\lambda\lambda$ 4959,5007 at $\lambda_{obs} = 1.733 - 1.785$ μ m(H band), and [OI] λ 6300, H α , [NII] $\lambda\lambda$ 6548,6583, and [SII] $\lambda\lambda$ 6717,6730 at $\lambda_{obs} = 2.2 - 2.4$ μ m(K band).

SMMJ14011 lies behind the $z = 0.25$ galaxy cluster A1835, and is gravitationally lensed by the cluster potential (see Section 6 of Chapter 4 for a discussion of the lensing mechanism). Although the presently available data sets allow only a rough estimate of the detailed matter distribution within the cluster, a very thorough approach to determine its lensing potential, and especially the magnification of SMMJ14011+0252, has been recently published by Smail et al. (2005). Their

⁴Using the flat $\Omega_{\Lambda} = 0.7$ cosmology with $H_0 = 70$ $\text{kms}^{-1} \text{Mpc}^{-1}$ leads to $D_L = 21.04$ Gpc and $D_A = 1.66$ Gpc at $z = 2.565$. The size scale is 8.03 kpc/”. The age of the universe with this redshift and cosmological model is 2.5 Gyrs. Most of the studies of the overall SMG population described in the previous section was derived for a flat $\Omega_{\Lambda}=0.73$ cosmology with $H_0=71\text{kms}^{-1}\text{Mpc}^{-1}$. In this cosmology and at a redshift of ~ 2.5 , luminosity and size distances are larger by a few percent. Given the large scatter of luminosities and sizes within the SMG population, and the uncertainties in the measurements, these differences appear negligible.

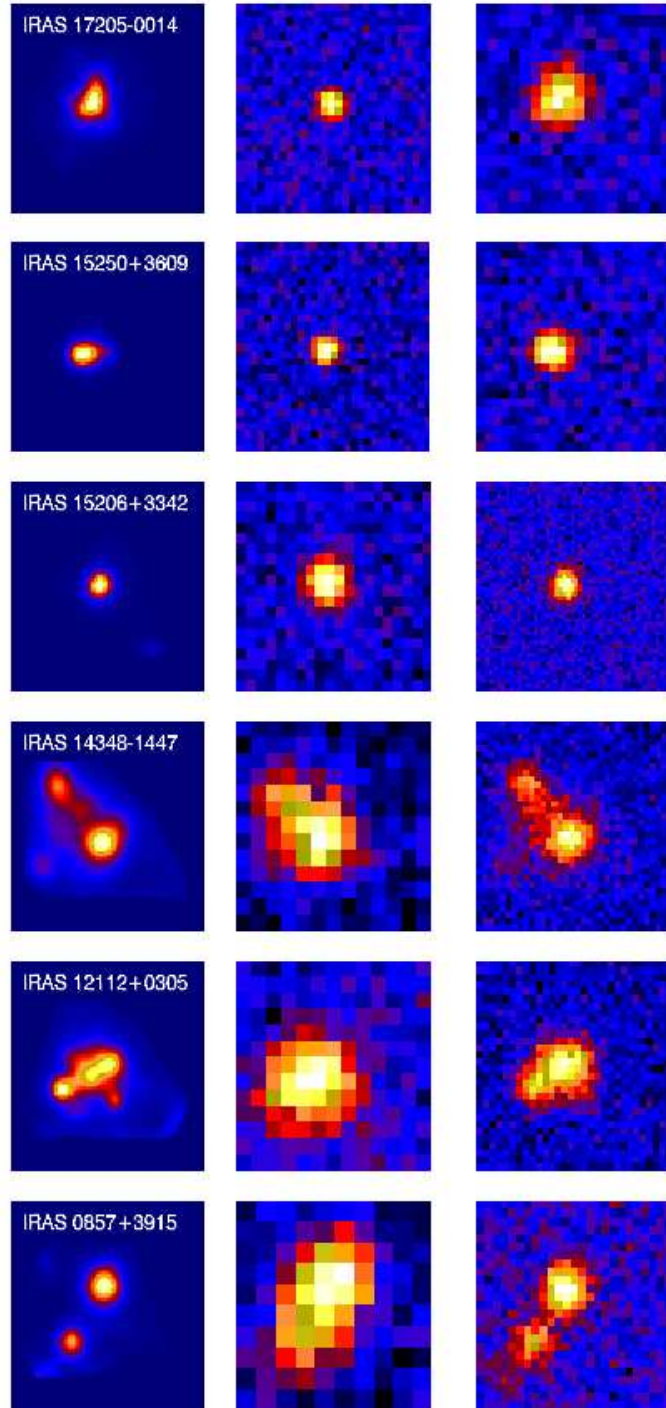


Fig. 1.— $H\alpha$ line images of the Colina et al. (2005) sample of low-redshift ULIRGs. Left column: Input images, middle column: targets placed at $z = 2$ with observational constraints like in ground-based, non-AO observations with SPIFFI/SINFONI, right with observational constraints similar to SINFONI-AO.

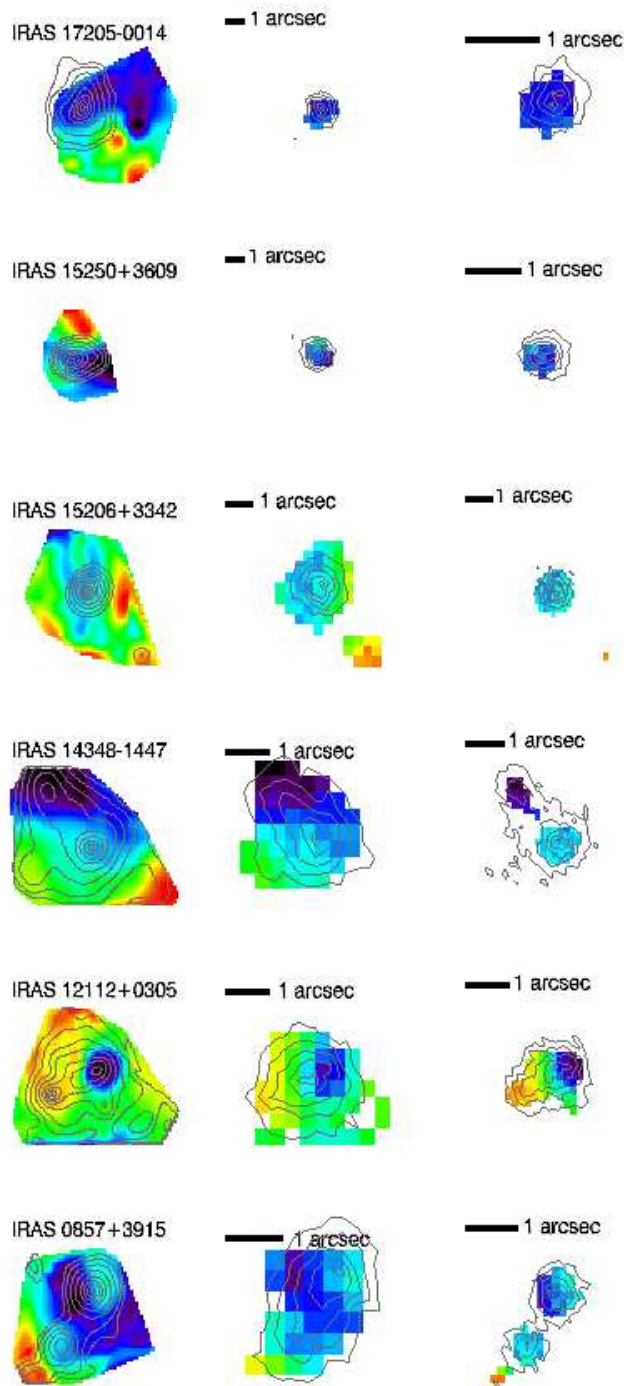


Fig. 2.— $H\alpha$ velocity maps of the Colina et al. (2005) sample. The three columns indicate the raw data (left column), and their $z = 2$ equivalents seen with the non-AO (middle column) and AO-assisted (right column) SPIFFI/SINFONI, respectively.

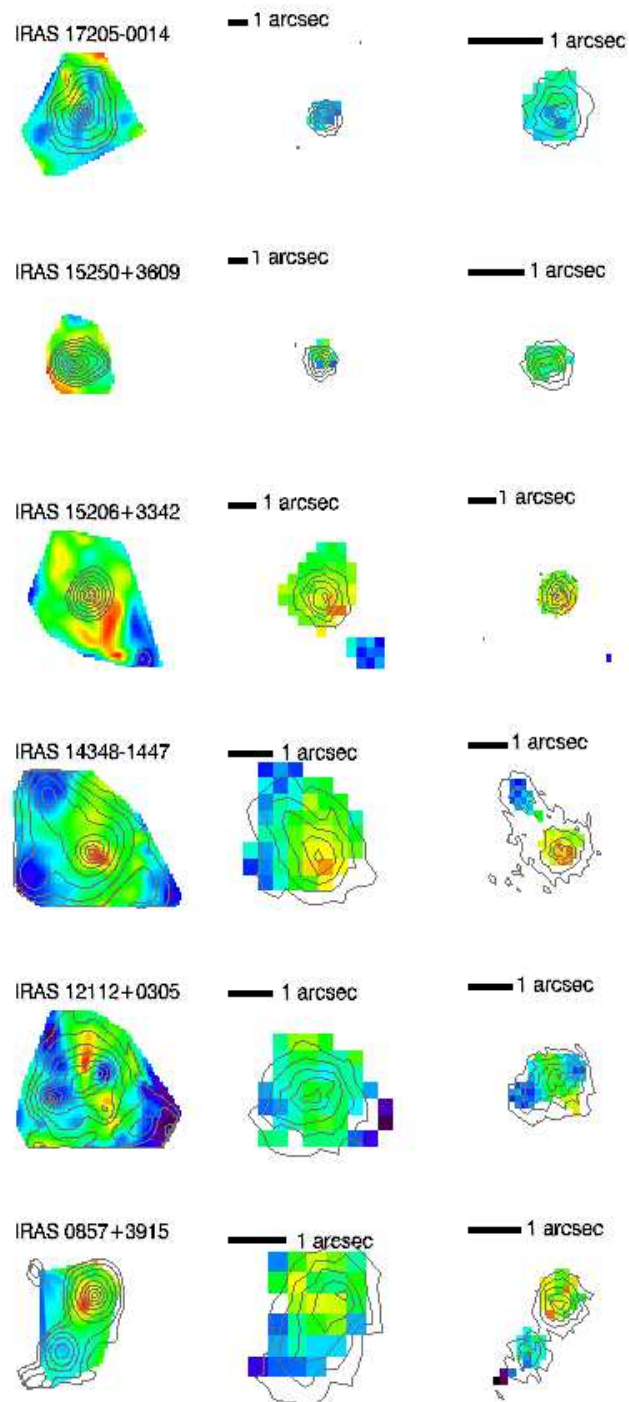


Fig. 3.— $H\alpha$ line dispersions (images) and $H\alpha$ contours in the Colina et al. (2005) sample.

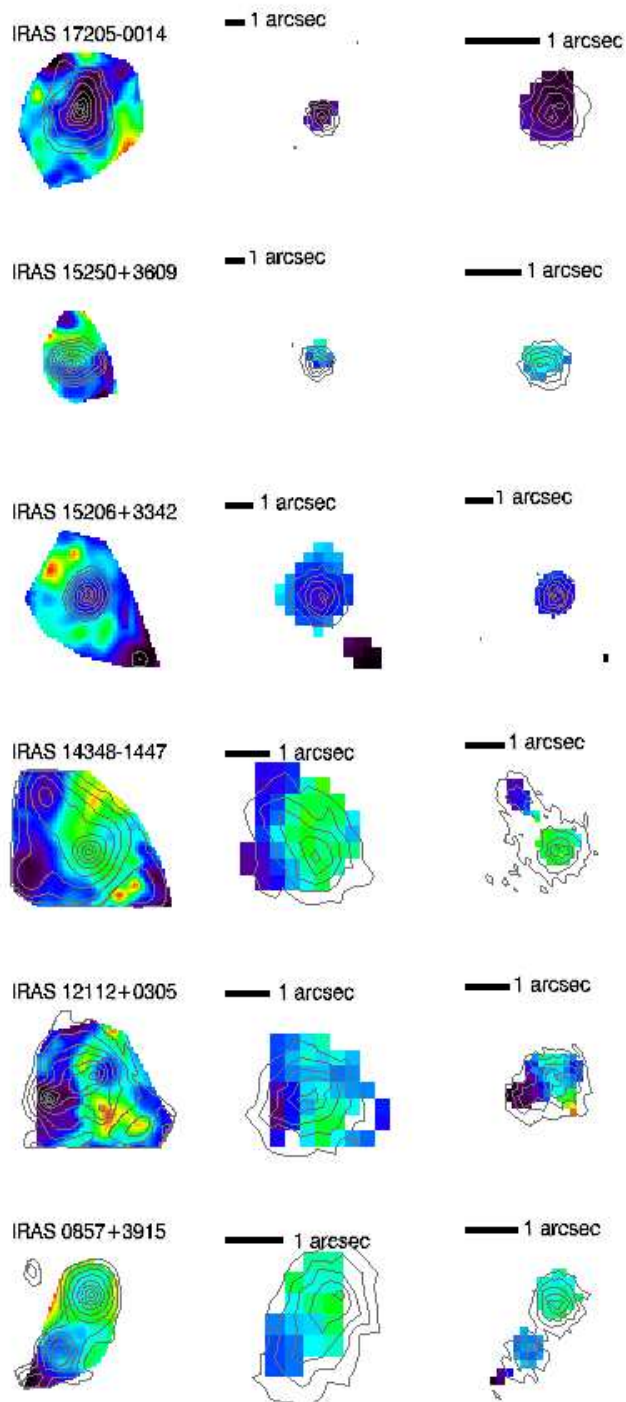


Fig. 4.— $[NII]/H\alpha$ line ratios (images) and $H\alpha$ contours in the Colina et al. (2005) sample.

best-fit models suggest magnification factors $\mathcal{M} = 3 - 5$. This is in agreement with the results by Baker et al. (2005), who suggest $\mathcal{M} = 2 - 4$.

Iverson et al. (2000) obtained HST-WFPC2 imaging of SMMJ14011+0252 through the F702W filter (roughly R-band) and found a number of well separated, but unresolved knots (see Fig. 5). $J - K$ color maps indicate that the colors vary across J1, with the reddest color ($J - K = 5.03$) reached in the northern part of J1. Iverson et al. (2001) attribute this to extinction and localize the starburst in this red knot. They find CO emission originating near J1n, but this depends crucially on the precision to which the data in the different wavebands can be aligned. Given the uncertainty in the astrometry, a minor controversy has erupted in the literature about the location of the CO and thus the nature of this source (e.g., Downes & Solomon 2003). An attempt to obtain a robust astrometry based on new data will be presented in Sec. 3.3.

The complexity of the source led Downes & Solomon (2003) to suspect that parts of the continuum emission might arise from an interloper within the foreground cluster, and might also lead to strong ($\mathcal{M} = 25$ and larger) gravitational lensing (Downes & Solomon 2003; Motohara et al. 2005) by a foreground galaxy. These concerns are now largely ruled out (Smail et al. 2005) and also this analysis finds that none of the components is in disagreement with being at $z = 2.6$. However, some of the most distinct spectral features are degenerate for the two redshifts. $P\alpha$ at $z \sim 0.25$ has a similar observed redshift as $H\alpha$ at $z \sim 2.56$, and some of the optical Balmer absorption lines at the cluster redshift coincide with rest-frame UV metal absorption lines at $z \sim 2.56$. This makes it difficult to disentangle contributions from the cluster and the background source based on existing data sets and with limited signal-to-noise ratios of the absorption line spectra.

SMMJ14011+0252 is dominated by a strong starburst ($SFR = 100 - 1000 M_{\odot} \text{ yr}^{-1}$) and shows no signs of an AGN, neither from its rest-frame optical emission line ratios which are sensitive to ionization/excitation by ionizing power-law spectral energy distributions as observed in AGN, from the rest-frame optical or UV morphology (see the next chapters), nor at X-ray wavelengths (Fabian et al. 2000).

SMMJ14011+0252 has a bluer companion (J2) at $\sim 2''$ distance with the typical colors of a Lyman-break galaxy (see Section 8). CO emission has been detected in the submillimeter source and main component J1, but not in the smaller J2. The similar redshifts of the two components (the redshifts from $H\alpha$ are $z_{J1} = 2.5652$ and $z_{J2} = 2.5635$) suggests they are physically related, as pointed out by Iverson et al. (2000); Tecza et al. (2004).

The complexity and relative brightness ($m_K = 17.8$ mag, Iverson et al. 2000) of SMMJ14011+0252 make it a very promising target for SPIFFI/SINFONI observations. Equivalent widths are remarkably large for a starburst dominated SMG (130 \AA rather than the average $76 \pm 25 \text{ \AA}$ in the Swinbank

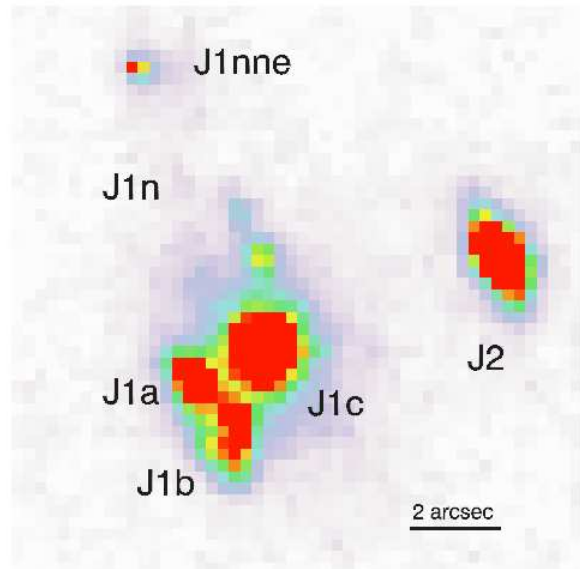


Fig. 5.— $F702W$ HST image of SMMJ14011+0252. Labels indicate the position of subcomponents.

sample). In addition, the line emission extends over $\sim 4''$, well suited to resolve it spatially and cover its full extent in the $8'' \times 8''$ SPIFFI field of view and with seeing-limited resolution. The analysis of the integrated SPIFFI data of SMMJ14011+0252 has already been analysed and published (Tecza et al. 2004). The main results include the supersolar metallicity ($12 + [O/H] = 8.96_{-0.10}^{+0.06}$ or supersolar by 0.27 dex) and high overall star formation rate (FIR emission indicates $\sim 400 M_{\odot}$ for a fiducial magnification factor of $\mathcal{M} = 5$).

The next chapters will show the clear advantages of integral-field spectroscopy for the analysis of complex sources, and reveal that SMMJ14011+0252 has an even richer phenomenology than previously thought. By combining the SPIFFI-GI data with other multi-wavelength data sets now available for this source, earlier ambiguities, e.g. concerning the astrometry and magnification, can be resolved.

3.2. SPIFFI and complementary data sets

SPIFFI data of SMMJ14011+0252 were obtained in the J, H and K-bands during the SPIFFI commissioning and ‘‘Guest Instruments’’ runs in spring 2003. Individual exposure times and the observing dates are summarized in Table 1 in Chapter 3. Total exposure times were 340 min in K, 95 min in H and 60 min in J. The data were calibrated using the UKIRT faint standard FS135 and agree within a few percent with the magnitudes previously published for SMMJ14011+0252. The size of the seeing disk was also determined from standard star measurements and is $\text{FWHM} = 0.6'' \times 0.4''$ in right ascension and declination, respectively.

Although these SPIFFI-GI data form the core of this analysis, a large number of complementary data sets was available to supplement and refine the interpretation of the SPIFFI data and the overall nature of the source. Ivison et al. (2001) obtained high-resolution optical imaging of the A1835 field through the F702W ($\equiv R_{702}$) filter of the WFPC2 onboard the HST. The reduced image was kindly provided by R. Ivison. There is also a 1.4 GHz continuum map of A1835, which was obtained with the NRAO Very Large Array (VLA) by Ivison et al. (2001), and the CO (3–2) and 242 GHz continuum maps of SMMJ14011+0252 obtained with the IRAM Plateau de Bure Interferometer (PdBI) by Downes & Solomon (2003). These authors, Rob Ivison and Dennis Downes kindly provided these data. In addition, ISAAC J, H, and K band images are available from the ESO archive. These images were reduced as described in Bremer et al. (2004). The ISAAC near-infrared images proved to be useful both for a broad band photometric study of SMMJ14011+0252 and for a comparison of the colors of the J14011 complex with the foreground cluster galaxies. In addition, deep VLT FORS 1 V-band image of the field of A1835 was obtained, reduced, and is described in (Lehnert et al. 2005). A. Barger kindly provided the rest-frame UV spectra taken with LRIS on the Keck 10m telescope and published in Barger et al. (1999).

3.3. Absolute astrometry

When interpreting multi-wavelength data to reveal the internal structure of high-redshift galaxies, precise alignment of the multi-wavelength data sets on sub-arcsec level obviously plays a crucial role in deciding on the nature of submm sources. However, a proper alignment is often difficult to obtain with typical absolute astrometric uncertainties of $\gtrsim 1''$ in the individual wavebands, limited fields of view, and rare suitable reference point sources across the electromagnetic spectrum. This is also the case for SMMJ14011+0252. Different relative astrometric alignments have been

proposed in the literature (cf. Downes & Solomon 2003; Ivison et al. 2001), especially for the CO and rest-frame optical data, resulting in vastly different interpretations of the data. Again, this highlights the key role of accurate astrometric alignment.

The recently obtained ISAAC and FORS images allow to obtain a new and more robust astrometry for the field of SMMJ14011+0252. Exploiting the fact that the VLA radio and PdBI millimeter maps are already within one common coordinate frame (the “radio” frame), the VLA sources visible in the deep V-band image of A1835 (Lehnert et al. 2005) could be aligned with the VLA sources which fell within the field of view of the V-band image. The V-band image was crucial for this, because neither of the earlier optical or near-infrared images had a large enough field of view to allow to assign a sufficiently large number of radio counterparts to the optical/near-infrared sources. In this case, a sample of six radio sources could be cross-identified in the V-band. The measured rms scatter of the resulting alignment is $0.04'' \times 0.08''$, which is vastly superior (a factor of almost 10) to the intrinsic absolute astrometric calibration of either band alone.

All the other optical/near-infrared data were then referenced to the V-band image using a large number of sources that can be identified in both the HST and ISAAC near-infrared images to reduce the relative uncertainty in their relative positions. The K-band ISAAC image of SMMJ14011+0252, using predominately the positions of J1c and J2, is then used to put the SPIFFI data into the common frame (assuming the pixel scale as determined during commissioning the instrument). Since the referencing is done at a single wavelength, i.e., the K-band, uncertainties in the relative positions of the two data sets are marginal beyond the issue of the sampling. In other words, this alignment is limited by S/N and the ability to measure accurately the peak in the flux distribution of J1c and J2 which is much smaller than a single pixel in either data set ($0.25''$ for SINFONI or $0.14''$ for ISAAC).

At the end of this procedure, all data are – to the precision of the original alignment of the V-band and radio map – in the radio frame. The greatest source of relative uncertainty is the small number of radio point-sources that have counterparts within the FORS V -band image ($0.04'' \times 0.08''$). The total absolute uncertainty is somewhat larger: Downes & Solomon (2003) suggests an absolute astrometric uncertainty in the CO map of 0.3 arcsec which includes a term for the uncertainty due to the fitting of the position (which is equal to half of the beam size divided by the signal-to-noise) and an astrometric uncertainty from the calibrators of ~ 0.2 arcsec. Adding this and a fiducial uncertainty of $0.14''$ (the pixel size of the ISAAC data) in quadrature yields a total absolute uncertainty of $0.33'' \times 0.34''$ in right ascension and declination for the registration of CO to rest-frame optical and UV data. This is within 1.4 SPIFFI-GI pixels.

This alignment rules out previous claims that the CO emission might be significantly offset from the UV and optical positions of J1. The position of the CO data is shown in Fig. 30 as contours overlaid on the HST R_{702} and K-band ISAAC images. More difficult is to uniquely assign it with either J1n or J1c. Within the uncertainty of $0.33''$ (now dominated by the astrometric uncertainty of the CO relative to the radio data), associating the CO emission with either position (source) is possible. The CO could also be situated between the two components.

3.4. Multi-wavelength morphological properties

Rest-frame optical continuum emission

The SPIFFI line-free K band continuum image is shown in the left panel of Fig. 6 with the R_{702} contours. The continuum image was obtained following the method outlined in Section 6 of

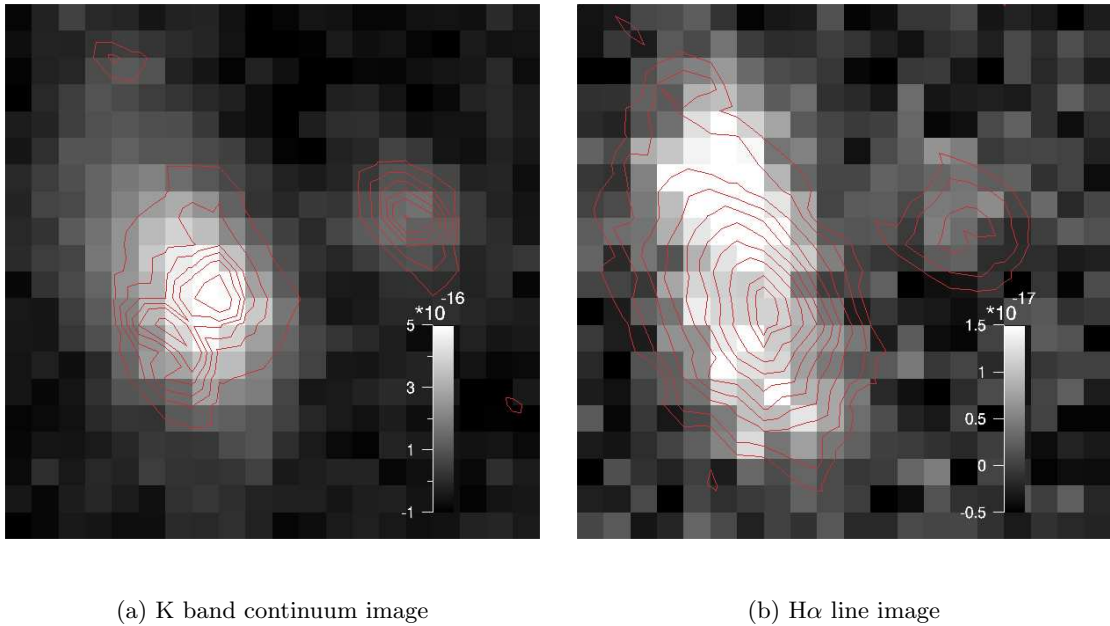


Fig. 6.— *Line-free K band continuum image constructed using the SPIFFI data with the HST R₇₀₂ intensities shown as contours (left). The right panel shows the continuum-free SPIFFI H α line image with the line-free K-band continuum morphology as contours.*

Chapter 3.

J1 is spatially resolved both in right ascension and declination. Apart from the rather symmetric emission around J1c, J1 is elongated, most likely reflecting the stretching by gravitational lensing due to the cluster potential and possibly by individual cluster galaxies. This confirms the findings of Ivison et al. (2001) that the morphology of the near-infrared continuum differs from that found with the HST. Although in either wave-band, the intensity peaks at J1c, the K band emission is smoother and more extended. Most striking is the difference along J1n, where diffuse K band emission, which has no counterpart at shorter wavelengths, and is found to stretch nearly north-south over $>1.5''$ towards J1nne.

Even across the near-infrared wavebands, J1 changes its morphology, resulting in strong color variations. Since the ISAAC near-infrared images are not only deeper, but have also a better spatial resolution⁵ than the SPIFFI-GI data, in the following, the ISAAC data will be used to discuss the morphology. Nonetheless, the integral-field data is vital for the photometry, because it allows to estimate the contamination by line emission also in the broad-band images. This correction is most important in K, where H α and [NII] line emission together exceed 150 Å in EQW. In addition, the perfect alignment of the continuum and line images in the integral-field data can be – and was – largely translated to the imaging data.

Fig. 7 shows the seeing-matched $J - K$ color image of SMMJ14011+0252 J1 and J2. Colors were derived from AB magnitudes, and are ~ 1 mag redder than colors defined within the Vega system. Contours show the H α line image. As previously described (Ivison et al. 2001), diffuse emission arising from J1n has redder colors than J1c, although, as the earlier analyses could not

⁵ $FWHM = 0.43''$ in the K band measured from stars within the field of view.

consider, but comparison with the SPIFFI line image will show (Section 3.5), it is contaminated by line emission. At peak value, the contamination reddens the colors by less than 0.2 mag, hence it is not strong enough to explain the full range of color variations within J1. Although the reddest colors in J1n ($J - K \sim 2.8$) are reached $\sim 2''$ to the north-east of J1c, the zone of comparably red continuum emission ($J - K \sim 2$) stretches approximately to J1c, where it contrasts with the diffuse and bluer ($J - K \sim 1.5$), surrounding halo.

In contrast to previous near-infrared data, however, the K band imaging now allows to identify another red area which coincides with the comparably bright knots J1a and J1b in the HST image. J1a/b has previously not been identified at near-infrared wavelengths, but in these data surprisingly turns out to be rather red ($J - K \sim 2$). Although $H\alpha$ and [NII] line emission was found over this region, it does not have a significant impact on the color. In the following the region south of J1c, which contains these knots, will be referred to as J1s. The prominence of the two knots J1s in the R₇₀₂ image arises from the much smaller PSF of the HST data rather than an intrinsically very blue color at observed optical bands.

3.5. Nebular line emission

Morphology

Among the three SPIFFI data cubes, $H\alpha$ and [N II] $\lambda 6583$ are by far the strongest emission lines. With $R \sim 2000$, the spectral resolution of the SPIFFI data allows not only to safely separate the two lines, but also to spectrally resolve either of the lines over most of the emitting regions. Line fluxes are large enough to find significant spatial variations in velocity, dispersions and line ratios across the source. Continuum-subtracted line images are extracted from the SPIFFI data cube with the method outlined in Section 6 of Chapter 3. To assess the morphology of the nebular line emission, Figure 6 shows the continuum-subtracted $H\alpha$ line image with the Isaac K band contours overlaid. Consistent with the results of Tecza et al. (2004); Motohara et al. (2005); Swinbank et al. (2004), strong $H\alpha$ line emission is observed over an approximate area of $1.5'' \times 4.0''$ across J1 and J1n, peaking in J1n. No line emission was found to originate from J1nne. At J1c, line emission is also observed, although at lower intensity and lower equivalent width. Comparison with equivalent widths shows that the irregularities of the line emission indeed reflect variations in the intrinsic line fluxes, and not in the extinction, as might be the case given the color variations across the source.

Although the general morphology of the [NII] $\lambda 6583$ line emitting regions is similar to that of $H\alpha$, the line ratios vary significantly. The line maps are shown in Fig. 8. The [NII]/ $H\alpha$ ratio reaches a maximum of 0.7 ± 0.1 in J1n. This peak is displaced by ~ 1.5 pixels from the location of brightest $H\alpha$ flux, roughly situated in the middle between J1c and the maximum of the Balmer line emission. The zone of relatively large [NII]/ $H\alpha$ ratio stretches from north-east to south-west across J1c. Line

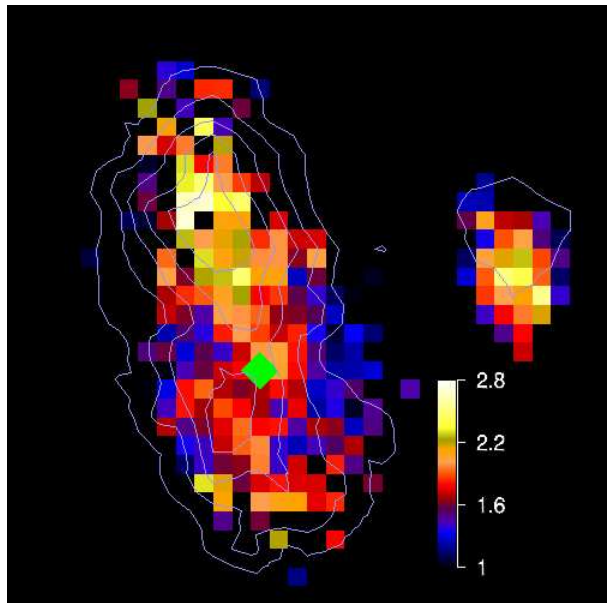


Fig. 7.— $(J - K)_{AB}$ color map of SMMJ 14011+0252 (from ISAAC imaging). The overlaid contours are the distribution of $H\alpha$ line flux. The green diamond indicates the position of the continuum peak J1c.

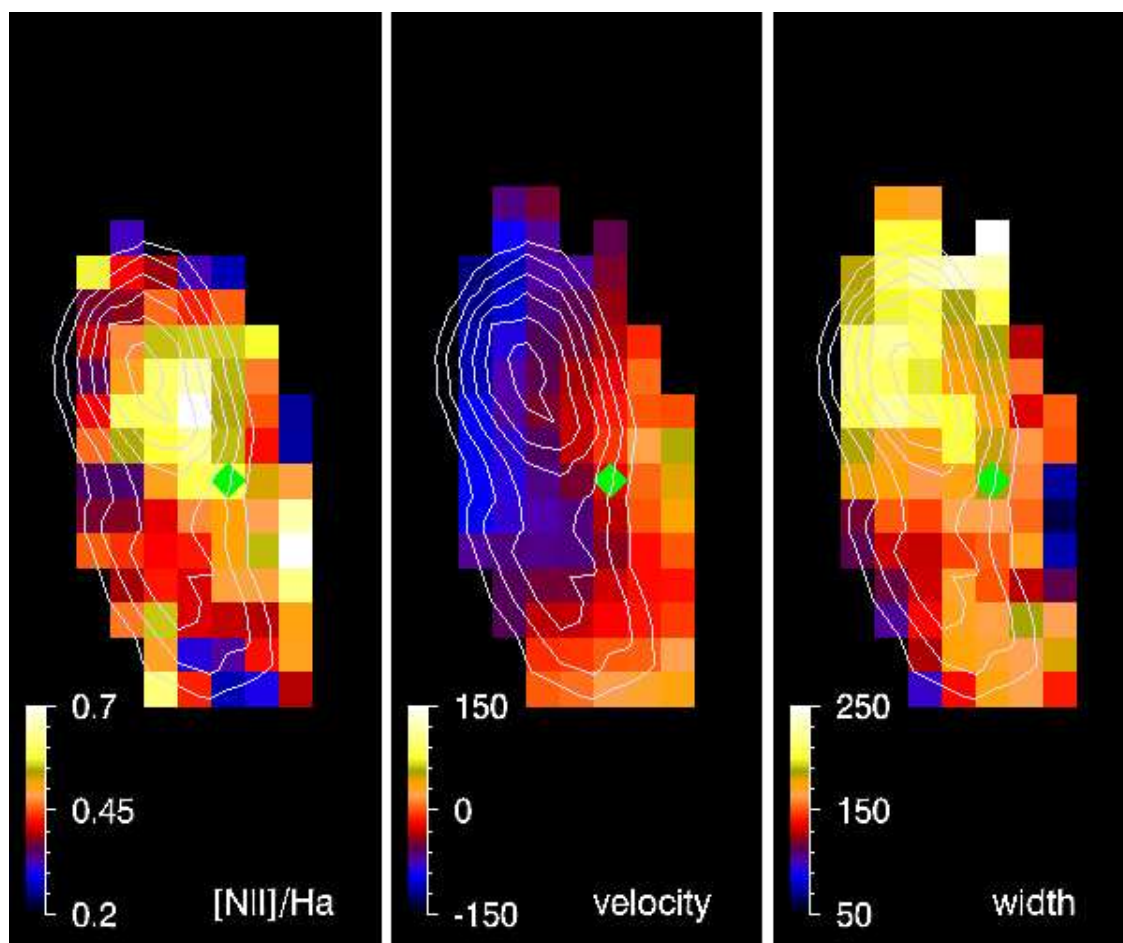


Fig. 8.— Spatial distributions of $[NII]/H\alpha$ ratio, velocity and $H\alpha$ line widths for J1. Contours indicate the $H\alpha$ flux, from 1 to $5 \times 10^{-21} \text{ Wm}^{-2}$. Velocities and widths are given in km s^{-1} . Typical uncertainties are $\sim 10 \text{ km s}^{-1}$ for the velocity and 15 km s^{-1} for the width. The green diamond in each figure shows the position of maximum continuum flux J1c.

ratios around J1s are significantly lower, with typical values around 0.4 ± 0.04 . Line widths also vary across the source, with intrinsic FWHMs in J1n being relatively large ($\text{FWHM} \sim 220 \pm 20 \text{ km s}^{-1}$) as compared to J1s ($\text{FWHM} \sim 170 \pm 18 \text{ km s}^{-1}$).

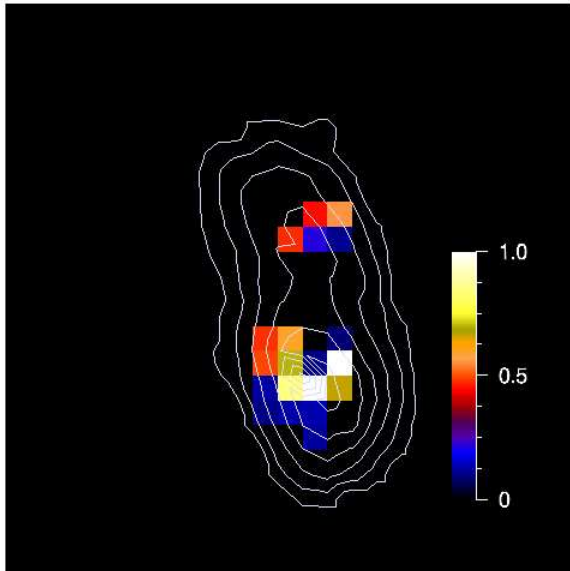


Fig. 9.— $[\text{OIII}]\lambda 5007/\text{H}\beta$ ratios in areas of strongest H band line emission. Contours yield the $\text{H}\alpha$ line image for orientation. $[\text{OIII}]$ and $\text{H}\beta$ emission in J1s coincides with the center of the faint $\text{H}\alpha$ emitting disk. In J1n, the $[\text{OIII}]/\text{H}\beta$ ratio reaches its maximum, and coincides with the area of strongest $[\text{NII}]$ emission.

Exposure times in the H band were considerably shorter than in K. However, $\text{H}\beta$ and $[\text{OIII}]\lambda 5007$ line emission is bright enough to obtain line images integrating over 3×3 pixels ($0.75'' \times 0.75''$). The comparably low signal-to-noise ratios and the proximity of prominent telluric residuals make it difficult to isolate the $[\text{OIII}]$ line emission. Emission lines are therefore only used when their observed wavelength agrees with their expected wavelength (determined from $\text{H}\alpha$) within uncertainties of 1σ and when their flux (assuming the $\text{H}\alpha$ line width) exceeds 3σ to mitigate against the effects of the night sky emission. Fig. 9 shows the resulting $[\text{OIII}]/\text{H}\beta$ ratios. $[\text{OIII}]\lambda 5007$ is detected in two areas, one coincident with the $\text{H}\alpha$ peak between J1a and b. Line ratios are ~ 0.3 . The second area in J1 where both $[\text{OIII}]$ and $\text{H}\beta$ were detected aligns with the maximum $[\text{NII}]$ emission in J1n. $[\text{OIII}]/\text{H}\beta$ line ratios exceed unity here.

Spatially resolved kinematics

The K-band integral-field data of SMMJ14011+0252 J1 are of superb quality and allow to map the kinematic properties of the source across an area of $1.75'' \times 3.25''$ with precisions of $\sim 10 \text{ km s}^{-1}$. The $\text{H}\alpha$ velocity and width maps are shown in Fig. 8. Velocity varies by 190 km s^{-1} in roughly diagonal direction, increasing from north-east to south-west. Although the velocity gradient is continuous, it is not strictly monotonous, because the data suggest velocity maxima in two locations, one slightly north-west from J1c, the other in the southern part of the source. The two peaks reach maxima of $\sim 110 \text{ km s}^{-1}$ and $\sim 130 \text{ km s}^{-1}$ respectively, the minimum between these peaks is $\sim 50 \text{ km s}^{-1}$. Using the Monte Carlo generated error estimates at the three reference points, the difference between the minimum and each of the maximum velocities is significant to 4.4σ . The right panel of Fig. 8 shows the measured $\text{H}\alpha$ FWHMs. Widths are between 130 km s^{-1} and 250 km s^{-1} , and generally higher in J1n than in J1s. Statistically speaking, however, line width in J1n and J1s are only marginally different, due to the large scatter: In J1n, the average width is $198 \pm 32 \text{ km s}^{-1}$ in J1s $157 \pm 35 \text{ km s}^{-1}$.

Integrated properties of the ionized gas in J1n, J1c, and J1s

Having identified regions of rather uniform line emission, the discussion will now turn to the differences between these zones. Larger apertures are used for this study, to enhance the significance of the data, and also to be sensitive to more subtle variations between these zones. Line properties are summarized in Table 3.

To differentiate between the different regions in J1, integrated spectra of J1n and J1s are compared, adding an additional zone J1c. Pixels are taken to belong to J1c, if they are within $0.25''$ north or south of the continuum peak. This coincides approximately with the size of the seeing disk but does tend to also minimize correlations between J1n and J1s. Obtaining a truly isolated spectrum of J1c is nearly impossible, because J1n and J1s are close in projection, as comparison with the emission line maps shows (see Sec. 3.5). Pixels south of this region are grouped into J1s, whereas pixels north of it constitute J1n.

To take the full line emission into account, spectra are integrated over all pixels shown in the velocity map along right ascension (i.e. over all pixels along a slitlet where $H\alpha$ emission is found at significant levels).

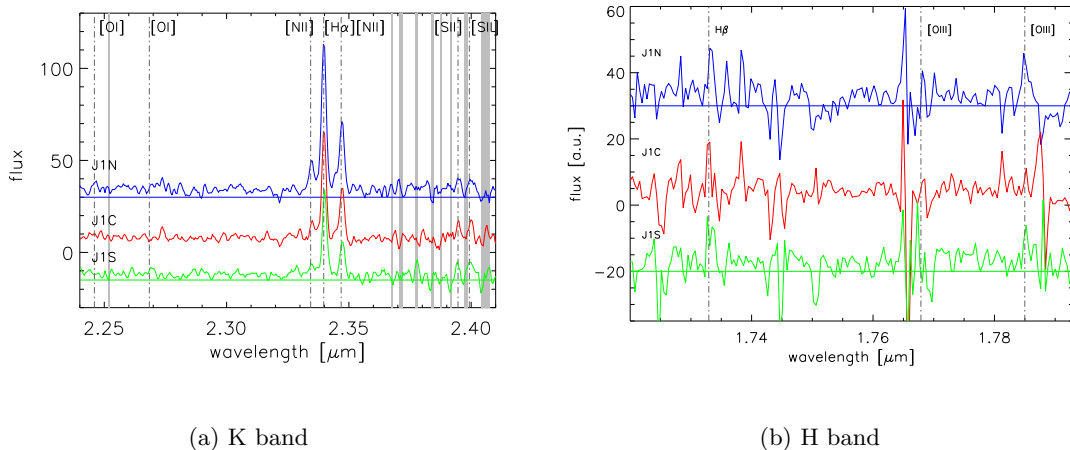


Fig. 10.— Spectra of J1n, J1c, and J1s in H (upper panel) and K (lower panel). Vertical dot-dashed lines show the expected positions of optical emission lines at $z=2.565$, irrespective of whether they are actually observed. With increasing wavelength, they are $[OI]\lambda 6300$, $[OI]\lambda 6363$, $[NII]\lambda 6548$, $H\alpha$, $[NII]\lambda 6583$, $[SII]\lambda 6717$, $[SII]\lambda 6730$. Vertical light grey bars indicate the position of night sky line residuals. A velocity offset between J1n and J1s was found on a $\sim 2\sigma$ level. The $[NII]/H\alpha$ ratio is lower in J1s than in J1n and J1c. Forbidden lines are most prominent in J1c, and were not observed (except for $[NII]$) in the faintest region J1s.

The resulting K band spectra are shown in Fig. 10. J1n and J1s have a velocity offset of 61 ± 9 km s^{-1} , significant on a $\sim 6.6\sigma$ -level. $[NII]/H\alpha$ ratios are 0.52 ± 0.05 , 0.43 ± 0.05 and 0.55 ± 0.05 in J1n, J1s, and J1c, respectively. Again, high values are reached in J1n and J1c, which are larger by $\sim 1.4\sigma$ than those in J1s. Relative velocities of the three regions are summarized in Tab. 1. The velocity of J1c agrees with that of J1n within the uncertainty. In agreement with the width map, the $H\alpha$ line width of the integrated emission in J1c is (marginally) smaller than in J1s, which in turn is smaller than in J1n. All emission line data are summarized in Table 3.

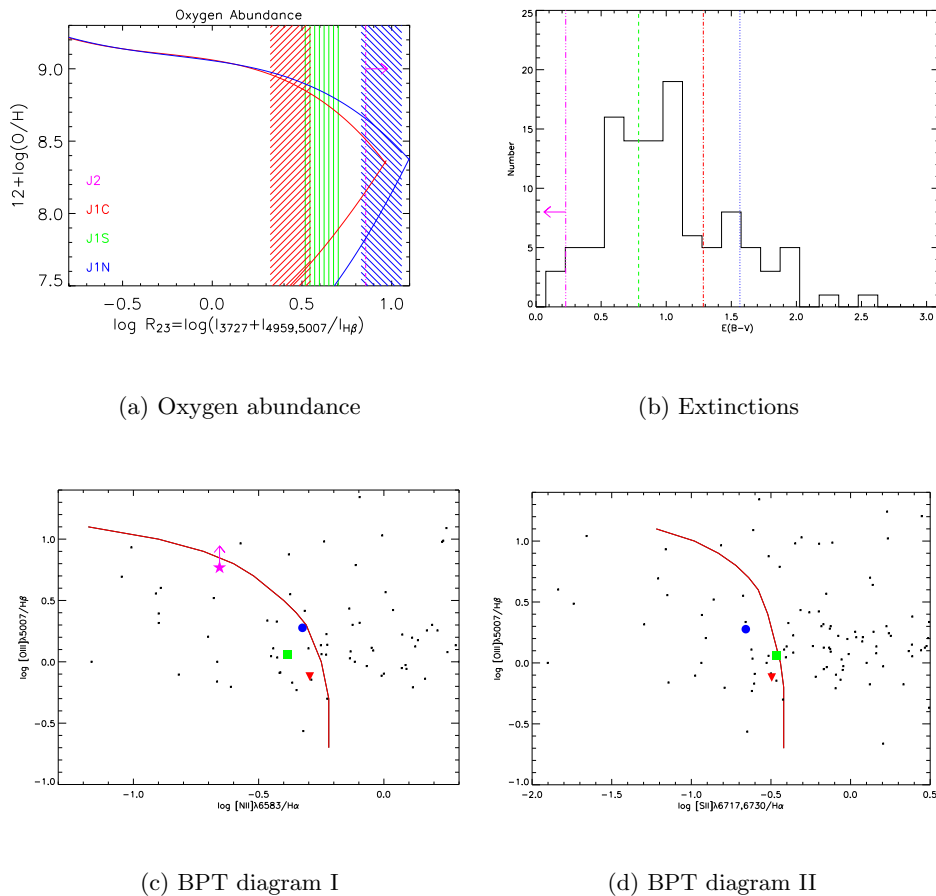


Fig. 11.— Line diagnostics for J1n (blue), J1s (green) and J1c (red). Top left: Extinction corrected R_{23} oxygen abundances. Blue and red lines represent the abundances for low and high excitation emission line gas. The large $[NII]/H\alpha$ ratios indicate that the upper branch applies. Top right: Extinction, measured from the $H\alpha/H\beta$ ratio. The histogram shows typical values for local ULIRGS (Veilleux et al. 1999). Bottom: BPT diagrams to divide AGN from HII regions (red lines). Black dots indicate the sample of local ULIRGS of Veilleux et al. (1999).

Following the method outlined in Section 1.3, line fluxes were corrected for extinction, using the observed $H\alpha/H\beta$ ratio, and a galactic extinction law. Separate $E(B-V)$ values were obtained for J1s, J1c, and J1n. They are represented in the upper right panel of Fig. 11 by the green, red, and blue line, respectively. Their numerical values are summarized in Table 1. The black histogram of low-redshift ULIRGS (taken from Veilleux et al. 1999) is added for comparison. Clearly, although all components of J1 have extinctions that are within the wide range observed in low redshift ULIRGS, J1n is most heavily extinguished, whereas J1s has average extinction with respect to the low-redshift sample. J1c falls in between, and is probably contaminated by line emission from other zones.

Diagnostic diagrams comprising the emission lines in the K band, and those in the H band ($[\text{OIII}]\lambda 5007$ and $\text{H}\beta$), are given in the lower panel of Fig. 11. The emission line ratios are clearly in the region of either direct ionization from massive stars in HII regions or diffuse ionization like observed in the Milky Way and other nearby galaxies (see discussion in Lehnert & Heckman 1996a). These findings are in agreement with X-ray observations (Fabian et al. 2000), where SMMJ14011+0252 was not detected. Comparing the ratio of the $850\mu\text{m}$ to 2keV flux, Fabian et al. (2000) find that e.g. the starburst dominated Arp 220 would equally be too faint at X-ray wavelengths to be detected, if it was at $z \sim 2.6$.

For comparison the sample of low-redshift ULIRGS by Veilleux et al. (1999) is shown in Fig. 11. Emission line ratios in SMMJ14011+0252 are well within the range spanned by the ULIRGS, and extinctions also seem similar. Line ratios are consistent with photoionization by massive stars. Hence J1 appears to be a fairly “typical” starburst-dominated ULIRG. Note that this is not the case for J2, which is not a submillimeter-selected galaxy, but fullfills the Lyman-break selection criteria. Because it will be discussed in more detail in a later section, it is also given in the diagrams. J2 has a very low extinction and different ionization properties than J1 and most of the Veilleux et al. (1999) sample. While such an analysis of optical emission line ratios has significant discriminating power, the ULIRG results show the diversity in emission line properties which may well be the case for the high redshift submm sources as well.

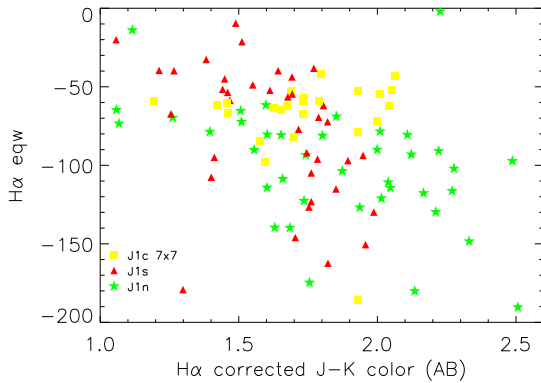


Fig. 12.— $H\alpha$ equivalent width (in \AA) vs. $(J - K)_{AB}$ colors. Negative values indicate emission. Green stars indicate J1n, red triangles J1s, and yellow squares J1c, respectively. Colors are corrected for line emission.

Although the scatter is large, not surprisingly given the generally high extinction and possible range of ages in the stellar population, $J - K$ color and $H\alpha$ equivalent width are remarkably well correlated over the whole of SMMJ14011+0252. Investigation the color versus $H\alpha$ equivalent width as a function of their continuum location indicates a correlation within the regions J1a/b and J1n, while within J1c there is no correlation. The larger scatter in J1n is due to its generally low continuum surface brightness making it intrinsically difficult to measure. Non-parametric tests are best suited to quantify the correlation in the presence of large scatter. Both the Spearman test and Kendall’s τ yield significances $< 5\%$ for a correlation in J1n, and $< 1\%$ for J1s. Small values in the non parametric tests indicate a high correlation significance. Gaussian distributions have significances ~ 0.5 in both tests.

The difference to the low-redshift correlation might arise from the fact that Liu & Kennicutt

From the flux-calibrated and extinction-corrected spectra, star formation rates can be estimated using Equation 4.9 in Chapter 4. Resulting star formation rates are $110 M_{\odot} \text{ yr}^{-1}$ for J1s, $307 M_{\odot} \text{ yr}^{-1}$ for J1c, and $695 M_{\odot} \text{ yr}^{-1}$ for J1n, not correcting for lensing. The values for J1n and J1s differ by more than a factor 6. J1c falls between (both in star-formation rate and spatially).

Perhaps surprisingly, comparison of the $H\alpha$ equivalent widths with the $J - K$ color map reveals a positive correlation between the relative intensity of recent star formation and continuum color, opposite to local galaxies with enhanced star formation (e.g. Liu & Kennicutt 1995). Fig. 12 shows the $J - K$ color as a function of $H\alpha$ equivalent width. Although the scatter is large, not surprisingly given the generally high extinction and possible range of ages in the stellar population, $J - K$ color and $H\alpha$ equivalent

(1995) compare the integrated spectra of galaxies, whereas here, different apertures are used that were extracted within one source. Liu & Kennicutt (1995) therefore find that the line emission gets more and more extinguished as the overall dust content of the galaxy increases. Here, an individual source is spatially resolved and the measurement is sensitive (in comparison) to the distribution of the dust within the galaxy. The positive correlation implies that, although extinction is highest in the most intense star-forming regions (in the sense of the highest ratio of young to old stellar population as indicated by the ratio of ionizing to optical continuum photons), the escape fraction of H α photons is comparably large at least along certain lines of sight. In other words, the dust is inhomogeneously distributed. This is in agreement with the results of Chapman et al. (2003) who

were surprised to find Ly α line emission in some SMGs. They also come to the conclusion that this is due to clumpy dust distribution so that the escape fraction of Ly α photons must be comparably high. Spatial resolution and correlation with rest-frame optical color suggests that the line emission is effectively less obscured than the continuum in agreement with the general results of Calzetti (1997) for local actively star-forming galaxies. Overall, the relationship between H α and $J - K$ color illustrates that the reddening in J1 is dominated by extinction, and not by age.

Since the density-sensitive line doublets [OII] $\lambda\lambda$ 3726,3729 and [SII] $\lambda\lambda$ 6717,6730 are detected and spectrally resolved, it is possible to estimate the electron density in the line-emitting gas (see the formalism described in Section 1.1 of Chapter 4). Since both line doublets are comparably faint, the densities are only estimated from the integrated spectrum. Measured line ratios are $R_{[SII]} = I(6717)/I(6730) = 1.25$, and $R_{[OII]} = I(3726)/I(3729) = 1.07$. The calibration diagram for an electron temperature $T_e = 10^4$ K gas is shown in Fig. 13. Shaded areas indicate the [SII] and [OII] 1 σ areas and suggest an electron density estimate of $\rho_e \approx 300 \text{ cm}^{-3}$.

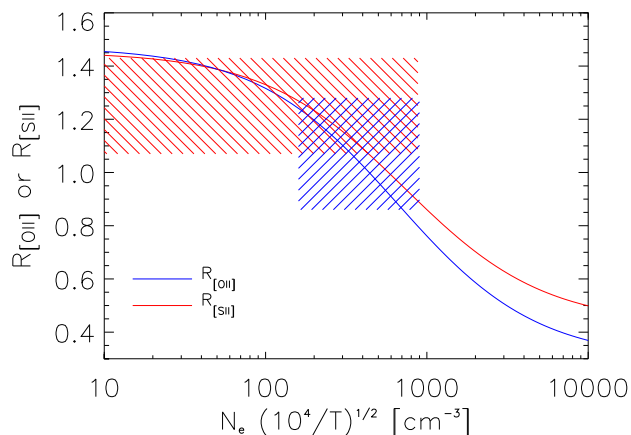


Fig. 13.— *Electron densities in SMMJ14011+0252. Shaded areas indicate the 1 σ range spanned by the measured [OII] and [SII] ratios, respectively.*

3.6. Is J1c a faint A1835 cluster member?

It has previously been suggested (Downes & Solomon 2003; Motohara et al. 2005; Smail et al. 2005) that the J1 complex is contaminated by continuum emission from a faint member galaxy of A1835 at $z \sim 0.25$. The importance of this hypothesis is beyond simply having a low redshift source contaminate the photometry and equivalent width estimates; the mass of this source might provide an additional source of lensing and given the alignment, it might dominate over the simple estimate of lensing strength based on the cluster potential. (i.e., be a case of strong lensing, $M \sim 10 - 20$). If J1 was indeed strongly lensed, then its extreme intrinsic luminosity and star formation rate would be accordingly lower and its morphology strongly determined by the foreground galaxy. In addition, the presence of a spectral break has been identified (Tecza et al. 2004). If this break is

due to emission at $z = 2.565$ then it is consistent with the 4000 \AA spectral break of a comparably old ($> 10^8$ yrs) stellar population. But obviously, this argumentation breaks down if there is a major contribution from a low-redshift source to the overall continuum emission of J1c.

In the following, it will therefore be attempted to scrutinize these claims in a number of approaches, all of which favour that J1c is at a comparable redshift as the other components of J1. But this overall discussion is in the spirit of setting a robust limit on the possible contribution of a foreground cluster galaxy.

The apparent deficit of $H\alpha$ line emission near the continuum peak of J1c has been reported several times (Swinbank et al. 2004; Motohara et al. 2005) as evidence for J1c being at low redshift. However, this statement is not very secure. The present analysis sheds some doubt as to whether the single-disk picture is appropriate (see Section 3.10). However, even if J1 consists of only one single disk, low-redshift analogs exist where $H\alpha$ does not peak near the core. Assuming a fiducial magnification factor of $\mathcal{M} \sim 5$, the physical size of this region of apparent $H\alpha$ offset from the continuum peak is about 1 kpc. Similar behaviour, although rare, has been found in nearby ($z < 0.01$) starburst galaxies, e.g. MRK 0363, where the $H\alpha$ line image shows extended, clumpy star formation and peaks at roughly the same distance from the continuum center (Chitre & Joshi 2001). A simple astrophysical explanation for the absence of $H\alpha$ line emission near the peak of J1c might be that the starburst is optically thick even in the rest-frame R band. Given the large extinction and high rest-frame far-infrared luminosity of J1, this appears rather likely.

The spatially-resolved kinematics discussed in Sec. 3.5 might provide the best constraints to rule out that J1 consists of multiple images strongly lensed by a foreground source. Depending on the proposed lensing model, several candidate multiple images have been identified, none of which is in agreement with the intrinsic velocity field of J1. If the components were multiple images of the same region, then their velocities should be equal. The overall velocity gradient across J1 is not in agreement with a set of multiple images of the same region centered around J1c. In addition, colors, equivalent widths, line ratios, and velocity dispersions differ in the claimed multiple images. A foreground galaxy – if it exists – must therefore be of relatively low mass or at a redshift that is not within A1835, so that its potential does not produce multiple images.

Recently, Swinbank et al. (2004) have reported the identification of absorption lines, including $H\delta$ to $H8$, in the optical spectrum of J1 published in Barger et al. (1999), which they claim are consistent with an A star-dominated spectrum at the cluster redshift of $z = 0.25$. Rest-frame UV spectra of high-redshift galaxies generally have a wealth of absorption lines, but unfortunately their equivalent widths are often low. In addition, these lines are often of different origin: some arise in stellar atmospheres, others from the winds of young early-type stars, and some originate from the ISM. Therefore they have small velocity offsets depending on the source of the emission, making their analysis even more difficult. A. Barger has kindly provided this spectrum for the present analysis.

To take account of this complexity, the rest-frame UV spectrum of J1 will not be compared with a model spectrum, but with the composite spectrum of 811 Lyman-break galaxies of Shapley et al. (2001), shifted to the redshift of J1, $z = 2.565$. The J1 spectrum and the composite are shown in Fig. 14, and the principal emission lines are labeled. This is not to suggest that this composite spectrum is an appropriate analogue to the SMMJ14011+0252 spectrum, but just to illustrate the strong UV lines that are likely to be in a spectrum of any star-forming source at high redshift. The agreement of the J1 spectrum with the LBG composite is remarkable, given that the galaxies belong to different populations. What is the most appropriate strategy to decide whether the J1 spectrum shows the imprints of absorption by a foreground galaxy? The presence of a high-redshift

source is obviously indicated by the Ly α line and its peculiar line profile. It therefore appears most robust to assume the “high-redshift-only” scenario as null hypothesis and to verify whether absorption lines are present in the spectrum that can be identified assuming a $z = 0.25$ interloper. Only two such lines are apparent in the spectrum: Ca H and H δ , and none of them exceeds 3σ . At $z = 0.25$, Ca H falls at an observed wavelength of $\lambda_{obs} = 4917.13 \text{ \AA}$, which is 1.06 \AA from a night sky line. H δ alone is certainly not significant enough to support this claim. Absorption lines in the Barger et al. (1999) spectra can therefore not prove or disprove the presence of a $z = 0.25$ absorber; they simply may be too weak to be seen in this spectrum.

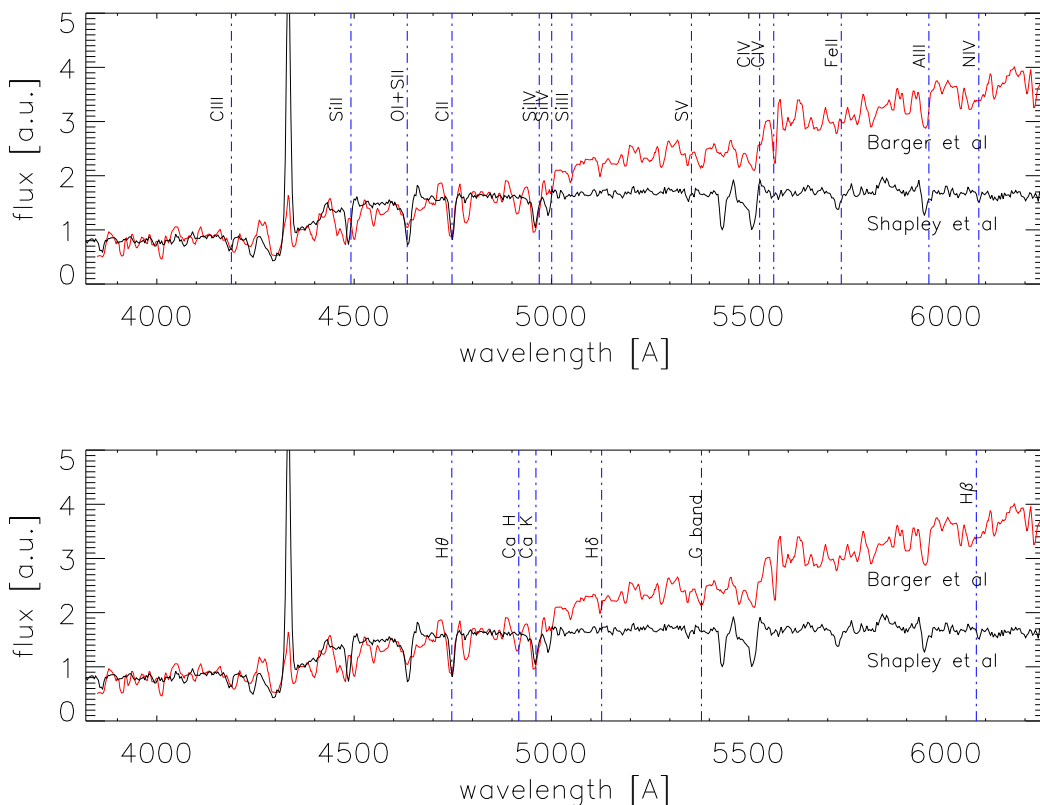


Fig. 14.— *Absorption lines in the SMMJ14011+0252 J1 rest-frame UV spectrum. The upper panel shows the line identification for an absorber at $z = 2.565$, the lower panel the lines for a $z = 0.25$ absorber. The J1 spectrum is shown in red, the black spectrum shows the Shapley, Steidel, Pettini, & Adelberger (2003) composite of 811 Lyman Break Galaxies placed at the redshift of J1.*

In an alternative approach, the spectral slope of the continuum detected in the Barger et al. (1999) spectrum will now be scrutinized. However, neither the Kennicutt (1992) spectral atlas of galaxies (for the $z = 0.25$ hypothesis) nor the Kinney et al. (1996) atlas of UV spectra of nearby galaxies could provide appropriate comparison spectra. None of the Kennicutt (1992) spectra had a spectral index approximately as steep as that of J1, and the UV spectra lacked resolution and signal-to-noise at the relevant wavelengths $\lambda \sim 1300 \text{ \AA}$.

Therefore, artificial SEDs were fitted, using the stellar population synthesis models of Bruzual & Charlot (2003). For the high-redshift hypothesis, the model was constrained to be a continuous, 200 Myr old burst with a star-formation rate of $500 M_{\odot} \text{ yr}^{-1}$, matching the best-fit near-infrared fit done by Tecza et al. (2004). The extinction, especially in the rest-frame UV, is hard to model

based on first principles and over large wavelength ranges. This is even more the case for the dust-enshrouded high-redshift submillimeter sources, which are very unlikely well fit by an extinction model that is tailored to match the Milky Way. Various input values were therefore adopted, and the best fit was obtained for an $A_V=2.1$ in the ISM, using the two-component model by Bruzual & Charlot (2003).

The result is shown in Fig. 15. The SMMJ14011+0252 spectrum is shown in blue, the black line indicates the model. Both SEDs are convolved to the same resolution and have the same binning. Although not all features are perfectly fit, the overall spectral slope can well be reproduced, and over the full spectral range. The largest discrepancies arise redward from 2150 Å (rest-frame), where the night-sky is difficult to suppress. Note the absence of strong spectral features in the modelled SED, which is in accord with the faintness of absorption lines in the spectrum of Barger et al. (1999).

To try the cluster member interloper hypothesis, the observed spectrum was placed at $z \sim 0.25$ where it covers rest-frame wavelengths from 3200 Å to 7200 Å and hence contains the Balmer series from H α to the Balmer limit. Neither H α nor H β or H γ line emission or absorption is observed. In spite of the comparably low signal-to-noise ratio at observed wavelengths of ~ 8300 Å, the spectra published in Barger et al. (1999) suggest that strong H α line emission would not be concealed, assuming typical equivalent widths and extinctions. It can therefore especially be ruled out that the hypothetical foreground source is dominated by a young stellar population, because this would inevitably lead to large equivalent-width H α emission. Hence a spectrum dominated by stars earlier than $\sim A$ can be ruled out.

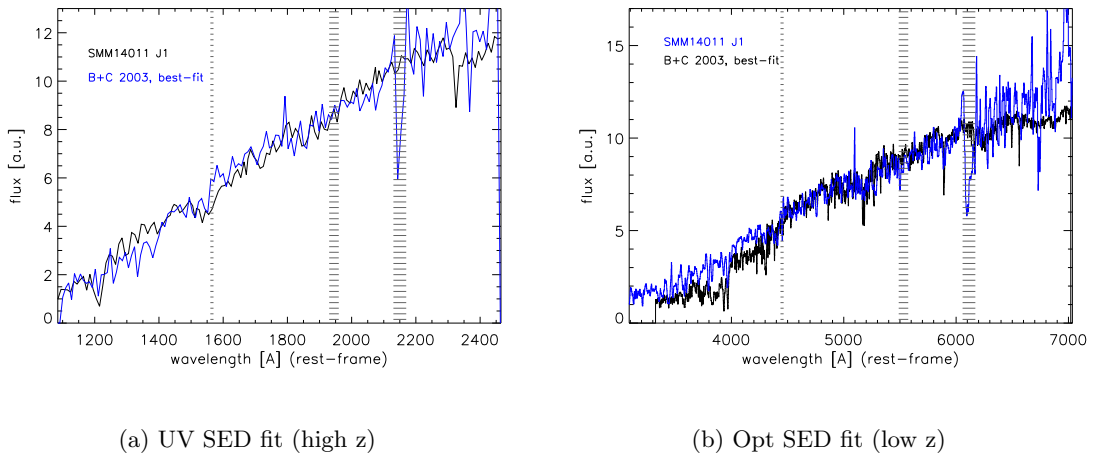


Fig. 15.— *Bruzual & Charlot (2003) model fits to the optical spectrum of J1 obtained by Barger et al. (1999), using different hypotheses regarding the redshift of J1. In each panel, the spectrum is shown in blue, black lines yield the model. Hatched areas indicate the location of strong night sky lines. The upper panel shows the evolutionary model suggested by the near-infrared emission and assuming $z \sim 2.6$. The lower panel shows the best fit model assuming $z = 0.25$ and the model parameters described in the text. Clearly, the spectral index of the data can not well be reproduced in the $z = 0.25$ model. In addition, modeled absorption lines have equivalent widths that should have led to a significant detection in the data.*

A typical feature of old stellar populations is a strong spectral break at ~ 4000 Å rest-frame wavelength (hence $\lambda_{obs} \sim 5000$ Å at $z = 0.25$). Clearly, the data shown in Fig. 15 do not reveal a pronounced spectral break. In addition, strong absorption lines are usually superimposed on the

SED, which are equally not observed in the J1c data. To examine whether such a behaviour might be due to untypical behaviour of an evolved stellar population, e.g. due to high metallicity or age, the model parameters were varied, constraining the maximum age to 10 Gyrs (formation redshift $z_f \sim 10$), which is 500 Myrs less than the age of the universe at $z \sim 0.25$. Even if the hypothesized cluster member formed earlier, the additionally elapsed time would not have a major impact on the evolutionary state of the galaxy after 10 Gyrs.

The best fit model population has $A_V=1.6$, Z_\odot , and was formed in an instantaneous burst 10 Gyrs ago. The impact of metallicity is marginal (Z_\odot and $2.5 \times Z_\odot$ were tested). The observed and modeled SEDs are shown in Fig. 15. Even for this best-fit model, systematic differences are evident, namely a flux deficit at blue wavelength, and flux excess on the red side of the spectrum. Furthermore, the relative strengths of absorption lines in the model do not agree with observation. This especially holds for the Ca H+K and H6 and H7 lines claimed by Swinbank et al. (2004). Neither could the Balmer lines be modeled at the observed relative strength with respect to the claimed Ca H+K lines, nor does the line ratio between the two Calcium lines agree with the predictions. Although this might be due to the low signal-to-noise ratios of the data, it does not strengthen the claim that these lines are indeed observed. Generally speaking, all modeled absorption line equivalent widths are larger than observed.

Although no model was found that would lead to as steep a spectral slope as that observed within the age of the universe at $z=0.25$, fits to model SEDs alone are not necessarily unique. Especially, the observed spectrum in the interloper-hypothesis is likely a combination of the high and low-redshift SEDs, which would result in a very complex overall spectral shape. Fitting a single burst model therefore is certainly an oversimplification. However, the fits suggest that a foreground source – if it exists – can only have a marginal contribution to the overall continuum emission in the spectrum by Barger et al. (1999). This is further supported by the consistency of the star-formation histories derived from the near-infrared and optical data.

Even if the high-redshift source dominates the optical SEDs, the relative contribution of an assumed $z = 0.25$ galaxy might be higher in the observed infrared. Hence in another approach, the deep ISAAC photometry in the J, H and K band will now be combined with the HST R₇₀₂ image, to investigate whether the hypothesis of a foreground galaxy at the redshift of A1835 is plausible, and to constrain its impact on the interpretation of the SMMJ14011+0252 J1 data.

The very rich, irregular morphology of the J1 complex make it difficult to a priori identify the most likely low-redshift component. The source is therefore subdivided into a set of very small (0.3 ") apertures, extracted over all regions of J1 (and also J2). Apertures are included in the analysis, if in all bands all constituent pixels exceed a signal-to-noise ratio of 3. This procedure does subsample the atmospheric seeing disk, and it leads to double-counting of neighboring pixels. This does not pose a problem, because the aim is to merely identify which portion of J1 (if any) might most likely origin from a member galaxy of the foreground cluster.

SExtractor (Bertin & Arnouts 1996) is used to select a comparison sample of cluster members, which may have similar colors, if there is a source within the J1 complex at low redshift, and assuming that all galaxies within the images and with sizes $>$ few pixel belong to A1835, except SMMJ14011 J1 and J2. Spatial position (and “stellarity”, i.e., a SExtractor morphological criterion to distinguish between stars and extended sources) were used to cross-identify the sources in the different wavebands. In addition, the expected colors for A0..A5 stars were calculated from a blackbody spectrum, to explicitly examine the SED of an A-star dominated population. The spectra were placed at redshifts within $\pm 5000 \text{ km s}^{-1}$ of the cluster redshift (which is about 5 times the velocity dispersion of the cluster).

A color-color diagram is constructed using the $R_{702} - J$ color as a function of $J - H$ color. This is a rather unusual combination. It is tailored to discern the Balmer break and extinction in the UV continuum at the redshift of SMMJ14011, whereas it does not cover a particular feature in the SED of a galaxy with approximately the cluster redshift, $z = 0.25$. Therefore such a diagram should isolate galaxies with old stellar population which are typically seen in low redshift clusters in the red part of the color-color diagram. Therefore it can be expected that this color-color relation will yield a good discrimination between the two redshift hypotheses.

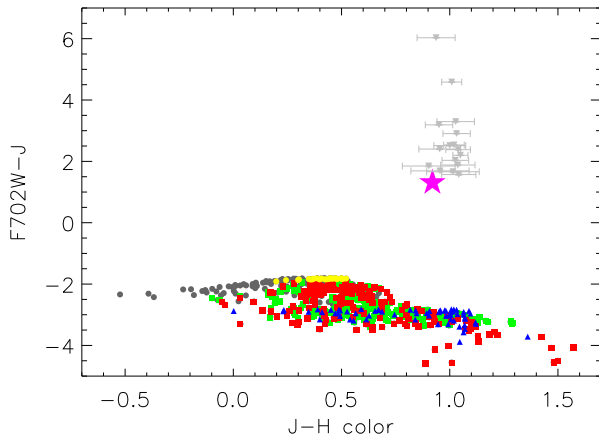


Fig. 16.— $F702-J$ color as a function of $J-H$ color for different apertures along SMMJ14011 J1 and for galaxies within A1835. The colored data points show the position of apertures within J1 for different regions of the source. Yellow points highlight J1c. The light gray upside-down triangles show the colors extracted from equal apertures centered on the cores of cluster galaxies. The magenta star indicates the color that would be obtained for a population of A stars.

distinct region of color space. In addition, the data points of J1c are well within the color-color range of J1. In fact, using the intrinsic color of the source to be that of bluest parts of J1, namely $R_{702}-J \approx -3$ and $J-H \approx 0.25$ (and a cluster galaxy with $R_{702}-J \approx 2$ and $J-H \approx 1$), and considering how much of a component with colors of a cluster galaxy would need to be “added” to explain the color of J1c, it is found that the amount of light within the J1c region must be small ($<5\%$ of the total flux). Using the absolute magnitude versus velocity dispersion for early type galaxies from Pahre et al. (1998) suggests that the velocity dispersion of any foreground galaxy is $\lesssim 75 \text{ km s}^{-1}$. This upper limit is very conservative as the formal limit could be almost 50% lower. However, given the color range of the cluster members and the range of color within J1 itself, it is best to be cautious. This limit is within $\sim 1\sigma$ of the limit for the velocity dispersion estimated by Smail et al. (2005) (they placed an upper limit $\lesssim 55 \pm 15 \text{ km s}^{-1}$).

Hence neither photometry, nor spectroscopy at wavelengths between 4000 \AA and 25000 \AA confirms the claim that J1c is an interloping cluster member of A1835. This is in agreement with Smail et al. (2005), who also come to the conclusion that a low-redshift source, if it exists, can only have a negligible impact on either the photometry or the gravitational lensing of J1.

If the continuum emission of J1c is dominated by foreground emission, then it will be comparably red. It is therefore compared with the colors found in equally sized apertures centered on the nuclei of cluster galaxies, to extract the reddest representative colors within the cluster. In addition this resembles the situation that is to be expected for an interloping source: The high-redshift emission will be most efficiently extinguished near the center of the foreground galaxy, hence this will be the region where the foreground SED will be least diluted by the background source.

The result is shown in Fig. 16. The different small colored symbols indicate the colors of the J1 apertures, distinguishing between the different components of the source (see section 3.4 for a detailed discussion of the colors within SMMJ14011+0252). It is obvious that the colors of the cluster galaxies and A-stars lie in distinct

3.7. Spatially resolved morphology and gas dynamics of J1 in the source plane

In Section 3.5 the rich phenomenology of line emission in SMMJ14011+0252 J1 was presented. However, so far the geometric distortion caused by the gravitational lens has not been taken into account. The stretching introduced by the “cosmic telescope” obviously complicates determining the morphology of the source. Using the lensing model of Smail et al. (2005), the approximate appearance of the velocity field in the source plane will be reconstructed. Because the magnification axis does not coincide with the velocity gradients and preferred axis of line emission, in the de-lensing process, the intrinsic images do not only change their geometry, but are also effectively rotated.

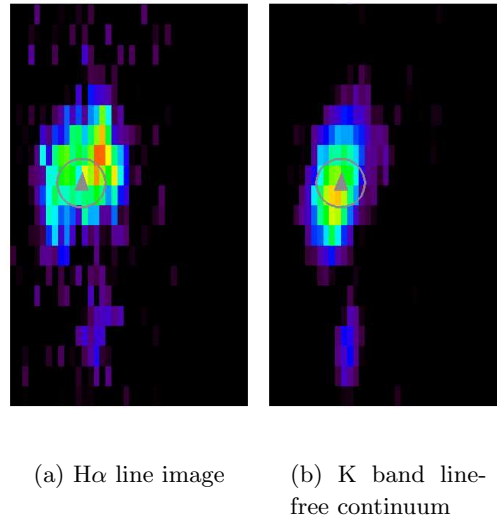


Fig. 17.— *Morphology of the K band continuum and H α line emission in the source plane. The triangle and circle indicate the CO position and uncertainty, respectively.*

3.8. Evidence for a starburst-driven superwind in J1n

The emission line data of J1 show evidence for a galactic wind in more than one way, but they also reveal differences between the three components J1n, J1c and J1s. As noted by Tecza et al. (2004) and in agreement with the previous measurement by Ivison et al. (2000), the H α lines are shifted $\sim 500 \text{ km s}^{-1}$ to the red with respect to the UV absorption lines both in J1 and J2. This phenomenon is commonly observed in high-redshift galaxies and is usually attributed to line absorption in outflowing gas due to the gas being seen in projection against the bright continuum. The gas on the other hand is observed on both the front- and back-side of the outflow leading to velocities closer to systemic compared to the absorption line gas.

Furthermore, in J1c and J1n, both H α and [NII] $\lambda 6583$ have blue wings, again indicating outflows (Lehnert & Heckman 1996a). Close-

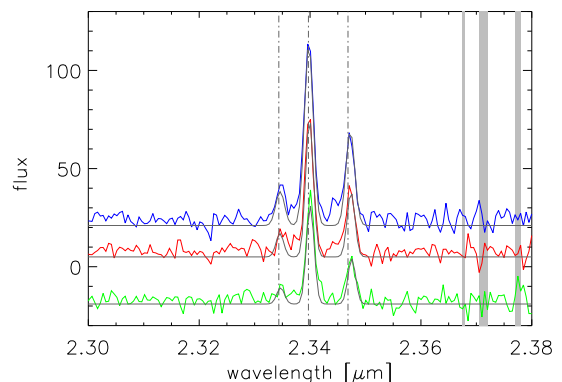


Fig. 18.— *A closeup of the H α + [NII] line complex in J1n, J1c and J1s is shown in blue, red and green, respectively. Line fits are shown in black. Blue wings are prominent in J1n and J1c, but not in J1s.*

ups on the $H\alpha$ + $[NII]$ line complex in J1n, J1c and J1s are shown in Fig. 18 together with Gaussian fits to the line cores. Gaussian fits to the residuals hint blueshifts with relative velocities of $\Delta v \sim -330 \text{ km s}^{-1}$ for the $H\alpha$ lines and $\Delta v \sim -350 \text{ km s}^{-1}$ for $[NII]$ in both J1n and J1c.

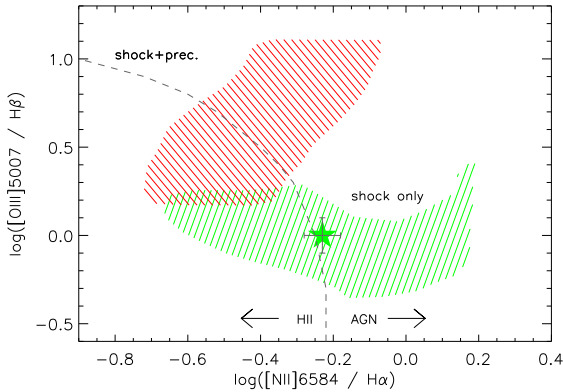


Fig. 19.— *Line ratios for the most shock-like areas in J1n (green star). Red and green hatched areas indicate the shock only and shock+precursor models of Dopita & Sutherland (1996), the dividing line between HII regions and AGN is shown in gray Osterbrock (1989).*

from this source. Detailed models of the line emission properties of shocks have been calculated e.g. by Dopita & Sutherland (1995).

The measured $[OIII]/H\beta$ and $[NII]/H\alpha$ ratios in J1n allow to give a scenario for the physical properties of the shocks, suggesting that the shock moves with $\Delta v \sim 230 \text{ km s}^{-1}$ into a low-density environment which is stabilized by a magnetic field of $\sim 1\mu\text{G cm}^{3/2}$. The envelopes to the Dopita & Sutherland (1996) models are shown in Fig. 19 for both pure shock models and models which take a precursor into account. The precursor is formed by the ISM ahead of the shock front which is ionized by the upstream ionizing photon flux from the shock front. The influence of such a precursor in SMMJ14011+0252 J1 is obviously small.

The astrophysics of galactic winds leads to correlations between line emission quantities, that can be used as powerful constraints to identify galactic superwinds (Lehnert & Heckman 1996a). One of these diagnostics involve the correlation between the $[NII]$ line width and the $[NII]/H\alpha$ ratio. This is because shocks ionize the gas in superwinds, leading to enhanced $[NII]$ emission. In the velocity range relevant for winds, line luminosities increase with increasing shock speed. Since the wind component is relatively weak compared to the integral emission of photoionized regions, the enhanced offsets manifests as line width.

This relationship is shown in Fig. 20 for J1n and J1s. Visual inspection indicates that the $[NII]$ line emission in J1n (red dots) does hint the presence of a wind, but not the emission from J1s (blue-green squares). Pearson's correlation coefficients are $R_{J1n} = 0.75$ for J1n, and $R_{J1s} = 0.05$ for J1s. For samples where the scatter cannot be neglected, as is the case here, nonparametric test are more robust, therefore the Spearman rank test and Kendall's τ were also calculated and equally hint a clear correlation in J1n and no correlation in J1s. Namely, for J1n, $R_{spear} = 1.3 \times 10^{-3}$ and $R_{\tau} = 3.3 \times 10^{-3}$ and for J1s, $R_{spear} = 0.67$ and $R_{\tau} = 0.73$, respectively. Small values in the non-

Such kinematic offsets are the characteristic signature of galactic winds (Heckman et al. 1990; Lehnert & Heckman 1996a,b), which are driven by star forming regions in low-redshift starburst galaxies and are even observed in highly dust-enshrouded ULIRGS (Rupke, Veilleux, & Sanders 2002; Martin 2005). About 10% of the total $H\alpha$ line flux from J1n and J1c arise in the wing (11% for J1n and 9% in J1c). For $[NII]$, the wings contribute 23% (J1n) and 27% (J1c). $[NII]$ to $H\alpha$ line ratios are accordingly larger, and reach values of 0.83 in J1n and 1.6 in J1c.

$[NII]/H\alpha$ line ratios are enhanced in galactic winds, due to shocks and when the wind entrains the ISM. The large $[NII]/H\alpha$ ratios observed in J1n (~ 0.7) are not in agreement with HII regions, which would typically lead to ratios $[NII]/H\alpha \sim 0.3$, but indicate that shocks contribute considerably to the overall line emission

parametric tests indicate a high correlation significance. Gaussian distributions have significances ~ 0.5 in both tests.

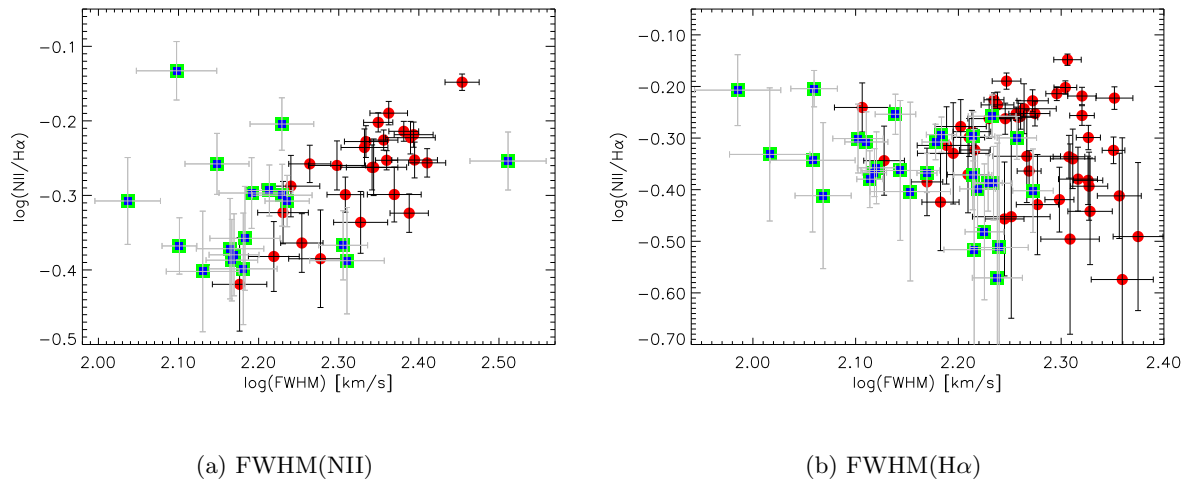


Fig. 20.— $[NII]\lambda 6583/H\alpha$ line ratio as a function of $[NII]$ FWHM for J1n (red dots) and J1s (blue-green squares). $[NII]$ FWHM and line ratio are clearly correlated in J1n, but not in J1s. For the $H\alpha$ FWHM, no similar correlation is found in J1n or J1s.

Correlations of this kind can also help to constrain directly whether the wind has a strong impact on the measured emission line kinematics. The correlation between FWHM and $[NII]/H\alpha$ ratio implies that the relative importance of shock heating increases in the more kinematically disturbed gas, just as observed in more detail in nearby starburst galaxies (Lehnert & Heckman 1996a). This should be contrasted with diffuse photo-ionization of gas due to massive stars. In such a case, the low ionization line ratios such as $[NII]/H\alpha$ can be very high but since this is due to photo-ionization, not shocks, then no correlation with line width will be expected.

In the following, these correlations will be used to investigate whether the line emission is a reliable tracer of the large-scale virialized kinematics in the gravitational potential of J1, or whether it is also dominated by mechanical heating as in a starburst driven outflow.

Fig. 21 shows the correlations between line properties for the $[NII]$ lines in J1n. The data are given separately for spatial pixels with high and low $[NII]/H\alpha$ ratios. Light gray boxes indicate pixels where $[NII]/H\alpha < 0.55$, red dots pixels where $[NII]/H\alpha > 0.55$. Line widths and fluxes are correlated, with $R = 0.74$ and Spearman and Kendall significances of $\mathcal{O}(10^{-5})$ for the low $[NII]$ component, and $R = 0.83$ and non-parametric significances of $\mathcal{O}(10^{-2})$. None of the other line properties appear to correlate with each other. Particularly, the position of the $[NII]$ line centroids are not correlated with flux or line width, suggesting they are dominated by large-scale gravitational motion. This is the case for pixels with high and low $[NII]/H\alpha$ ratios.

The corresponding diagrams for $H\alpha$ are shown in Fig. 22. FWHM and line fluxes of the photoionized lines correlate mildly ($R = 0.44$, non-parametric significances $\lesssim 0.04$), but not those where the NII ratio indicates shock ionization. A stronger correlation is found between FWHM and velocity for the photoionized lines (with $R = -0.43$ and non-parametric significances < 0.01).

These correlations are not indicative of a strong wind contribution. The only correlations found are for the gas that has an $[NII]/H\alpha$ ratio in agreement with photoionization by young stars.

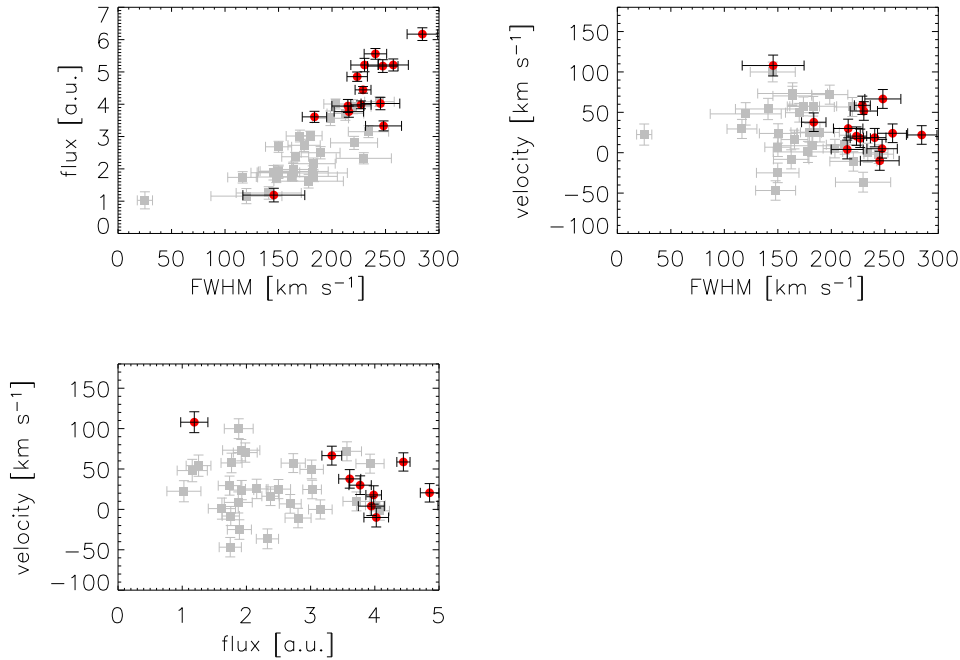


Fig. 21.— *Emission line correlations for [NII] in J1n. Gray dots indicate pixels with low-ionization ($[NII]/H\alpha < 0.55$), red dots pixels with high ionization ($[NII]/H\alpha > 0.55$).*

This is probably not due to the small sample size of “wind-like” spatial pixels, because, since they have generally higher line fluxes, the scatter in these pixels should be minimal.

Studies of low-redshift starburst galaxies also come to the conclusion that the wind does not have a large influence on the observed large-scale $H\alpha$ velocity field. Lehnert & Heckman (E.g. 1996a) have shown directly that starburst-driven superwinds have only a marginal influence on the measured $H\alpha$ rotation curves in local disk starburst galaxies.

How does the outflow observed in SMMJ14011+0252 relate to the low-redshift winds? In low-redshift galaxies, starburst-driven winds have generally rather low surface brightness and are optically thin to most radiation. Maximum $H\alpha$ surface brightnesses are $\lesssim 800 L_{\odot} pc^{-2}$ which translates into a maximum observed flux of $f_{obs} = 2.3 \times 10^{-21} W m^{-2} pix^{-1}$ for the adopted cosmology. The $H\alpha$ flux in the blue-shifted component of the $H\alpha$ emission in J1n/c is about 10 % of the total $H\alpha$ flux, or $\sim 1.1 \times 10^{-19} W m^{-2} pix^{-1}$. Comparing this with the maximum $H\alpha$ fluxes in the sample of Lehnert & Heckman (1996a) indicates that the $H\alpha$ flux in SMMJ14011+0252 J1 is brighter by about an order of magnitude than the wind fluxes at low redshift (note that also the wind components in the low-redshift ULIRG sample of Luis Colina, discussed in Section 2 of this chapter, are too faint to be observed when shifted to $z = 2$).

The $[NII]/H\alpha$ line ratios (also the $[OIII]/H\beta$ ratios as far as can be seen from the moderate-depth exposures taken in the H band) are highest $0.7''$ away from J1c, but also not coincident with the maximum $H\alpha$ emission in J1n. This suggests that the underlying galaxy is actually seen through the wind, so that the main contribution of the wind component is in $[NII]$ while the $H\alpha$ emission is less affected.

The SMMJ14011+0252 data allow to probe deeper into the physical properties of the wind: Having resolved the $[OII]$ line doublet into its two components at $\lambda=3726 \text{ \AA}$ and $\lambda=3729 \text{ \AA}$, and

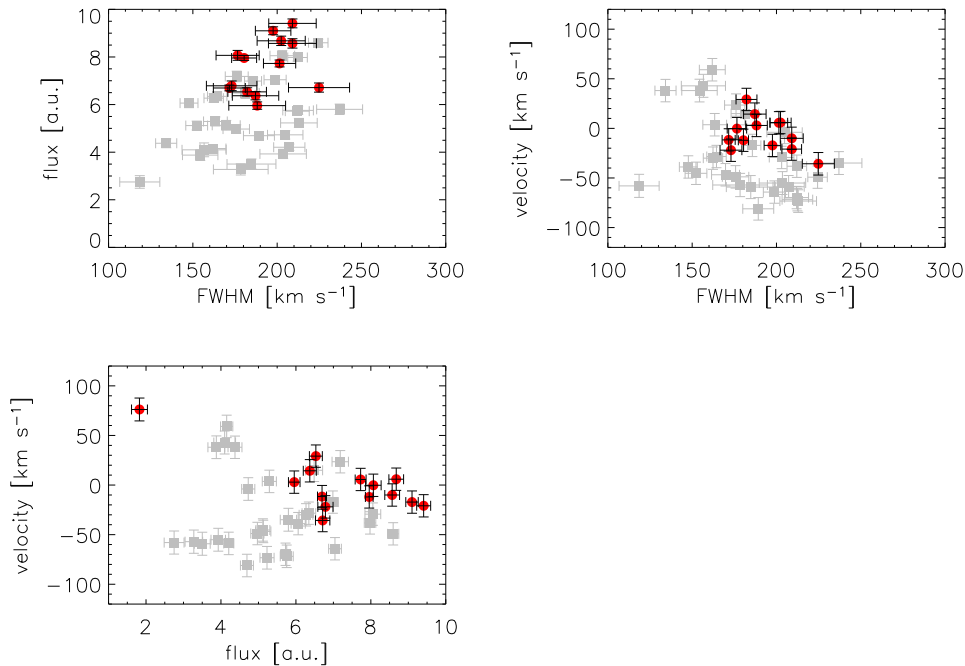


Fig. 22.— *Emission line correlations for H α in J1n.*

the [SII] doublet into $\lambda = 6717 \text{ \AA}$ and $\lambda = 6730 \text{ \AA}$ (see section 3.5), the line ratios allow to calculate the electron density and pressure in the line partially ionized zone. The density n_e can be converted into the pressure P following the method described in Lehnert & Heckman (1996a) and based on the prescriptions of Shull & McKee (1979):

$$P \approx 4 \times 10^{-12} n_e \text{ dyn cm}^{-2} \quad (6.1)$$

Comparison with Fig. 13 yields an electron density of $\sim 300 \text{ cm}^{-3}$, which translates into a pressure of $1.2 \times 10^{-9} \text{ dyn cm}^{-2}$. This result is in excellent agreement with the values found by Lehnert & Heckman (1996a) for the superwind environments of low-redshift starbursts. They exceed the pressures observed in the local ISM of the Milky Way by factors of about $10^3 - 10^4$. In other words, and even accounting for a possibly denser ISM in SMMJ14011+0252 as compared to the Milky Way, the gas is strongly over-pressurized, which is the necessary ingredient for an expanding or outflowing gas bubble – the wind.

The H α flux also allows to estimate the amount of hydrogen that is ionized and accelerated in the outflow. Using equation 4.20 in chapter 4, and the electron density $n_e \sim 300 \text{ cm}^{-3}$ (see section 1.1) yields an approximate gas mass:

$$M_{HII} = 9.98 \times 10^6 M_{\odot} \quad (6.2)$$

that are currently being accelerated by the wind. But this is a lower limit since the H α emission represents the swept-up ambient ISM that is entrained and shock heated by the wind material. The amount of gas in the outflow is likely to be several orders of magnitude higher. All these findings provide good and consistent evidence that star formation driven feedback plays an important role

in the dynamics of J1. Intriguingly, differences between the three regions are also found, indicating that the different regions of star formation also cause different feedback. Whereas it seems to be strongest in J1n, its influence in J1c is not quite as strong, and comparably small in J1s.

What is the ultimate fate of this gas? Using $\Delta v \sim 330 \text{ km s}^{-1}$ as an estimate (rather a lower limit, due to the unknown inclination angle and the fact that the optical emission line gas is very unlikely at the terminal velocity of the wind material) for the bulk velocity of the outflow and $r_e \sim 2.5 \text{ kpc}$, a critical mass will now be estimated for which the gas velocity equals the escape velocity of the galaxy. Using equation 4.15 to estimate the mass of a bulge with given velocity dispersion and

$$E_{bind} = 0.4GM_{bulge}^2/R_e, \quad (6.3)$$

to calculate the binding energy, the critical mass is:

$$M_{crit} = 10 \frac{\sigma^4 r_e}{G} \sim 7 \times 10^{10} M_\odot \quad (6.4)$$

This is larger than the mass estimate for the total enclosed mass of the J1 complex out to the orbit of J2 ($\sim 20 \text{ kpc}$). However, the surrounding dark matter halo will probably increase the total mass by about an order of magnitude. Hence the outflowing gas will probably not become unbound from the galaxy potential. Radiative cooling has been neglected in the estimate, but will lower the kinetic energy in the flow to some degree. The starburst driven wind appears strong enough to slow down the star-formation, but it cannot remove the gas from the halo. At low redshift however there is evidence for much high velocities in the wind material (e.g., Lehnert, Heckman, & Weaver 1999).

3.9. Is SMMJ14011+0252 a maximal burst?

Observations of low-redshift starburst galaxies suggest a fundamental upper threshold for the star-formation rate in galaxies (Lehnert & Heckman 1996b; Meurer et al. 1997), possibly indicative of self-regulation processes that limit the gas collapse (and subsequent star-formation) by the means of the negative feedback of superwinds. The properties of the starburst-driven wind of SMMJ14011+0252 J1n have been studied in the previous section and hint that this galaxy might also be in a phase of “maximal bursting”. It is therefore interesting to investigate how SMMJ14011+0252 J1 relates to the “maximal burst” galaxies observed at low redshift.

For low-redshift star-forming galaxies, Meurer et al. (1997) propose an upper bound of $\text{SFR}_{max} \sim 45 M_\odot \text{ yr}^{-1} \text{ kpc}^{-2}$ within one half-light radius $r_{1/2}$. While this exact value depends on the choice of cosmology, the initial mass function, the relative role of extinction, the ability to measure half-light radii accurately at wavelengths where a substantial fraction of the bolometric luminosity originates, it provides a useful guide on how much feedback is necessary before star-formation becomes “self-limiting” (see also Lehnert & Heckman 1996a,b). The same quantity will now be calculated for J1n and J1s. It is fortunate in this context, that the gravitational lensing only increases the apparent surface of the source, but not the surface brightness. Therefore, when deriving a surface brightness from the observed luminosity and surface, the lensing does not add additional uncertainty.

The morphology of J1 is very complex and, independently from the adopted scenario of the nature of J1, the properties of J1n are sufficiently distinct from the remainder of the source, that

it is justified to analyze J1n separately. The wind component of the H α emission is $\lesssim 10\%$ of the H α flux, therefore its impact on the result will be negligible. The half-light area $A_{1/2}$ is estimated by selecting those pixels in J1n that are above the 50% percentile of the flux distribution, adopting to the method applied by Erb et al. (2003). The resulting area is 17 pixels, or 1.1'' (68.5 kpc² with the adopted cosmological model). Both the H α and H β fluxes were measured from this region to correct the H α emission for extinction. The intrinsic H α flux is $F_{H\alpha} = 1.1 \times 10^{-18} \text{ W m}^{-2}$, which (using equation 4.9) yields a star-formation rate of 450 $M_{\odot} \text{ yr}^{-1}$, and a star-formation rate density of $7M_{\odot} \text{ yr}^{-1} \text{ kpc}^{-2}$.

The estimated flux and surface depend strongly on the low-surface brightness H α emitting regions in J1n and therefore on the accuracy of the background subtraction. However, as was seen from adopting a range of cutoff values ($0 \dots 5\sigma$ of the background fluctuations), the star-formation rate density is in all cases $\lesssim 10M_{\odot} \text{ yr}^{-1} \text{ kpc}^{-2}$.

The same method was used to estimate the star-formation rate density in J1s. In this component, $A_{1/2} = 0.875 \square''$ (or 56.4 kpc), and the extinction-corrected star-formation rate is 150 $M_{\odot} \text{ yr}^{-1}$. The star-formation rate density, however, is only by a factor ~ 2 smaller: 3 $M_{\odot} \text{ yr}^{-1} \text{ kpc}^{-2}$. Star-formation rates based on H α luminosities tend to be lower than estimates based on infrared luminosities, because the most heavily star-forming regions are optically thick to the H α emission, and will therefore be missed. The far-infrared and radio luminosity of SMMJ14011+0252 have been measured and yield star-formation rates (for J1 total) of 1260 – 3900 M_{\odot} and 650 M_{\odot} , respectively (Ivison et al. 2000). Correcting for the fiducial $\mathcal{M} \sim 5$ yields intrinsic rates of 250 – 780 M_{\odot} and 130 M_{\odot} respectively.

These measurements have too low spatial resolution to set a meaningful constraint on the half-light radius. To estimate an upper bound on the star-formation rate in SMMJ14011+0252 J1, therefore, $A_{1/2, J1n}$ will be used, assuming that all far-infrared emission comes from the region around the peak H α emission in J1n. This upper bound on the star-formation rate density is 57 $M_{\odot} \text{ yr}^{-1} \text{ kpc}^{-2}$. This is somewhat higher than the limiting 45 $M_{\odot} \text{ yr}^{-1} \text{ kpc}^{-2}$ of Meurer et al. (1997), but within the same range, keeping the large uncertainties in mind. In addition, it is not possible to gauge the contribution of J1s from the far-infrared data. If the relative contributions to the H α emission in J1n and J1s are representative for the fractional contribution to the far infrared luminosity from the two components (i.e., the physical conditions are similar in both components) and taking the different $A_{1/2}$ into account, the star-formation rate densities in J1n and J1s are 38 and 24 $M_{\odot} \text{ yr}^{-1} \text{ kpc}^{-2}$ in J1n and J1s, respectively.

Since these numbers are in broad agreement with the formation rates expected for a maximal burst, it is interesting to ask what mechanism destabilized the gas to initialize the burst? If the underlying physics is similar at $z \sim 2.6$ to the processes acting at low redshift, can J1 become gravitationally unstable without an external perturber? A simple criterion can be constructed to judge the stability of gas disks (e.g., Elmegreen 1999). Tacconi et al. (2005) have discussed this question for their sample of 14 SMGs and find that a gaseous disk can become gravitationally unstable if:

$$\sigma/v_c \leq 0.35f_{0.4} \tag{6.5}$$

where $f_{0.4}$ denotes the gas fraction in multiples of 0.4. Since the CO emission in J1 is not spatially resolved, no velocity gradient can be estimated. However, the SPIFFI data do allow such an estimate, valid for the kpc scale star-formation observed in H α . Using the observed gradient $\sim 90 \text{ km s}^{-1}$ H α average velocity dispersion $\sigma = 77.7 \pm 18$ and anticipating the $i > 60^\circ$ inclination

estimate from section 3.10 yields

$$\sigma/v_{cJ1} = 0.75 \gg 0.35f_{0.4} \equiv 0.22 \quad (6.6)$$

This indicates that in the single-disk scenario, the gas collapse necessary to fuel the high star-formation rates traced in H α over radii of several kpc, and consistent with a “maximum burst” cannot occur by a self-induced disk collapse. It should be noted that J1 has similar line widths observed in H α and CO. An external perturbing potential, at least to zeroth order, appears necessary.

3.10. Spatially-resolved kinematics and dynamical modelling

Although a wealth of new results in the past years has led to a much improved picture of SMGs, the basic question about their nature is still a matter of vivid discussion. Are they disk galaxies with an irregular light profile or do they have intrinsically complex gas distributions, e.g. as a consequence of on-going mergers (see also Chapter 4)? These questions are not only very interesting in themselves, they are also crucial to obtain robust mass estimates. It is clear that photometry alone does not allow to uniquely distinguish between the two hypotheses.

The precision and spatial extent of the kinematic maps of SMMJ14011+0252 are outstanding for a starburst dominated submillimeter galaxy at $z \sim 2.6$, and they are probably the best available data of this kind presently available. Although the picture is of course complicated by the anisotropic gravitational lensing, this can be accounted for when modelling the observed data.

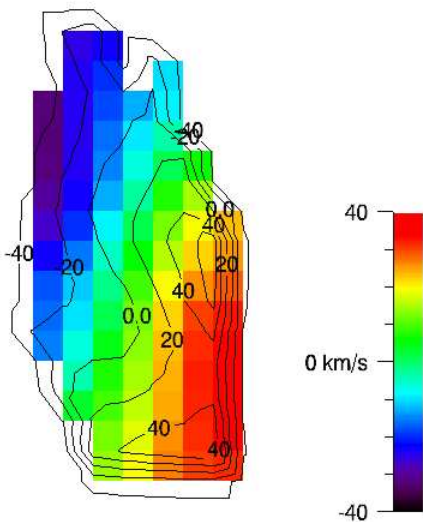


Fig. 23.— *Velocity map of the best-fit exponential disk, contours indicate the measured map.*

A number of models was generated using the DYSMAL package kindly provided by R.Davies. As part of this thesis, the original code was modified to include the stretching by the gravitational lens, varying signal-to-noise ratios and different H α flux distributions. The package was then complemented by a fitting routine to automatically extract the kinematic information using the same rebinning and smoothing of individual spectra as used for the data (see Chapter 4 for further details on the package).

The ultimate goal is to find the model with the minimal number of free parameters that reproduces the observed velocity field reasonably well. Since all models can only be crude approximations, obtaining a quantitatively optimal representation of the data (i.e. $\chi^2/n_{pix} \sim 1$) might be too much to ask for. Another limitation is the accuracy with which the lensing model can be constrained. Small changes in the lensing direction and magnification factor can have a measurable and significant impact on the result, and especially on the values of the fit parameters. However, at least qualitatively the observed velocity pattern should be reproduced,

i.e. no large-scale residuals should remain in areas where the signal-to-noise ratio is high (i.e., near the center of the light distribution).

Single rotating disk hypothesis

The model with the least number of physical parameters which leads to an overall velocity gradient and comparably small dispersion, is the single rotating disk. Following the strategy to find a kinematic fit that well describes the data and requires the least number of fit parameters, therefore, this scenario will be tested first. The beauty of the exponential disk model is its simplicity, therefore the model can be fitted with a small number of parameters and in a very quantitative way. This will now be exploited.

To fit the inclination and tilt of J1, 64 models with different inclination i (inclination of the disk normal with the line of sight) and tilt θ are generated. The best fit model is identified by maximizing the number of spatial pixels in the data that have counterparts in the model. The measured flux distribution of J1 cannot be used directly for a χ^2 fit, because it is very irregular, and does obviously not trace the smooth light profile of an exponential disk. In the single-disk hypothesis, this is attributed to varying mass-to-light ratios and irregular dust distribution.

Using the simple pixel matching, good fits were obtained for $\theta = 230^\circ - 250^\circ$ and $i = 70^\circ - 90^\circ$ (> 105 of 108 pixels in the data had matching pixels in the model), different values yielded matching fractions of 97 pix and less. For the following, $\theta = 240^\circ$ will be adopted. The morphology strongly disfavors inclinations $i \ll 60^\circ$, but they will not be dismissed from the fits, because inclinations play a major role for the kinematics, unlike the tilt. The observed distribution of H α emitting gas might not adequately trace the disk geometry, so that a model with a good kinematic fit would be appealing in spite of the geometry.

J1 obviously does not have the light profile of an exponential disk, neither in the line emission nor in the continuum. Therefore the assumption of constant M/L is abandoned, and the measured H α line image is used to scale the line fluxes in the simulated cubes, so that the signal-to-noise ratios in the model are matched to the data pixel by pixel. The reconstructed velocity and width maps are shown in Fig. 23 and 24, respectively. In spite of the varying signal-to-noise values, the flux distribution has no impact on the reconstructed maps.

Mass and inclination have the largest influence on the observed dynamics of a rotating disk galaxy. To explore the best fitting parameter range, the observed velocity and dispersion maps are fitted with 208 models with inclination varying between 20° and 90° (in steps of 10°) and 26 mass assumptions between $1 \times 10^9 M_\odot$ and $6 \times 10^{10} M_\odot$, varying roughly logarithmically. The two-dimensional map of the reduced χ^2 s is shown in Fig. 26. To simplify the plot, only

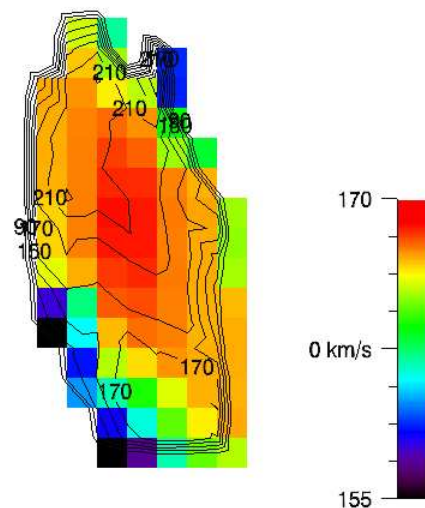


Fig. 24.— *Spatial distribution of FWHMs for the best-fit exponential disk, contours indicate the measured map.*

masses between 10^9 and 10^{10} are shown. χ^2 s are generally large, $\chi^2 \gtrsim 10$ per pixel. The seeing causes correlations between neighboring pixels, so that the number of degrees of freedom (n_{dof}) will be smaller than the number of pixels. However, this will decrease, not increase, the reduced χ^2 . Therefore, the true reduced χ^2 s will be even larger than found here. However, this can only be a qualitative statement. Due to the uncertain n_{dof} , the χ^2 can be used to identify the best-fitting model, but not to estimate the goodness of fit.

For highly inclined systems (as constrained by the morphology), the best-fitting mass is $2 \times 10^9 M_\odot$. If the disk has a very low inclination (which is not supported by the morphology or any other external constraint), then the mass is $> 5 \times 10^9 M_\odot$. In addition, low inclinations are disfavoured by the line widths (see Fig. 26 for the map of χ^2 s when fitting the widths.)

The best-fit ($\chi^2 = 9.23 \text{ pix}^{-1}$, $i = 80^\circ$, $M = 2 \times 10^9 M_\odot$) modelled velocity and width maps are shown in Fig. 23 and Fig. 24. The most striking difference is that the artificial velocity field appears smoother, and does not have the two velocity maxima and minima seen in the data.

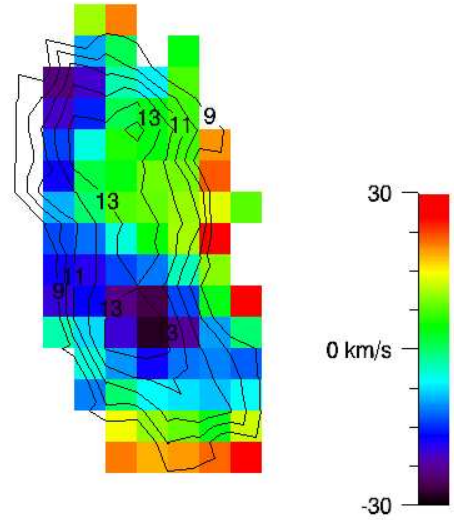


Fig. 25.— *Residual map of the best-fit model velocity field.*

The best-fit ($\chi^2 = 9.23 \text{ pix}^{-1}$, $i = 80^\circ$, $M = 2 \times 10^9 M_\odot$) modelled velocity and width maps are shown in Fig. 23 and Fig. 24. The most striking difference is that the artificial velocity field appears smoother, and does not have the two velocity maxima and minima seen in the data.

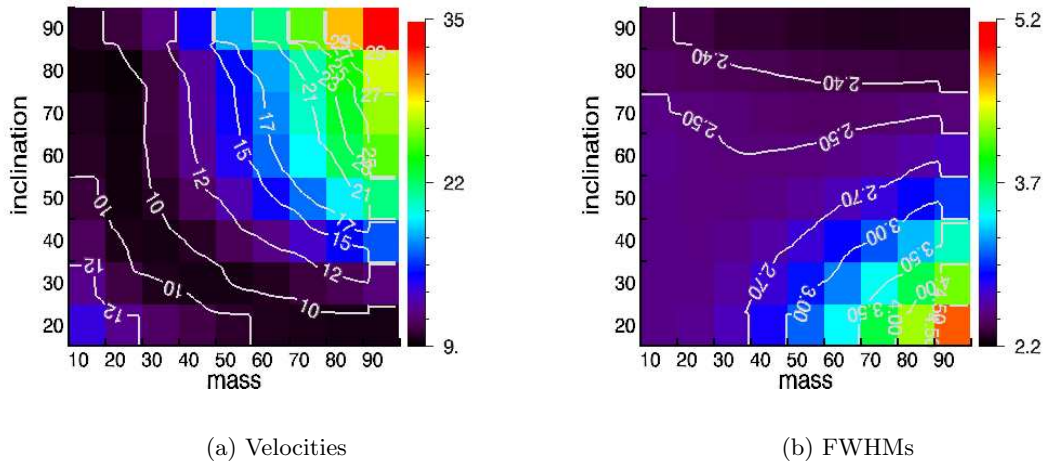


Fig. 26.— χ^2 s of the velocities as a function of mass (abscissa) and inclination (ordinate) for the single rotating disk scenario. Masses are given in units of $10^9 M_\odot$.

The systematic differences between the model and the data are also obvious from the residual map (Fig. 25), subtracting the model from the data. The model explicitly adopts the observational constraints, especially seeing, spectral resolution and the pixel scale, so that correlations between neighbouring pixels cannot explain the non-random spatial distribution of the residuals. The model also accounts for the image-stretching by the gravitational lens, which of course is influenced to an unknown degree by the uncertainty in the lensing model. However, small variations of the lens

direction will influence the morphology of an exponential disk, but will not “bend” the kinematic field in the way observed, if the stretching is approximately linear.

To quantify whether the shape of the residual map is as expected from random fluctuations, the run test (Section 4 of Chapter 4) is used. For a map of 82 pixels, the expected number of runs is 42 ± 4.5 , compared to 24 runs observed. This is a discrepancy of 4σ . Hence this test suggests that the residuals are not randomly distributed.

How plausible is the best-fit model astrophysically? Other mass estimates include, e.g. the stellar mass, $M_{\text{stellar}} = 2.7 \times 10^{10} M_{\odot}$ (correcting for lensing with $\mathcal{M} = 5$), derived from the near-infrared (rest-frame optical) flux or the dynamical estimate from the orbital motion of J2, $M_{\text{dyn}} = 6 \times 10^{10} M_{\odot}$. Both estimates indicate that the single-disk scenario yields a mass estimate that is too low by about an order of magnitude. Hence also astrophysically, in case of J1 the single rotating disk does not appear to be a very plausible description of the data as suggested by the significance of the fit itself.

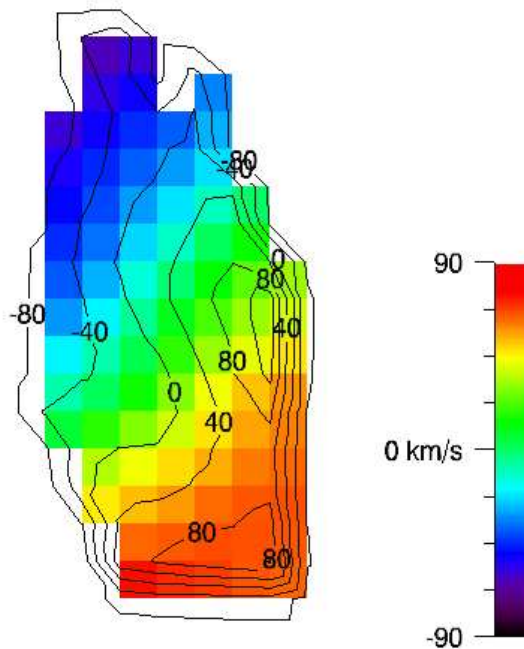


Fig. 27.— *Velocity field of a disk galaxy with prominent central bulge. Contours yield the observed velocity field of J1. The measured values are rescaled by an arbitrary amount to approximately match the modelled values.*

Bulge + disk hypothesis

As recently shown by Tacconi et al. (2005), SMGs appear to be the progenitors of low-redshift massive, dynamically hot⁶, early-type galaxies, in much of a similar way as the low-redshift ULIRGs. If this is the case, and if the SMGs are the dominating evolutionary stage towards this endpoint, then it might be worthwhile to try whether the peculiar kinematics of J1 are due to a central bulge component. Given that the morphology of the source is distorted by the gravitational lens, and is also intrinsically very irregular, this hypothesis cannot be tested from the morphology.

It might be tempting to identify the bright continuum source J1c with a forming central bulge. Comparison with integral-field spectroscopic data of local ULIRGs (e.g., Colina et al. 2005) however indicates that the rest-frame optical continuum morphology in highly dust-enshrouded system is not a very good tracer of mass. Here, the bulge was placed at the center of the $H\alpha$ distribution, however, this is only one pixel away from J1c, and the offset is therefore marginal. The model again uses the $H\alpha$ line image of J1 to scale the flux.

⁶Triaxial orbital distribution

However, also the modelled distributions of relative velocities and line widths in J1 are not in agreement with the bulge+disk hypothesis. This was tried for a number of models with different ratios of bulge and disk mass (ranging from factors 0.3 – 3), and bulge and disk size (with bulge size varying from 0.1''- 0.5''). The disk radius is 0.6'', approximately matching the spatial extent of the emission line gas.

A qualitative comparison already rules out this scenario, as seen from the following comparison of the kinematic fields. Parameters for the specific model shown here are $r_{bulge} = 0.3''$, ratio of bulge/disk mass = 1.5, $M_{total} = 1.0 \times 10^{10} M_{\odot}$. Disk inclination is 80° and tilt $\theta = 240^{\circ}$. Fig. 27 shows the modelled velocity map, and the contours indicate the measured velocity distribution. The comparison is only qualitative, therefore matching numeric values are not needed. However, the isovelocity lines of the data are significantly bent and indicate the two velocity maxima and minima, which are clearly not seen in the data.

The comparison of the modelled and measured velocity fields shows that already qualitatively the model is not a good representation of the data. This excludes a ‘‘kinematically evident’’ contribution from a dynamically hot, central bulge component in J1, provided that it is traced by the nebular emission lines.

Does J1 have Two Rotational Centers?

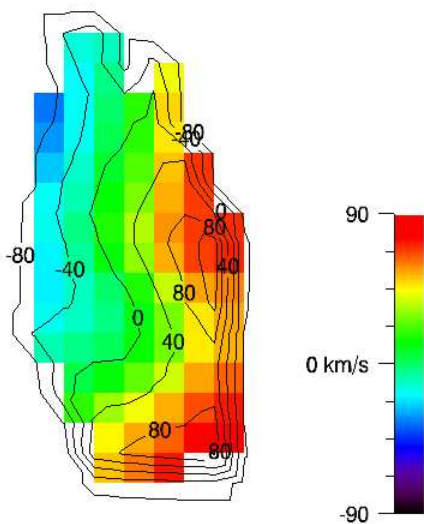


Fig. 28.— *Velocity field of the model placing two independently rotating components at the position of the maximum H α flux in J1s and J1n*

Some traits of the velocity and width maps indicate that the kinematics are dominated by rotation about two different centers, one placed in J1n, one in J1s. The velocity field has two significant peaks and dips. Roughly assigning pixels north of J1c to J1n and pixels south of J1c to J1s shows that the line widths in the two areas are different at 2σ , with $FWHM(J1n) = 207 \pm 15 \text{ km s}^{-1}$, $FWHM(J1s) = 170 \pm 13 \text{ km s}^{-1}$. Uncertainties relate to the r.m.s. scatter in the centroids within each sample.

The astrophysical picture behind this assumption is of course that two rotating gas clouds or galaxies are undergoing a merger. This can be motivated by analogy with low-redshift ULIRGs where often major mergers are the origin of highly disturbed kinematics and extreme star-formation. One of the open questions regarding SMGs is whether similar mechanisms are at work in this population, too, or whether evolutionary aspects (e.g. high gas fractions, see Goldader et al. 2002) are the cause

of the extreme star formation. To convincingly prove the last, the first option must be ruled out. Can this be done based on the kinematics observed with SPIFFI?

It is clear, if this is the correct scenario, that the kinematic fit will likely not yield the correct dynamical parameters, because the dynamics are dominated by the merger, and not the large-scale

gravitational potential of each component. Nonetheless, qualitatively, the agreement between model and data is surprisingly good, especially the two peaks and dips can be modelled quite convincingly (Fig. 28). The line widths are not adequately reproduced, which is fairly surprising in this scenario, because the dynamics are not dominated by the large-scale gravitational field in this scenario.

Overall, the detailed modelling indicates that the observed spatially-resolved kinematics in J1 are not adequately reproduced assuming virialized rotation around one single center of mass, however, the morphology of the velocity field can be surprisingly well modelled with two rotational centers, placed at the position of maximum H α emission in J1n and J1s. This analysis therefore points towards a scenario where J1 consists of two interacting gas-rich disks, maybe two merging galaxies near coalescence, similar to low-redshift ULIRGs. Adequately modelling such complex kinematics with the low physical resolution of a $z = 2.5$ galaxy, and the crude models used here, is not very promising. In addition, such a model will not yield the properties of the large-scale gravitational potential, because the system is very likely not virialized, and the lines are broadened by the interaction.

3.11. Rest-frame UV-optical emission and the nature of J2

This analysis also includes component J2 of SMMJ14011+0252, which is about $1.3''$ north-west from J2c. Multi-wavelength photometry (e.g. Ivison et al. 2000) indicates that J2 is considerably bluer than the J1 complex at observed optical wavelengths. As pointed out by Smail et al. (2005), its rest-frame UV colors fulfill the selection criteria of $z \sim 3$ Lyman-break galaxies, although its redshift is somewhat lower. In the near infrared however, J2 has similar colors as J1c ($J - K = 2.2$). It appears rather elongated in the K band, whereas its J band morphology is rather spherical. This manifests as the red band across J2 in the $J - K$ color image in Fig. 7. The reddest color ($J - K = 2.4$) is reached at the continuum peak. These color variations show that also J2 is spatially resolved in the ISAAC images.

The different behavior at optical and near-infrared wavelengths might indicate that J2 is less extinguished than J1 (leading to larger spectral indices at shorter wavelengths, but less affecting the colors at longer wavelengths), has lower metallicity, or is dominated by a younger stellar population. It will be shown in the following that the first two assumptions find support from the spectral analysis of J2, whereas Motohara et al. (2005) have found that also the second assumption contributes. In addition, they constrain the age of the dominating stellar population $t_{SF,J2} \sim 5 \times 10^7$ yrs, and the stellar mass to be about $10^8 M_{\odot}$.

Previously, only the integrated H α emission from this component was identified (e.g., Tecza et al. 2004), suggesting that it is physically related to J1, with a velocity offset of $\sim 160 \text{ km s}^{-1}$. However, identification of a single line is not sufficient in this case to robustly identify the redshift of J2, because P α emission at the redshift of the foreground cluster falls at a similar observed wavelength.

SPIFFI H and K band spectra of J2 are shown in Fig. 29. They confirm earlier findings (e.g. Tecza et al. 2004), that the spectrum of J2 (blue line) is blueshifted with respect to J1, with an offset of $-160 \pm 18 \text{ km s}^{-1}$. However, in addition to detecting H α , also [NII] $\lambda 6583$ line emission in the K band can be identified, and most of all the [OIII] $\lambda\lambda 4959, 5007$ pair in the H band data. Gaussian line fits are given in red, the residuals are shown in green. For the fit, all redshifts and line widths were fixed to the value of H α . This unequivocally shows that J2 indeed does not belong to the foreground cluster. H β , on the contrary, is too faint to be observed, possibly due to the lower signal-to-noise ratios in the H band data and an interfering nearby night sky line remnant.

H α emission in J2 is spatially resolved and is found within an area of $\sim 1.25'' \times 0.75''$, offset from the continuum emission by $\sim 0.4''$ to the north-east. Extracting both line and continuum information from the same data cube means that this offset is significant. From east to west, there appears to be a small overall velocity gradient of $\sim 47 \pm 13 \text{ km s}^{-1}$, only marginally measured, but consistent with the narrow, unresolved line widths in the integrated spectrum.

If these velocities originate from virialized motion, then these findings place an upper limit on the dynamical mass of J2, assuming that the motion is along the line of sight (see Eq. 4.1). With a fiducial magnification factor of $\mathcal{M} = 5$, the radius is $\sim 2 \text{ kpc}$, half the east-west extent of $1.25''$ in the adopted cosmology. The resulting mass estimate is then $M_{J2} = 2 - 4 \times 10^8 M_{\odot}$, about a factor 20 lower than the average mass of Lyman break galaxies in the sample of Pettini et al. (2001), and within a few percent of the total mass of the J1 complex (see Section 3.13 of Chapter 4).

The lines identified in the H band contradict the findings of Motohara et al. (2005), who claim to have found H β , but not [OIII]. This is easily explained by their much lower spectral resolution ($R = 210$), and the somewhat unfortunate position of telluric features with respect to the J2 line emission: As can be seen in Fig. 29, H β falls within a few Angstroms of a strong night sky line. With $R = 210$, it is impossible to isolate these two features. [OIII] $\lambda 5007\text{\AA}$ is at the onset of a telluric absorption band. Again, high spectral resolution is crucial for a good telluric correction, and for detecting the line with reasonably good signal-to-noise.

The 3σ flux limit to the H β line flux, $F(\text{H}\beta) \leq 9 \times 10^{-21} \text{ W m}^{-2}$, suggests a comparably low extinction of $E(\text{B-V}) \leq 0.23$. Correcting for this extinction, the intrinsic H α luminosity is at most $L_{\text{H}\alpha} = 2.3 \times 10^{35} \text{ W}$ for an unlensed source (using $\mathcal{M} = 5$). With the calibration of Eqn. 4.9, this yields a (lensed) maximum star formation rate of $\sim 18 M_{\odot} \text{ yr}^{-1}$. Accounting for a magnification of 5 by the cluster lensing, the star formation drops to a few $M_{\odot} \text{ yr}^{-1}$ – which is below the typical range of blue, star forming BX galaxies at similar redshift (e.g. Erb et al. 2003), and a factor 100 lower than the peak star-formation rates in J1.

The [O/H] abundance of J2, estimated from R_{23} in a similar way as described in Section 3.5 and in Tecza et al. (2004), is shown as magenta vertical dot-dashed line in Fig. 11. H β is not observed, only an upper limit can be given, which translates into a lower limit on R_{23} . Due to its position in the diagram, this adds only marginal uncertainty to the oxygen abundance, which is significantly lower than in J1, $12 + [\text{O}/\text{H}] < 8.5$. The detection of [NII] $\lambda 6583$ with $[\text{NII}]/\text{H}\alpha \sim 0.22$ indicates that the upper branch of R_{23} applies, placing a lower limit of $12 + [\text{O}/\text{H}] > 8.35$.

Line diagnostics are shown in Fig. 11, together with the results for the components of the J1 complex. The magenta star (or line) represents J2. [SII] line emission was not observed, therefore J2 is only present in the [NII]/H α vs. [OIII]/H β diagram. The upper limit on the H β flux turns into a lower limit on the [OIII]/H β ratio. As for J1, the diagram indicates comparably high ionization for J2, placing it near the limit of the AGN portion of the diagram. The position of J2 is very distinct from that of the J1 components, indicating higher ionization or temperature. It is plausible that this is a direct consequence of the low metallicity.

3.12. Relating J1 and J2

The line connecting J1 and J2 is almost perpendicular to the magnification axis, and will therefore be hardly magnified at all. This results in a fiducial distance of $\sim 17 \text{ kpc}$, neglecting the lensing. Together with the relative velocity of 160 km s^{-1} , this short relative distance indicates that J1 and J2 are physically related.

It has been argued that J1 and J2 might be bright (or low-extinction) patches of a single, underlying massive galaxy with the center situated in – or maybe an arcsec west of – J1c. Both the observed velocity field and velocity dispersions disfavour this picture. At a projected distance of $\sim 2.25''$ from J1c, J2 has a relative velocity of $\Delta v \sim -160 \pm 18 \text{ km s}^{-1}$. Extrapolating this velocity gradient along the opposite direction, and assuming solid body rotation ($v \propto R$) about J1c, the gradients should be similar, but with opposite signs. For the outermost line emitting regions in J1c, which are offset from J1c by about $0.8''$, therefore velocities of $+\sim 56 \text{ km s}^{-1}$ should be reached. However, observed lines in this area are *blueshifted* with respect to J1c, with velocities of $\sim -40 \text{ km s}^{-1}$, more than 90 km s^{-1} , or about 4σ , different from the observed value. This is in good agreement with the observed velocity dispersions in J1 and J2. All emission lines in J2 are very narrow, and cannot be resolved in the SPIFFI data. This is consistent with the marginal velocity gradient of $\lesssim 50 \text{ km s}^{-1}$. Line widths throughout J1, on the contrary, are well resolved in the SPIFFI data, and reach intrinsic values between 150 and 230 km s^{-1} .

If the $\text{H}\alpha$ emitting material was distributed within a stable disk (like in spiral galaxies), then these very different line widths would indicate that regions in very different dynamical states – some parts dynamically hotter with larger line width, some parts colder with smaller width – co-exist within the same galactic disk. Such a configuration would hardly be stable, e.g. due to phase mixing, which should smooth out these differences within a few $\times 10^7 - 10^8$ years. The different line widths (and marginally, velocity gradients) rather suggest that J1 and J2 are distinct sources, with J2 having a much lower mass than J1.

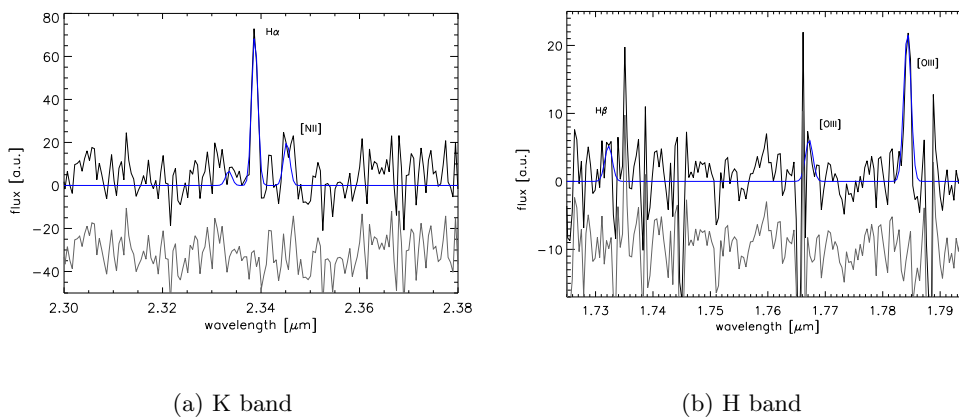


Fig. 29.— *Integrated H and K band spectra of J2. A Gaussian fit to the emission lines is shown as blue line. Fit parameters for all line fits were kept fixed at the values found for $\text{H}\alpha$. Fit residuals are shifted by arbitrary, negative amounts along the ordinate and are shown in gray.*

Comparing the oxygen abundances of J2 and the components of the J1 complex (Fig. 11) equally suggests that J2 is not evolutionarily related to J1. Although the faintness of the $\text{H}\beta$ emission in J2 makes it difficult to robustly measure R_{23} for this source, the different oxygen fluxes in J1 and J2, together with a limit on the $\text{H}\beta$ flux in J2, allow to safely place a lower limit on R_{23} , which is significantly different from that in J1.

The different metallicities allow an interpretation that even goes beyond the dynamical evidence that J1 and J2 are not parts of the same galaxy. As previously discussed (see Section 1.2), metallicities give a record of the integral star-formation history of a galaxy. In the simple closed-box model, metallicities can only increase, however, models allowing for more complexity (outflow of

metal-enriched gas, inflow of cold primordial gas) might be more appropriate. With some caution, this allows a statement about the underlying drivers of matter assembly: the dark matter halos. If J1 and J2 were gas clumps within the potential wells of the same dark matter halo driving their collapse and formation, then why should the integral star-formation histories be so vastly different (see e.g., Immeli et al. 2004)? This shows that J1 and J2 are individual galaxies, and do not just trace substructure in the same halo.

Orbital time scales can be estimated from the observed relative velocity and distance between J1 and J2. With $\Delta v = 160 \text{ km s}^{-1}$ and $D \sim 17 \text{ kpc}$, the orbital time scale is $\sim 6.5 \times 10^8 \text{ yrs}$. The unknown inclination angle makes this estimate uncertain by factors of a few. Statistically speaking, intrinsic velocities will be factors $\sim \sqrt{2}$ higher than those observed. Models of galaxy mergers (e.g. Mihos & Hernquist 1996) suggest that coalescence happens within a few orbits. For this merging pair of an LBG and a SMG, this means that J2 will be accreted most likely by a redshift $z \gtrsim 2$.

Interestingly, the dominating stellar population in J1c has an age of about half the orbital time, about $2 \times 10^8 \text{ years}$ (Tecza et al. 2004). Could a past nearby encounter have caused the starburst seen in J1? By comparison with low redshift mergers and interacting galaxies, this appears unlikely, because of the large mass difference between J1 and J2. (J2 has at most a few percent of the mass of J1.) In the standard picture, only major mergers, where both components have approximately similar masses, can cause catastrophic collapse and star-formation rates as observed in ULIRGS. The dynamical estimates suggest that J2 has at most a few percent of the mass of J1 (but of course this limit is strongly influenced by the very weakly constrained geometry and mass distribution of the individual components). While this might increase star-formation in J2, it should have no major impact on J1.

One noticeable exception is harassment during near-central head-on collisions at high relative velocities ($\Delta v \sim$ a few hundred km s^{-1}) which lead to collisional ring galaxies. Interestingly, collisional ring galaxies have CO line widths $\sim 100 - 200 \text{ km s}^{-1}$, about the width observed in J1, but lower than in more typical SMGs (Greve et al. 2005). In addition, the blue rings in the galaxies indicate that at least in some part of galaxy, star-formation is relatively unobscured. And maybe the most fascinating implication is that the remnants often have bulges that are off-center. This would automatically explain the unusual position of J1c. Is J1 a collisional ring at $z = 2.5$? Although collisional ring galaxies are not a good suggestion to explain the nature of the overall SMG population, J1 seems peculiar in many ways (large $\text{H}\alpha$ equivalent width, low CO line widths), that it might be worthwhile investigating this hypothesis in this particular case a bit more in depth.

A closer comparison of the dynamics and photometric data of J1, however, does not support this hypothesis. Far-infrared luminosities in collisional ring galaxies are an order of magnitude lower than in ULIRGS, and J1 has a luminosity in the typical range of SMGs. The star-forming outer rings are bluer than the more central parts in ring galaxies. This is not in agreement with the irregular $J - K$ color map of J1 shown in Fig. 7. The $J - K$ color distribution does not indicate the typical radially-symmetric color distribution (except for inclination) that is typical for collisional rings. The mass ratio $M(J2)/M(J1) \sim 0.01$ is about an order of magnitude smaller than observed e.g. in the Cartwheel galaxy, where models indicate a lower limit on the mass ratio $\gtrsim 0.25$ to approximately reproduce the observed gas distribution (Vorobyov 2003). Moreover, the relative velocity (160 km s^{-1}) is comparably low (initial relative velocities in models are up to $\sim 400 \text{ km s}^{-1}$). In addition, the sizes of collisional ring galaxies are larger, e.g. the outer ring of the Cartwheel has a radius of 34 kpc, which is a factor ~ 5 too large.

Little is known about merging processes of massive galaxies at high redshift. It might well be that the higher gas fractions (Tacconi et al. 2005, find gas fractions ~ 0.4 in SMGs), will ease the

collapse of significant gas masses. However, without dedicated simulations of minor mergers of very gas-rich galaxies, this can only be speculative. If the low-redshift Universe is a reliable guide in understanding high-redshift galaxies, however, it can be nearly ruled out that a nearby encounter with J2 has caused the dramatic gas collapse in J1.

3.13. The relative mass budgets and the evolutionary state of SMMJ14011+0252

This analysis shows that the picture of J1 being a single, largely uniform, rotating disk, might be too much of an over-simplification. The detailed modelling of the spatially-resolved kinematics rather points towards two separate galaxies J1s and J1n, at a relative distance of at most a few tens of kiloparsecs. Under these circumstances, deriving masses from the intrinsic velocity field, is not trivial, because the virial assumption is not necessarily correct.

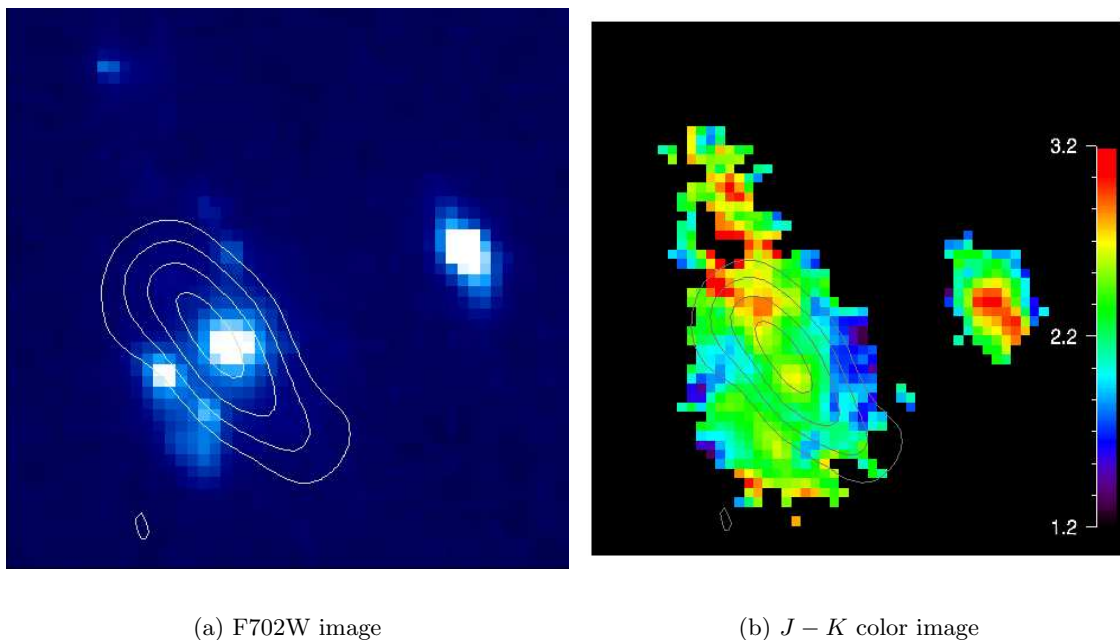


Fig. 30.— *Location of the J1 CO emission (contours) with respect to the R_{702} image (top) and the $J - K$ color map (bottom). The CO emission appears spatially resolved and stretched by the gravitational lens. Its spatial coincidence with J1c is not perfect, but the peak emission seems to be marginally offset to the north-east (by $\sim 0.3''$) and better align with J1n.*

Fortunately, it is possible to derive a mass estimate that is unaffected from these uncertainties, using the relative velocity of J2. §3.11 gave the arguments why J2 is a separate, although physically related source. Having found that J2 has a mass of a few $\times 10^8$ at most, the barycenter can be safely placed at J1c (also consistent with the astrometry plausibly placing the CO peak near the position of J1c). Although this does not perfectly match the suspected barycenter of the J1 complex as suggested from the reconstructed source-plane appearance, J1c is easy to localize, and is offset by only about 1 pixel ($\sim 0.25''$), so that the additional uncertainty will be marginal. This mass estimate is based on the assumption of virial motion of J2 about the barycenter of J1, hence from the measured velocities, the mass is estimated using Equation 4.1, assuming that the motion is perpendicular to the plane of the sky. The connecting line between J2 and the

barycenter is roughly perpendicular to the velocity gradient, therefore the lensing is neglected. With the measured velocity gradient of 160 km s^{-1} , and within a radius of $1.3''$ ($\sim 10.5 \text{ kpc}$ in our cosmology) the dynamical mass estimate for the overall J1 complex is at least $\sim 6.2 \times 10^{10} M_{\odot}$, and possibly a factor 2 – 3 larger due to the unknown inclination.

Stellar mass

The stellar mass was estimated with the population synthesis code STARS2000 and parameters taken from Tecza et al. (2004). They found that the observed SEDs in the J, H and K-band is well reproduced with a 200 Myrs old continuous burst and extinction $A_V = 0.7$. This crucially includes a spectral break between the J and H bands, which was identified as the characteristic 4000\AA break of an intermediate age stellar population at the redshift of J1, $z = 2.565$. The same model was used earlier in this Chapter (Section 3.6) to successfully fit the slope of the rest-frame UV spectrum of J1 obtained by Barger et al. (1999).

STARS2000 predicts the observed K-band magnitude with a given population and redshift for a star-formation rate $SFR = 1 M_{\odot} \text{ yr}^{-1}$. With the above model, $m_{K,mod} = 24.85 \text{ mag}$. The total stellar mass can then be obtained by comparison with the observed K-band magnitude $m_{K,obs}$:

$$M_{stellar} = 10^{0.4(m_{K,obs} - m_{K,mod})} \times \tau \equiv f \times \tau \quad (6.7)$$

The factor f is the average star-formation rate over the burst duration τ . $m_{K,obs}$ is corrected for the fiducial magnification of the gravitational lens, $\mathcal{M} = 5 \equiv 1.75 \text{ mag}$. The resulting average star-formation rate is $f = 140 M_{\odot} \text{ yr}^{-1}$. Over a burst time of $2 \times 10^8 \text{ yrs}$, this yields a total stellar mass of $2.7 \times 10^{10} M_{\odot}$.

The stellar mass can also be estimated from the FIR star-formation rate ($250 - 780 M_{\odot} \text{ yr}^{-1}$, adopting and correcting for a magnification factor $\mathcal{M} = 5$) and assuming that all stars in J1 were formed in the ongoing burst with a total length similar to a dynamical timescale $\tau_{dyn} = r_{max}/(2v_{obs})$ (this corresponds to the simple causality arguments used, e.g., in Lehnert & Heckman 1996a). To obtain upper limits, the largest radii observed within J1 are used (corrected for the magnification), $r_{max} = 3 \text{ kpc}$, and the observed velocities ($0.5 \times$ peak-to-peak) are taken at face value $v_{obs} = 95 \text{ km s}^{-1}$. Resulting stellar masses are $7.8 \times 10^9 M_{\odot}$ and $2.4 \times 10^{10} M_{\odot}$ for the 250 and $780 M_{\odot} \text{ yr}^{-1}$ formation rate, respectively. These numbers are overall consistent with the above estimates. Following Ivison et al. (2000), the uncertainties in the SFR comprise, e.g., differences in the calibration for $0.1 - 100 M_{\odot} \text{ yr}^{-1}$ standard Salpeter and also top-heavy IMFs, under the assumption that there is no major contribution from a non-thermal source, i.e., an AGN.

Ionized hydrogen mass

The mass of ionized hydrogen will now be estimated following Eqn. 4.20. Extinction-corrected $\text{H}\alpha$ fluxes were measured separately for J1n and J1s, therefore separate mass estimates will be given. The estimate depends on the electron densities, which can be calculated from the ratio of the two components of the $[\text{SII}]\lambda\lambda 6717, 6730$ or $[\text{OII}]\lambda\lambda 3726, 3729$. $[\text{SII}]$ lines were measured separately in J1n and J1s and are similar within large error bars. $[\text{OII}]$ emission is too faint for a robust measurement of the ratios. Therefore, electron densities are assumed to be uniform across both components ($\sim 300 \text{ cm}^{-3}$).

The masses of ionized hydrogen are then:

$$M_{H\alpha, J1n} = 1.1 \times 10^8 M_{\odot} \quad (6.8)$$

$$M_{H\alpha, J1s} = 3.6 \times 10^8 M_{\odot}, \quad (6.9)$$

in J1n and J1s, respectively.

However, these can only be lower limits on the overall ionized gas mass. Not all gas within SMMJ14011+0252 will be ionized, and although the luminosity is extinction corrected, the strongest star-forming regions might be hidden between many optical depths of dust and will therefore be missed.

Gas and dust masses

Downes & Solomon (2003) have measured the luminosity of CO line emission and the dust continuum from SMMJ14011+0252 J1, and estimated the mass of molecular H₂ and He. Correcting for different cosmologies and gravitational lens models, their estimate implies that SMMJ14011+0252 J1 contains $\sim 1.5 \times 10^{10} M_{\odot}$ in gas and $\sim (0.25 - 1) \times 10^8 M_{\odot}$ in dust.

Obviously, these estimates can only be approximate, because they involve an empirical conversion to estimate the overall molecule content from the CO measurement in a ULIRG-like environment. SMGs are similar to ULIRGs in many ways (see, e.g., Tacconi et al. 2005). In this picture, $M_{gas}/L_{CO} = 0.8 M_{\odot} (K \text{ km s}^{-1} \text{ pc}^{-2})$.

The interstellar medium of SMMJ14011+0252 obviously also contains neutral gas which will be dominated by hydrogen (HI). Lacking a direct measurement of the HI content of SMMJ14011+0252, it is necessary to make a rough estimate of the total potential HI. In the local Universe, Keres, Yun, & Young (2003) have estimated the co-moving mass contribution of the cold molecular gas and compared it to HI of the interstellar media of galaxies. They find that an averaged ratio of H₂ to HI of about 0.5 to 0.65, which increases with H₂ mass, reaching about 2 for galaxies with $M_{H_2} \sim 10^9 M_{\odot}$. At very high infrared luminosities, similar to what is found for the SMGs, galaxies show H₂ to HI mass ratios of $\sim 4-20$ (Mirabel & Sanders 1989). Taking a rough value of 10 would imply a neutral Hydrogen content of about $10^9 M_{\odot}$, which is likely near the lower limit of the actual value.

The relative mass budgets

The results of the previous sections allow now to estimate the relative contributions to the total mass budget of J1. Most mass within a radius of ~ 20 kpc apparently comes from stars, $f_{stars} \sim 44\%$. Interestingly, the average star-formation rate necessary to build up the population emitting the observed K-band luminosity is lower by a factor ~ 2.5 than the formation rate observed. If this is not due to uncertainties in the model (or the far-infrared star-formation rates), then this could indicate that SMMJ14011+0252 is near the zenith of its star-formation, or that the starbursts in SMGs are not steady phenomena, but are “flickering” with many short episodes of high SFR and periods of relative quiescence, $\mathcal{M} = 5$ is an upper limit to the magnification of the gravitational lens, therefore it cannot help solving the discrepancy. Using smaller \mathcal{M} would increase the discrepancy.

However, the comparably low star-formation rate necessary to model the observed K-band luminosity does indicate that nearly all stars in J1 that are currently observed, might have formed in the on-going burst. This is in agreement with the observation (see Section 3.6) that the UV emission can be well fitted with the same burst model as the optical SEDs. If an old ($\gg 2 \times 10^8$ yrs) stellar population was contributing to the optical emission, but had already faded in the UV, then this should have become evident by different fits. Finally, it should also be noted that this adds more (circumstantial) credence to J1c being at high redshift. Not only does any observation indicate the need for a foreground source, it is also possible to consistently incorporate J1c into the star-formation history of J1.

The molecular gas mass is $1.5 \times 10^{10} M_{\odot}$ or $\sim 25\%$ of the dynamical mass (with an estimated uncertainty of a factor ~ 2 , Neri et al. 2003). The range of plausible HI masses would roughly increase this by a few to 100%. In the simple scenario that there is no on-going molecular gas supply, and that the current star-formation rate ($\text{SFR}_{\text{FIR}} = 350 M_{\odot} \text{ yr}^{-1}$) will remain constant for the remainder of the burst, this reservoir will be depleted in another 4.3×10^7 yrs. Comparing this time-scale with the burst-duration of 2×10^8 yrs, then J1 seems to have almost depleted its available gas. Although speculative, this is somewhat supported by the average SMG gas fraction $f_{\text{gas}} \sim 0.4$ that Tacconi et al. (2005) find in their SMG sample.

This could also explain some of the oddities of J1 as compared to other high-redshift galaxies, such as the super-solar metallicity (Tecza et al. 2004). Generally speaking, high-redshift galaxies are rather metal-poor (Shapley et al. 2004; Erb et al. 2004). The metal-enrichment in J14011 likely indicates that it is more evolved than the more populous BX sources.

In the low-redshift Universe, the mass metallicity relationship (Tremonti et al. 2004) indicates that higher-mass galaxies are also more metal rich, but maybe this does not exactly apply to J1. The enclosed dynamical mass within 20 kpc ($6 \times 10^{10} M_{\odot}$) is only marginally higher than the masses of BX galaxies at similar redshift ($4.4 \pm 3.4 \times 10^{10} M_{\odot}$ on average). The Erb et al. (2003) masses were obtained from the velocity dispersions, which makes them comparably robust against the impact of the unknown inclination. However, even if J2 is on a little inclined orbit, this will not increase the intrinsic enclosed mass by factors $\gtrsim 2 - 3$. Moreover, this effect is in parts balanced by the much larger radius of the enclosed mass in the J1–J2 system (20 kpc) as compared to the BX sample ($\lesssim 10$ kpc). Hence it might be that SMMJ14011+0252 J1 is indeed comparably evolved, and that this extra evolution is due to the ongoing burst. Direct comparison with other SMGs would be very helpful. Such data are currently not available, but will be soon, also through the ongoing SINS survey at MPE.

The detailed measurements that are now available for SMMJ14011+0252 J1 also allow another fascinating estimate: The amount of dark matter within the inner halo of a $z = 2.6$ galaxy. Using only the observed luminous matter will yield an upper limit on the non-visible matter budget. Whereas in the inner few kpcs, where the $\text{H}\alpha$ emission of J1 can be traced, the luminous and dynamical masses are approximately equal, at $R \sim 20$ kpc they are different by factors of 1.5, possibly up to ~ 5 if the inclination of the J2 orbit around J1 is $\gtrsim 20^\circ$.

3.14. J14011 and the evolutionary role of SMGs

Nearly all high-redshift galaxy populations presently known are candidates for being the progenitors of the most massive early-type galaxies at low redshift (LzEGs). This is in parts justified, because models of structure formation and direct surveys at intermediate redshift suggest formation redshifts $z \gtrsim 1 - 2$ for these objects. LzEGs are dominated by old, metal-rich stellar populations,

and give no indications of recent star-formation. They are very gas-poor, disfavoring future rejuvenization.

It is very likely that the galaxies acquired their early-type morphology during the SMG phase. For a collisionless stellar system with $M \sim 10^{11}$, relaxation time scales are $\sim 10^{16}$ yrs (S.White, IMPRSS lecture 2003), much longer than a Hubble time. Hence it is more likely that the bulge formed while the gas fraction – and hence the dissipative component – was still high. The observed velocity field of J1 cannot be modelled with an isolated thin disk, but indicates bulk rotation in SMMJ14011+0252 in at least one gravitational potential, hence the transition will most likely occur during the SMG phase or is already on-going. If the ionized gas in the wind approximately represents the gas mass that is driven out of the galactic plane and will ultimately be cool enough to fragment, collapse and form stars, then its mass of $10^7 M_{\odot}$ alone is certainly not sufficient to form a large bulge.

What is the evidence that SMGs like SMMJ14011+0252 are the progenitors of low-redshift massive galaxies? Hierarchical models of structure formation imply that the most massive overdensities in the Universe formed early at redshifts $z \gg 3$ and that their growth-rates decreased afterwards (Mo & White 2002). In other words, most of the mass of massive low-redshift galaxies must already have by and large been in place by $z \sim 2$. Early modelling results that conflicted with this broad outline were due to models having incomplete physics for feedback which lead to late gas accretion causing spheroids to be bluer than observed.

The early rapid evolution of massive galaxies is also supported by the mass-metallicity relationship (Tremonti et al. 2004), implying that the most massive galaxies are also most strongly evolved. Metallicity traces the integral star-formation history of a galaxy, as discussed in Section 1.2. SMMJ14011+0252 J1 has a super-solar metallicity (Tecza et al. 2004), whereas most galaxies at redshifts $z = 2 - 3$ with R_{23} measurements seem to rather have subsolar metallicity (Pettini et al. 2001). Shapley et al. (2004) report nearly solar metallicities in a sample of $z \sim 2$ BX galaxies, however, due they used N2 (Pettini & Pagel 2004), which likely has a significant systematic offset to R_{23} (Ellison & Kewley 2005) and is sensitive to ionization. Although no equally detailed metallicity measurements have been attempted for other SMGs yet (Tecza et al. 2004, used R_{23}), circumstantial evidence that they are comparably metal-rich is given e.g., by their comparably bright CO emission, indicating that they cannot be very metal poor.

High metallicity also implies that the enriched gas remained within the potential wells of the galaxy. This again favors massive systems, and feedback mechanisms, that are not powerful enough to remove the gas from the galaxy. As was shown in Section 3.8, star-formation driven feedback in J1 cannot accelerate the wind to the escape velocity of the halo potential (although the terminal velocities of the wind material might not be observed with the optical emission line gas). This is in spite of J1 being near the (empirically found) “maximal” possible burst rate. The feedback due to star-formation does have the impact of limiting the overall star-formation rate and thus controlling the gas depletion time. Hence it appears unlikely that star formation can drive much stronger feedback than currently observed, unless if another mechanism sets in, namely an AGN. There is no evidence for an AGN in SMMJ14011+0252, including radio and X-ray data. Therefore it is possible that J1 will retain its metals beyond the SMG phase and down to $z = 0$.

In addition, LzEGs reside in clusters. Evidence for an over-density of $H\alpha$ emitters around SMMJ14011+0252 has recently been found by Dannerbauer et al. (2005). Similar overdensities around high-redshift radio galaxies are viewed as forming galaxy clusters (e.g. Kurk et al. 2004). Between redshifts $z = 2$ and 0, a substantial fraction of these galaxies will probably be accreted by J1, but overall their mass will not increase the mass of J1 by factors much greater than 2. If J1

does not undergo another major merger while still being at high redshift, by $z \sim 0$, its most likely mass range will be a few $\times 10^{11} M_{\odot}$.

Table 1:: H α relative velocities, line ratios and extinctions.

(1)	J1n (2)	J1c (3)	J1s (4)	J2 (5)
rel velocity	0.0	12 ± 10	61 ± 12	-160 ± 18
width	220 ± 20	165 ± 22	184 ± 21	not resolved
$\log([\text{NII}]/\text{H}\alpha)$	-0.325	-0.296	-0.386	-0.656
$\log([\text{SII}]/\text{H}\alpha)$	-0.658	-0.495	-0.466	0.0
$\log([\text{OIII}]\lambda 5007/\text{H}\beta)$	0.277	-0.12	0.061	0.768
E(B-V)	1.566	1.285	0.788	0.228

Table 2:: Emission lines in J2

zone (1)	ID (2)	λ_{rest} (3)	z (4)	λ_{obs} (5)	FWHM_{obs} (6)	FWHM_{int} (7)	flux (8)
J2	[OIII]	5007	2.5636 ± 0.00019	1.7843 ± 0.00013	13 ± 1	<50	0.28 ± 0.01
J2	[OII]	3727	2.5649 ± 0.0002	1.3286 ± 0.0001	16 ± 2	<50	0.09 ± 0.002
J2	H β	4861	0	0	0	0	< 0.09
J2	H α	6563	2.5635 ± 0.00018	2.3387 ± 0.00017	14 ± 1	<50	0.31 ± 0.02
J2	[NII]	6583	2.5628 ± 0.0004	2.3454 ± 0.0004	24 ± 10	<50	0.07 ± 0.01

Column (1) – area. Column (2) – line ID. Column (3) – Rest-frame wavelength in \AA . Column (4) – Redshift. Column (5) – Observed wavelength in μm . Column (6) – Measured line width in \AA . Column (7) – Intrinsic line width in km s^{-1} . Column (8) – Flux in 10^{-19} Wm^{-2}

Table 3:: Emission lines in J1

zone (1)	ID (2)	λ_{rest} (3)	z (4)	λ_{obs} (5)	FWHM_{obs} (6)	FWHM_{int} (7)	flux (8)
J1n	H α	6563	2.5651 ± 0.00017	2.3397 ± 0.0004716	23 ± 1	259 ± 10	2.03 ± 0.04
J1n	[NII]	6583	2.5654 ± 0.00018	2.3471 ± 0.00016	26 ± 1	305 ± 11	1.05 ± 0.02
J1n	[NII]	6548	2.5658 ± 0.00019	2.3349 ± 0.00018	31 ± 2	377 ± 25	0.53 ± 0.01
J1n	[SII]	6717	2.5654 ± 0.00023	2.3949 ± 0.00021	26 ± 3	296 ± 38	0.26 ± 0.01
J1n	[SII]	6730	2.5663 ± 0.00031	2.4001 ± 0.00029	32 ± 6	373 ± 70	0.29 ± 0.01
J1n	[OIII]	5007	2.5652 ± 0.00021	1.7851 ± 0.00015	14 ± 2	188 ± 30	0.17 ± 0.01
J1n	H β	4861	2.5657 ± 0.00020	1.7333 ± 0.00014	11 ± 2	118 ± 20	0.13 ± 0.01
J1n	[OII]	3727	2.5656 ± 0.00028	1.3289 ± 0.00015	16 ± 3	349 ± 60	0.21 ± 0.01
J1s	H α	6563	2.5656 ± 0.00017	2.3401 ± 0.00016	22 ± 1	240 ± 8	1.09 ± 0.03
J1s	[NII]	6583	2.5658 ± 0.00019	2.3474 ± 0.00017	22 ± 1	238 ± 17	0.47 ± 0.01
J1s	[NII]	6548	2.5667 ± 0.0004	2.3354 ± 0.0004	66 ± 9	835 ± 116	0.43 ± 0.01
J1s	[SII]	6717	2.5726 ± 0.00028	2.3997 ± 0.00026	33 ± 5	388 ± 90	0.28 ± 0.01
J1s	[SII]	6730	2.5578 ± 0.00022	2.3944 ± 0.00021	14 ± 3	104 ± 23	0.14 ± 0.01

J1s	H β	4861	2.5658 ± 0.00020	1.7333 ± 0.00014	14 ± 2	194 ± 23	0.17 ± 0.01
J1s	[OIII]	5007	2.5655 ± 0.00023	1.7853 ± 0.00016	13 ± 3	178 ± 34	0.11 ± 0.01
J1s	[OII]	3727	2.5669 ± 0.00031	1.3294 ± 0.00016	23 ± 3	506 ± 72	0.23 ± 0.01

Column (1) – area. Column (2) – line ID. Column (3) – Rest-frame wavelength in \AA . Column (4) – Redshift. Column (5) – Observed wavelength in μm . Column (6) – Measured line width in \AA . Column (7) – Intrinsic line width in km s^{-1} . Column (8) – Flux in 10^{-19} Wm^{-2}

Table 4.: Emission lines in J1c

zone (1)	ID (2)	λ_{rest} (3)	z (4)	λ_{obs} (5)	FWHM_{obs} (6)	FWHM_{intr} (7)	flux (8)
J1c	H α	6563	2.5652 ± 0.00017	2.3398 ± 0.00016	21 ± 1	225 ± 6	1.37 ± 0.03
J1c	[NII]	6583	2.5655 ± 0.00018	2.3472 ± 0.00016	24 ± 1	275 ± 14	0.75 ± 0.02
J1c	[NII]	6548	2.5665 ± 0.00024	2.3354 ± 0.00022	33 ± 4	402 ± 45	0.37 ± 0.01
J1c	[SII]	6717	2.5653 ± 0.00021	2.3948 ± 0.00020	19 ± 2	194 ± 28	0.23 ± 0.01
J1c	[SII]	6730	2.5659 ± 0.00021	2.3999 ± 0.00020	23 ± 2	246 ± 30	0.29 ± 0.01
J1c	H β	4861	2.5649 ± 0.00019	1.7329 ± 0.00013	3 ± 1	0 ± 1	0.12 ± 0.01
J1c	[OIII]	5007	2.5654 ± 0.00021	1.7852 ± 0.00014	5 ± 1	0 ± 1	0.06 ± 0.01
J1c	[OII]	3727	2.5668 ± 0.0004	1.3293 ± 0.00022	16 ± 5	337 ± 106	0.07 ± 0.01

Column (1) – area. Column (2) – line ID. Column (3) – Rest-frame wavelength in \AA . Column (4) – Redshift. Column (5) – Observed wavelength in μm . Column (6) – Measured line width in \AA . Column (7) – Intrinsic line width in km s^{-1} . Column (8) – Flux in 10^{-19} Wm^{-2}

4. SMMJ04431+0210

4.1. Introduction

The second submillimeter-selected galaxy studied with SPIFFI/SINFONI, SMMJ04431+0210, is both fainter ($K = 19.4 \pm 0.1$) and smaller than SMMJ14011+0252. It was detected in 1998 during the SCUBA Cluster Lens Survey (SCLS) carried out by Smail et al. (1998) who measured a submillimeter flux at $850 \mu\text{m}$, $S_{850} = 7.2 \pm 1.7 \text{mJy}$.

SMMJ04431+0210 is gravitationally lensed by the $z = 0.18$ foreground cluster MS 0440+02, with an additional magnification due to a nearby, edge-on cluster spiral. The lensing analysis of Smail et al. (1999) suggests a magnification factor $\mathcal{M} = 4.4$. The intrinsic submillimeter flux $S_{850} = 1.6 \text{mJy}$ indicates that SMMJ04431+0210 – at least its submillimeter emission – is comparably faint and as such, is representative of submm sources with high surface densities, unlike many of the targets selected for detailed follow-up observations. Therefore it is typical for the galaxies which make up a substantial fraction of the cosmic FIR background (Blain et al. 2002; Smail et al. 2002).

CO measurements of the $J = 3 - 2$ transition are reported by Neri et al. (2003); Tacconi et al. (2005). The emission nominally peaks $\sim 0.4'' - 0.5''$ south-west from the optical position (Tacconi et al. 2005). It is difficult to estimate the accuracy of the alignment based on the published data sets, but using the precision of the alignment of SMMJ14011+0252 as a lower bound, this offset corresponds to about 1σ . Tacconi et al. (2005) give an upper bound to the intrinsic (lens-corrected) size of $0.8'' \times 0.18''$, corresponding to $6.4 \times 1.4 \text{ kpc}$ in right ascension and declination, respectively. Tacconi et al. (2005) report a double-peaked CO(3-2) profile in their high-resolution data, where the two peaks are spatially offset by $0.7'' \pm 0.3''$.

Neri et al. (2003) have measured a CO(3-2) FWHM = $350 \pm 60 \text{ km s}^{-1}$ and give a redshift of $z_{\text{CO}} = 2.5094 \pm 0.0002$, which corresponds to the H α redshift of Frayer et al. (2003) ($z_{\text{H}\alpha} = 2.5092 \pm 0.0008$)⁷ within the uncertainty of $\sigma_{\Delta z} = 0.00058$ on the difference between the redshifts.

ISAAC H and K band longslit spectroscopy published by Frayer et al. (2003) also indicates that SMMJ04431+0210 might be a worthwhile target for detailed follow-up studies with SINFONI. They find relatively broad H α emission (FWHM = $520 \pm 40 \text{ km s}^{-1}$) and a insignificantly narrower [NII] $\lambda 6584$ line (FWHM = $440 \pm 60 \text{ km s}^{-1}$ with a ratio [NII]/H α = 0.47 ± 0.06). They detect [OIII] $\lambda 5007$ in the H-band spectrum, but not H β (3σ upper limit of $2.7 \times 10^{-17} \text{ erg s}^{-1} \text{ cm}^{-2}$), which suggests [OIII]/H β > 1.5. Using this limit and case B recombination line ratios, they estimate that H α is extinguished by at least 1.6 mag. The line emission originates from within radii of $\sim 1.1''$ (or an intrinsic size of $\sim 2 \text{ kpc}$), similar to the isophotal size indicated by their K-band imaging data.

Radio emission was not detected in this source using the VLA at 1.4 GHz is $70 \mu\text{Jy}$ (~ 5 GHz in the rest-frame; 3σ upper limit on the radio emission is $70 \mu\text{Jy}$, Smail et al. 2000). With $R - K = 6.34 \pm 0.27$ (Frayer et al. 2003), SMMJ04431+0210 is an ERO⁸. However, this might relate more to the dust obscuration of the AGN than to the stars, because for sources exceeding barely the seeing disk, a nuclear point source is very difficult to separate from the extended emission.

⁷In the adopted concordance cosmology ($\Omega\Lambda = 0.7$, $H_0 = 70 \text{ km s}^{-1} \text{ Mpc}^{-1}$, $z = 2.51$ corresponds to a luminosity distance $D_L = 20491.4 \text{ Mpc}$, an angular size distance $D_\theta = 1663.3 \text{ Mpc}$, and a cosmic age of $t = 2.559 \text{ Gyrs}$. One arcsec corresponds to a linear size of 8.046 kpc .

⁸“Extremely Red Object”, an empirical color criterion indicative of old and (or) dusty stellar populations or very rarely, galaxies at high redshifts $z > 5$.

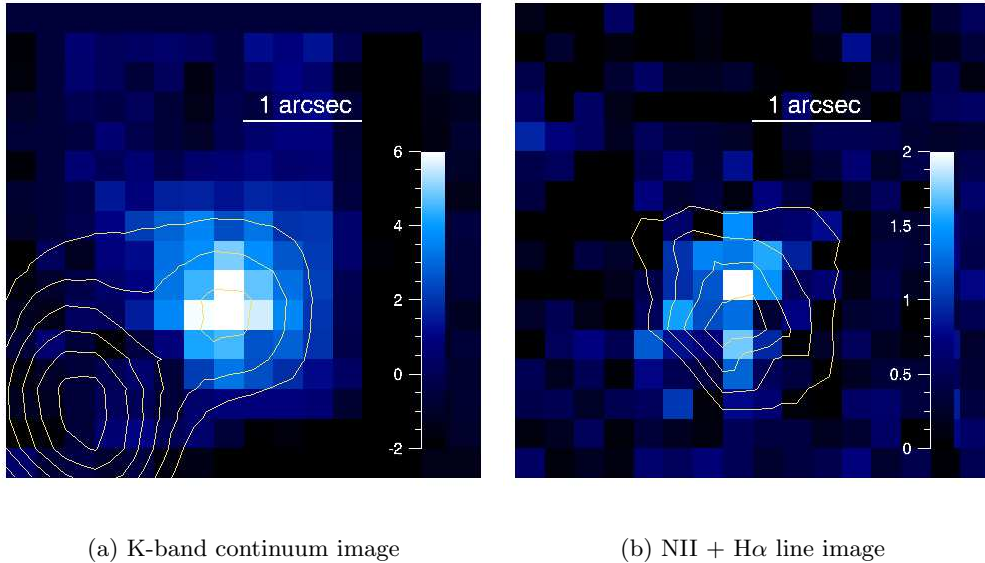


Fig. 31.— *Continuum and line morphology of SMMJ04431+0210. Emission from the foreground spiral galaxy was removed from the continuum image with the method described in Section 4.1. Contours in the continuum image indicate the unmanipulated image. Contours in the line image indicate the continuum morphology. In either image, the colorbar indicates the fluxes in units of $10^{-17} \text{ W m}^{-2} \mu\text{m}^{-1} \square''$.*

The present K-band data set on SMMJ04431+0210 was taken in November 2004 and April 2005 with the SINFONI-GTO instrument. Data had also been obtained during one of the SPIFFI-GI runs, but were not deep enough to derive robust results. Combining the GI and GTO data did not improve the data quality significantly. Total on-source integration time was 640 min. To approximate the resolution, the cube was rebinned to a spatial pixel scale of $0.25'' \text{ pix}^{-1}$ and a spectral binning of $0.00049 \mu\text{m}$.

Reducing the SMMJ04431+0210 data set was complicated by the proximity of the foreground approximately edge-on spiral cluster galaxy, which makes the background subtraction more difficult. In order not to bias the background estimate by this foreground signal, the “on-off averaging” explained in Section 3 was not applied for this data set. As a result, residual backgrounds are larger, and night sky lines residuals are comparably stronger. However, if this correction had been applied, then a correct flux calibration could not have been assured.

4.2. Removal of foreground emission

The nucleus of the lensing foreground galaxy N1 is separated by only $0.75'' \times 3.15''$ from SMMJ04431+0210. At $z = 0.18$, this corresponds to a projected radial distance of $\sim 10 \text{ kpc}$ between the nucleus of N1 and N4, and the two sources nearly overlap. The foreground source does not contribute to the line image (Fig. 4.1), but contributes significantly to the continuum emission. Removing a fitted isophotal model of N1 from the data leads to strong residuals, probably due to small scale structure within the spiral (Frayer et al. 2003). This approach is further complicated by the fact that, to minimize observational overheads, a dither pattern had to be chosen where only about half of N1 falls within the field-of-view.

Therefore, a different strategy was adopted to remove the foreground emission. For each slitlet, the light profile was measured separately, flipped about its peak, and removed from the image. The result is shown in Fig. 4.1, where the contours indicate the emission of the spiral galaxy. The K-band magnitude of N4 was measured from this image, using a $2'' \times 2''$ quadratic aperture. $m_K = 19.3 \pm 0.4$ mag, in good agreement with the $m_K = 19.4 \pm 0.1$ mag found by K-band imaging (Frayser et al. 2003).

4.3. Continuum and line morphology

The continuum image with the foreground source removed, shown in Fig. 4.1, appears mostly featureless. The size was determined from fitting a Gaussian ellipse to the source, using all pixels in the image where the flux exceeds 5σ , and is 3.6×5.2 pixels along the x and y coordinate, respectively. The ellipse is tilted by $\sim 15^\circ$. The seeing disk was measured from the combined image of all standard stars, weighted by the corresponding fraction of on-source observing time. The seeing disk was found to be 2.75×1.8 pixels, or $0.7'' \times 0.45''$. The intrinsic size of SMMJ04431+0210 is then obtained by deconvolving the size along the x and y coordinates with the size of the seeing disk, and correcting for the tilt, resulting in an ellipse of $0.95'' \times 1.3''$ along the minor and major axis, respectively. This is in agreement with the $1.1''$ FWHM size measured by Frayer et al. (2003). The advantage of course with the 3-dimensional SINFONI data is the more robust measurement of the size of the source compared to a simple longslit spectrum. Given that this source is lensed and its isophotal size is therefore asymmetric, this is crucial.

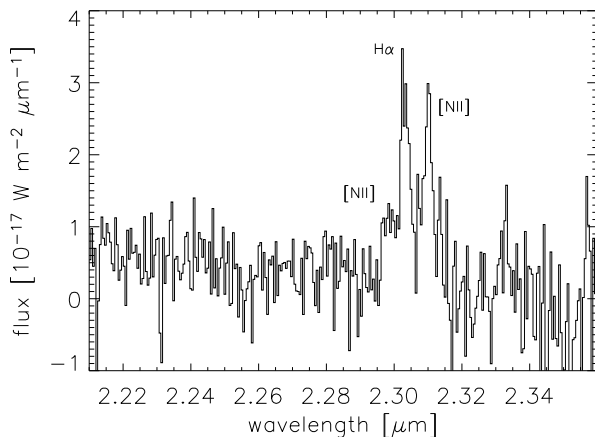


Fig. 32.— *Integrated spectrum of SMMJ04431+0210 summing over all 39 spatial pixels where the fitted $H\alpha$ line flux exceeds 5σ in 3×3 box apertures.*

Line emission is comparably faint in SMMJ04431+0210, especially if compared with the other SMG in this thesis, SMMJ14011+0252. As the following chapter will show, [NII] and $H\alpha$ emission are roughly co-spatial, and with little variation in the emission line ratios. The right panel of Fig. 4.1 therefore shows the continuum-removed, combined $H\alpha + [NII]$ image, obtained with the method outlined in Section 6 of Chapter 3. The line emitting regions appear elongated in north-south direction, roughly along the magnification axis of the gravitational lens and extending over $0.75'' \times 1.2''$ in declination and right ascension, respectively. This is about the same size as the continuum emission. It is marginally resolved in both directions, and slightly exceeds the spatial extent of the continuum emission along the declination axis. It peaks about $0.25''$ south from the continuum center. This offset can be explained by the overall faintness of line emission across the source, as inspection of the spectral slice contributing to each individual spatial pixel has shown. Integrated over all pixels where both continuum and line images exceed 3σ per pixel, the rest-frame equivalent width of the $[NII]+H\alpha$ line emission has an equivalent width of $W(H\alpha + [NII]) = 57 \pm 15 \text{ \AA}$.

Line emission is comparably faint in SMMJ04431+0210, especially if compared with the other SMG in this thesis, SMMJ14011+0252. As the following chapter will show, [NII] and $H\alpha$ emission are roughly co-spatial, and with little variation in the emission line ratios. The right panel of Fig. 4.1 therefore shows the continuum-removed, combined $H\alpha + [NII]$ image, obtained with the method outlined in Section 6 of Chapter 3. The line emitting regions appear elongated in north-south direction, roughly along the magnification axis of the gravitational lens and extending over $0.75'' \times 1.2''$ in declination and right ascension, respectively. This is about the same size as the continuum emission. It is marginally resolved in both directions, and slightly exceeds the spatial extent of the continuum emission along the declination axis. It peaks about $0.25''$ south from the continuum center. This offset can be explained by the overall faintness of line emission across the source, as inspection of the spectral slice contributing to each individual spatial pixel has shown. Integrated over all pixels where both continuum and line images exceed 3σ per pixel, the rest-frame equivalent width of the $[NII]+H\alpha$ line emission has an equivalent width of $W(H\alpha + [NII]) = 57 \pm 15 \text{ \AA}$.

4.4. Line emission

The integrated spectrum of SMMJ04431+0210 was obtained from summing over all pixels where the $H\alpha$ emission exceeds 5σ . The SINFONI data are seeing-limited and given the seeing at the time of the observations, the data are over-sampled (greater than Nyquist). To mitigate against loss of signal-to-noise due to over-sampling the spatial resolution, 3×3 pixel apertures (roughly corresponding to a spatial resolution element centered on the pixel in the middle) were used to estimate the significance of the line flux. Only the central pixels of each aperture were then used in constructing the source maps.

The spectrum is shown in Fig. 4.3. $H\alpha$ and the two [NII] lines are detected at 22.5σ , 21.3σ and 8.7σ , respectively. Line widths are similar to those found by Frayer et al. (2003), namely $\text{FWHM}_{H\alpha} = 442 \pm 37 \text{ km s}^{-1}$ for $H\alpha$ and $\text{FWHM}_{[\text{NII}]} = 358 \pm 34 \text{ km s}^{-1}$ for [NII] $\lambda 6583$. Using the ratio $[\text{NII}]/H\alpha = 0.8 \pm 0.1$ and the equivalent width derived in the previous section (which used the imaging data that are easier to correct for residual background), the $H\alpha$ equivalent width is $W(H\alpha) = 42 \pm 6 \text{ \AA}$. This ratio is about a factor 1.6 higher than the value given by Frayer et al. (2003), but is within the typical range of equivalent widths measured in SMGs (20 – 40 \AA , Swinbank et al. 2005).

The comparably large [NII]/ $H\alpha$ ratio and line widths suggest that the main ionizing source is not photoionization by hot stars. Continuum emission of SMMJ04431+0210 appears dominated by a relatively bright point source, although the small size extent makes it impossible to robustly separate the point source from the extended emission. All these are indications that SMMJ04431+0210 has a strong AGN component.

Yet clearer evidence comes from the broad line emission with $\text{FWHM} = 2300 \text{ km s}^{-1}$ that the SINFONI data reveal for the first time, and which is consistent with a broad line AGN. Its position coincides with the peak of the continuum emission, and its spatial distribution corresponds approximately to the SINFONI PSF. A spectrum of the nucleus, integrated over a $0.75''\times 0.75''$ box aperture, is shown in Fig. 4.4. Blue lines yield the fit to the broad and narrow components. The width of the broad line is in the range of broad lines given by Swinbank et al. (2004), $\langle \text{FWHM} \rangle = 2250 \pm 830 \text{ km s}^{-1}$.

4.5. Spatially resolved kinematic data

The spatial extent of SMMJ04431+0210 only marginally exceeds the seeing disk, especially perpendicular to the magnification axis of the gravitational lens. Nonetheless, extracting the spatially

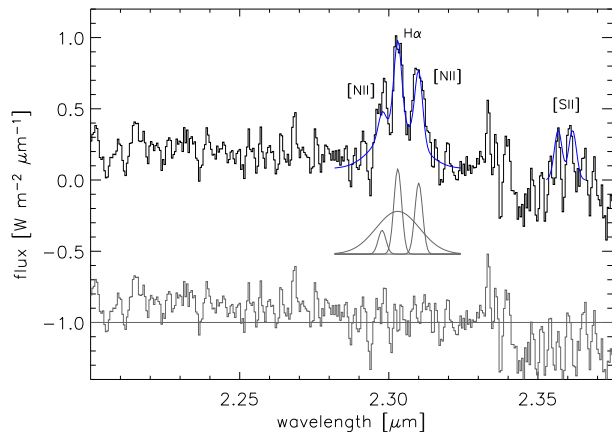


Fig. 33.— *Spectrum of the $0.75''\times 0.75''$ aperture centered on the nucleus of SMMJ04431+0210. The upper panel shows the spectrum (smoothed over 3 pixels spectrally to approximate the resolution), and the line fit (blue). The lower spectrum yields the fit residual. The fit components are shown between the two spectra.*

resolved spectral information does indicate some substructure. Fig. 4.10 shows some of the spectra which were extracted from $0.75'' \times 0.75''$ box apertures and smoothed over 3 pixels in spectral direction.

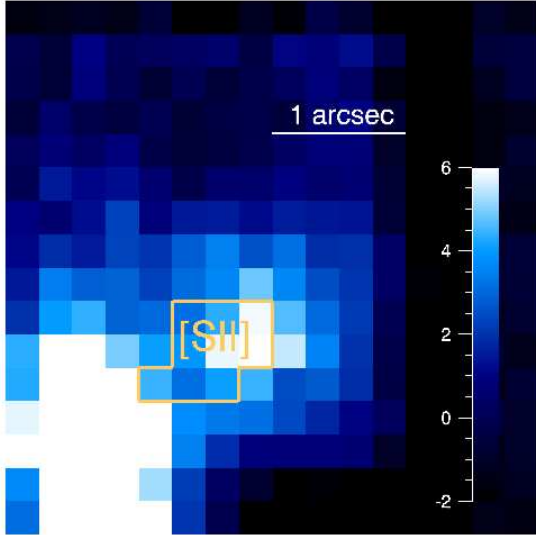


Fig. 34.— *Spatial region where [SII] emission is detected (the image shows the continuum emission).*

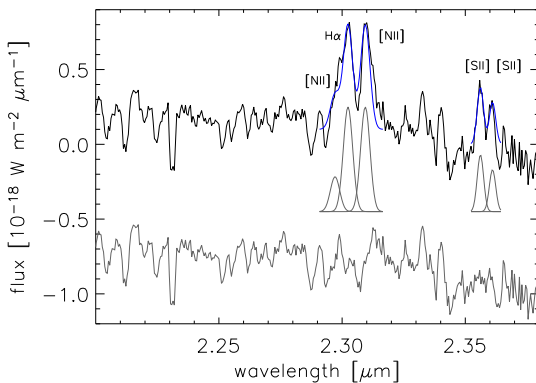


Fig. 35.— *Integrated spectrum of the area with brightest [SII] emission (blue). Residuals are shown in gray, the middle panel shows the line fit.*

Overall, the spectra show very inhomogeneous widths, line profiles and line ratios. Parts of this are certainly due to the relatively large line widths, which lower the signal-to-noise ratios per spectral bin, although the overall significance of the line detection (using the integrated line flux, $\Delta f_{line}/f_{line}$) might be higher. Nonetheless, the spectra indicate a comparably large intrinsic variability of line properties compared with star-forming galaxies at similar redshifts, especially SMMJ14011+0252, the other SMG in this thesis. This is especially the case for the [NII]/H α line ratios. Interestingly, they do not reach their highest values in the central pixel, but in the more peripheral regions, especially to the south ($0.0'' / -0.5''$) and west ($0.5'' / 0.0''$). This might indicate that SMMJ04431+0210 has extended narrow line regions like sometimes observed in low-redshift AGN (Tadhunter 1991).

Maps of the spatial distribution of line ratios and kinematic data are shown in Fig. 36. The small insets in each panel yield the $\pm 1\sigma$ range of the data. In each panel, the contours indicate the signal-to-noise ratios of the fitted spectral lines in steps of 2σ , starting from 3σ . The contours are marginally stretched along the magnification axis. The signal-to-noise values decrease for constant flux and increasing line width. Therefore the location of maximum signal-to-noise does not coincide with the peak in the emission line flux.

Although the scatter is considerable, the velocity map in the upper left panel of Fig. 36 indicates a significant velocity difference perpendicular to the magnification axis, and roughly in east-west direction. No velocity shear is found along the magnification direction. These patches also appear to have larger line widths (FWHMs are shown in the upper right panel of Fig. 36 and reach $\gtrsim 700 \text{ km s}^{-1}$). Equally, [NII]/H α ratios are larger than on average in these patches. All these findings indicate that these structures are related to the AGN, which is located inbetween the two patches.

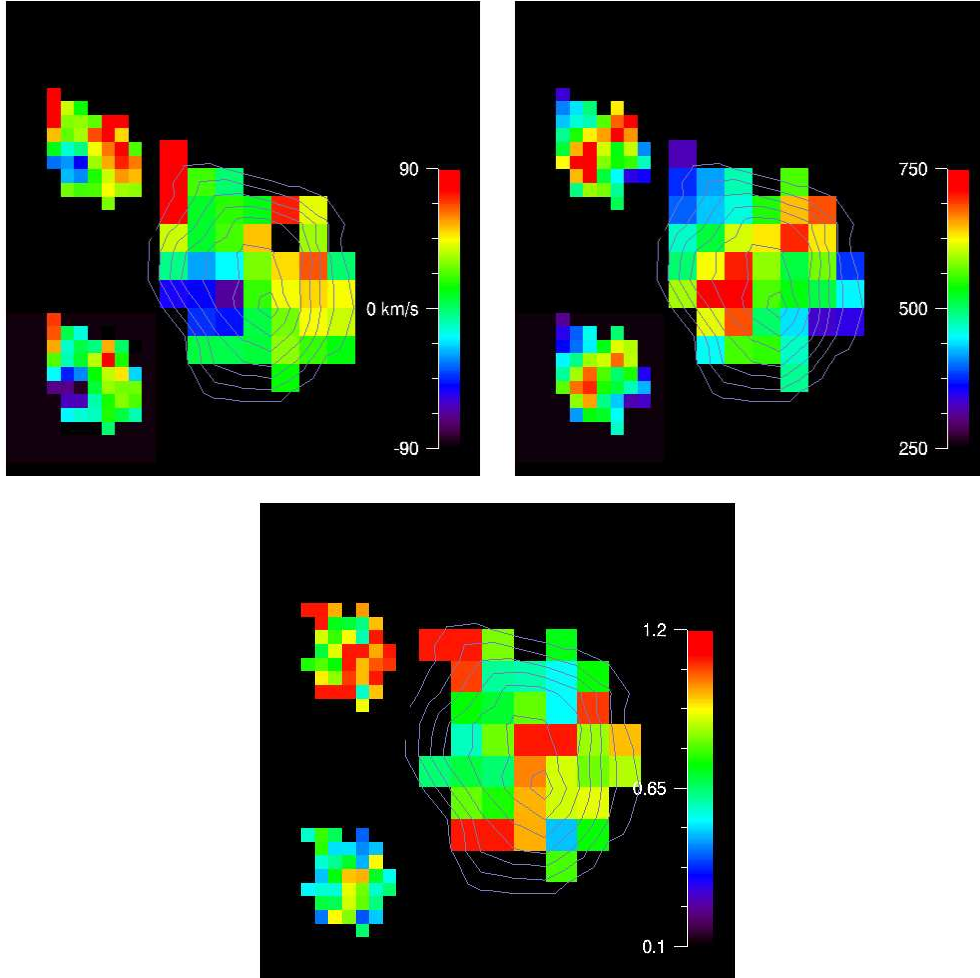


Fig. 36.— upper left: Map of relative velocities, given in km s^{-1} . upper right: Map indicating the FWHMs, given in km s^{-1} . lower panel: Map indicating the $[\text{NII}]$ to $\text{H}\alpha$ line ratio. In each map, the upper (lower) inset indicate the upper (lower) $\pm 1\sigma$ range.

4.6. Line emission in the high-excitation regions

Fig. 4.5 indicates the region in SMMJ04431+0210 where $[\text{SII}]\lambda\lambda 6717, 6730$ emission is found. The emission is marginally detected in the $0.75'' \times 0.75''$ apertures covering this area, but is more significant in the integrated spectrum of all pixels of this region (shown in Fig. 4.5). Because the signal-to-noise ratio of the $[\text{SII}]$ lines varies in a different way from the other lines and the lines fall into a spectral region where telluric absorption and the thermal emission in the K-band are significant sources of additional background, the lines are not detected in the integrated spectrum of SMMJ04431+0210. They are well-detected in a aperture adapted to the region with the brightest line emission and in the spectrum over a seeing disk centered on the nucleus. The spectrum integrated over 3×3 pixels centered on the nucleus is shown in Fig. 4.5.

The ratio of $[\text{SII}]\lambda\lambda 6717, 6730$ to $\text{H}\alpha$ emission in this zone is $[\text{SII}]/\text{H}\alpha = 0.76 \pm 0.2$. The line ratio of the two $[\text{SII}]$ lines is $F_{6717}/F_{6730} = 1.25 \pm 0.2$. Ratios of $[\text{NII}]$ to $\text{H}\alpha$ are also high in this zone, $[\text{NII}]/\text{H}\alpha = 1.08 \pm 0.12$. Frayer et al. (2003) have measured $[\text{OIII}]\lambda 5007$ emission of SMMJ04431+0210 and put a 3σ limit on $\text{H}\beta$. Using their results, the $[\text{OIII}]/\text{H}\beta$ ratio is $[\text{OIII}]/\text{H}\beta \gtrsim$

1.48. Using these line ratios, the position of SMMJ04431+0210 in the BPT diagnostic diagrams (chapter 4) can be constrained (Fig. 4.6). SMMJ04431+0210 clearly falls into the region of AGN in both diagrams.

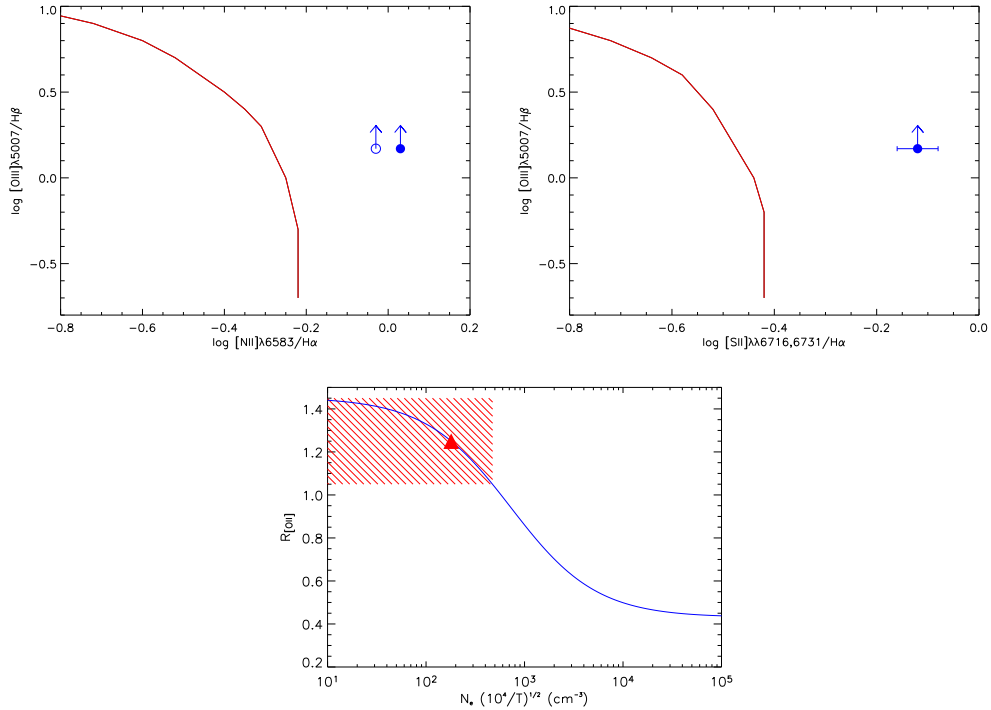


Fig. 37.— Density and BPT diagrams of SMMJ04431+0210. The [NII] and [SII] emission both indicate that SMMJ04431+0210 is dominated by the AGN. The [SII] BPT diagram uses the spectrum of the brightest emission of [SII]. In the [NII] BPT diagram, the filled (empty) circle indicates the [NII]/H α ratio extracted from the [SII] emitting region (total source), respectively.

Following the method outlined in Section 1.1, the ratio of the [SII] doublet can also be used to estimate the electron density in the emitting gas. The calibration function is shown in Fig. 4.6. In spite of the large uncertainty of the measurement, densities can be constrained to be $\lesssim 475 \text{ cm}^{-3}$.

4.7. Narrow line emission

Previous NIRSPEC data of SMMJ04431+0210 led to the suspicion that there is a zone of narrow line emission in SMMJ04431+0210 that is significantly offset from the nucleus (Frayser et al. 2003). The NIRSPEC data had an on-source integration time of 120 minutes and a spectral resolution of $R = 1500$. Due to the faintness of the line emission, the authors had to smooth their data heavily. From their published spectra, one can infer that the narrow line emission contributes significantly (30% – 50%) to the total H α emission of N4.

In the SINFONI data, such a bright isolated region of narrow line emission could not be identi-

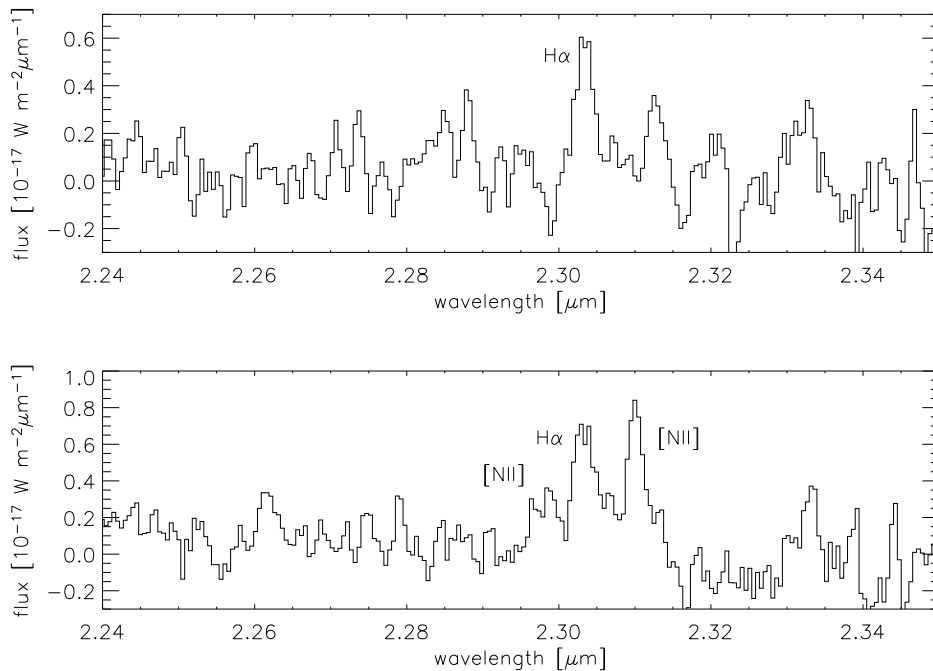


Fig. 38.— Spectra integrated over the narrow line regions. The upper panel shows the spectrum to the north-east of the nucleus, the lower panel the spectrum south from it.

fied. To investigate what the possible origin of this discrepancy might be, the most likely position of this off-nuclear emission was determined from the spatial offset in the published two-dimensional NIRSPEC spectrum and the slit position. A corresponding spectrum was extracted from the SINFONI data cube and smoothed it to the NIRSPEC resolution of $\lambda R \sim 15\text{\AA}$. The original spectrum was also rebinned to the according bin size.

The unmodified, smoothed, and the rebinned spectra are shown in Fig. 39. Excess flux is found, but is very faint, and coincides spatially with the area of comparably narrow line emission in the width map in Fig. 36. In Fig. 36 the zone of relatively narrow line emission extends in north-eastern direction from the nucleus over ~ 10 pixels ($0.63''$) with an integrated $H\alpha$ flux of $F_{H\alpha} = 1.6 \times 10^{-20} \text{ W m}^{-2}$. The integrated spectrum is shown in Fig. 38. The ratio $[NII]/H\alpha = 0.44 \pm 0.1$ is somewhat higher than the ratio found by Frayer et al. (2003) ($[NII]/H\alpha = 0.16 \pm 0.06$), but it is consistent with the line ratio expected for a star-forming region. The line width is $\text{FWHM} = 234 \pm 21 \text{ km s}^{-1}$. No velocity offset relative to the nucleus was found.

The star-formation rate in this zone can be estimated using equation 4.9. From the measured $H\alpha$ flux and for the adopted cosmology, the star-formation rate in this region is $SFR = 6.1 \mathcal{M}^{-1} M_{\odot} \text{ yr}^{-1}$. Assuming that the star-formation rate density in SMMJ04431+0210 is uniform across the galaxy, and using the diameter $\sim 1''$ as size estimate, the total star-formation rate is $SFR \sim 30 \mathcal{M}^{-1} M_{\odot} \text{ yr}^{-1}$, or $7 M_{\odot} \text{ year}^{-1}$ considering the magnification factor of $\mathcal{M} = 4.4$. These estimates are based on the observed $H\alpha$ flux and are not extinction-corrected. The corrected rates are likely factors of a few higher. The area of narrow-line emission that stretches towards south west from the nucleus in Fig. 36 has overall broader line emission ($335 \pm 35 \text{ km s}^{-1}$) and a ratio $[NII]/H\alpha = 1.02 \pm 0.13$, consistent with shock ionization.

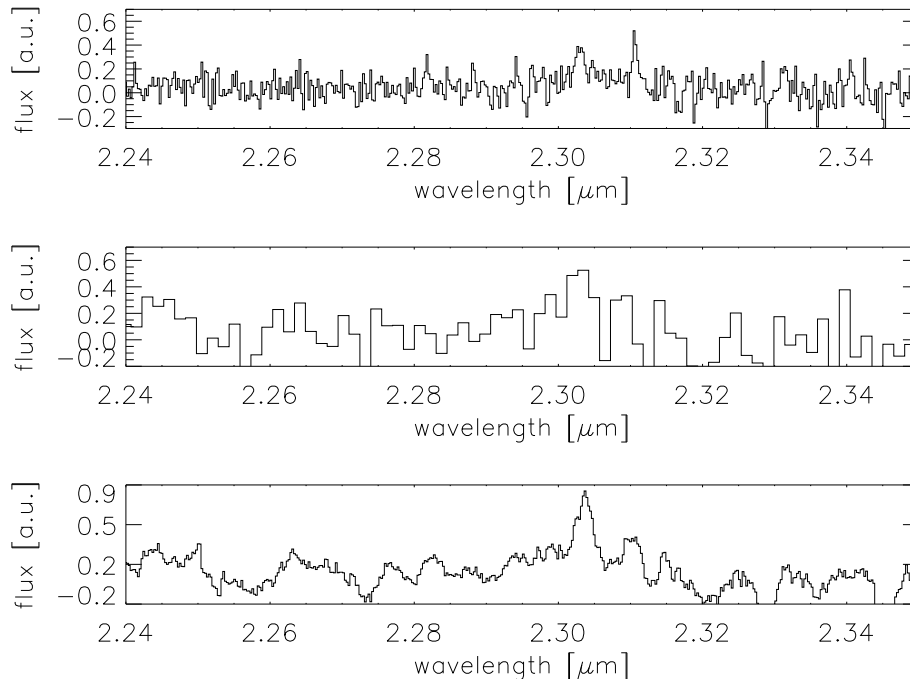


Fig. 39.— *The narrow line spectrum in the north-eastern part of the source. Panels show (top to bottom): The unmanipulated SINFONI data, the same spectrum rebinned to a resolution of 15\AA , the same spectrum smoothed to a resolution of 15\AA .*

4.8. Approximate appearance of N4 in the source plane

Using the lensing model of Smail et al. (2001), a crude estimate can be given for the appearance of SMMJ04431+0210 in the source plane. The continuum and line emission are both dominated by the AGN. Size estimates for the central emitting region in AGN are within light days, which – even if gravitationally lensed – are not spatially resolved. Hence only the fainter extended emission of SMMJ04431+0210 will be stretched by the lens. The magnification axis is roughly along the major axis of the foreground spiral N1. The tilt of N1 ($\alpha \sim 15^\circ$) was measured from the K-band image in Frayer et al. (2003) (their Fig. 1).

The corrected kinematic maps are shown in Fig. 4.9. The source appears elongated with a ratio of major to minor axis of ~ 1.3 . Interestingly the narrow line emission gas seems to be aligned with the major axis, as would be expected if it is distributed in a galactic disk. The regions where ionization, line widths and relative velocities reach their maximum appear rather oriented along the minor axis.

4.9. The mass of SMMJ04431+0210

The large line widths in SMMJ04431+0210 suggest that the dynamics are strongly influenced or even dominated by the AGN over several kpc of the central region of the source. It is difficult to judge from the current data set the influence of the AGN on the dynamics of the optical line emitting gas. In a study of local Seyfert galaxies Nelson & Whittle (1996) found a one-to-one correspondence between the velocity dispersion of the stars and the line widths of the [OIII] emission line. Sources

with strong, linear radio emission had [OIII] lines that were generally wider than what would be suggested by the velocity dispersion of the stars in the bulge. The fiducial dividing line between those sources influenced by the radio emission about $10^{22.5} \text{ W Hz}^{-1}$ at 1.4 GHz. The upper limit on the radio emission from SMMJ04431+0210 is $70 \mu\text{Jy}$ which gives a limit about 30 times this dividing line.

It is thus difficult to tell the impact of the radio source on the extended line emission, but at least superficially, the properties of SMMJ04431+0210 are consistent with it not having a large dynamical impact on the narrow line region.

If this is the case, then Nelson & Whittle (1996) suggest that the narrow-line region line widths can be used to estimate the velocity dispersion of the central regions near the supermassive black hole. From the [OIII] line width and the half-light radius of SMMJ04431+0210 from the SINFONI data, $M_{\text{spheroid}} = 1.3 \times 10^{11} M_{\odot}$.

Only a small (and unknown) fraction of the hydrogen gas in SMMJ04431+0210 will be ionized, however, combining this estimate with a few plausible assumptions can serve as a lower limit on the gas mass and be used as a consistency check with the above estimate.

Using equation 4.20 given in Section 5.4, the gas mass can be estimated from the luminosity of the line emission. Because the density in the AGN and star-formation dominated regions might be different, only the $H\alpha$ luminosity in the spectrum of the [SII] emitting region is used. With the adopted cosmology, the measured $H\alpha$ flux $F_{H\alpha} = (4.2 \pm 0.5) \times 10^{-20} \text{ W m}^{-2}$ translates into a luminosity $\mathcal{L} = (1.7 \pm 0.2) \times 10^{37} \mathcal{M}^{-1} \text{ W}$. (With a magnification $\mathcal{M} = 4.4$, the intrinsic, lens-corrected, luminosity is $\mathcal{L} = 3.2 \times 10^{36} \mathcal{M}^{-1}$.) Using equation 4.20 then yields a gas mass of:

$$M_{H\alpha} > 5.9 \times 10^8 M_{\odot} \quad (\text{lensed}) \quad (6.10)$$

$$M_{H\alpha} > 1.1 \times 10^8 M_{\odot} \quad (\text{unlensed}) \quad (6.11)$$

for the measured and magnification-corrected luminosities, respectively. These estimates are not corrected for extinction, which will increase the gas mass by factors of a few. (Estimating the extinction from the 3σ limit on the $H\beta$ flux, $F_{H\beta} < 2.7 \times 10^{-20} \text{ W m}^{-2}$, and the total $H\alpha$ flux mea-

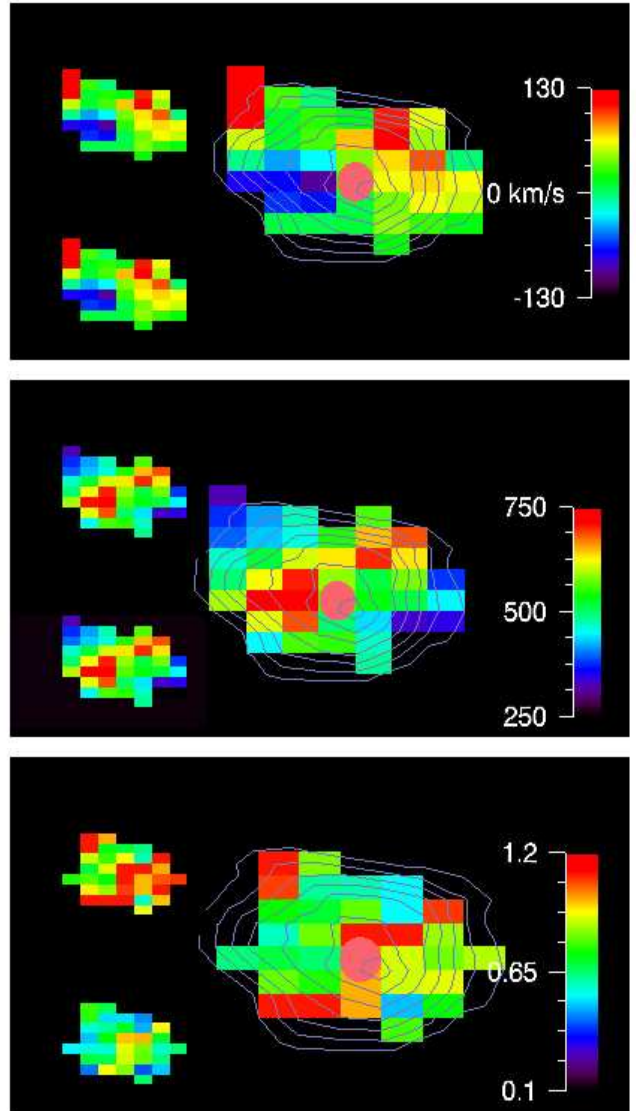


Fig. 40.— Maps of the velocities, FWHMs, and [NII]/ $H\alpha$ ratios (top to bottom) The upper (lower) insets indicate the upper (lower) $\pm 1\sigma$ range.

sured with SINFONI, the intrinsic H α flux is at least $3\times$ higher than the measured flux). Assuming that densities are roughly similar across the entire galaxy, the gas masses are again higher by a factor ~ 2 . Overall, these considerations imply that the ionized gas masses can be up to $1 - 2 \times 10^9 M_{\odot}$. This is a few times higher than the ionized gas mass in SMMJ14011+0252 ($5 \times 10^8 M_{\odot}$). The reason is probably the additional photoionization by the AGN in SMMJ04431+0210, enhancing the filling factor of ionized gas. Nonetheless, because only a small fraction of the hydrogen gas in SMMJ04431+0210 is expected to be ionized, this is a very conservative lower bound.

Neri et al. (2003) have estimated a molecular gas mass of $M_{CO} = 8 \times 10^9 M_{\odot}$ from the CO line luminosity of SMMJ04431+0210. Using the average gas fraction derived by Tacconi et al. (2005), $f_{gas} \sim 0.42 \pm 0.2$, this yields a rough mass estimate of $\sim 2 \times 10^{10} M_{\odot}$.

Alternatively a mass estimate can be given based on the FWHM of the CO emission (350 km s^{-1} , Neri et al. 2003; Tacconi et al. 2005). Greve et al. (2005) estimate $M_{CO,vir} \sim 10^{10}$ for an edge-on disk. Corrected for inclination, the mass is likely factors of a few higher.

In spite of the considerable uncertainties in each estimate, these results suggest that SMMJ04431+0252 has a mass of most likely a few $\times 10^{10} - 10^{11} M_{\odot}$.

4.10. SMMJ04431+0210 and SMMJ14011 – are they typical SMGs?

Comparing SMMJ14011+0252 J1 and SMMJ04431+0210 illustrates that SMGs are by no means a homogeneous sample. This is also indicated by the large scatter of the intrinsic properties of SMGs, discussed in the introduction to this chapter. The two sources presented in this section represent most of the diversity of the SMG population: SMMJ04431+0210 is dominated by AGN emission (like 40% of the overall population, Swinbank et al. (2004)), whereas SMM14011+0252 J1 does not show any sign of AGN activity and is dominated by a strong starburst like $\sim 60\%$ of the class. Perhaps surprising in this context is that intrinsically, SMMJ14011+0252 is nonetheless the brighter of the two sources, with $m_K = 19.6$ mag rather than $m_K = 21.0$ mag for SMMJ04431+0210 (both magnitudes are corrected for lensing).

No firm dynamical mass estimate can be given for SMMJ04431+0210 from the SINFONI data. Comparing the CO luminous masses (to estimate the gas masses) indicates that SMMJ14011+0252 J1 has a factor 1.6 more gas. Given the uncertainties of factors of few in this estimate, this means that the gas masses are similar. Accounting for the large scatter in the mass estimates of SMMJ04431+0210 indicates that the masses of the two SMGs will be similar within at most factors of a few.

The AGN also complicates the star-formation rate estimates of SMMJ04431+0210. Given the possible range of far-infrared spectral energy distributions, uncertainties in the initial mass function (especially at the low mass end of the stellar distribution which dominates the mass estimates), and the intrinsic possible combinations of AGN contribution to the bolometric luminosity, Frayer et al. (2003) estimate a robust range of $\text{SFR} = 100 - 2000 M_{\odot} \text{ yr}^{-1}$. Comparison of the H α SFRs in SMMJ04431+0210 and SMMJ14011+0252 hints that SFRs are $\lesssim 100$ in SMMJ04431+0210 and factors $\gtrsim 2 - 3$ higher in SMMJ14011+0252. This could either indicate an intrinsic difference, or that the star-formation is more dust-enshrouded or more compact in SMMJ04431+0210. More compact star-formation in SMMJ04431+0210 is disfavored by the CO data (Downes & Solomon 2003; Tacconi et al. 2005), which indicate that the sizes of the CO gas distribution is at least similar in the two galaxies, if not larger in SMMJ04431+0210.

Kaspi et al. (2000) have argued for using the luminosity of the 5100\AA continuum to estimate

the black hole mass. $\lambda_{rest} = 5100 \text{ \AA}$ approximately corresponds to the spectral range of the H-band continuum flux density in Frayer et al. (2003). The observed Balmer decrement yields an extinction correction ~ 1.95 mag. This is not strictly correct, because the line and continuum emission (generally speaking) have different extinctions, but it serves as a rough guideline and is not less precise than the uncertainties in the empirical relationships used for this comparison. In addition, the contribution of the stellar continuum is neglected. The 5100\AA continuum luminosity indicates a black hole mass estimate

$$\frac{M_{BH}}{M_{\odot}} = 5.71^{+0.46}_{-0.37} \times 10^7 \frac{\lambda L_{\lambda}}{10^{44} \text{ ergs s}^{-1}}^{0.545 \pm 0.036} \equiv 4.6 \times 10^7 M_{\odot} \quad (6.12)$$

For $M_{spheroid} \lesssim 1.3 \times 10^{11}$, the local $M_{BH} - \sigma_{bulge}$ relationships (Ferrarese 2002; Tremaine et al. 2002) predict black hole masses of $(1.0 - 1.2) \times 10^8 M_{\odot}$, about a factor 2 larger than the direct estimate. This is a reasonably good agreement, given the large uncertainties in both mass estimates (the black hole mass alone is uncertain by factors of a few, and the line widths are uncertain by $\sim 30\%$, not accounting for the uncertain radius and systematic uncertainties of the estimates). In addition, the Kaspi et al. (2000) correlation implies an ‘‘average’’ radiative efficiency for PG quasars at moderate redshifts, which might not be strictly appropriate for SMGs.

Interestingly, in an X-ray study of submm galaxies, Alexander et al. (2005) suggest that supermassive black holes in SMGs are of the same order of magnitude in mass and are accreting at roughly 1 to a few 10s of percent. Both of their estimates for these quantities are very similar to what is estimated here, using a different set of assumptions. Although the constraints are weak, it is impossible to escape the conclusion that even at these redshifts, the growth of the both the black hole and the central spheroidal regions of SMGs must be evolutionarily related. The conclusion relies on a set of assumptions, which are all reasonable when measured against our overall understanding of the AGN.

Attributing all the submm emission to star-formation in SMMJ04431+0210, from the molecular gas measurements, the gas consumption time scale is about 8 – 80 Myrs for a $SFR = 100$ to $1000 M_{\odot} \text{ yr}^{-1}$ (the approximate range given in Frayer et al. 2003). This rough time scale is similar to that estimated for local AGN (10-100 Myrs Martini 2004, and references therein). If the AGN in SMMJ04431+0210 is similar to local ones, then even a simple timescale argument would suggest that both the galaxy and supermassive black hole are co-eval and such a hypothesis is not limited by the amount of available gas. In other words, the gas fraction of SMMJ04431+0210 is $\sim 40\%$ (Downes & Solomon 2003; Tacconi et al. 2005) with a gas depletion time scale of about 10 – 100 Myrs, very similar to the Salpeter time (time necessary for the mass to grow by a factor of e at the Eddington accretion rate) of a 10^7 to $10^7 M_{\odot}$ black hole. Thus, even if the accretion is only a several 10s of percent of Eddington, and the gas in SMMJ04431+0210 is consumed by star-formation, both the galaxy and black hole have sufficient time and available gas masses to effectively double in mass. Both independent lines of evidence suggest the co-eval growth of galaxies and supermassive black holes. Of course many more such studies are required to put these hypotheses on a statistically sound footing beyond the speculative discussion given here.

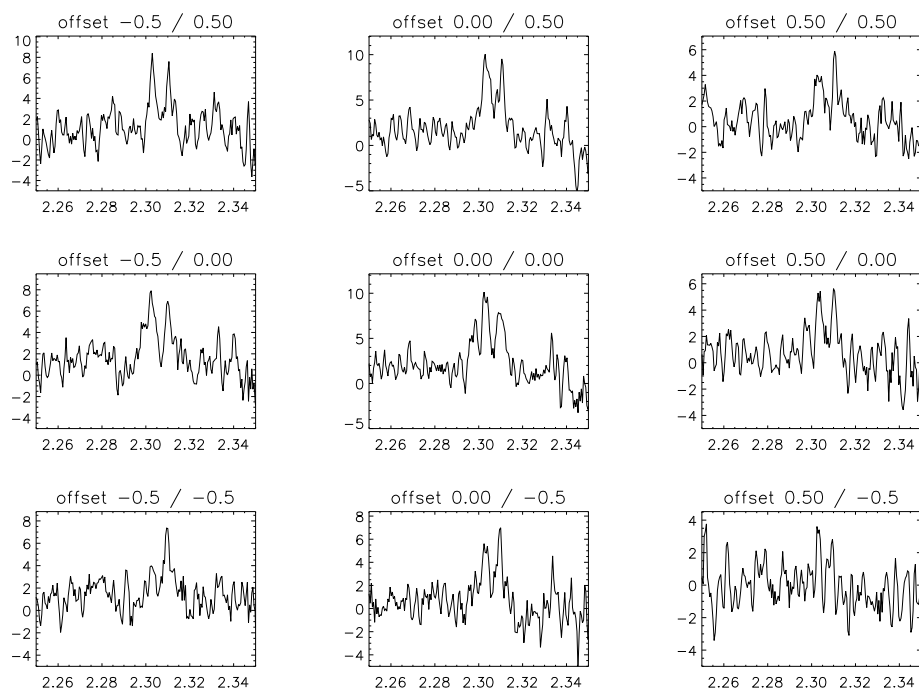


Fig. 41.— *Sequence of spectra integrating over 3×3 pixels extracted from within SMMJ 04431+0210. The nucleus is shown in the center, relative distances of each spectrum from the nucleus are given in seconds of arc. The spectra are smoothed over 3 pixels along the spatial axis.*

Chapter 7

Lyman Break Galaxies Under a Microscope: The Small Scale Dynamics and Mass of an Arc in the Cluster 1E0657-56

1. Introduction: Strong lensing and the 1E0657 arc core

Lyman-Break Galaxies are particularly small and faint, even for being at high redshift, with typical half-light radii of $\lesssim 0.3''$ (Giavalisco, Steidel, & Macchetto 1996). Studying the spatially-resolved properties (e.g. dynamics, metallicities) of their rest-frame optical emission line gas in detail means driving the current generation of instrumentation to its limits, as will become clear from the next Chapter. Results based on this type of measurement are biased towards the strongest line emitting sources (e.g., starbursts) which may not be representative of the overall population or only sample selected regions within each source (e.g., concentration of the line emission to the central regions, variation in the extinction, etc.; Lehnert & Heckman 1996b). This bias may in turn lead to intrinsic systematic uncertainties (e.g., not sampling the full rotation curve or being sensitive to hydrodynamic effects like galactic-scale outflows or complex dynamics due to mergers). Such worries are not without a substantial basis. It is known that LBGs are actively forming stars, and their morphologies are often complex and do not resemble any of the Hubble types in the nearby Universe. This suggest that mergers, extinction and the distribution of the emission line gas may be important factors in interpreting the observed dynamics of $z \sim 3$ LBGs.

Some of these worries could be mitigated against if it was possible to “zoom into” a small region around the center of a $z \sim 3$ LBG. A highly magnified circum-nuclear region with a well-defined rotation curve would be concrete evidence that at least some sources in this population are dominated by rotation. Although a galaxy in the throws of a major merger can have complex dynamics even in its core, on small scales, it is hard to conceive how it could be mimicking a “rotation curve”. A merger would have broad lines and proportionally small velocity gradient which should be obvious. On the other hand, on large scale, blurred by seeing, it is easily possible for a merger to masquerade as a rotating disk due to the large relative velocity offsets and the seeing merging the velocities into a smooth curve.

The only way currently available to zoom into high-redshift galaxies at size scales below ~ 1 kpc

is through the observation of strongly lensed sources within the critical radius of massive galaxy clusters at intermediate redshift. In spite of the increasing number of detected strong gravitational arcs, spectroscopic follow-up observations with good resolution and signal-to-noise ratios have been carried out only for very few sources. The number is virtually zero if one considers strongly lensed galaxies with high quality, spatially-resolved near-infrared spectra. The sample with detailed observations is quite inhomogeneous, ranging from low-extinction Lyman Break Galaxies (such as MS1512-cB58 at $z = 2.7$; Yee et al. 1996) to dusty submillimeter sources (e.g. MS0451.6-0305 at $z = 2.9$; Borys et al. 2004). Another spectacular recent example is the Lynx arc, a lensed HII galaxy at $z = 3.4$ (Fosbury et al. 2003).

Strongly lensed sources are a necessary complement to the unmagnified ones. They make it possible to observe parts of galaxies at very high physical resolution. Given the debate as to whether or not spatially resolved dynamics is due to rotation or something more complex, this is not a mere academic advantage. Unfortunately, the regions magnified are effectively random cutouts of the galaxy – results might not at all be representative for the integrated properties of the object. In addition, the detailed modelling of the lensing potential is crucial. This can be a problem since sometimes there are insufficient constraints to construct accurate lensing models. Consequently, morphologies, size scales, and how sources are “parceled” may be highly uncertain and are certainly model-dependent.

Spatially-resolved kinematics of gravitational arcs are only rarely addressed in the literature. Franx et al. (1997) obtained spatially resolved Ly α and SII λ 1260 emission line spectra of a $z = 4.0$ lensed starburst galaxy in the CL 1358+62 field, finding an overall blueshift of SII with respect to Ly α , and velocity differences of about 300 km s^{-1} over a diameter of a few kpc. Unfortunately, Ly α is susceptible to optical depth effects which may dominate the line centers and widths. Thus Ly α cannot generally be used to track the dynamical masses of galaxies. Franx et al. (1997) conclude that the line emission most likely traces an outflow, with Ly α being apparently redshifted due to absorption by neutral gas, and is *not* indicative of the large-scale gravitational motion. Lemoine-Busserolle et al. (2003) studied a pair of $z \approx 1.9$ galaxies, lensed by the cluster AC114, and separated by ~ 34 kpc in the source plane. In one of the two cases, they spatially resolved the H α and [OIII] λ 5007 lines for one of the galaxies (AC114-S2) and derived a mass of approximately $1 \times 10^{10} M_{\odot}$ within the inner 1 kpc (actually beyond their velocity measurements). However, these are not galaxies in the “classical” redshift range of Lyman break galaxies, and they have different physical and photometric properties. Finally, from a rest-frame optical integrated spectrum of the strongly lensed LBG MS 1512-cB58, Teplitz et al. (2000) estimate a dynamical mass of $1.2 \times 10^{10} M_{\odot}$ from the velocity dispersion estimated using the Balmer emission lines.

The strongly lensed $z = 3.24$ ¹ galaxy behind the $z = 0.3$ X-ray cluster 1E0657-56 (Tucker et al. 1998) is different from most other well-studied high-redshift gravitational arcs. Its high magnification (> 20) presents a good opportunity to investigate the properties of LBGs at high physical and spectral resolution. Rest-frame UV data of the $\sim 14''$ long 1E0657-56 gravitational arc were initially obtained by Appenzeller et al. (1998) during the commissioning of FORS1. Photometry in B, g, R and I was taken, as well as longslit spectra (Mehlert et al. 2001). Its lensing configuration suggests the simultaneous magnification of a high surface brightness region at the south-eastern tip of the source that may be associated with the “core” of the galaxy as well as a more highly magnified, lower surface brightness region apart from the core (“arc” Mehlert et al. 2001). The arc

¹Using the flat concordance cosmology with $\Omega_{\Lambda}=0.7$ and $H_0 = 70 \text{ km s}^{-1} \text{ Mpc}^{-1}$ leads to $D_L = 27.9$ Gpc and $D_A = 1.5$ Gpc at $z = 3.24$ (the redshift of the arc and core). The size scale is $7.5 \text{ kpc}''$. The age of the universe at this redshift and cosmological model is 1.9 Gyrs.

shows a complex substructure: Mehlert et al. (2001) identify three faint knots of similar surface brightness within the arc, each separated by a few arcseconds. These 3 knots lie to the northwest of the core. The knots and core are spatially resolved along the axis of greatest magnification, and unresolved perpendicular to it in the ground-based imaging of Appenzeller et al. (1998). Mehlert et al. (2001) propose that the central highest surface brightness region of the lensed galaxy, lying near, but outside the cusp-caustic, is seen as the bright arc core, whereas a fainter outer region of the same galaxy, which touches the cusp-caustic, is split into three merging images, and constitutes the full extent of the arc. Their modeling suggests a magnification factor of ~ 20 , or 3.25 mag for the core and higher by an unspecified amount for the arc.

The rest-frame UV spectra in Mehlert et al. (2001) show absorption lines of moderate strength, with strong Ly α and Ly β absorption. No emission line is seen, arguing against a dominant spectral contribution from hot O stars.

Given the interesting configuration of this source and the wealth of supplementary data, it was observed in one of the SPIFFI “Guest Instruments” runs. The SPIFFI-GI commissioning-team obtained deep K band data of 1E0657-56 arc core, covering the core as well as the neighboring and parts of the subsequent bright arc knot. Observations between April, 6th and 11th 2003, were carried out under variable conditions, so that only 190 out of 300 minutes total integration time were used in the final cube. The size of the seeing disk was determined from the light profile of the standard star to be 0.6'' and 0.4'' in right ascension and declination, respectively.

2. Evidence that “Arc + Core” is a LBG

Undoubtedly, one of the best-studied class of galaxies at high redshift are the Lyman break galaxies (LBGs) at $z \sim 3$. As discussed by Pettini et al. (2001) and Shapley, Steidel, Pettini, & Adelberger (2003), for example, these are low-metallicity, actively star-forming galaxies of sufficient number density that they may represent the phase of bulge/spheroid growth of M^* galaxies. However, their small spatial extent ($\sim 0.3''$ in the rest-frame UV continuum, e.g., Giavalisco, Steidel, & Macchetto 1996) makes it difficult or even impossible to obtain high-quality spatially resolved spectra of these sources. Relatively weak velocity gradients have been found for two LBGs (Pettini et al. 2001), but these tend to have large projected angular sizes and irregular morphologies making the interpretation of the velocities difficult. Although rest-frame UV morphologies of local galaxies are often very irregular, and dominated by star-forming regions and complexes, those inhomogeneities are typically on scales of 10 to a few 100 parsecs (in the adopted cosmology, angular sizes of < 0.1 arcsec). At the redshifts of the LBGs, such scales are smoothed by the seeing in typical conditions and are no longer resolved. The light profiles of these galaxies, however, often appear elongated, and dominated by two unresolved rest-frame UV bright spots at distances of a few kpc. Such a geometry and scales are more consistent with galaxy pairs or mergers. However, the small spatial extent and faintness of these sources make it difficult to distinguish between these two hypotheses, especially when only ground-based observations (without adaptive optics) are available.

The study of gravitationally lensed Lyman break galaxies is one way to overcome the limited spatial resolution of ground-based data without adaptive optics. However, only one strongly lensed LBG has so far been identified, MS1512-cB58 at $z \sim 2.73$, a rather low redshift for this population. Since the redshift $z = 3.24$ of the 1E0657 arc and core galaxy is near the average redshift of the LBG sample ($z = 3.13 \pm 0.06$), and its physical properties are very similar, it is of major interest to investigate whether this target quantitatively satisfies the LBG color selection at $z \sim 3$. Therefore

initially, data sets previously obtained by Mehlert et al. (2001), Appenzeller et al. (1998) will be reviewed and reanalyzed, and a currently unpublished ACS image².

2.1. Rest-frame UV colors

The FORS1 rest-frame UV spectrum covers the full spectral range used for the Lyman-break color selection. By convolving the spectrum with the corresponding filter curves used to select LBGs (digitized from Fig. 1 in Steidel et al. (2003)), and deriving the colors directly from the flux ratios, it is possible to measure *a posteriori* whether the gravitational arc and core in 1E0657 fulfill the Lyman break criteria³. In an analogous way, the magnitude measured in the FORS R-band can be translated into the \mathcal{R} band magnitude used by Steidel et al. (2003). To illustrate the method graphically, the SED of the core together with the digitized filter curves is shown in Fig. 1. For the 1E0657 giant arc one obtains the colors and magnitudes:

$$\begin{aligned}\mathcal{R} &= 21.53 \\ G - \mathcal{R} &= 0.94 \\ U - \mathcal{G} &= 2.73 (> G - \mathcal{R} + 1)\end{aligned}$$

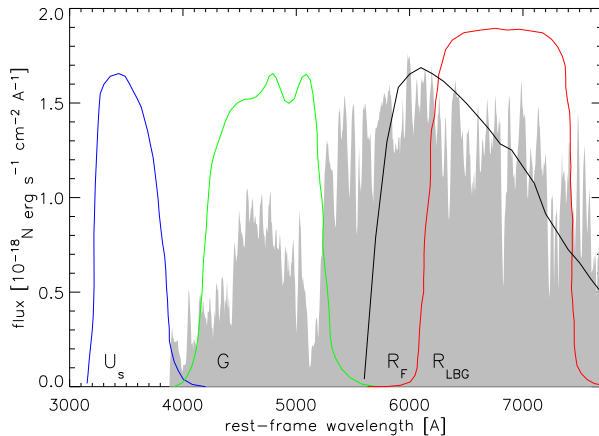


Fig. 1.— *Transmission curves for the filters used in the Lyman-Break color selection (U_s, G, R_{LBG}), and observed optical spectrum of the core (gray shaded area). R_F denotes the filter curve of the FORS R-band filter.*

$$\begin{aligned}\mathcal{R} &= 21.15 \\ G - \mathcal{R} &= 0.92 \\ U - \mathcal{G} &= 2.71 (> G - \mathcal{R} + 1)\end{aligned}$$

Comparison with the Lyman-break criteria given in Steidel et al. (1999) shows that all three selection criteria are fulfilled, i.e. the gravitational arc in 1E0657 is a Lyman-break galaxy. The \mathcal{R} band magnitude is not corrected for the $\mathcal{M} \sim 3.3$ mag magnification, because it is mainly an observational limit to ensure a homogeneous selection in spite of varying sensitivities and fluxes in the different wavebands, and to minimize color biases at the faint end. However, even if the magnitude is corrected for lensing, the \mathcal{R} -band magnitude of the arc, $\mathcal{R} = 24.83$, is brighter than the Lyman-break selection cutoff of $\mathcal{R} = 25.5$. The SEDs of the arc and core are very similar, so that it is not very surprising that also the core is within the Lyman-break range:

²The image was kindly, quickly, and generously provided by Christine Forman-Jones before its release into the HST archive

³The integrated spectra were kindly provided by S. Seitz and R. Saglia

Integrated R-band fluxes within the 26 mag isophote were used for this comparison (see Table 1 of Mehlert et al. 2001). However, similar results are obtained for all magnitudes given in Mehlert et al. (2001).

2.2. Rest-frame UV spectroscopy

Rest-frame UV spectroscopy of the arc and core with FORS1 on the VLT were described by Mehlert et al. (2001) and allows a detailed comparison of the UV emission with that in the K-band from SPIFFI.

The rest-frame UV spectra were integrated over the core and an identical aperture was used to extract the SPIFFI data. In addition, a longslit spectrum of Mehlert et al. (2001) extends over the full extent of the arc (which is about twice the surface covered with SPIFFI). At a redshift of $z \sim 3.24$, wavelengths between $\sim 1000 \text{ \AA}$ and $\sim 1800 \text{ \AA}$ fall within the FORS bandpass and were obtained with good signal-to-noise ratios. The spectra are dominated by continuum emission, with a comparably broad, asymmetric Ly α absorption line. No significant Ly α emission was detected either in the arc nor in the core. The asymmetric, broad blue wing of the Ly α line is typical for high-redshift galaxies, and is due to absorption by neutral hydrogen in the ISM. A number of narrow metal absorption lines are superimposed, which originate from stellar winds in the atmospheres of hot, massive stars and from the ambient interstellar medium. Unfortunately, these spectra have signal-to-noise ratios too low to robustly investigate the significant UV stellar photospheric diagnostic lines, especially in regions of night sky lines. Mehlert et al. (2001) investigated the strong stellar wind lines of SiIV 1400 and CIV 1550 to determine the metallicities of the gas.

The continuum slope is a reasonable age and extinction indicator in high redshift galaxies. Given that most of the strong absorption lines in the UV are due to stellar winds and absorption by gas in the ambient ISM, they are not very useful for determining the ages of galaxies. These lines are more a probe of the metallicity, extinction, luminosity, and gas dynamics of starburst galaxies (Heckman et al. 1998). In addition, the continuum slope is much better defined in these data, which can be fitted with population synthesis models, such as STARBURST 99 (Leitherer et al. 1999) to make an approximate age determination (although it is still degenerate with the extinction). STARBURST 99 was chosen for this particular source, because it concentrates on the rest-frame UV emission of starburst galaxies and is widely used within the astrophysics community. Population synthesis is described in more detail in Section 2 of Chapter 4.

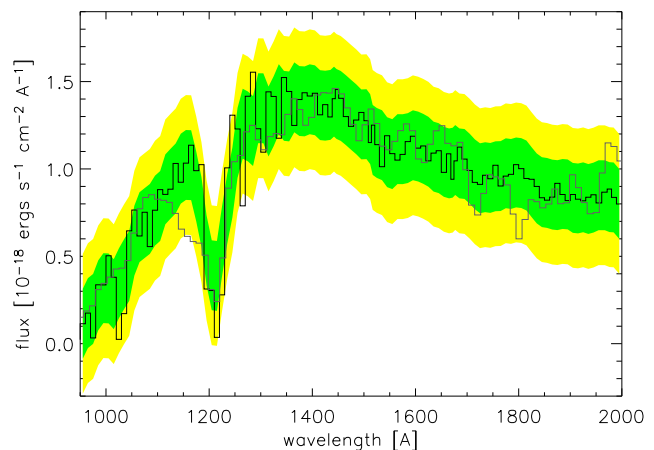


Fig. 2.— *The rest-frame UV SED of the arc (gray line) and the best-fit STARBURST99 model (black line) assuming an instantaneous burst 8×10^7 yr ago and no extinction. The green and yellow bands indicate the 1 and 2- σ uncertainties of the data.*

In a burst of star-formation, the presence of a strong UV continuum in itself restricts the age of the dominant population to less than a few hundred Megayears, due to the short lifetimes of the most massive stars that have hot enough atmospheres to emit a substantial number of UV photons. From the analysis of the rest-frame optical lines, it is known that 1E0657 arc+core have subsolar metallicities, hence the model used metallicities measured in the Small Magellanic Cloud. A Salpeter IMF was used, with $1 M_{\odot}$ and $100 M_{\odot}$ lower and upper mass cut-offs. An equally-spaced grid of ages between 0.5 and 15×10^7 yr was modelled in steps of 5 Myr. The best fit was found in both the arc and the core for a population that formed in an instantaneous burst 8×10^7 yr ago, and has no extinction. The fit to the core together with the data, convolved to match the rather coarse resolution of the model ($\sim 10 \text{ \AA}$) is shown in Fig. 2. The green and yellow bands indicate the 1 and $2\text{-}\sigma$ uncertainties of the data.

Although the presence of the UV continuum alone makes the fit rather unique in a burst model, it is interesting to ask how well the model is constrained. A detailed, statistical assessment of this question is difficult due to the large number of partly degenerate parameters and correlations within the data. However, a rough estimate of at least parts of the parameter space can be given by varying the input parameters (especially the age) and examining from which values on the disagreement between data and model will systematically exceed 3σ . It was found that within the calculated grid of models, systematic discrepancies either in the blue or red wavelength range (or both) were found for ages below 6×10^7 yr in the arc (5×10^7 yr in the core due to the smoother spectrum) and for ages above 1.1×10^8 yr in either part of the source. For the concordance cosmology, this means the burst occurred at $z \lesssim 3.4$. The stellar mass estimate follows directly from the modeled luminosity and the distance modulus. The according ranges of stellar mass within the arc are $3.5 - 10 \times 10^9 M_{\odot}$ and $2 - 7 \times 10^9 M_{\odot}$ in the core. These values are not corrected for lensing.

2.3. Continuum morphology and the half-light radius of the core

High-resolution imaging of the arc and core have been recently obtained with the ACS camera on-board the HST. The image taken through the F814W filter (roughly I-band) is shown in Fig. 12. To estimate the spatial resolution, an artificial PSF was created using the TinyTim package (Krist & Hook 1997). Sizes were measured by fitting a two-dimensional Gaussian. FWHMs are $0.089''$ in both right ascension and declination. The profiles along right ascension for the PSF and the arc are compared in Fig. 3.

Both arc and core are spatially resolved in the direction perpendicular to the magnification axis. Intrinsic profile widths are determined by deconvolving the observed diameter with the diameter of the PSF generated by TinyTim:

$$\text{FWHM}_{\text{intr}} = \sqrt{\text{FWHM}_{\text{obs}}^2 - \text{FWHM}_{\text{psf}}^2}$$

The unlensed diameter of the arc varies between $\sim 0.3 - 0.6''$ ($2.4 - 4.8$ kpc), the core reaches an unlensed diameter of $0.113''$ (0.9 kpc) across its brightest part.

The ACS image reveals the complexity of the source. The arc is composed of irregular high surface-brightness patches, maybe giant star-forming HII regions, embedded into a continuous structure with lower surface brightness, which itself also does not have a very smooth, regular shape. The core has an overall higher surface brightness, with a bright, unresolved spot in the middle, and two arms in an S-like shape.

Along the magnification axis, the central region of the core has a diameter of $\sim 0.4''$, about 4 times larger than the unlensed $0.113''$ diameter perpendicular to it. The full extent of the core along the lensed direction is $2.3''$. The northern arm shows a relatively bright, unresolved patch. Arc and core do not seem to connect directly, but are offset by $0.3'' \times 0.15''$ (~ 2.3 kpc, correcting for a magnification factor of $\mathcal{M} = 20$) in right ascension and declination, respectively. An unresolved, somewhat higher surface-brightness patch appears at the end of the arc, where it is closest to the core.

If 1E0657-56 arc and core both satisfy the Lyman-break color criteria, then how do their morphologies compare to those of the overall $z \sim 3$ Lyman-break population? The major axis of the core is about $2.3''$ long. This translates into an intrinsic size of ~ 1.3 kpc, correcting for a $\mathcal{M} = 20$ magnification factor, and assuming that the major axis of the core is along the magnification axis. Giavalisco, Steidel, & Macchetto (1996) have analyzed HST imaging of 19 sources, and find typical half-light radii of $r_e \sim 0.2 - 0.3''$, or $1.6 - 2.4$ kpc, in the range of the unlensed sizes of the arc and the core, respectively. Along the magnification axis, this is about the extent of the core. Although this can only be a crude comparison due to the intrinsic uncertainties of the strong gravitational lensing, it does suggest that a representative part, possibly more than half of the background Lyman-break source, is magnified into the core. This does not mean, however, that this includes the full galaxy, because also the size scale of the unlensed sources probably only trace the highest-surface brightness, central parts of the underlying systems. However, this does suggest that 1E0657 core is a representative zoom-in the Lyman-break population, in agreement with the similar physical properties and photometry.

Apart from the much better resolution of the ACS data, the F814W and FORS R-band morphologies are very similar, as can be seen from Fig. 13, which shows the F814W image smoothed to the spatial resolution of the FORS data. Contours indicate the FORS R-band fluxes. $R - I$ colors were derived from $2''$ apertures centered on the core and the bright spots along the arc, and are uniform within the uncertainties.

The effective SPIFFI field of view is also shown in Fig. 12 (white box). It covers the arc core, and about half of the $14''$ long arc, including about half of the middle knot (named ‘knot 3’ in Fig. 4). However, the core is near the edge of the data cube, and is not fully contained in all individual data frames, decreasing its signal-to-noise values.

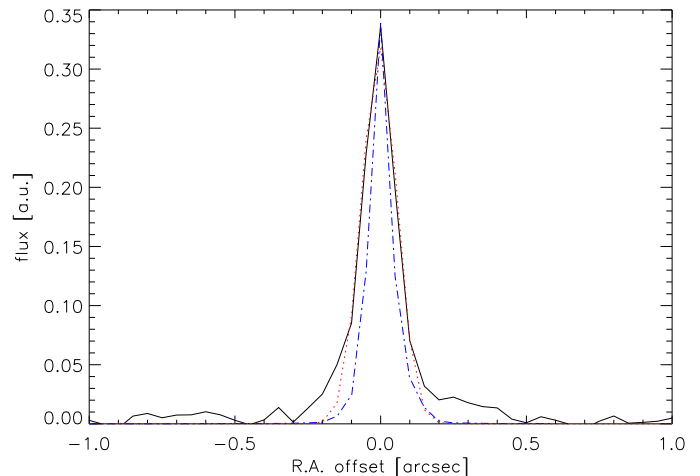


Fig. 3.— Profile of the PSF (blue dot-dashed line) and the light profile of the core perpendicular to the magnification axis (red dotted line).

3. Results and analysis

3.1. Continuum and emission line morphology

Fig. 4 shows the integrated SPIFFI $[\text{OIII}]\lambda\lambda 4959, 5007$ line image of the $z = 3.24$ arc and core. Contours indicate the rest-frame UV, FORS R band data. To the precision of the alignment (about 1 pixel or $0.25''$), the positions of the rest-frame UV and the SPIFFI K band data cube overall coincide (this holds for both the $[\text{OIII}]\lambda\lambda 4959, 5007$ line emission and the line-free K-band continuum). However, the maxima of the brightness profiles of the core in the FORS and the SPIFFI data are displaced by $\sim 1 - 2$ pixels. This can be easily explained by the rather low signal-to-noise ratio in the SPIFFI data, and is not a sign for an intrinsic difference.

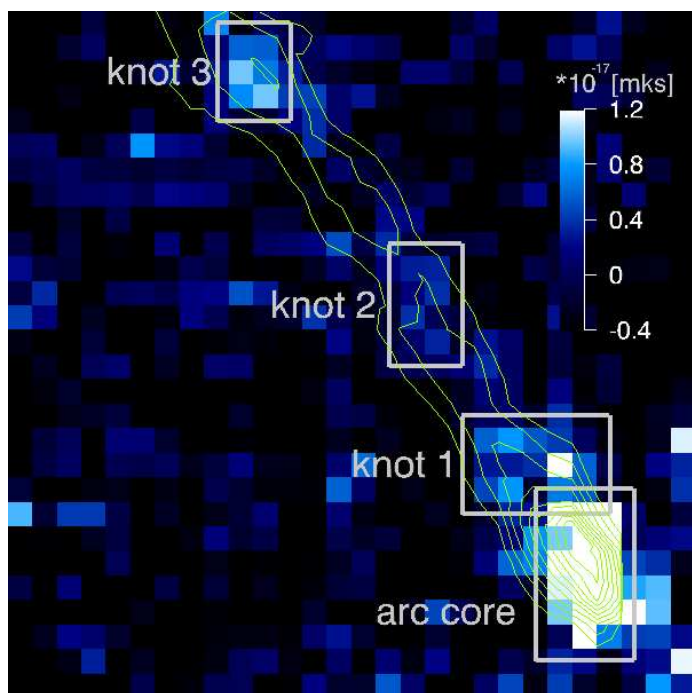


Fig. 4.— Continuum subtracted, combined $[\text{OIII}]\lambda\lambda 4959, 5007$ line image of 1E0657 arc and core. Contours indicate the distribution of rest-frame UV emission from the FORS1 R-band image (Mehlert et al. 2001) in steps of 2σ starting at 10σ .

are not sufficient to firmly rule out the presence of such a population, it does raise confidence that the rest-frame UV spectra trace the main stellar component of this galaxy.

Interestingly, the best-fit parameters are also in agreement with the K-band continuum flux measured with SPIFFI. At $z = 3.24$, wavelengths between 4788 \AA and 5590 \AA are redshifted into the K-band ($2.03\text{-}2.37\mu\text{m}$). The model predicts a total K-band magnitude $K = 20.3$ mag for the core, whereas the SPIFFI data yield an integrated magnitude $K = 20.5$.

Performing a similar measurement for the arc is more difficult, because the continuum emission has a very low signal-to-noise ratio in each spatial pixel, due to the large spatial extent of the arc, and also, because the arc is only partly contained in the data cube. Nonetheless, the overall similarity of the arc and the core spectrum in the UV make it likely that an equally good agreement for the expected and measured K band magnitudes could be found for the arc as well.

Hence there is no sign for an underlying, older stellar population, that would already have faded in the rest-frame UV, but still be present in the rest-frame $\sim V$ -band. Although the precision of the data

3.2. Integrated spectra: Ionization of the gas, metallicity and star-formation rate

Spectra were extracted from within the light blue boxes in Fig. 4. The flux-calibrated, integrated spectrum summing over all boxes is shown in Fig. 6, line properties are summarized in Tab. 2. Rest-frame optical emission line ratios can be used to infer the source of ionization of the emission line gas. A full set of diagnostic lines allows to distinguish whether the heating source is

massive stars, an active galactic nucleus, or mechanical energy input from either stars or AGN as evidenced by significant shock heating. Based solely on the near-infrared data, this would be rather difficult, because $[\text{OIII}]\lambda 5007$ and $\text{H}\beta$ do not constitute a complete set of robust line diagnostics. This ratio depends on both the ionization of the gas and its metallicity. In other words, both low metallicity gas excited by hot, massive stars and solar metallicity gas excited by strong shock or a power law ionizing continuum typical of an AGN can lead to high ratios of $[\text{OIII}]\lambda 5007/\text{H}\beta$. Complementary to the line ratios are of course the line widths. For example, if an AGN was the excitation mechanism, then a broad component to the line profile might be observable. Unfortunately, the signal-to-noise ratio of the spectrum and the faintness of the $\text{H}\beta$ emission make it difficult to set a sensitive upper limit to the amount of broad line emission. Taken at face value, the observed line widths, which are $\sim 150 \text{ km s}^{-1}$ and therefore rather low and similar across both arc and core, would disfavor the presence of an AGN. Moreover, the line ratios appear uniform across the entire source, although in some apertures, the measured $\text{H}\beta$ flux is not highly significant.

Another line of evidence that this source does not harbor an AGN comes from the characteristics of the rest-frame UV spectrum in Mehlert et al. (2001). If there were a strong AGN in the core, then one would expect to observe a power-law continuum as seen in quasar spectra. In fact, the rest-frame UV spectrum is dominated by absorption, not by emission lines, and some of the strong absorption lines are dominated by the contribution of stellar winds (e.g., $\text{CIV}\lambda\lambda 1548, 1550$) as opposed to lines in the ambient ISM. Lines of this strength cannot be significantly diluted by an AGN as would be the case if an optically evident AGN was the main ionizing source. Strong extinction, which might hide an embedded AGN at rest-frame UV, but not rest-frame optical wavelengths, seems unlikely, because the source has overall blue colors (see also Section 2.2). If only the AGN was dust-enshrouded and embedded in an unextincted host, then the central extinction might hide the ionizing source from the host as well as from the observer, so that the main source of the observed ionization would still be the stellar emission.

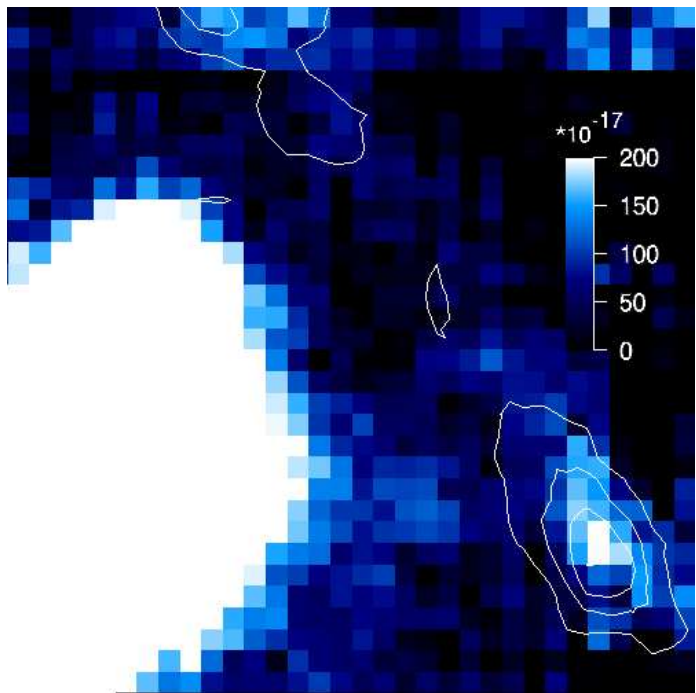


Fig. 5.— *K* band continuum morphology of the 1E0657 arc+core galaxy. Contours yield the distribution of $[\text{OIII}]\lambda 5007$ line emission in steps of 1σ , starting at 2σ .

Since photoionization of hot stars seems the most likely source of ionization, the strong $[\text{OIII}]$ emission compared to $\text{H}\beta$ is a rough indicator of an overall low metallicity. The classical metallicity estimate based on R_{23} (see Section 1.2 of Chapter 4) from the *K* band spectrum alone cannot be obtained, because $[\text{OII}]\lambda 3727$ is missing. Therefore the measured $[\text{OIII}]/\text{H}\beta$ ratio of 3.9 results in a mere *lower bound* to the R_{23} of $\log R_{[\text{OIII}]}$ = 0.59 ± 0.14 . For low-metallicity galaxies, the $[\text{OII}]/[\text{OIII}]$ ratio can be rather precisely estimated, as was shown by Kobulnicky et al. (1998) for a sample of low-redshift star-forming dwarf galaxies (Section 1.2 of Chapter 4). For the measured $\log R_{[\text{OIII}]} = 0.59 \pm 0.14$ their calibration suggests $\log R_{[\text{OII}]} = 0.4 \pm 0.15$. The estimated $R_{23,\text{est}}$ of

the integrated spectrum of the 1E0657 arc core galaxy is then 0.99 ± 0.2 .

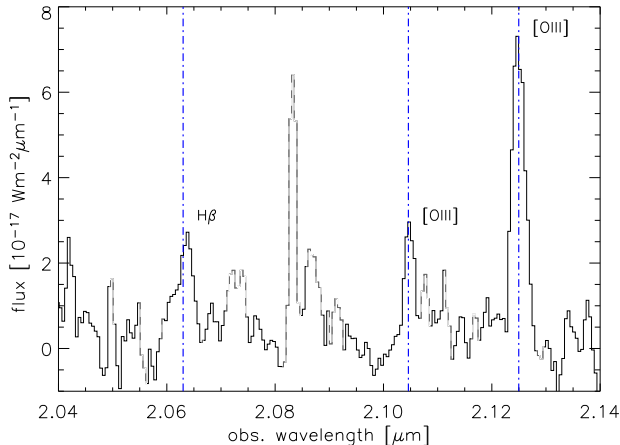


Fig. 6.— *Total spectrum of the arc+core. Dotted lines indicate the position of strong night sky lines. Blue vertical dot-dashed lines show the expected position of emission lines.*

The integrated $H\beta$ emission yields also an estimate of the star formation rate (the procedure is described in Section 2.1 of Chapter 4). For the adopted cosmology, the measured $H\beta$ flux of $F_{H\beta} = 6.7 \pm 0.6 \times 10^{-20} \text{ W m}^{-2}$ yields an $H\beta$ luminosity of $0.7 \times 10^{36} \text{ W}$. Neglecting extinction, the Balmer decrement is $H\alpha/H\beta \approx 2.75$ (in analogy to Pettini et al. 2001). The empirical relationship of

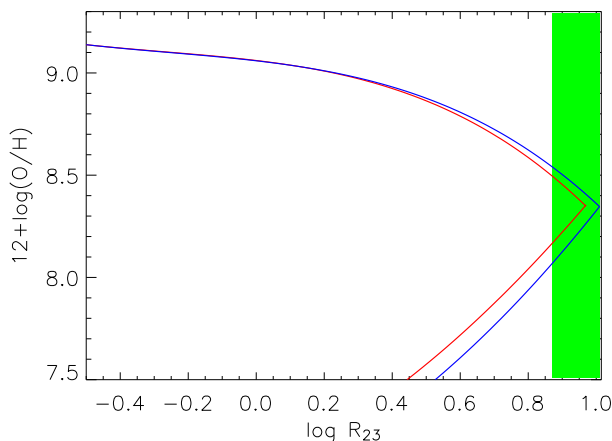


Fig. 7.— *Oxygen abundance in the arc+core. The blue (outer) and red (inner) curves indicate the metallicity for the highest and lowest ionization, the green vertical band indicates the R_{23} estimate.*

about $E(B-V) \sim 0.13$ are appropriate for typical LBGs. In fact, Shapley, Steidel, Pettini, & Adelberger (2003) suggest something more subtle.

They find that galaxies with $\text{Ly}\alpha$ in absorption typically have higher extinction than LBGs

The resulting oxygen abundance estimate is shown in Fig. 7. The measured line ratios place 1E0657-55 arc core fortuitously at metallicities where both the uncertainty due to the missing [OII] data and the ambiguity of the metallicity estimate by the two-valued relationship are minimized. The resulting metallicity including all uncertainties is $12 + \log[\text{O}/\text{H}] = 8.34^{+0.26}_{-0.34}$. Taking this estimate of R_{23} at face value and accounting only for the intrinsic ambiguity of the R_{23} estimator itself implies that the best estimates are $12 + \log[\text{O}/\text{H}] = 8.23\text{--}8.44$, or 0.45% of the solar abundance (taken to be 8.69 ± 0.05 following Allende Prieto, Lambert, & Asplund 2001).

Kennicutt (1998) (see Section 2.1) yields then $\text{SFR} = 131 M_{\odot} \text{ yr}^{-1}$, not correcting for lensing. If the magnification factor is $\mathcal{O}(20)$, the intrinsic star-formation rate is $\sim 7 M_{\odot} \text{ yr}^{-1}$. This estimate obviously is a lower limit, because it does not account for extinction. However, as the modeling of the UV spectrum has shown (Sec. 2.2), even at very short wavelengths, a good fit can be obtained without any extinction. Since this galaxy has colors and a rest-frame UV spectral slope similar to LBGs at $z \sim 3$ (Shapley, Steidel, Pettini, & Adelberger 2003), it is appropriate to use values consistent with those of LBGs. Steidel et al. (1999) and Shapley, Steidel, Pettini, & Adelberger (2003) suggest that values of

with strong Ly α emission. By splitting their LBG sample into quartiles, Shapley, Steidel, Pettini, & Adelberger (2003) find that for the quartiles of LBGs with the strongest Ly α absorption on average $E(B-V)=0.17$ magnitudes (Their “Group 1” which has a typical equivalent width in Ly α of ~ -15 Å.) Assuming that $A_V=3.2 E(B-V)$, implies $A_V\approx 0.5$ magnitudes. Converting this to the extinction at H β (a small correction) implies an extinction and lensing corrected star-formation rate of $\sim 11 M_\odot \text{ yr}^{-1}$. Assuming a value typical for HII regions in and the integrated spectra of nearby galaxies which is $A_V \sim 1$ mag, the star-formation rate would be about $17 M_\odot \text{ yr}^{-1}$. Given the uncertainties in this estimate, the best one can say is that star-formation rates much in excess of 20 are strongly disfavored.

3.3. Spatially-resolved emission line properties of the arc knots and core

Fig. 8 shows the separate spectra of the core and of the three boxes along the arc. They are smoothed by 3 pixels (15\AA) to approximately match the resolution. Although the faintness of the H β line along the arc inhibits a detailed comparison of the metallicity and star formation rates between the core and the arc, [OIII]/H β ratios are roughly similar in all apertures, indicating that star formation rates and metallicities do not alter significantly.

The redshifts of the [OIII] $\lambda 5007$ lines, on the contrary, do vary for the different apertures, monotonically decreasing with increasing spatial offset from the core. With respect to the integrated arc core, relative velocities are $\Delta v_{knot1} = -104 \pm 27 \text{ km s}^{-1}$ for knot 1, $\Delta v_{knot2} = -152 \pm 27 \text{ km s}^{-1}$ for knot 2, and $\Delta v_{knot3} = -239 \pm 20 \text{ km s}^{-1}$ for knot 3.

Emission line properties of these regions are summarized in Tab. 2. Whereas the data are of high enough quality to derive robust estimates also of the position of the line centroids, the line wings partly overlap with a strong night sky line residual, adding uncertainty to the measured line widths. This applies especially to the lines extracted from along the arc, due to their lower signal-to-noise values, and because their slightly smaller redshifts worsen the blending with the OH line. However, the total arc spectrum as well as the brightest knot have $\text{FWHM}_{[\text{OIII}]\lambda 5007} \lesssim 200 \text{ km s}^{-1}$, in broad agreement with the H β line in the brightest arc knot. Therefore, the measured values are not used, but a fiducial $\text{FWHM}_{[\text{OIII}]\lambda 5007} = 182 \text{ km s}^{-1}$ is assumed for all line widths along the arc, as given in Tab. 2, irrespective of the generally larger measured values (which are $300 - 400 \text{ km s}^{-1}$).

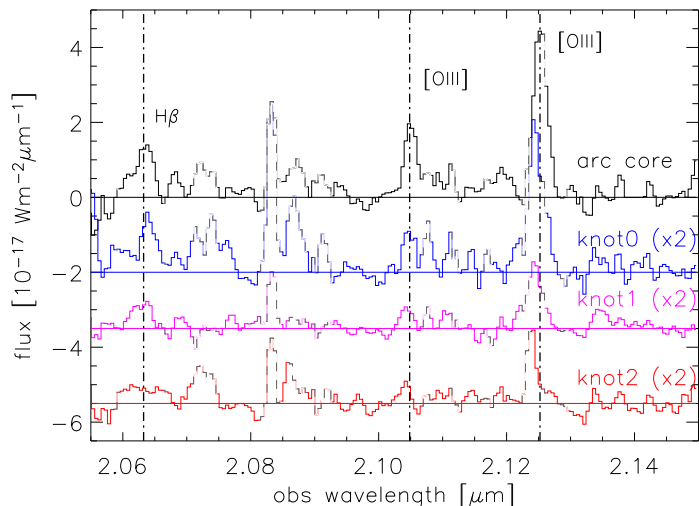


Fig. 8.— Spectra of the core and knots 1 to 3 are shown in black, blue, magenta, and red, respectively. Arc spectra are scaled by factors 2. Dotted lines indicate strong telluric OH lines, the vertical dot-dashed lines show the expected position of [OIII] and H β emission lines at the redshift of the core [OIII] $\lambda 5007$ line.

Within the core, good signal-to-noise ratios for $[\text{OIII}]\lambda 5007$ can be obtained for yet smaller apertures. The line fluxes in these apertures are rather uniform, few $\times 10^{-17}$ ergs $\text{s}^{-1} \text{cm}^{-2}$. Because the source is not resolved perpendicular to the lensing direction, which is roughly along one slitlet in the data cube, spectra are extracted of the core separately for each row. The resulting spectra are shown in Fig. 9, relative velocities as a function of distance in Fig. 10. Measured velocities increase smoothly from north to south, with a total velocity gradient of $\sim 150 \text{ km s}^{-1}$.

Note that the relatively uniform emission line fluxes across the core indirectly support the interpretation that the arc+core galaxy is indeed an isolated, and not a merging or interacting galaxy. The S-shaped morphology in the core could either originate from an isolated disk galaxy, or indicate tidal arms. However, comparing the observed line fluxes with those observed in low redshift interacting galaxies, shows that tidal arms would be too have too low surface fluxes in the optical line emission. For, e.g. the Antennae NGC4038/39 or NGC4438, typical $\text{H}\alpha$ surface fluxes are $\lesssim 7 \times 10^{-16}$ ergs $\text{cm}^{-2} \text{arcsec}^{-2}$ (see Boselli et al. 2005, for NGC4438, the Antennae surface brightness was measured from WFPC2 data kindly provided by S. Mengel). At redshifts ~ 2 these correspond to observed surface fluxes of $\mathcal{O}(10^{-22})$ ergs $\text{s}^{-1} \text{cm}^{-2} \text{arcsec}^{-2}$, too faint by several orders of magnitude. This neglects that these estimates are for the brightest patches, which extend over $\sim 1''$ in the nearby galaxies, but do not have the physical radii to extend over $1''$ the high redshift data, even accounting for the lensing and differences in the line fluxes of $[\text{OIII}]\lambda 5007$ (measured in 1E0657 core) and $\text{H}\alpha$ (measured in the comparison sample).

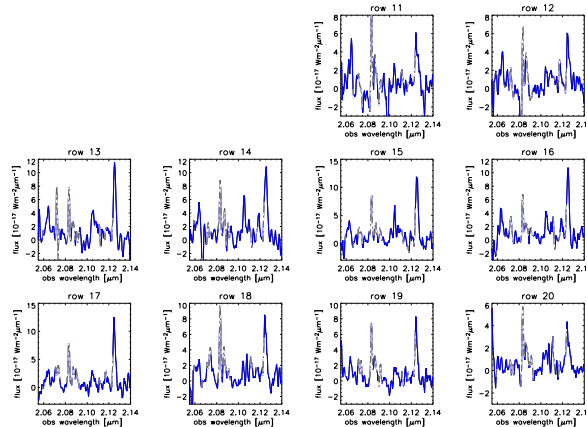


Fig. 9.— Spectra from which the relative velocities were extracted to derive the velocity curve shown in Fig. 10. Dotted lines indicated where the spectra are influenced by strong atmospheric line emission.

4. Discussion

4.1. Mass estimates of the arc core

1E0657 arc+core is a unique source. Its spatially resolved kinematics reveals monotonically decreasing velocities from South to North in the core within a high-resolution, spatially resolved zoom into the inner $\sim 1 - 2$ kpc. Although velocity gradients have been observed in other LBGs, their interpretation is difficult, mainly because the sizes of most of these sources barely exceed the FWHM of the seeing disk, so that spatially resolved *and uncorrelated* kinematic data points are difficult to obtain.

With the assumptions discussed in Section 3 of Chapter 4 and using Equation 4.1, a mass estimate

$$M_{disk} = 5.5 \times 10^8 M_{\odot} \quad (7.1)$$

follows, if the hypothesis that the velocity gradient originates from virialized motion in a disk is correct. A rotation velocity of half the overall velocity gradient was assumed (73 km s^{-1}) and half the observed extent over which [OIII] λ 5007 line emission could be traced ($2r = 2.3''$) corrected by a magnification $\mathcal{M} = 20$. Due to the unknown orientation of the source, the intrinsic value is likely a few times higher.

If, however, an isothermal sphere is a good approximation to the effective potential of 1E0657 core, just based on the line widths, and ignoring the velocity gradient, then the mass estimate would be

$$M_{sphere} = 2.3 \times 10^9 M_{\odot} \quad (7.2)$$

according to Equation 4.15 and accounting for the limitations discussed in Section 3 of Chapter 4.

An analogous approach to estimate the masses of LBGs was made by Pettini et al. (2001), who only had the [OIII] λ 5007 line width measurements to derive the average mass of their sample of 11(+3 additional) LBGs. With an average half-light radius of $\langle r \rangle_e = 0.3''$ (or 2.3 kpc), and average dispersion $\langle \sigma \rangle = 70 \text{ km s}^{-1}$, they find an average virial mass of $M_{pett} = 1.3 \times 10^{10} M_{\odot}$, about a factor 10 larger than what is found in 1E0657 arc. They conclude that, using Equation 4.14, they obtain similar masses with the disk hypothesis. For 1E0657 core this estimate translates into a mass of

$$M_{disk,sig} = 1.3 \times 10^9 M_{\odot} \quad (7.3)$$

Unlike the Pettini et al. (2001) sample however, the present data set of 1E0657 arc allows to directly compare these mass estimates. The major uncertainty, apart from the inclination and relative orientation of the lensing axis with respect to the kinematic major axis, is the half-light radius, which depends crucially on the exact magnification factor. Since all three mass estimates depend linearly on the radius, however, this will not affect the relationships between the different estimates. Indeed, the three measurements roughly agree, the largest uncertainty being again the unknown orientation of a rotating, virialized disk, which can easily amount to a factor of a few and reach the estimates based on the line widths within a factor of a few. In other words, the line widths of the integrated emission yield a fair estimate of the velocity gradient in this LBG, if no inclination can be measured, and if order-of-magnitude estimates are sufficient.

Stellar mass estimates derived from population synthesis fits to the rest-frame UV spectrum were presented in 2.2. The core has a stellar mass of $M_{stel} = 3.5 - 10 \times 10^9 M_{\odot}$ not correcting for lensing. With a magnification factor of $\mathcal{M} = 20$, the ratio of stellar to dynamical mass is of order $M_{stellar}/M_{dyn} \sim 0.3$.

But does the observed velocity gradient really represent a rotation curve? Seeing is the major source of correlation for ground-based observations, and the stretching induced by the gravitational lensing helps to at least partly overcome this limitation. The projected scale on the sky is $\sim 2.3''$, or

about 6 seeing disks, so that a set of uncorrelated data points can be extracted. Roughly speaking, data points originating from adjacent columns are correlated due to this beam-smearing effect, but all other data points are not. Nonetheless, the observed gradient is observed to be smooth within the uncertainties, so that it can be ruled out that the regular appearance comes from the seeing.

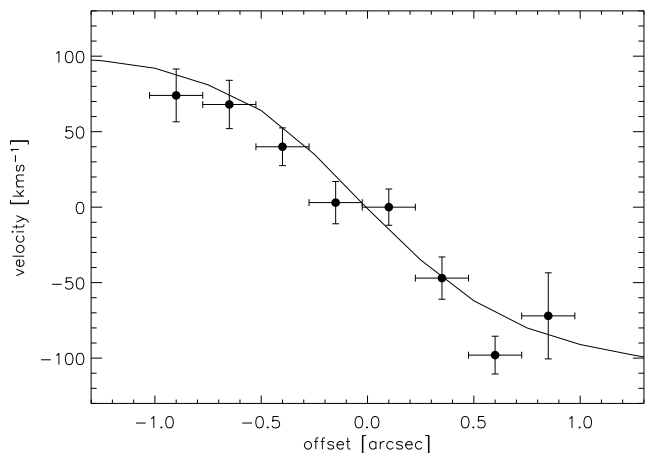


Fig. 10.— Velocity curve of the $[OIII]\lambda 5007$ emission lines in the E0657 core, assuming a magnification factor $\mathcal{M} = 20$ (black dots). The dark gray line shows the model fit of a $10^9 M_{\odot}$ edge-on exponential disk, assuming signal-to-noise ratios and spatial resolution as in the data cube.

A mass of $1 \times 10^9 M_{\odot}$ was found to be a good estimate. This neglects uncertainties due to the inclination and orientation of the rotation axis relative to the axis of magnification. On the other hand, it does take into account, e.g., the influence of the limited spatial and spectral resolution. Nonetheless, it still serves as a lower bound to the intrinsic mass, because both inclination and the position angle of the kinematic major axis with respect to the direction of maximum amplification cannot be determined independently.

The velocity curve is shown in Fig. 10, with the black dots indicating the measured data, while the dark grey line yields the input model curve. Blue upside-down triangles indicate the measured position-velocity curve of the simulated disk galaxy with the same characteristics as the data. Both distributions agree within the measured uncertainties.

Note the steeper slope of the input model. The flattening is a direct outcome of the seeing and coarse gridding. Hence, although the turnover points could not be identified directly, the slope of the distribution is in good agreement with the assumption that the velocity gradient originates from virialized rotation, traced out to just quite one disk scale length. It is also interesting that the total radius over which the line emission could be traced, is nearly identical for the simulated and the observed high-redshift galaxy. This shows that assuming an exponentially declining emission line surface brightness (at least on scales that can be spatially resolved) cannot be too far from the true distribution. This is in agreement with what is found for nearby disk galaxies (e.g., Freeman 1970).

Nonetheless, calling this gradient a rotation curve is somewhat premature, because it is rising linearly and does not show the characteristic turnover points very clearly. This might – in spite of the lensing – be simply due to the decreasing surface brightness of disks with increasing radius. To examine this assumption more quantitatively, the observed velocity gradient was compared with a simulated rotation curve, using the DYSMAL package kindly provided by R. Davies. The simplest dynamical assumption was made, which is an exponential disk with a constant mass-to-light ratio. The instrumental characteristics, such as spatial and spectral resolution, and the peak signal-to-noise ratio were adjusted to the data. The total enclosed mass was scaled such that the velocity difference between the measured and simulated maximum and minimum velocities match.

In a somewhat complementary approach, the measured velocity gradient can also be compared with the measured rotation curves of local disk galaxies. Rotation curves for a sample of ~ 30 nearby galaxies with high-resolution rotation curves obtained from combining CO, optical line emission, and HI-measurements are given, e.g. by Sofue & Rubin (2001). The envelope of their distribution was digitized and is shown in Fig. 11 together with the data points extracted from the core under the assumption of a magnification factor $\mathcal{M} = 5$ (red boxes), $\mathcal{M} = 10$ (black dots) and $\mathcal{M} = 20$ (blue upside-down triangles), respectively. The distance is flipped around the ordinate. All measured data were corrected by a factor $1/0.6$, which was found to approximate the influence of seeing and random inclinations for a statistical sample (Rix et al. 1997). Hence, this galaxy is assumed to show the typical “behavior”, i.e., average seeing and inclination. The observed values lie robustly within the measured range of local rotation curves, and this does not critically depend on the chosen magnification factor.

Not very surprisingly, the data fall within the lower range of the comparison sample. This adds even more credence to the assumption that the velocity gradient indeed traces only the inner parts of a rotation curve. Comparing the properties of rotation curves of nearby disk galaxies of different mass, Sofue & Rubin (2001) find that low-mass spiral galaxies tend have increasing rotation speeds out to larger radii (up to several kpc) than do the more massive galaxies. However, most galaxies, regardless of mass, appear to rise out to 500 pc and this rise corresponds roughly to the region of the bulge of the galaxy (Bender et al. 1992). Thus the lack of a turnover in the rotation curve may not be that surprising. More interesting perhaps is a comparison between the mass distributions of this LBG with nearby galaxies. Adopting a magnification factor of 20, the mass estimate of $10^9 M_\odot$ is appropriate for the inner ≈ 500 pc. This is very close to the typical dynamical mass estimate for a sample of Virgo cluster spiral galaxies from Sofue et al. (2003) for the inner 500 pc (which range from about 10^8 to $7 \times 10^9 M_\odot$).

Steidel et al. (1996) suggested that, based on the similarity of the co-moving densities of high redshift and local luminous ($L \gtrsim L^*$) galaxies, the high star-formation rates, and complex morphologies, that $z \approx 3$ LBGs represent the formation of the spheroidal component of massive galaxies. The dynamical measurements have some bearing on this issue. The enclosed mass within 500 pc is indeed similar to that found in typical $\approx L^*$ spiral galaxies. The scale of 500 pc is approximately the half light radius of a bulge of a nearby early type spiral galaxy (Bender et al. 1992). Given the similarity of the size and enclosed mass, this supports the conclusion of Steidel et al. (1996) that in fact LBGs could be the inner spheroid component during a period of rapid growth. More subtly, the agreement implies that perhaps the full mass was in place, just mostly in a gaseous phase and not a complete stellar bulge.

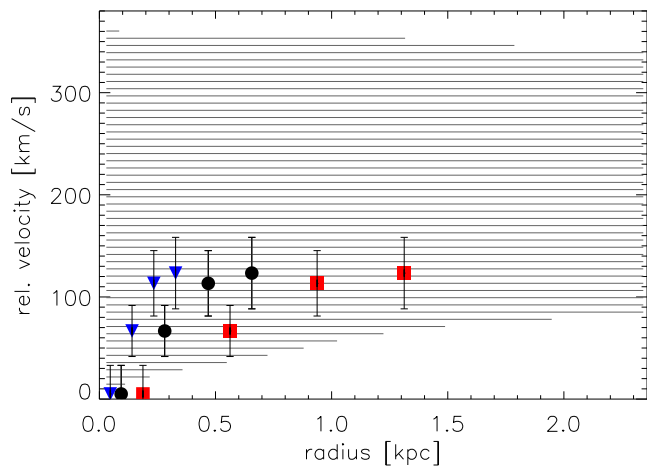


Fig. 11.— The hatched area shows the envelope to the rotation curves of local disk galaxies, blue upside-down triangles, black dots, and red squares indicate the rotation curve of 1E0657 core if the magnification factor is $\mathcal{M} = 20, 10, \text{ and } 5$, respectively.

4.2. Is the 1E0657 arc core galaxy typical for a LBG at $z \sim 3$?

As shown in Section 2, 1E0657-56 arc+core appears to be a rather unevolved Lyman-break galaxy. Although the rest-frame UV spectrum superficially resembles the composite (average) spectrum of 811 Lyman-break galaxies compiled by Shapley, Steidel, Pettini, & Adelberger (2003), it has a bluer spectral slope, probably a sign of lower extinction and age. This is in agreement with the best-fit age of 300 Myrs that Shapley, Steidel, Pettini, & Adelberger (2003) find for their average spectrum compared to the best-fit 50 – 110 Myrs of 1E0657 arc+core. Nonetheless, the rest-frame UV spectral fit of E0657 arc+core is based on parameters that are within the (not very well constrained) parameter range found within the Lyman-break population at $z \sim 3$ (see also Papovich et al. 2001). Rest-frame optical fluxes and line widths are rather typical (see also the detailed comparison of 1E0657 with the Pettini et al. (2001) sample in Tab. 1). Shapley et al. (2001) suggests that low-extinction, low-metallicity LBGs are rather young and unevolved. This is in excellent agreement with the comparably young age found in 1E0657 arc and core. In Section 2.3 it was also noted that it had a half-light radius rather similar to the general population of LBGs at $z \sim 3$. Thus in many ways, the 1E0657 arc core appear to lie within the range of typical characteristics of LBGs. But what about the results directly related to the SPIFFI data?

Table 1:: Comparison of 1E0657-56 arc core with the Pettini (2001) LBGs.

	1E0657 arc	1E0657 core	av. LBG	Q0256-000C17
z	3.24	3.24	3.13 ± 0.17	3.28
FWHM _[OIII]	160	182	173.5 ± 68	125
F(H β)	0.34 (all)		2.265 ± 1.19	≤ 0.45
W(H β)	$\gtrsim 33$		26.7 ± 11.3	≤ 8
Kab	20.5 (all)		22.0 ± 0.6	none
B	27.41	27.04	none	
g	23.49	23.1		
R	25.18	25.04	23.69 ± 0.33	23.89
I	24.74	24.36	none	
GminR	(B-R) 2.23	(B-R) 2.24	0.81 ± 0.24	0.27
blueshift	-330 (all)		-226 ± 291	+60
L1500	1.05 (lens.)	1.19 (lensed)	2.42 ± 0.69	2.3
SFR	10 (all)		38.7 ± 22.6	≤ 9
O/H	8.23-8.44 (all)		8.04-8.55	none

Physical properties of 1E0657 arc+core in comparison with the average LBG population and the particularly similar Q0256-000C17.

4.3. Comparison with star-formation rate

Interestingly, and again following the quartile division of the Shapley, Steidel, Pettini, & Adelberger (2003) sample, LBGs with strong Ly α absorption also have highest average star-formation rates compared to the other quartiles with weaker Ly α absorption and strong Ly α emission. The average star-formation rate is $\sim 100 M_{\odot} \text{ yr}^{-1}$ for the quartile of LBGs with the strongest Ly α

absorption. The arc and core, despite the strong Ly α absorption, are substantially below this rate.

There are several reasons why the arc+core might have a star-formation rate substantially below the typical LBG at similar redshifts. They are: (1) the galaxy could have an intrinsically lower star-formation rate compared to the typical LBG with strong Ly α absorption. For LBGs with strong Ly α absorption, the uncertainty in the mean value due to statistical sampling is only $5 M_{\odot} \text{ yr}^{-1}$. Thus the deviation of the arc and core is significant. (2) Another hypothesis is that only a part of a much larger galaxy is magnified, thus under-estimating the real total star-formation rate. (3) That the spectra originate from only one of the multiple images and thus only a fraction of the total flux is investigated. While it is difficult to make robust arguments as to which of these hypotheses is favored, there are circumstantial arguments to favor the first hypothesis.

The lensing model of 1E0657-56 indicates that the core is singly lensed and is magnified by a factor of 20. In addition, the best fitting model suggest that the arc is composed of multiply lensed images of the lower surface brightness material close to (at least one side) of the core (see Mehlert et al. 2001). In Section 2.3 it was argued that the arc and core are extended in the direction perpendicular to the direction of maximum stretching. The half-light radius of both the arc and core were consistent with that found in general for LBGs at $z \sim 3$. Unless there is also radial magnification, for which there is no independent evidence, then this would tend to favor the hypothesis that the whole source is magnified, not a small portion of it. The fact that the physical extension of the core as magnified into the arc is multiply lensed is more of a problem. Since that light is subdivided into multiple components, unless the whole arc is observed, the total flux is inevitable underestimated. However, this part of the lensed galaxy is more highly magnified and yet has significantly lower surface brightness and total flux. It is therefore likely not a strong contributor to the estimate of the total star-formation rate.

4.4. Mass-to-light ratio and the stellar population of the core

One of the most powerful constraints on the nature of the stellar population of a self-gravitating system is its mass to light ratio. The K-band spectrum allows to estimate the flux density at rest-frame B-band. From this flux density and the dynamical mass estimate, one can attempt to constrain the age of the stellar population of the arc core. Assuming an extinction of $E(B-V)=0.17$ magnitudes which is typical of LBGs with strong Ly α absorption (see Section 3.3 and Shapley, Steidel, Pettini, & Adelberger 2003), and $A_B=4 E(B-V)$, follows $M_{dyn}/L_B \approx 0.4 M_{\odot}/L_{\odot}$. To constrain the stellar population, it is necessary to compare this result with a stellar population model. For consistency, a similar set of models is adopted as was used to model the UV spectral shape. A ratio $0.4 M_{\odot}/L_{\odot}$ is consistent with an age of about 200 Myrs for a wide range of star-formation histories.

This result is important for a number of reasons. First, it adds credence to the suggestion that the core is a LBG. The estimated ratio is quite similar to that estimated for LBGs generally. Since there are additional dependancies on this estimate compared to those generally for LBGs, this is an important confirmation that properties like the magnification are probably not grossly wrong. However, the most significant reason is that it provides an independent constraint on the stellar population that only relies on a magnitude and the dynamical mass estimate. In this sense it is simpler that having to rely on modelling of the SED, although admittedly to quantify the age, it is necessary to use a stellar population synthesis model just as for the SED fitting. Finally, the result suggests that the measured kinematics are at least proportional to the dynamical mass of the galaxy. Since the ages derived from the mass-to-light ratio agree with what is estimated from

fitting the UV spectrum, it must imply that the dynamical mass estimates cannot be off by more than a factor of a few. This is entirely consistent with the uncertainty in the inclination and other geometric factors (like the extent to which the line emission probes the full gravitational potential, see e.g., Lehnert & Heckman 1996b).

4.5. Final evolutionary state of the core

Combining the star-formation rate and kinematic measurements, allows to estimate the dynamical time of the inner region of the 1E0657-56 “core”. Since orbital motion is observed, the dynamical time scale of the 1E0657-56 “core” follows from setting:

$$t_{dyn} = 2\pi R/V_{circ} = 30 V_{circ,100}^{-1} R_{0.5} \text{ Myrs} \quad (7.4)$$

where $V_{circ,100}$ is the circular velocity in units of 100 km s^{-1} and $R_{0.5}$ is the radius in units of 500 parsecs. For starbursts in local galaxies, it has been estimated that they have typical durations of $10^{7 \text{ to } 8}$ yrs or several dynamical timescales (e.g., Lehnert & Heckman 1996b; Kennicutt 1998; Förster Schreiber, Genzel, & Lutz 2003). Since generally speaking LBGs have properties similar to low redshift starburst galaxies (e.g., Meurer et al. 1997), it is not unreasonable to assume that the LBG phase will last for roughly a proportionally similar time. Of course, compared to the typical LBG, the 1E0657-56 “core” is a factor of 10 less massive but that is predominately due to the smaller radius over which the dynamics are sampled. Therefore, the typical dynamical time scale estimate for an unlensed LBG may be a factor of a few longer (larger radius and slightly higher average rotation speed, Shapley, Steidel, Pettini, & Adelberger 2003). This would suggest that the intense star-formation in the 1E0657-56 “core” will last for an additional few 100 Myrs but no longer. Of course, it may already be at the end of its intense star-formation episode – this dynamical estimate only puts a likely upper limit. A similar conclusion was reached by Shapley et al. (2001) based on multi-band optical through near-infrared imaging.

5. Summary and conclusions

An analysis of the UV spectrum, optical and near-infrared photometry, and 3-dimensional K-band (rest-frame optical) spectroscopy with SPIFFI of the high redshift “arc and core” lensed by the cluster 1E0657-56 was presented. This strongly lensed high redshift galaxy was found from this analysis (of both publicly available and the SPIFFI data), to be an excellent target for studying the fine spatial details of a $z \approx 3$ Lyman Break galaxy. The Lyman break nature of this source was argued for through the use of data from and the arguments in Mehlert et al. (2001). The SPIFFI data and results verify and extend this comparison. Its mass-to-light ratio and stellar age are within the range estimated for a general population of LBGs. A significantly lower star-formation rate was found than is typically estimated for LBGs. This can be explained however by only seeing the inner portion of the light distribution in only considering the core. However, this analysis does not suggest that is the correct hypothesis, instead favoring that the source is simply at the low end of the star-formation rate distribution.

Magnifying the inner region of a LBG at $z \approx 3$ has allowed valuable insights into the structure and nature of LBGs. The total mass within 500 pc is rather modest, only about $10^9 M_{\odot}$, and about a factor of 10 less than estimated by samples of unlensed LBGs. However, this mass is also typical for the inner regions of local $\approx L^*$ spiral galaxies. It may be that the inner regions of high redshift LBGs may have already substantially collapsed by $z \approx 3$ but are still gas rich and the stars in the

inner several 100 parsecs will form over the next several 100 Myrs, perhaps less. Thus the end product of this phase of evolution may be a galaxy with a substantial (majority?) fraction of its final mass within the inner 500 pc already in place. Does this suggest inside-out galaxy formation?

Table 2:: Emission lines in 1E0657 arc+ core

zone (1)	line (2)	λ_{rest} (3)	z (4)	λ_{obs} (5)	FWHM (6)	intr. FWHM (7)	flux (8)
total source	[OIII]	5007	3.2439±0.00005	2.1249±0.00011	26±2	229±21	20.038±0.6
total source	H β	4861	3.2453±0.00016	2.0637±0.00030	25±7	223±61	6.7±0.6
total arc	[OIII]	5007	3.2423±0.00013	2.1241±0.00026	23±6	146±37	4.3±0.4
total arc	H β	4861	3.2442±0.0007	2.0631±0.0013	35±34	423±413	1.7±0.4
arc core	[OIII]	5007	3.2446±0.00008	2.1253±0.0005	24±1	160±8	11.7±0.2
arc core	H β	4861	3.2449±0.00031	2.063 ±0.00020	31±4	182±18	4.7±0.2
arc 1	[OIII]	5007	3.2433±0.00012	2.1246±0.00008	32±2	61	6.4±0.1
arc 1	H β	4861	3.2460±0.00032	2.0640±0.00020	24±5	200±39	1.75±0.1
arc 2	[OIII]	5007	3.2427±0.00013	2.1243±0.00009	31±2	182	2.73±0.5
arc 2	H β	4861	3.2438±0.00033	2.0629±0.00021	37±5	182	1.48±0.4
arc 3	[OIII]	5007	3.2419±0.00013	2.1239±0.00008	16±1	182	1.9±0.09
arc 3	[OIII]	4959	3.2430±0.0009	2.1041±0.0009	17±10	182	0.54±0.14

Column (1) – Regions as defined in Figure 4. Column (2) – Line id. Column (3) – Rest-frame wavelengths in Å. Column (4) – Observed wavelengths in μm . Column (5) – Redshift of the line. Column (6) – Full-width at half-maximum measured in Å. A fiducial FWHM = 182 km s⁻¹ were adopted in the arc when individual line widths could not well be determined. Column (6) – Intrinsic FWHMs corrected for instrumental resolution units of km s⁻¹. Column (7) – Line fluxes in units of 10⁻²⁰ W m⁻².

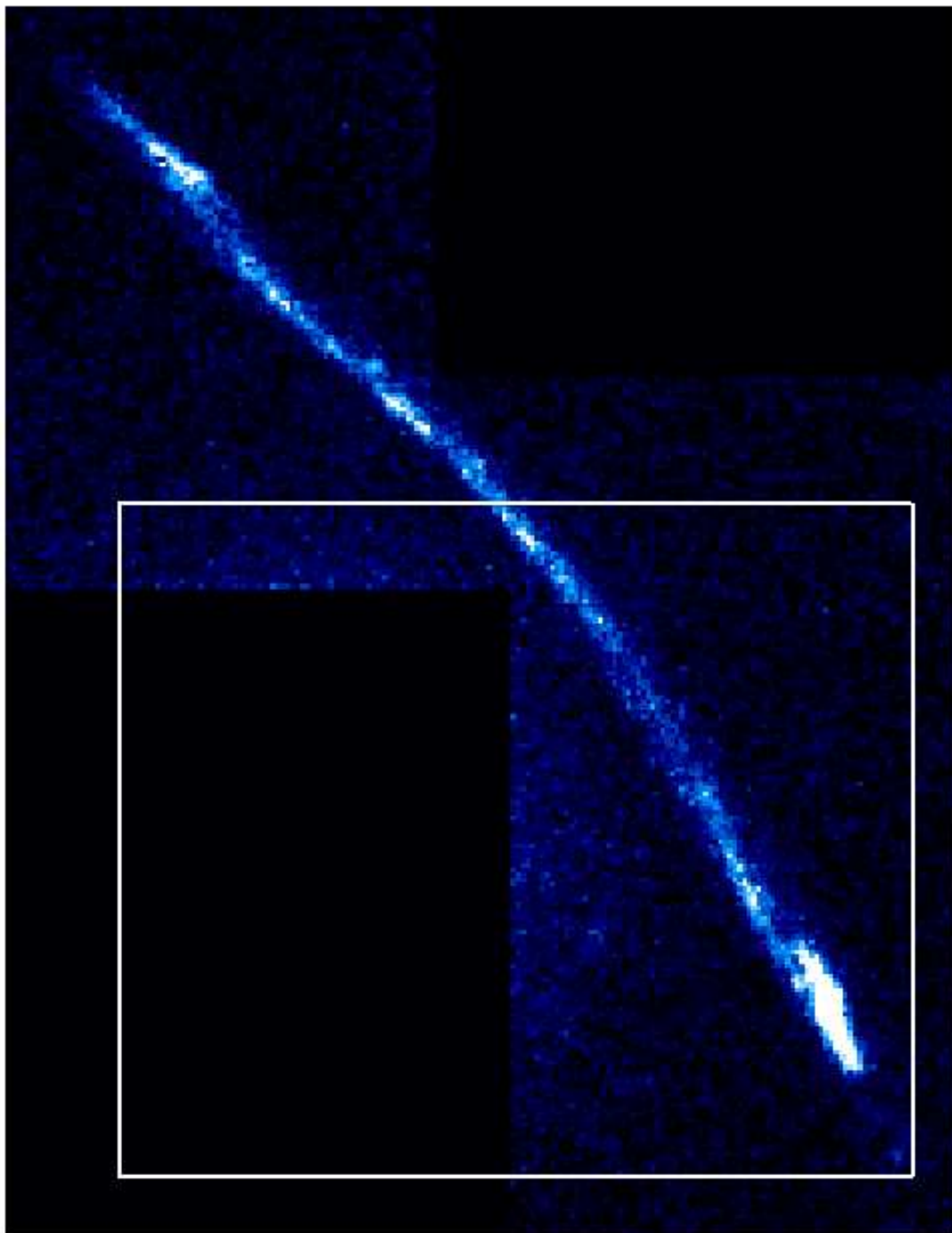


Fig. 12.— ACS $F814W$ image of the giant arc. The box indicates the SPIFFI field of view. Approximately half of the arc is within the SPIFFI field of view, although the central bright knot falls too close to the edge of the data cube and is strongly affected by residuals that could not be suppressed. The final FOV is rectangular rather than square because of the dither pattern used in obtaining the data.

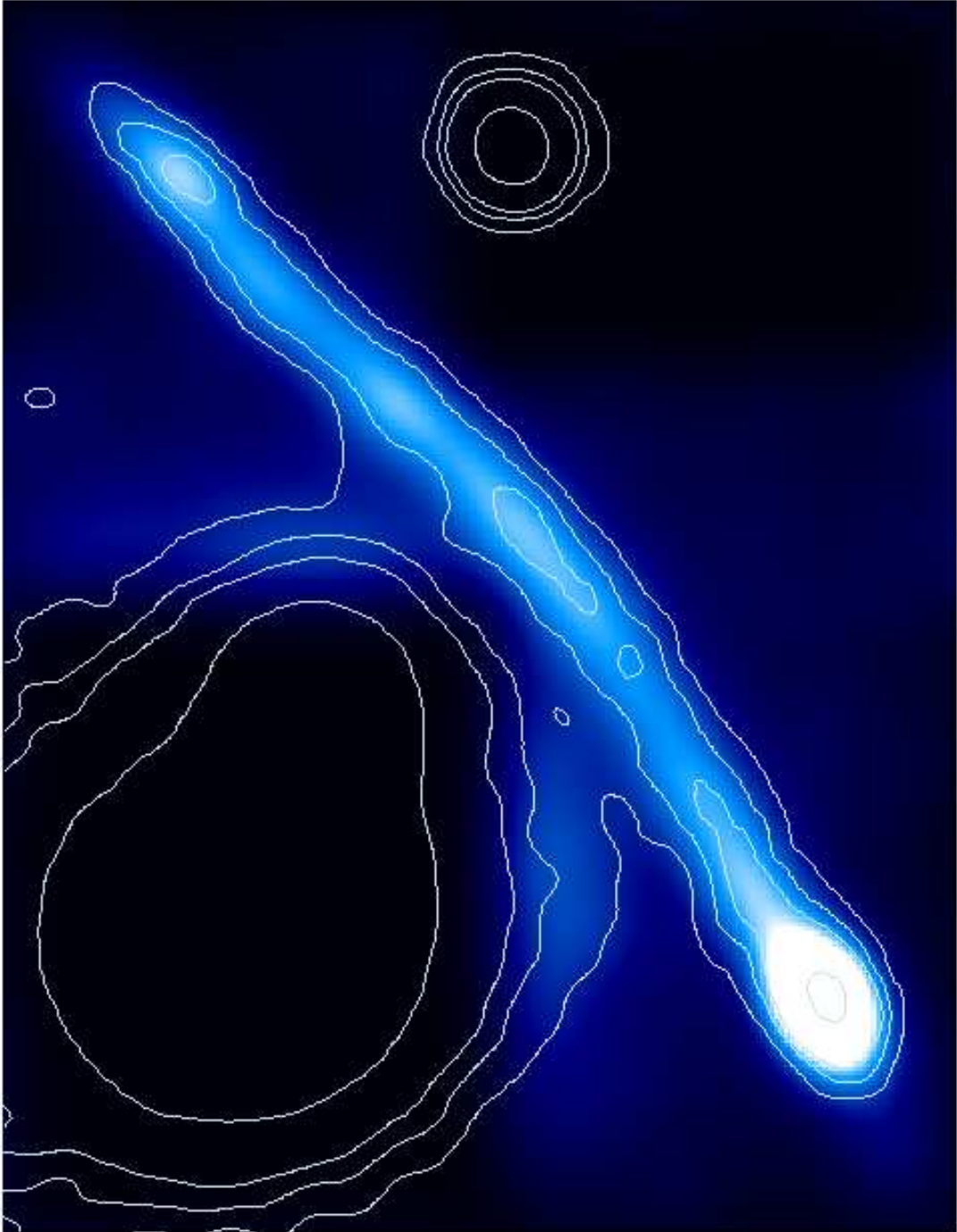


Fig. 13.— ACS $F814W$ image of the giant arc, smoothed to approximately match the PSF of the FORS R -band image (show in blue/white color palette), with the FORS R -band image shown as contours. Contour levels are shown as in Fig. 4. The original R -band image has been slightly smoothed to reduce the pixelation of the image and to facilitate a more robust comparison with the ACS image with has a much better sampling of the morphology of the arc.

Chapter 8

Dynamics of $z \sim 3$ Lyman-break galaxies

1. Introduction

UV-selected galaxies are probably the best studied galaxy population at redshifts $z > 2$. Almost 2500 galaxies have been identified by the Steidel et al. team alone, who pioneered the method (Steidel & Hamilton 1993), and they spectroscopically confirmed that 957 of these galaxies are at redshifts $z > 2$ (Shapley, Steidel, Pettini, & Adelberger 2003).

This chapter discusses the dynamics of three members of a subsample of these galaxies, the so-called Lyman Break Galaxies (LBGs) at $z \gtrsim 3$.¹ The Lyman discontinuity at rest-frame UV wavelengths marks the onset of the Lyman continuum in the SED and is further enhanced by the absorption of ionizing photons with wavelengths bluer than the hydrogen ionizing threshold (912 Å) in interstellar and intergalactic neutral hydrogen.

For certain redshift and filter combinations, this Lyman break will lead to characteristic colors. If the bluest band is blueward of the Lyman-break (or contains it), the galaxy will not or only marginally be detected in this band. In filters redward from the break, it will appear relatively gray, because the UV continuum of low-extinction galaxies is relatively flat. For $z \gtrsim 3$, the Lyman-break falls into the U band, therefore these galaxies are also referred to as “U-band drop-outs”. Namely, the Lyman-break selection requires

$$\mathcal{R} \leq 25.5 \tag{8.1}$$

$$G - \mathcal{R} \leq 1.2 \tag{8.2}$$

$$U_n - G \geq G - \mathcal{R} + 1 \tag{8.3}$$

employing a dedicated filter set in use at Keck. The limit on \mathcal{R} band magnitude is set to ensure that the sample is reasonably complete and bright enough for follow-up spectroscopy.

¹Results of studies of gravitationally lensed LBGs have been presented in the last chapter. The comparison of lensed and unlensed galaxies introduces considerable uncertainties, especially when dealing with strongly lensed targets where only a small part of the galaxy is being magnified, like, e.g., MS1512-cB58. For this reason, the discussion will now concentrate on the unlensed LBG population to give a framework for the subsequent analysis of three unlensed LBGs.

The technique is best suited to select galaxies with young stellar populations and low extinction, but will obviously miss heavily extinguished galaxies, such as SMGs, or galaxies which are dominated by old stars.

Typical half-light sizes of $z \sim 3$ LBGs are $0.3''$, or ~ 2.5 kpc (Giavalisco, Steidel, & Macchetto 1996). About 3% of this sample hosts optically evident AGN (Steidel et al. 2002), in agreement with CHANDRA X-ray measurements (Nandra et al. 2002). Possibly, a considerable fraction of LBGs does not host supermassive black holes (Hosokawa 2004).

The morphologies of LBGs are mostly irregular, not strongly changing with wavelength at observed optical and NIR bands (Giavalisco 2002). Many LBGs consist of several bright, compact knots embedded into diffuse nebulosities (Giavalisco 2002). Overall, they are rather spherical than elongated. It is not yet clear what the origin of this morphology is. Comparison with local galaxies suggests mergers (Giavalisco, Steidel, & Macchetto 1996), but it might also be that only the most strongly star-forming, brightest parts of these galaxies are observed, due to either extinction or low surface brightness of the underlying structure. Detailed studies of the kinematics of a large number of these sources would help elucidate their nature.

The Lyman break selection criterion is sufficiently broad so that LBG colors are quite inhomogeneous. They range from nearly flat SEDs across the rest-frame UV and optical wavebands to EROs (Shapley et al. 2001). $z \sim 3$ LBGs are more luminous than the local galaxy population. Nagamine (2002) find that the measured luminosities of $z \sim 3$ LBGs agree well with expected luminosities derived from hydrodynamical modelling of galaxy formation in a Λ CDM universe. However, they caution that the observed LBG population is probably only the luminous end of a larger and fainter population at that redshift.

Shapley et al. (2001) constrain the ages and evolutionary states from population synthesis modelling of the rest-frame UV/optical SEDs of 107 LBGs with measured K-band magnitudes, assuming constant star-formation. They find an average age of 320 Myrs and large scatter of $\sim 10 - 500$ Myrs. Star-formation rates are between 5 and $940 M_{\odot} \text{ yr}^{-1}$, with a median of $45 M_{\odot} \text{ yr}^{-1}$. In addition, they find a negative correlation between age and extinction, and a positive correlation between age and stellar mass, suggesting that younger galaxies are richer in dust. Based on these correlations, they propose an evolutionary sequence of LBGs, with the young objects being in an early phase of a strong ($200 M_{\odot} \text{ yr}^{-1}$) burst, producing dust that will later on be lost, so that they reappear in the sample when they are “old” LBGs with comparably moderate ($25 M_{\odot} \text{ yr}^{-1}$) star formation rates.

Shapley et al. (2001) find a characteristic stellar mass of $m_{star}^* \sim 1.2 \times 10^{10}$, and for 20% of the sample $m_{star} < 4 \times 10^9 M_{\odot}$. Similar values are found by Papovich et al. (2001) for 30 LBGs in the HDF-N², assuming continuous or declining star-formation rates. They caution that these masses could be underestimated by factors $\sim 3 - 8$ if older (and fainter) populations are present.

The photometric properties of LBGs beyond the UV rest-frame UV and optical range are not very well known. Barmby et al. (2004) have recently analyzed the SPITZER IRAC rest-frame near-infrared photometry of 16 spectroscopically confirmed $z \sim 3$ LBGs (and 22 candidates). Their analysis hints broad consistency between the rest-frame UV/optical SED fits and the near-infrared emission. This supports the view that these galaxies are not dominated by old stellar populations and that the rest-frame UV SEDs are representative for the stellar content of these galaxies.

Chapman et al. (2000) have tried to obtain submillimeter (rest-frame far-infrared) data of a

²Hubble Deep Field North

sample of 16 LBGs, and detected only one (West MMD11), which in turn is $5\times$ brighter than expected from the rest-frame UV flux and model SEDs. However, that source has several components, and the submillimeter emitter cannot uniquely be identified with the LBG.

Shapley, Steidel, Pettini, & Adelberger (2003) did a thorough study of the rest-frame UV spectra of 811 LBGs at $z \sim 3$. In their composite spectrum, they identify a wealth of absorption lines arising in stellar photospheres, stellar winds, and the ISM. They find a blueshift of on average 650 km s^{-1} between the stars and the ISM absorption lines, indicating that large scale outflows (galactic winds) are a common feature in this class of objects. In addition, they explicitly show that nebular emission lines originating from HII regions (including the hydrogen Balmer lines and [OIII]) are at rest with respect to the photospheric (stellar) lines. This is very important for the subsequent analyses, because [OIII] emission lines will be used to trace the bulk kinematics of the galaxy.

Metallicities cannot be inferred from the rest-frame UV absorption lines, because the lines are saturated. Therefore Pettini et al. (2001) have obtained rest-frame optical spectroscopy of 13 LBGs, and measured R_{23} in 5 sources. Oxygen abundances cannot very tightly be constrained, but values exceeding the solar value are excluded. [OIII] line widths indicate dynamical masses $\sim 10^{10} M_{\odot}$, if the broadening comes from large-scale virialized motion. This assumption cannot be tested with longslit spectroscopy and has large inherent observational uncertainties. This is why integral-field data are particularly valuable (see Chapter 2).

This thesis includes a small sample of 3 LBGs at redshifts $z \gtrsim 3$. Another, serendipitously included LBG at a slightly lower redshift is SMMJ14011+0252 J2, discussed in the context of the physically related submillimeter bright companion J1 (section 3). J2 and the strongly lensed LBG 1E0657 arc+core will be included in the overall discussion at the end of this chapter.

At redshifts $z \sim 3$ the strong nebular emission lines $H\beta$ and [OIII] $\lambda\lambda 4959,5007$ fall into the K-band, and are used for the subsequent analyses. [OII] $\lambda\lambda 3726,3729$ fall into the H-band, but no H-band data were taken. This analysis continues and extends the work of Pettini et al. (2001), who found spatially resolved velocity shears for 2 galaxies. All targets are taken from their sample.

2. Q0347-383 C5

The $z = 3.23$ Lyman-break galaxy Q0347-383 C5³ is among the largest sources of this population and has a very irregular morphology. This is best seen in the WFPC2 F702W imaging that was obtained from the HST archive and reduced for this thesis (see Fig. 1).

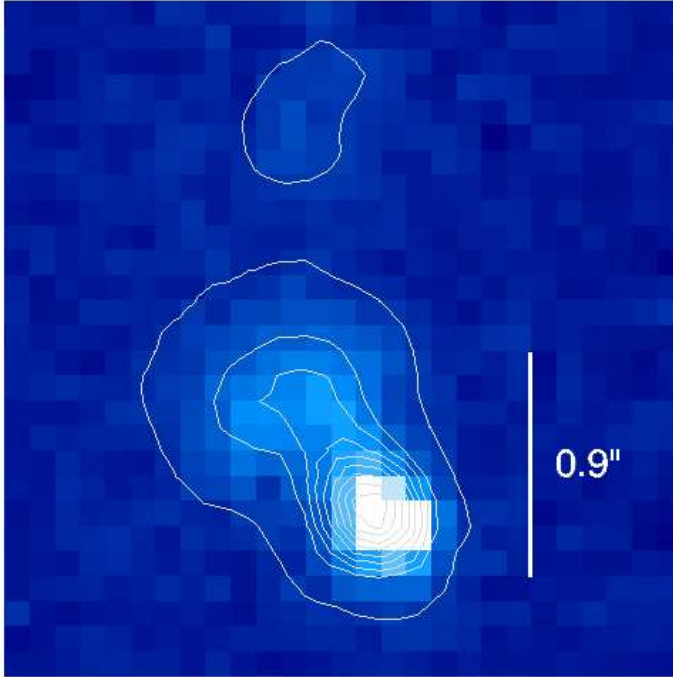


Fig. 1.— WFPC2-F702W image of Q0347-383 C5. The contours indicate the significance of the emission in steps of 3σ , starting at 3σ .

using ISAAC on the VLT-UT1. They detected prominent [OIII] lines and placed a 3σ -limit on $H\beta$ of $F_{H\beta} < 1.7 \times 10^{-17} \text{ erg s}^{-1} \text{ cm}^{-2}$. At the redshift of Q0347-383 C5, $H\beta$ falls at the wavelength of an atmospheric absorption band and is therefore very difficult to measure.

Q0347-383 C5 is one of two sources for which Pettini et al. (2001) found extended line emission and a spectral tilt indicating an intrinsic velocity shear of $\sim 70 \text{ km s}^{-1}$. This and the peculiar – and rather large – morphology make Q0347-383 C5 a very tempting target for deep follow-up observations using SINFONI.

K-band data were taken on December 20, 2004, using the SINFONI-GTO instrument and the 2nd engineering grade detector. At $z = 3.23$, the K-band bandpass corresponds to rest-frame wavelengths of $\sim 4700 \text{ \AA} - 5600 \text{ \AA}$, so that it covers $H\beta$ and the [OIII] $\lambda\lambda 4959, 5007$ doublet. The pixel scale is $0.125'' \text{ pix}^{-1}$, the spectral resolution was measured from night-sky lines and is 103.4 km s^{-1} . Total on-source exposure time was 4 hours, under very good and stable conditions. The seeing was carefully monitored during observations, with exposures of stars at similar position and air mass as the source taken every hour. The effective seeing disk of the combined cube is

³Using the flat $\Omega_\Lambda = 0.7$ cosmology with $H_0 = 70 \text{ km s}^{-1} \text{ Mpc}^{-1}$ leads to $D_L = 28.3 \text{ Gpc}$ and $D_A = 1.54 \text{ Gpc}$. The size scale is $7.48 \text{ kpc}''$. The age of the universe with this redshift and cosmological model is 1.9 Gyrs.

The brightest emission comes from a compact, marginally resolved knot, which has an intrinsic size of $0.13'' \times 0.18''$ ($0.97 \times 1.49 \text{ kpc}$). The size of the seeing disk ($0.1'' \times 0.1''$), which is used for deconvolution of the observed sizes, was determined from a nearby star on the same chip. The knot is separated by $\sim 0.6''$ (4.5 kpc) to the south from a more diffuse, elongated object. Between these two components, and partly overlapping with the fainter, diffuse object, extends an elongated, very thin structure, with a length of ~ 5 pixels (3.7 kpc) and unresolved across. About $1.6''$ (12 kpc) to the north-west from the brightest knot is another very diffuse source, that is marginally detected in the WFPC2 image (at $\sim 3\sigma$ per pixel). At $z = 3.23$, the F702W bandpass corresponds to rest-frame wavelengths of $\sim 2000 \text{ \AA}$.

Pettini et al. (2001) have obtained K-band longslit spectra of Q0347-383 C5

$0.55'' \pm 0.05'' \times 0.49'' \pm 0.04''$ in right ascension and declination, respectively. Uncertainties indicate the r.m.s. scatter between the FWHMs of the individually measured seeing disks.

2.1. Emission line morphology and spectral analysis

The spatial distribution of the [OIII] λ 5007 line emission is shown in Fig. 2. The image includes wavelengths of ± 1 FWHM around the peak integrated emission, and was obtained with the method described in Chapter 4. Contours indicate the expected flux distribution of two unresolved point-sources placed at the location of brightest line emission, and convolved with a two-dimensional Gaussian with FWHMs matching the seeing disk. The comparison is highly suggestive that [OIII] λ 5007 comes from two separated, unresolved line emitters at a distance $d_{proj} \sim 0.7''$ or 5.3 kpc. Limits on their size are set by the seeing disk. At 3σ , the radii are $< 2.7 \text{ kpc} \times 2.3 \text{ kpc}$ in right ascension and declination, respectively. The diffuse, faint source to the north was not detected.

It is difficult to accurately align the SINFONI and WFPC2 data, because of the small source size and different morphologies. The absolute astrometric uncertainty of the WFPC2 data set is $\sim 1''$ (Biretta et al. 2001), and the positional uncertainty of UT4 / SINFONI is difficult to estimate, but probably in the same range. The K-band continuum emission is too weak to be detected at a significant level, let alone to use it for the alignment. Using the pixel scales from the header information and shifting the southern [OIII] peak to the position of the bright knot in the WFPC2 image shows that the second [OIII] knot plausibly arises from the diffuse object, but a more precise statement cannot be made. The WFPC2 image and [OIII] contours are shown in Fig. 3.

The integrated spectrum of Q0347-383 C5 is shown in Fig. 4. The spectrum was integrated by summing over all spatial pixels in which the [OIII] λ 5007 emission exceeds 3σ . The redshift is $z = 3.2347 \pm 0.00065$. [OIII] λ 5007 is very prominent, but also [OIII] λ 4959 and $H\beta$ are detected with significances of 12σ and 5σ , respectively. Pettini et al. (2001) did not detect $H\beta$, but could only place an upper limit on the flux. Hence this is the first detection of $H\beta$ in this source. The flux is $F_{H\beta} = 8.76 \times 10^{-18} \text{ Wm}^{-2}$, the [OIII]/ $H\beta$ ratio is $[OIII]_{5007}/H\beta = 7.2 \pm 1.5$. Line widths are $\text{FWHM}_{5007} = 180 \pm 9 \text{ km s}^{-1}$ for [OIII] λ 5007 and $\text{FWHM}_{H\beta} = 69 \pm 11 \text{ km s}^{-1}$ for $H\beta$. The smaller $H\beta$ line width is probably due to its unlucky wavelength with respect to the telluric

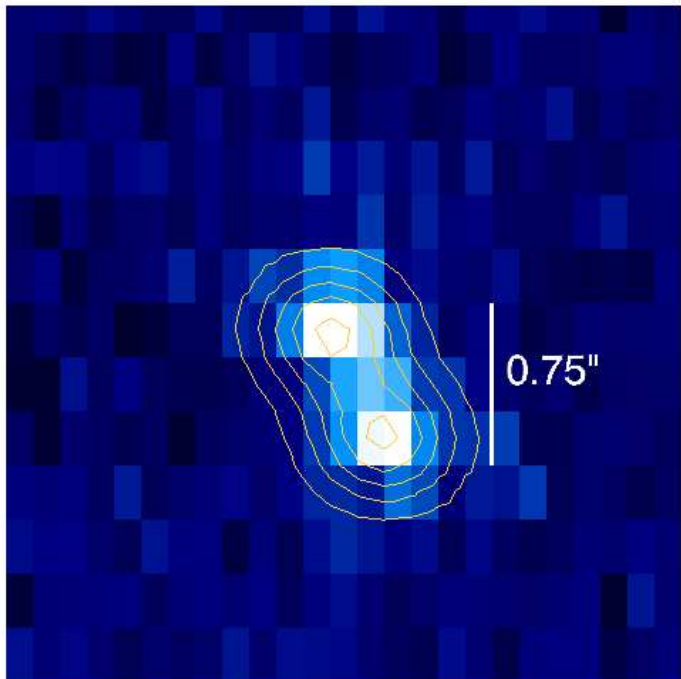


Fig. 2.— [OIII] λ 5007 line image of Q0347-383 C5. The contours show the expected morphology of two point sources at the position of the two bright knots under the influence of the seeing.

absorption. Intrinsic $H\beta$ fluxes might therefore be ~ 2.6 times higher. Emission line properties are summarized in Table 2.2.

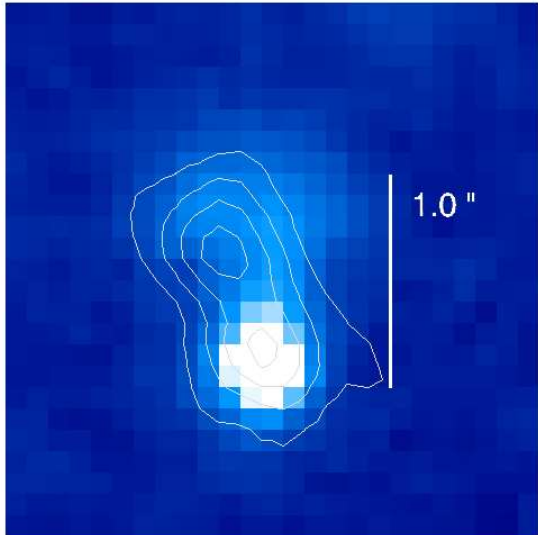


Fig. 3.— WFC2-F702W image of Q0347-383 C5. The contours indicate the spatial distribution of $[OIII]\lambda 5007$ line emission.

uncertainty. The red and blue line indicate the calibration curves for the lowest and highest possible ionizations, derived from the correlation between $\log[OII]/H\beta$ and $\log[OIII]/H\beta$ in Kobulnicky et al. (1998). Oxygen abundances range between 8.6 and 7.9. With respect to the solar oxygen abundance given by Allende Prieto, Lambert, & Asplund (2001), the oxygen abundance in Q0347-383 C5 is at least 0.09 dex lower, and 0.3 dex lower if the measured fluxes are taken at face value completed by the best-fit $[OII]$ estimate.

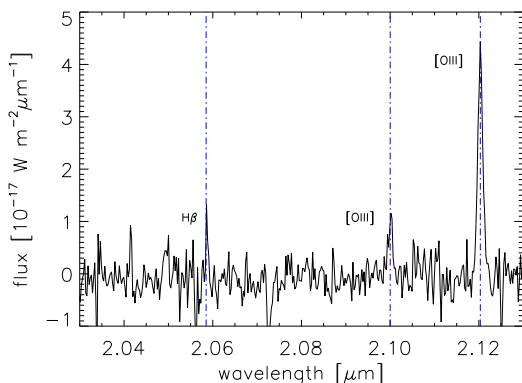


Fig. 4.— K-band spectrum of Q0347-383 C5. Blue dot-dashed vertical lines indicate the expected emission line positions.

An integrated K-band spectrum of this source has previously been obtained by Pettini et al. (2001). They measured an $[OIII]\lambda 5007$ flux of $F_{5007} = 7.2 \times 10^{-20} \text{ Wm}^{-2}$ at a redshift of $z = 3.2337$ and a line width of $\text{FWHM}_{5007} = 162 \pm 10 \text{ km s}^{-1}$. All values agree with the new SINFONI measurements. $H\beta$ was not detected by Pettini et al. (2001).

The integrated spectrum is also used for an overall R_{23} metallicity estimate of Q0347-383 C5. $[OII]$ is not measured, because it does not fall into the K band for $z = 3.23$. However, the $[OII]$ flux can be estimated using the method described in Section 1.2. With the measured uncertainties and the $\log([OII]/H\beta) = 0.4$ suggested by Kobulnicky et al. (1998) for low-metallicity galaxies and the observed $[OIII]/H\beta$ ratio, $R_{23} = 1.05$, or $R_{23} = 0.95$, if only the measured $[OIII]$ and $H\beta$ fluxes are used.

The green vertical bar in Fig. 5 indicates the metallicity range for these parameters. The lower bound, $R_{23} > 0.87$, is given for only the measured line fluxes and allowing for 1σ uncertainty.

The large signal-to-noise ratios and clear separation of the two knots make it very interesting to compare the spectra of the two knots. For the following discussion, the northern knot will be referred to as component A, and the southern knot as component B. Close-ups on the $[OIII]$ lines of the two spectra are shown in Fig. 6. The blue and red spectrum indicates component A and B, respectively. The relative spectral offset between the two spectra is obvious in both lines of the $[OIII]$ doublet, and is $\Delta v = 33 \pm 13 \text{ km s}^{-1}$, significant to 2.5σ . The emission line properties of Q0347-383 C5 are summarized in Table 2.2.

$H\beta$ is detected in both components, with fluxes of $F_{H\beta,A} = 6.6 \pm 1.8 \times 10^{-21} \text{ Wm}^{-2}$ and $F_{H\beta,B} = 5.7 \pm 1.8 \times 10^{-21} \text{ Wm}^{-2}$ in knot A and B, respectively. This allows to estimate star-formation rates in the two knots, using equation 4.9 and adopting a Balmer

decrement $H\alpha/H\beta = 2.86$. This value implies that extinction in Q0347-383 C5 is negligible.

Taking the measured $H\beta$ fluxes at face value, star-formation rates are $SFR(A) = 14 M_\odot$ and $SFR(B) = 12 M_\odot$ for components A and B, respectively. These rates should be viewed as lower limits. Intrinsic $H\beta$ fluxes might be factors of a few higher, because of extinction. Shapley et al. (2001) found for their LBG sample $E(B-V) = 0.2-0.4$, indicating that intrinsic fluxes might be factors 1.6 – 3 higher (for a galactic extinction law). Extinction corrected rates are therefore probably $SFR(A) = 19 - 36 M_\odot$ and $SFR(B) = 22 - 42 M_\odot$ for component A and B, respectively. In addition, the $H\beta$ line width is more narrow than those of $[OIII]\lambda 5007$. If this is due to the difficult observed spectral position of $H\beta$ with respect to the night sky lines and is not intrinsic, then the true star-formation rates will be accordingly higher.

The excellent quality of this data set allows to extract the spectral information even from smaller apertures. To map the velocity and dispersion fields, the $[OIII]\lambda 5007$ spectral lines were extracted from 3×3 pixel apertures ($0.375'' \times 0.375''$), which is still below the seeing disk. In addition, the spectra were smoothed over 3 pixel along the spectral axis. The result is shown in Fig. 7. Typical uncertainties are $\sim 20 \text{ km s}^{-1}$ in both maps. Velocities between the two components are significantly different, and do not vary smoothly, but abruptly near the mid point between the knots. FWHM line widths are overall rather similar, and marginally lower in the northern component. Towards north-west, lines are spectrally not resolved.

2.2. Q0347-383 C5 – A merging galaxy pair at $z=3.3$

Morphology and spatially-resolved kinematic properties of Q0347-383 C5 suggest that it is not an isolated galaxy, but a pair of two nearby, physically related and maybe interacting companions. The ratio of circular velocity v and dispersion σ can be used as a rough stability criterion if the line emission arises from two patches on a galactic disk (with inclination angle $i \sim 70^\circ$):

$$\frac{v/\sin i}{\sigma} \lesssim 0.5 \quad (8.4)$$

$v/\sigma \ll 1$, which indicates that random motions dominate over the bulk motion. This means that a disk-like configuration of the line-emitting gas would not be stable.

A similar result is found from the spatially-resolved velocity and width maps. A rotating disk would result in a smooth velocity gradient, would be dynamically hotter in the center (with larger

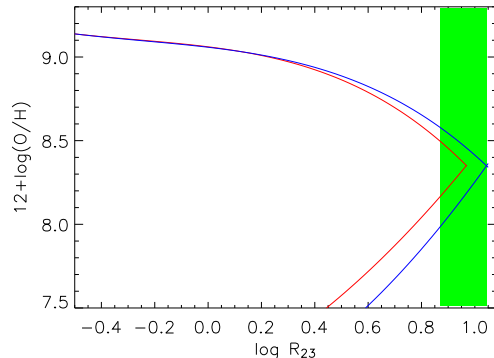


Fig. 5.— Oxygen abundance of Q0347-383 C5 as function of R_{23} .

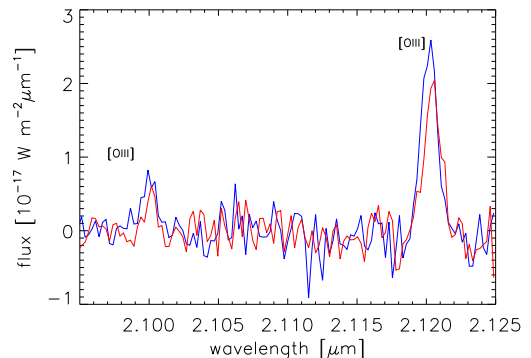


Fig. 6.— $[OIII]$ emission lines of component A (red) and B (blue).

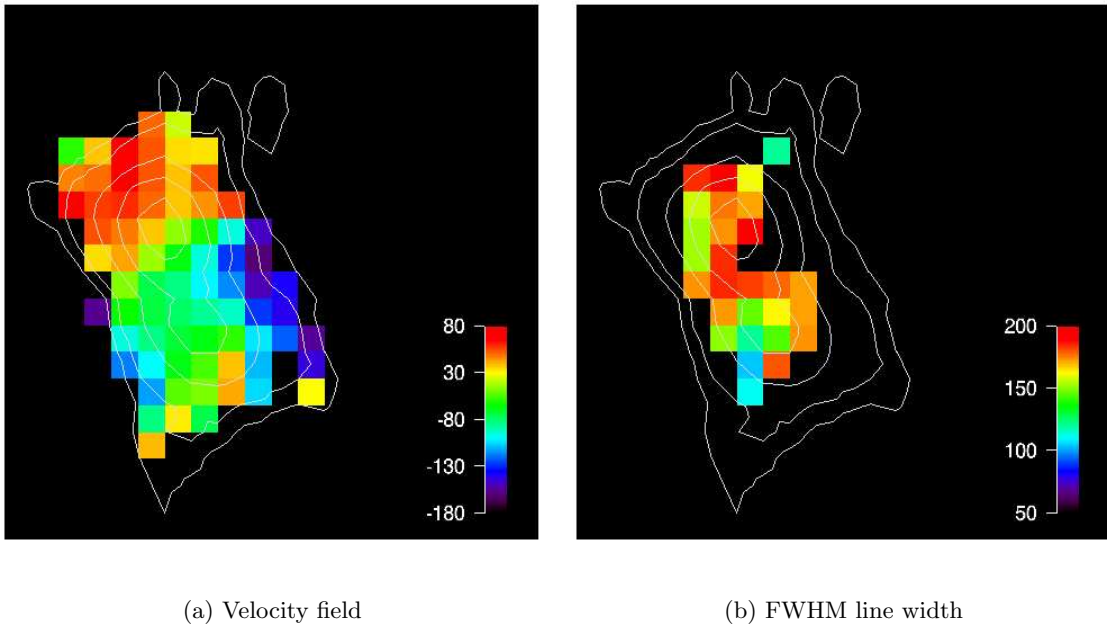


Fig. 7.— *Velocity and FWHM maps of Q0347-383 C5. The color bars yield the velocity and FWHM in km s^{-1} , respectively. Contours yield the [OIII] flux distribution.*

line widths), and cold outside along the disk. This behavior is not observed in the kinematic maps shown in Fig. 7, which rather suggest a sudden step in the velocity distribution roughly in the middle between the two knots, and only a marginal increase in line width in the center, but again different values in the two knots. These are the expected kinematic patterns of two nearby, not spatially resolved knots with a relative velocity shift.

Pettini et al. (2001) previously suggested that the peculiar morphology of Q0347-383 C5 might come from a wind triggered by high star-formation rates. However, such winds, when observed at low redshift and in more detail, usually have low surface brightness (Lehnert & Heckman 1996b), which makes them difficult to observe directly at high redshift. In the light of the new, spatially-resolved SINFONI data, the more likely scenario is that the faint, extended emission comes from a separate galaxy, which might have more extended continuum emission than the compact source. This is also supported by the similar [OIII]/ $H\beta$ ratios in the two knots. If parts of the source were a wind, then the line ratios should be different, due to shock excitation.

Could the compact source be an AGN? This appears unlikely, because it is marginally spatially resolved, and because of the relatively narrow [OIII] emission lines. [OIII]/ $H\beta$ ratios are high, but not atypical for low-metallicity, star-forming galaxies. In addition, the spectra of both components are rather similar, making it unlikely that the compact knot is dominated by an AGN. The AGN contamination of the LBG sample is rather low: Steidel et al. (2003) estimate that a fraction of 3% of all LBGs harbor AGN.

The properties of the two sources are not very different. The line emission is rather similar in both knots, with similar individual line fluxes and [OIII]/ $H\alpha$ ratios (within the uncertainties), star-formation rates and line widths. Both line-emitting regions are unresolved in the seeing-limited SINFONI data, suggesting their radii are ≤ 2.5 kpc.

Under these circumstances, the line widths are particularly interesting, because, given that

neither of the knots is spatially resolved, but both have spectrally resolved emission lines, they are the only available dynamical tracers for the mass of the two companions.

The radial distributions of the line-emitting gas in the two galaxies are obviously also not known. Therefore mass estimates will be given for the assumption that the gas is arranged in an isothermal sphere, and also for a flat distribution like in disk-galaxies. The 3σ estimate $r \sim 2.5$ kpc on the size of the line emitting region constrains the radius, which will yield upper limits to the mass. Velocity dispersions are $\sigma_A = 88 \pm 3$ km s⁻¹ and $\sigma_B = 77 \pm 3$ km s⁻¹ for components A and B, respectively. The dispersions differ by 2.6σ .

Using equations 4.14 and 4.15 yields mass estimates of

$$M_{disk} = 9.6 \times 10^9 M_\odot \quad (1.3 \times 10^{10} M_\odot) \quad (8.5)$$

$$M_{bulge} = 1.7 \times 10^{10} M_\odot \quad (2.3 \times 10^{10} M_\odot) \quad (8.6)$$

for component A (component B) and the disk and bulge hypothesis, respectively.

What will be the further evolution of this object? As previously discussed in Chapter 5, galaxy pairs with relative velocities smaller than their internal shear will coalesce within a few orbital time scales (e.g., Mihos, Richstone, & Bothun 1992). In this scenario, the orbital parameters can obviously not be deduced from morphological constraints, so that estimates can only be very rough.

The similar line widths and luminosities of the two line emitting knots suggest that both components have roughly equal masses, so the barycenter is placed near the midpoint of the two components. Using the projected distance to estimate the size of their orbits and the measured relative velocity offset v between them yields an orbital time-scale:

$$\tau_{orb} = \frac{\pi D_{A,B}}{v} = 5 \times 10^8 \text{ yrs} \quad (8.7)$$

where $D_{A,B}$ is the projected distance between the sources. This time scale is uncertain by factors of ~ 3 , due to the unknown inclination. The two components will most likely coalesce within a few dynamical time scales. In the adopted cosmology this corresponds to redshifts $\gtrsim 2$.

Table 1:: Emission lines in Q0347-383 C5

zone (1)	ID (2)	λ_0 (3)	z (4)	λ_z (5)	$FWHM_{obs}$ (6)	$FWHM_0$ (7)	flux (8)
total	[OIII]	5007	3.2347 ± 0.00032	2.1203 ± 0.00014	14 ± 1	180 ± 9	6.32 ± 0.26
total	[OIII]	4959	3.2348 ± 0.00024	2.1000 ± 0.00015	13 ± 2	167 ± 19	1.53 ± 0.22
total	H β	4861	3.2351 ± 0.00023	2.0587 ± 0.00015	8 ± 1	68 ± 11	0.88 ± 0.18
comp A	[OIII]	5007	3.2345 ± 0.00022	2.1202 ± 0.00014	14 ± 1	180 ± 8	3.94 ± 0.18
comp A	[OIII]	4959	3.2347 ± 0.00024	2.1000 ± 0.00016	14 ± 2	175 ± 21	1.02 ± 0.16
comp A	H β	4861	3.2353 ± 0.00023	2.0588 ± 0.00014	7 ± 1	35 ± 8	0.57 ± 0.12
comp B	[OIII]	5007	3.2350 ± 0.00022	2.1204 ± 0.00014	16 ± 1	207 ± 9	3.42 ± 0.18
comp B	[OIII]	4959	3.2349 ± 0.00024	2.1001 ± 0.00016	11 ± 1	136 ± 19	0.78 ± 0.14
comp B	H β	4861	3.2347 ± 0.00023	2.0585 ± 0.00015	8 ± 1	75 ± 10	0.66 ± 0.12

(1) location – (2) line ID. – (3) rest-frame wavelength in Å – (4) observed wavelength in μm . – (5) redshift – (6) measured $FWHM_{obs}$ in Å. – (7) intrinsic (deconvolved) FWHM in kms – (8) integrated line flux in 10^{-20} Wm^{-2}

3. Q0201+113 C6

Q0201+113 C6 at a redshift of $z = 3.055$ is one of the fainter sources in the Pettini et al. (2001) sample⁴. Using ISAAC on VLT-UT1, Pettini et al. (2001) measured an [OIII] $\lambda 5007\text{\AA}$ line flux $F_{[\text{OIII}]}$ = $4.3 \times 10^{-20} \text{ Wm}^{-2}$, and an H β flux of $F_{\text{H}\beta}$ = $(1.0 \pm 0.4) \times 10^{-20} \text{ Wm}^{-2}$, corresponding to a star-formation rate of $27 \text{ M}_{\odot}\text{yr}^{-1}$. Shapley et al. (2001) used Bruzual & Charlot (2003) population synthesis models to the rest-frame UV and optical photometric data and found the best agreement for a 3.2×10^8 yrs old population with $E(B-V) = 0.08$, undergoing a burst with a constant star-formation rate $SFR = 23 \text{ M}_{\odot}\text{yr}^{-1}$ and a stellar mass $M_{\text{star}} = 8 \times 10^9 \text{ M}_{\odot}$.

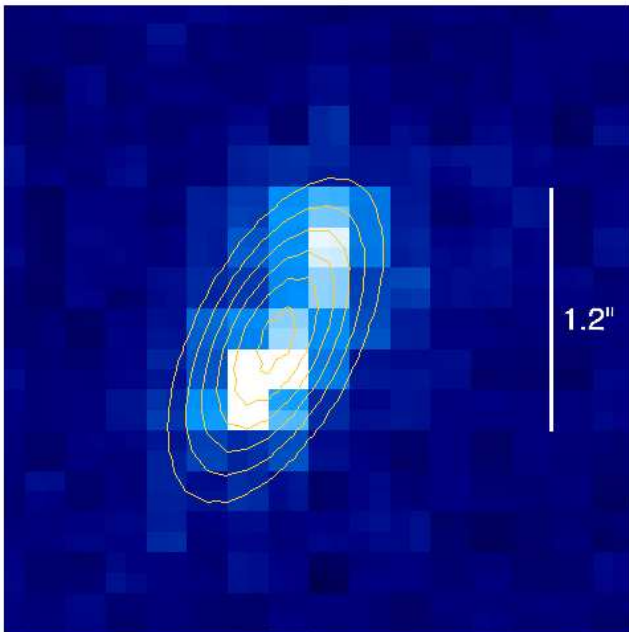


Fig. 8.— WFC2 *F606W* image of Q0201+113 C6. Contours indicate the best-fit Gaussian ellipse to the flux distribution.

Q0201+113 C6 an interesting target for detailed SINFONI follow-up observations. Data were taken on December 21, 2004 as part of the GTO-SINS program, and under not very favorable conditions. The seeing was about equal to the source size ($0.75'' \times 0.79''$) and air masses were near $\sec(z) = 2$. Accordingly, only 70 minutes of data were taken, but during the ongoing SINS program, this data set might be completed.

3.1. Results

In spite of the mediocre conditions, the source is clearly detected in the [OIII] $\lambda 5007\text{\AA}$ line image (see Fig. 10), and also in the integrated spectrum (Fig. 9).

WFC2 *F606W* imaging of Q0201+113 C6 was obtained from the HST archive and reduced for this thesis. The source appears elongated and has an irregular flux distribution with two peaks, separated by $\sim 0.7''$ or at a physical distance of ~ 5.4 kpc. The image is shown in Fig. 3. Contours indicate the best two-dimensional Gaussian fit, with FWHMs of 5.84×12.73 pixels in right ascension and declination, respectively. The spatial resolution was measured from a star within the WFC2 image, and is 4.8×4.5 pixels. This indicates that the source is spatially resolved in both directions, and its intrinsic size is 3.7×12.9 pixels ($0.33'' \times 1.2''$ or 2.5×9.2 kpc). If the source intrinsically has a disk-like morphology, then the axis ratio taken at face value yields an inclination $i = \arccos(a_{\text{min}}/a_{\text{maj}}) \sim 75^\circ$.

The comparably large line width measured by Pettini et al. (2001) (FWHM = $151 \pm 10 \text{ km s}^{-1}$) and the availability of high-resolution HST imaging make

⁴Using the flat $\Omega_{\Lambda} = 0.7$ cosmology with $H_0 = 70 \text{ km s}^{-1} \text{ Mpc}^{-1}$ leads to $D_L = 25.984 \text{ Gpc}$ and $D_A = 1.580 \text{ Mpc}$. The size scale is $7.66 \text{ kpc}''$. The age of the Universe with this redshift and cosmological model is 2.07 Gyrs .

Other lines are too faint to be significantly detected in 70 minutes. An integrated flux of $F_{[\text{OIII}]} = 3.3 \times 10^{-20} \pm 0.3 \text{ W m}^{-2}$ was measured with SINFONI, in agreement with the value found by Pettini et al. (2001). Astrophysical flux measurements are difficult, especially for faint sources. This is even more true in the presence of telluric absorption bands, as is the case here. The redshift $z = 3.056 \pm 0.00021$ was measured from the integrated data set, and the FWHM line width is $158 \pm 11 \text{ km s}^{-1}$. These values are in agreement with Pettini et al. (2001), who measured the redshift $z = 3.055$ and $FWHM = 151 \pm 10 \text{ km s}^{-1}$. The $[\text{OIII}]\lambda 5007\text{\AA}$ line has a blue wing, probably due to a starburst-driven wind (Lehnert & Heckman 1996a). Asymmetric line profiles are not unusual in high-redshift galaxies.

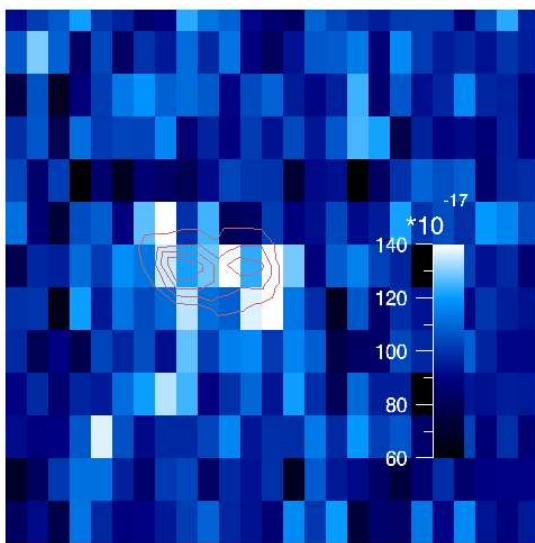


Fig. 10.— $[\text{OIII}]$ line image of Q0201+113 C6. Fluxes are given in $\text{W m}^{-2} \text{ arcsec}^{-2}$, i.e. per 64 pixels. Contours show the HST F606W image, in increasing steps of 10σ , starting at 5σ .

riterion discussed in Section 2 of this chapter can be used, comparing the 3σ limit on the velocity shear v and the dispersion σ :

$$\frac{v}{\sigma} = \frac{v_{\text{obs}} \sin i}{\sigma} < 0.67 \quad (8.8)$$

The velocity shear is corrected for an inclination $i = 75^\circ$ as derived from the WFPC2 image. The shear traces the large-scale ordered motion in the galaxy, whereas the velocity dispersion gives a

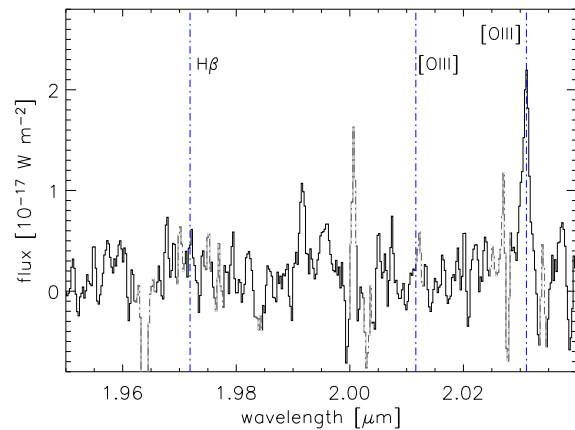


Fig. 9.— Integrated spectrum of Q0201+113 C6. Vertical blue dot-dashed lines indicate the expected position of lines at the systemic redshift of Q0201+113 C6, the spectrum is shown with a dotted line where night sky line residuals dominate.

An attempt was made to analyze the spatially resolved data set, but the low signal-to-noise ratios make it difficult to measure a significant velocity gradient. Data were extracted from 5×5 pixel apertures ($0.625'' \times 0.625''$) near the extremities of the source. Measured velocities differ by $11 \pm 10.3 \text{ km s}^{-1}$. A significant velocity shear could not be measured, however, the uncertainty can be translated into an upper limit to a velocity gradient. At 3σ confidence, relative velocities in excess of 44 km s^{-1} can be ruled out.

3.2. Dynamical mass estimates and the nature of Q0201+113 C6

Unfortunately, the data do not allow to map the two-dimensional flux and velocity distributions across the source, and to constrain the nature of the source using the integral-field kinematic information. However, the basic stability criterion

measure for the random motions. The resulting $v/\sigma \sim 0.67$ is near the value found for Q0347-383 C5 and is not in agreement with rotation in an isolated, stable, and self-gravitating disk.

The only auxiliary data set available for this source is the WFPC2 imaging. As previously discussed, the continuum emission is not very uniformly distributed, which might be due to extinction, or hint the presence of two nearby, unresolved sources. To illustrate whether this assumption is supported by the HST data, Fig. 3.2 shows the same image as Fig. 3, but with contours indicating the position of two unresolved sources, namely the PSF as measured from stars within the same WFPC2 chip. The morphology of Q0201+113 C6 is in agreement, but of course not uniquely explained, with being composed of two separate, unresolved components at a projected distance of $d_{proj} \sim 0.7''$ or 5.4 kpc.

How reliable is this conclusion? Lyman-break galaxies have overall low extinction. This has been confirmed by detailed SED fitting of the rest-frame UV emission of a large sample of U-band dropouts (Shapley, Steidel, Pettini, & Adelberger 2003). For Q0201+113 C6 specifically, Shapley et al. (2001) find a very low color excess $E(B-V) = 0.08$. In addition, as Pettini et al. (2001) showed from R_{23} ⁵ in a small sample $z \sim 3$ LBGs, including Q0201+113 C6, these sources are comparably metal poor. Namely, for Q0201+113 C6, they constrained $12 + [O/H]$ to be subsolar by at least 0.2 dex. Low metallicities also disfavor strong dust obscuration. Elmegreen et al. (2005); Ravindranath et al. (2004) discuss radial surface brightness profiles of high-redshift galaxies and conclude that those galaxies which can be spatially resolved with high-resolution ACS imaging, do indeed have approximately exponential profiles, or clumps whose number density declines exponentially.

The ‘‘patchy disk’’ scenario therefore seems to be rather unlikely for Q0201+113 C6. Therefore, also the HST data are rather indicative of a physically related pair of two individual, but physically related components, probably an early galaxy merger, rather similar to Q0347-383 C5, but with a marginally smaller projected distance (5 kpc instead of 6 kpc), and different morphology in the HST imaging.

A similar result is found when comparing the mass estimates obtained from the velocity dispersion of the integrated spectrum and the velocity shear. For a single, rotating disk with the above size estimates and 3σ limit on the velocity shear, the dynamical mass estimate is, using equation 4.1

$$M_{dyn, shear} < 5.4 \times 10^8 M_{\odot} \quad (8.9)$$

correcting for the inclination previously fitted to the WFPC2 morphology, $i = 75^{\circ}$. This is about $15\times$ lower than the stellar mass estimate of Shapley et al. (2001) ($M_{star} = 8 \times 10^9 M_{\odot}$).

However, the measured velocity shear is lower than the intrinsic shear, because the velocity map is ‘‘blurred’’ by the seeing. To fully take this effect into account, an exponential disk is modeled, using DYSMAL. The model parameters match the observational and instrumental constraints, and take the fitted source size and inclination into account. A velocity gradient $2v_c = 44 \text{ km s}^{-1}$ is found for a disk with $1.5 \times 10^9 M_{\odot}$ mass, significantly higher than the estimate based on the observed shear, but still a factor 8 lower than the stellar mass. In addition, the lines of such a disk are unresolved in the simulated SINFONI data.

Alternatively, the dynamical mass of Q0201+113 C6 can be estimated from the line width of the integrated spectrum (Equation 4.14) and is

$$M_{dyn, \sigma} = 1.3 \times 10^{10} M_{\odot}, \quad (8.10)$$

⁵The empirical R_{23} metallicity calibrator has been discussed in Section 4.

a factor 9 larger than the estimate based on the shear.

Comparing the mass derived from the line width and the shear is somewhat redundant with the v/σ calculation above, but also allows the direct comparison with the stellar mass estimate and therefore illustrates in a very quantitative way, that the 3σ limit on the velocity shear is tight enough to strongly disfavor the disk hypothesis.

An isolated disk can only be accommodated assuming that the bulk of the mass is not luminous (or has a too low L/M at rest-frame UV/optical wavelengths to be detected) and that the observed morphology is not representative for the underlying structure. In addition, the population synthesis modelling of Shapley et al. (2001) must be very unrealistic, or the observed stars are not within the gravitational potential as the line emitting gas. While this is certainly possible, it requires a very complex structure and it is unlikely that this very small sample contains two galaxies with a similar pattern of extinguished patches and physically unrelated emission line and stellar emission. Q0201+113 C6 certainly contains non-luminous matter (especially the dark-matter halo), and the observed light distribution only traces the inner parts of the halo. Hence the kinematics do not trace the full galaxy potential. However, in the case of Q0201+113 C6, the single disk hypothesis is not supported by the observed morphological and kinematic data.

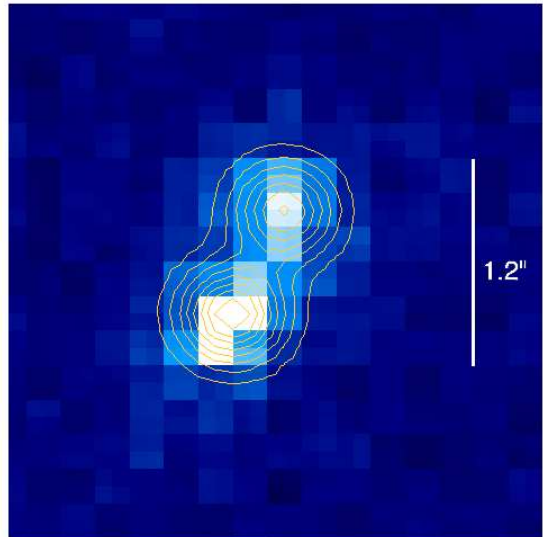


Fig. 11.— WFC2 $F606W$ image of Q0201+113 C6 with contours showing two unresolved components.

In the scenario of two nearby, orbiting and probably merging components, the orientation of the orbit is not constrained by the morphology of the source. In addition, if these two components are merging, then their orbital velocity probably does not reflect virialized motion, but is lower. Hence the velocity shear is not a reliable measure for the total mass of the system.

Alternatively masses can be estimated from the velocity dispersion of the emission lines (Chapter 4). Velocity dispersions of the two components are 79 ± 6 km s $^{-1}$ and 82 ± 8 km s $^{-1}$ respectively. The spatial resolution of the WFC2 image sets an upper limit to the radius of each component, $r \sim 1.7$ kpc. Because the radial mass profile of the components is not known, both estimates, assuming an isothermal sphere and a flat, edge-on mass distribution, will be given. The mass estimates are obtained using equations 4.14 and 4.15, respectively, and are

$$M_{bulge} = 1.2 (1.3) \times 10^{10} M_{\odot} \quad (8.11)$$

$$M_{disk} = 6.9 (7.4) \times 10^9 M_{\odot} \quad (8.12)$$

for component A (component B). Strictly speaking, these estimates should be viewed as an upper limit, because the lines might be broadened by the interaction between the galaxies. However, comparing the velocity dispersions seen in Q0201+113 C6 with the $\sigma = 98 \pm 9$ km s $^{-1}$ of 1E0657 core (Section 7) adds credence that the broadening is probably not very large.

As discussed previously and also in chapter 5, galaxy pairs with relative velocities smaller than

their internal velocities will merge within a few orbital time scales. Q0201+113 C6 appears to have a rather peculiar configuration, making it difficult to estimate the orbital time scale: The velocity shear taken at face value is very small (10 km s^{-1}) which might mean that the companions are either orbiting nearly in the plane of the sky or are near the point of their largest distance. In a statistical sense, both assumptions seem rather unlikely. Therefore, the measured shear and the 3σ limit will be used to constrain a range of possible orbital velocities, placing the barycenter at the midpoint between the two [OIII] emitting knots. At radii $r \sim 2.7 \text{ kpc}$, the orbital time scale is between $t_{min} = 1.5 \times 10^8 \text{ yrs}$ and $t_{max} = 1.6 \times 10^9 \text{ yrs}$. In either case, the galaxies will merge within at most a few Gyrs, possibly much faster, and will coalesce most likely at $z = 1 - 2$.

Table 2:: Emission lines in Q0201+113 C6

zone (1)	line (2)	λ_0 (3)	z (4)	λ_z (5)	FWHM_{obs} (6)	FWHM_0 (7)	flux (8)
total	[OIII]	5007	3.0562 ± 0.00021	2.0310 ± 0.00042	5 ± 2	158 ± 11	3.27 ± 0.30
comp A	[OIII]	5007	3.0562 ± 0.00021	2.0310 ± 0.00042	5 ± 3	185 ± 12	2.81 ± 0.23
comp B	[OIII]	5007	3.0564 ± 0.00022	2.0310 ± 0.00044	5 ± 4	195 ± 17	2.67 ± 0.30

(1) location. – (2) line ID. – (3) rest-frame wavelength in \AA . – (4) observed wavelength in μm . – (5) redshift. – (6) observed FWHM in \AA . – (7) intrinsic (deconvolved) FWHM in km s^{-1} . – (8) integrated line flux in 10^{-20} Wm^{-2} .

4. Q1422+231 D81

Q1422+231D81 at $z = 3.1$ ⁶ is one of the brighter sources in the Pettini et al. (2001) sample of 11 $z \sim 3.1$ LBGs, with a [OIII] λ 5007 flux $F_{[\text{OIII}]}$ = $1.8 \pm 1 \times 10^{-16}$ erg s⁻¹cm⁻² and an H β flux $F_{\text{H}\beta}$ = $4.1 \pm 0.4 \times 10^{-17}$ erg s⁻¹cm⁻². Pettini et al. (2001) have also measured R_{23} for this source, and constrain the metallicity to be solar or less (using the most recent estimate for the solar metallicity, $12 + [\text{O}/\text{H}] = 8.69$; Allende Prieto, Lambert, & Asplund 2001). No further data are available for this object.

The present data set was obtained during one of the SPIFFI-GI runs on April 7th and 8th, 2003. The total on-source integration time was 130 minutes with individual exposure times of 5 minutes. Data of Q1422+231D81 have also been taken in one of the SINFONI-GTO runs, however with less total exposure time (80 min) and mediocre seeing. (The size of the seeing disk was measured from the standard star and is $0.7'' \times 0.7''$). In addition, the most relevant [OIII] λ 5007 line is very close to a strong night sky line, which makes it crucial to have good weather conditions. The spectra of the GI run are less affected by the night sky line, therefore the GI data set was used for this analysis. A combination of the two data sets was made, however, this did not improve the signal-to-noise ratio, but rather broadened the lines, although the pixel scales were matched by shifting and resampling the data sets. The line widths in the individual combined cubes of the GI and the GTO run are consistent. The reason might be the different PSFs in the two data cubes, which will smear the velocity shear over the (relatively small) source and effectively broaden the line.

4.1. Results

Q1422+113 D81 is small and only marginally resolved in the SPIFFI image plane. The seeing disk was measured from the standard star and has a FWHM of $0.67'' \times 0.43''$ in the GI data. Fitting a two-dimensional Gaussian to the line image of the source yields a size of $0.83'' \times 0.46''$, hence Q1422+113 D81 is marginally resolved along right ascension, and unresolved along declination. To derive an intrinsic size estimate, the resolved axis is deconvolved with the size of the seeing disk, yielding $r = 0.46''$, or 3.5 kpc in the adopted cosmology. This is near the average size of $z \sim 3$ LBGs ($0.3''$, Gialalisco, Steidel, & Macchetto 1996). Since no deep, high-resolution HST imaging is available for this galaxy, this is the best size estimate currently available and will in the following be used as an upper limit to the half-light radius r_e of Q1422+113 D81.

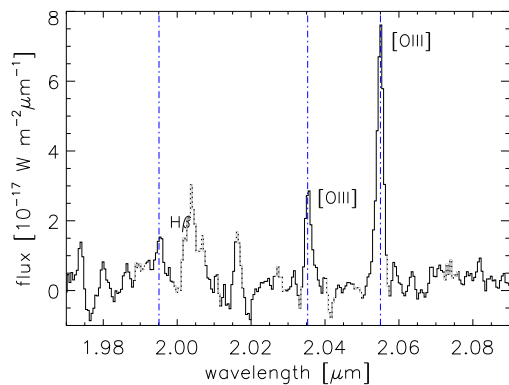


Fig. 12.— Total spectrum of the Q1422 LBG. Dotted lines indicate night sky line residuals, blue dot-dashed vertical lines show the expected emission line positions.

The integrated spectrum is shown in Fig. 12. It was extracted from a $1.5'' \times 1.5''$ aperture centered

⁶Using the flat $\Omega_\Lambda = 0.7$ cosmology with $H_0 = 70$ kms⁻¹ Mpc⁻¹ leads to $D_L = 26.4$ Gpc and $D_A = 1.57$ Gpc at $z = 3.1$. The size scale is 7.63 kpc $''$. The age of the universe with this redshift and cosmological model is 2.03 Gyrs.

on the maximum line emission, and smoothed over 3 spectral pixels to approximately match the resolution. Dotted lines indicate wavelengths where strong night sky line residuals were identified in the two-dimensional spectrum. Vertical dot-dashed blue lines show the expected position of emission lines at the systemic redshift. $[\text{OIII}]\lambda\lambda 4959, 5007$ and $\text{H}\beta$ are clearly observed, with signal-to-noise ratios of 19.9, 11.5, and 9.5 for $[\text{OIII}]\lambda 5007$, $[\text{OIII}]\lambda 4959$, and $\text{H}\beta$, respectively. Continuum emission is very faint, and can only marginally be discerned. Equivalent widths are accordingly large, best estimates for the rest-frame equivalent widths are $W_{[\text{OIII}]\lambda 5007} \sim 150 \text{ \AA}$, and $W_{\text{H}\beta} \sim 50 \text{ \AA}$.

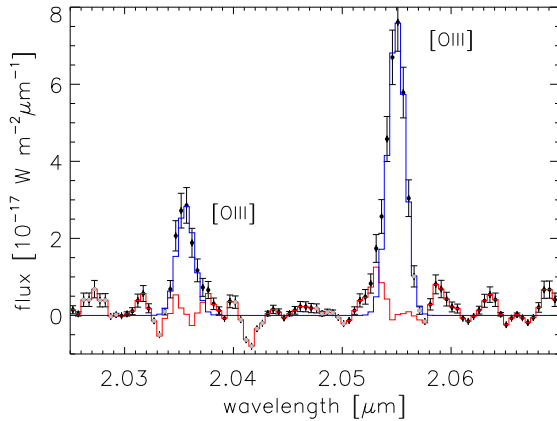


Fig. 13.— Closeup on the $[\text{OIII}]\lambda$ pair in $Q1422$. Black dots and error bars indicate the observed spectrum. Light gray dots show strong night sky lines, the blue line indicates the best Gaussian line fit.

$\text{H}\beta$ and $[\text{OIII}]\lambda$ line widths agree within the uncertainties. The total $[\text{OIII}]\lambda$ to $\text{H}\beta$ ratio is $[\text{OIII}]/\text{H}\beta = 5.76 \pm 0.84$.

The spectrum was flux calibrated using the star HD124909. This allows to calculate a star-formation rate from the observed $\text{H}\beta$ line flux, using equation 4.9 in section 2.1. In the adopted cosmology, the observed line flux $F_{\text{H}\beta} = 3.7 \times 10^{-20} \text{ W m}^{-2}$ yields a $\text{H}\beta$ -luminosity, $L_{\text{H}\beta} = 8.5 \times 10^{35} \text{ W}$. The $\text{H}\alpha$ flux can be estimated from the Balmer decrement $\text{H}\alpha/\text{H}\beta = 2.87$, neglecting extinction. This yields a star formation rate of $SFR = 65 M_{\odot} \text{ yr}^{-1}$. Pettini et al. (2001) measure $75 M_{\odot} \text{ yr}^{-1}$ from the $\text{H}\beta$ flux (not correcting for extinction and adopting a 0.1-100 IMF), and $45 M_{\odot} \text{ yr}^{-1}$ from the rest-frame UV continuum.

$z \sim 3$ LBGs are generally found to be low-extinction, $E(B - V) \sim 0.2 - 0.4 \text{ mag}$ (Shapley et al. 2001), suggesting intrinsic fluxes that are $\sim 1.6 - 3 \times$ higher than measured. With these estimates, the intrinsic star-formation rate might be as high as $\sim 100 - 200 M_{\odot} \text{ yr}^{-1}$.

The line profile of the $[\text{OIII}]\lambda 5007$ line is asymmetric with a blue wing. This is often observed in high redshift galaxies, and indicates the presence of outflowing gas, most likely driven by star-formation feedback (Pettini et al. 2001).

The lines are narrow, they have Gaussian widths of $75 \pm 6 \text{ km s}^{-1}$ ($[\text{OIII}]\lambda 5007$), $52 \pm 11 \text{ km s}^{-1}$ ($[\text{OIII}]\lambda 4959$), and $131 \pm 51 \text{ km s}^{-1}$ ($\text{H}\beta$). These are the intrinsic line widths, which are corrected for the instrumental resolution. The resolution is determined from the widths of night sky lines in the off-frames. The difference between the two $[\text{OIII}]\lambda$ lines is probably due to a night sky line residual near the $\lambda 4959 \text{ \AA}$ line. Due to the larger line flux of the $\lambda 5007 \text{ \AA}$ line, a nearby night sky line has a negligible influence on the emission line, as was confirmed by inspection of the two-dimensional spectrum. Especially, it has no impact on the line position, because the line centroids are unaffected across the source. The measured flux ratio between the two $[\text{OIII}]\lambda$ lines is $I(4959)/I(5007) = 0.34 \pm 0.03$, and agrees with the theoretically expected value. The

4.2. Comparison with NIRSPEC results

Comparison with near infrared spectra of Lyman Break Galaxies, e.g. obtained with ISAAC at comparable spectral resolution (c.f. Pettini et al. 2001) confirms that the line profiles of Q1422, especially that of $[\text{OIII}]\lambda 5007 \text{ \AA}$, are typical of Lyman Break Galaxies: Narrow, the core of the line is well fit by a single Gaussian. The line profiles show weak asymmetric blue wings, which is frequently observed in low redshift galaxies with strong evidence for driving galactic outflows (Lehnert & Heckman 1996a). That line together with a Gaussian fit is shown in Fig. 13.

However, comparing the SPIFFI spectra of Q1422 with data of the same source previously taken with NIRSPEC at Keck (Pettini et al. 2001), reveals significant differences in the profiles and widths of the lines, although the line ratios are about the same ($\text{H}\beta/[\text{OIII}]\lambda 5007 \text{ \AA} = 0.228 \pm 0.02$ in the NIRSPEC result, 0.233 ± 0.03 with SPIFFI). The NIRSPEC spectrum of Q1422+231 D81 is reproduced in Fig. 14. The core of the profile as obtained with SPIFFI can be well fitted with a narrow Gaussian, which does not appear to be the case for the NIRSPEC data. The NIRSPEC profiles, not just the one for Q1422, appear to be more square than a Gaussian and the line profile of Q1422 in particular does not have a blue wing like what is seen in the SPIFFI data. Most striking, though, is the difference in the line widths, the velocity dispersion being $116 \pm 8 \text{ km s}^{-1}$ for the NIRSPEC, and $75 \pm 6 \text{ km s}^{-1}$, 6σ or about a factor 0.65 lower for the SPIFFI data.

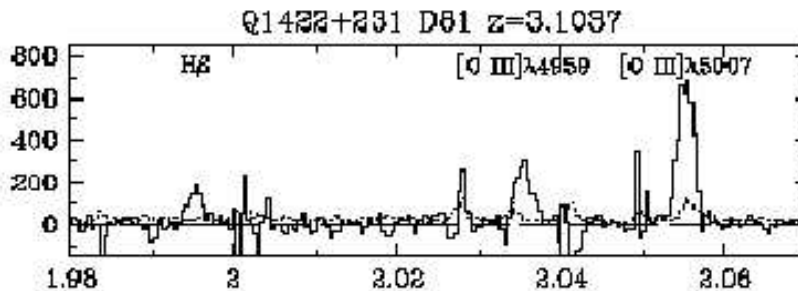


Fig. 14.— NIRSPEC spectrum of Q1422+231 D81, taken from Pettini et al. (2001).

This can only be due to a poorly understood systematic uncertainty in at least one of the two measurements, naturally a weak claim if it is based only on one source. Therefore the 12 ISAAC and NIRSPEC spectra as given in Pettini et al. (2001) were examined more closely. Source West MMD11 is not considered, because it has a complex morphology (Chapman et al. 2002) suggesting that the kinematics of its optical line emitting gas may not be dominated by gravity in a simple way.

The average line width of this sample is $96 \pm 2 \text{ km s}^{-1}$ and $93 \pm 3 \text{ km s}^{-1}$ for the two NIRSPEC observing runs, respectively. Given this consistency, the ensemble average line width of the NIRSPEC spectra is $95 \pm 2 \text{ km s}^{-1}$. However, the average width of their ISAAC sample is $66 \pm 1.4 \text{ km s}^{-1}$. The ratio of both samples is 0.69 ± 0.03 , which is in good agreement with the above offset between the two observations of Q1422. While this does not prove that the ensemble offset is needed, it is however very suggestive. Given the scatter and small number of objects in both samples, it seems puzzling that the ratio of their means agrees within a few percent with the ratio of the velocity dispersions that were obtained with the two measurements. This suggests that the NIRSPEC results are systematically larger than the data obtained with the VLT. This might be due to the lower spectral resolution of the NIRSPEC spectra, and the measured velocity dispersions being close to the instrumental limit.

4.3. Spatially resolved line emission

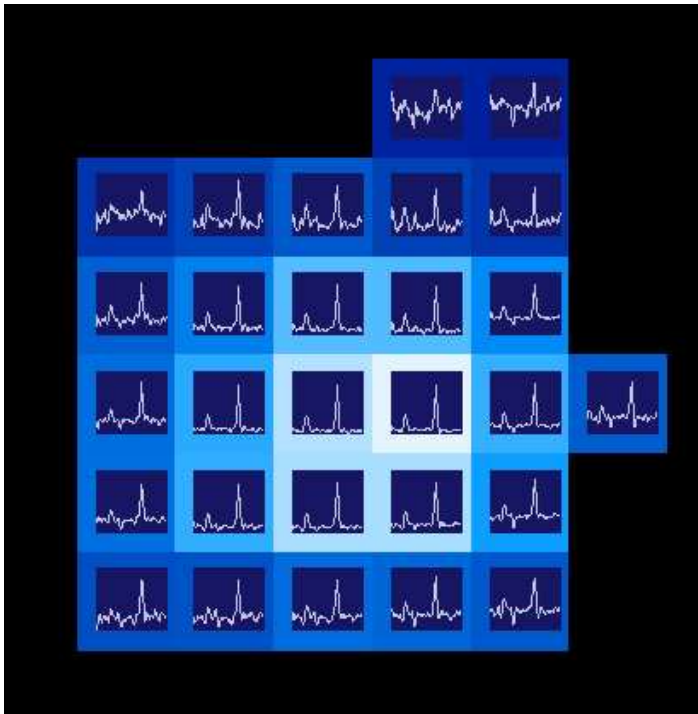


Fig. 15.— $[\text{OIII}]\lambda 5007$ line emission with the spectra overlaid, from which the velocity map was calculated. The spectra are extracted from boxes of $0.75'' \times 0.75''$, and are smoothed over 3 pixels spectrally, to approximate seeing and spectral resolution.

velocity curve shown in Fig. 17. The spatial distribution of line widths is shown in the right panel of Fig. 16. FWHMs are uniform within the scatter, with values $\text{FWHM} \sim 200 \text{ km s}^{-1}$.

4.4. What drives the dynamics in Q1422+113 D81?

Are these data sufficient to infer a plausible scenario of what drives the dynamics? The small $[\text{OIII}]/\text{H}\beta$ ratio and uniform and moderate line widths of $\sim 200 \text{ km s}^{-1}$ indicate that the lines are ionized by hot stars and that their kinematic properties are dominated by large-scale gravitational motion.

Deep HST imaging is available for the other two sources in this sample and yields comparably tight morphological constraints. Unfortunately this is not the case for Q1422+231 D81. The imaging data extracted from the SPIFFI cube unfortunately are comparably shallow and only trace the line emission. Q1422+231 D81 appears smaller than the two other sources, with a size deduced from the line image of $\lesssim 0.5''$ or 3.5 kpc (see Section 4.1). This is a factor ~ 2 smaller than the two other LBGs. Unlike the two other sources, the $[\text{OIII}]$ line emission of this galaxy peaks near the center and does not show two well pronounced, unresolved peaks like the other two galaxies. In addition, the line widths appear uniform. Although each of these indications can only be circumstantial, it hints that Q1422+231D81 probably is an isolated galaxy.

The $[\text{OIII}]\lambda 5007$ line has a good signal-to-noise ratio, so that spectral variations across the source can be studied. To approximately match the seeing disk, spectra were integrated over 3×3 pixel apertures ($0.75'' \times 0.75''$). Apertures were only used where $S/N > 5\sigma$.

Fitting the line centroids in each individual aperture results in a significant (5.8σ) velocity offset $\Delta v = 212 \pm 36 \text{ km s}^{-1}$. The velocity map is shown in Fig. 16. Velocities vary monotonically within the source, and are consistent with virialized motion around the center of the line emitting region. The gradient stretches from north-east to south-west. Velocities increase monotonically along right ascension, which indicates that the kinematic major axis is near this direction, and that the source is spatially not resolved along declination. The small size of the source of course makes it difficult to identify this axis morphologically as the kinematic major axis. The shear is also obvious in the veloc-

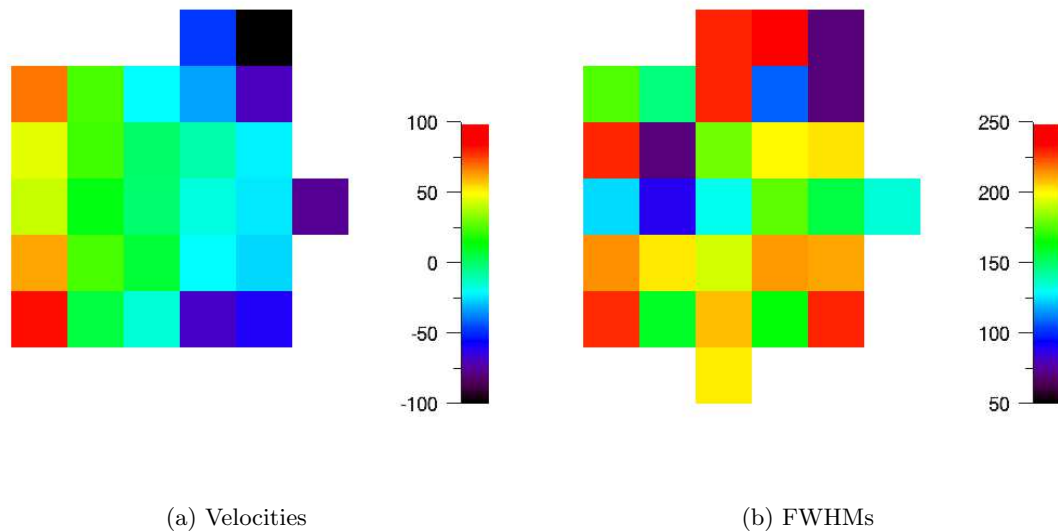


Fig. 16.— $[OIII]\lambda 5007$ velocity and FWHM maps of the Lyman break galaxy Q1422+231 D81. North is up, east to the left. The color bar yields the relative velocities (in km s^{-1}) with respect to the brightest $[OIII]$ line emission. One pixel corresponds to ~ 1.9 kpc. All errors are $< 30 \text{ km s}^{-1}$.

Another indication comes from comparing the random motions (traced by the Gaussian line width σ) with the bulk motion (v), v/σ . For rotating exponential disks and similar observational and instrumental constraints, $v/\sigma > 1$ for inclinations $i \gtrsim 30^\circ$. For Q1422+231 D81, $v/\sigma = 1.2$. This indicates that the gas is in a stable configuration within the large-scale gravitational potential and further supports the scenario that Q1422+231 D81 is a single, isolated disk.

If this interpretation is correct, then the most likely scenario is that the velocity shear in Q1422+231 D81 is the signature of a rotating disk. The velocity curve obtained from extracting the velocities along the gradient seen in Fig. 16 is shown in Fig. 17. It does not show the typical turnover points often observed in spiral galaxies at low redshift, but monotonically increases. In the exponential-disk interpretation, this means that the disk is not traced beyond the disk scale length. Is this worrisome? As shown in the figure, relative velocities are measured out to radii of ~ 6 kpc. Comparing this radius with the sample of low-redshift starburst galaxies by Lehnert & Heckman (1996a) indicates that the turnover radii in these galaxies are

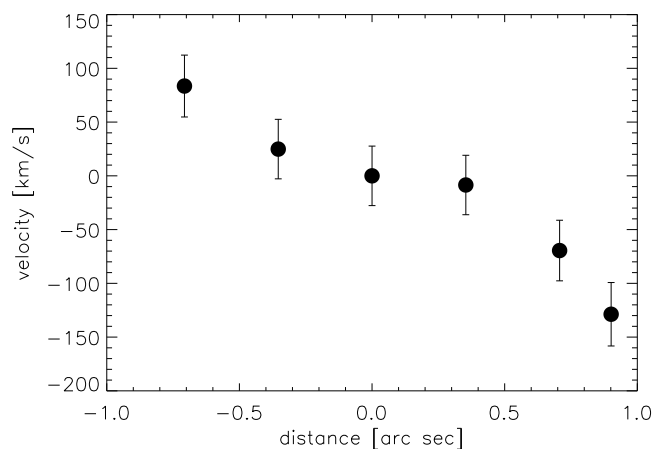


Fig. 17.— Velocity curve extracted along the velocity gradient of the Lyman break galaxy. The gradient exceeds the seeing disk by more than a factor 2.

$\lesssim 6.5$ kpc, so that it appears plausible that the turnover points are not detected because line emission is not traced to large enough radii or that they are undetected because of the scatter in the velocities.

4.5. Dynamical modelling and the mass of an isolated disk galaxy at $z=3.1$

To fully exploit the two-dimensional velocity field for the mass estimate, the measured data are fitted with exponential disks using the DYSMAL package (Section 4 of Chapter 4). It was tried to constrain the inclination and tilt angle of Q1422+231 D81 from the observed spatially-resolved maps directly, but the source is too small, and the scatter too large, to set meaningful constraints. Therefore the line image is used to constrain the morphology. The fitted Gaussian ellipse to the observed image suggests a lower limit on the inclination angle $i > 60^\circ$. This value is based on the measured size along right ascension (where the source is spatially resolved) and the resolution along declination (where it is not). Obviously, inclination is not a very well constrained parameter in this case.

The tilt is determined from fitting a Gaussian ellipse to the line image, with $\theta = -5^\circ$. Strictly speaking, for a source that is spatially resolved only along one axis, the tilt should be $\theta = 0^\circ$. The discrepancy is probably due to the noise and coarse gridding of the data. In the following, the measured value is used, but has a negligible influence on the result.

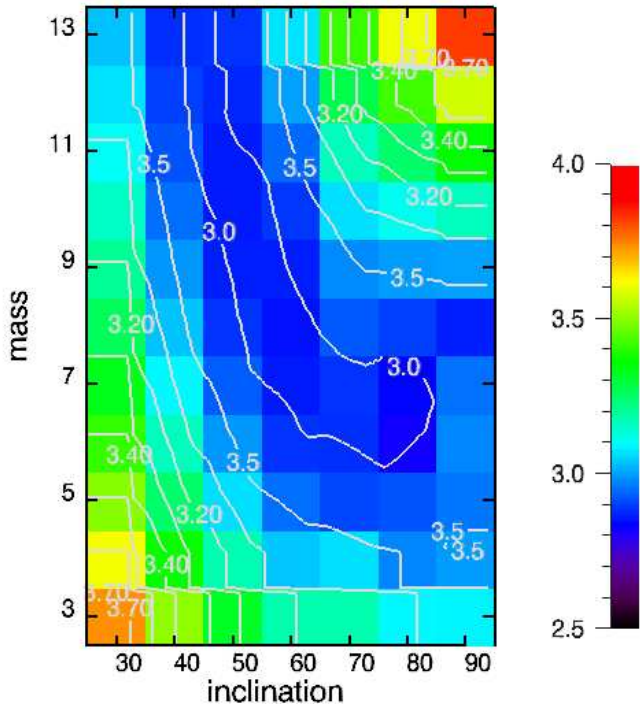


Fig. 18.— χ^2/n_{pix} as function of inclination (abscissa) and mass (ordinate, given in units of $10^9 M_\odot$) for fitted exponential disks to the velocity field of Q1422+231 D81.

The map of χ^2 s for different inclination and mass estimates is shown in Fig. 18. A range of $3 - 13 \times 10^9 M_\odot$ is tested, and inclinations $i = 30^\circ - 90^\circ$. Masses are varied in steps of $\Delta m = 10^8 M_\odot$, and inclinations in steps of $\Delta i = 10^\circ$. Smallest χ^2 s ($\chi^2/n_{pix} = 2.88$) are found along the dark blue ridge, and correspond to $M = 7 \times 10^9 M_\odot$ for Q1422+213 D81. If the limit on the inclination is not taken into account, then $M \lesssim 1.3 \times 10^{10}$, unless if the disk is nearly seen face on.

Since 28 pixels are used, and uncertainties on the velocity are typically $\lesssim 10 \text{ km s}^{-1}$, statistical errors are marginal. The overall fit uncertainty is therefore dominated by the poorly constrained inclination. The best-fit mass range ($\chi^2/n_{pix} < 3$) and $i = 60^\circ - 90^\circ$ is therefore $M = 7_{-3}^{+5} \times 10^9 M_\odot$.

As discussed in Chapter 4, the χ^2 cannot be used to calculate a goodness-of-fit, because of the hard-to-quantify number of degrees of freedom (i.e. uncorrelated spatial elements) in the data. Therefore, the non-parametric run test is again used. For the $n=26$ observed pixels, the residual map (difference

between model and data pixel by pixel) has $r_{obs} = 9$ observed runs, with $r_{exp} = 11.37 \pm 1.9$ expected. Hence data and model agree within 1.2σ .

Line widths were also fitted with the model, but observed widths are systematically higher than expected, with very inhomogeneous χ^2 s, which monotonically rise with decreasing signal-to-noise. The broadening corresponds to $\sim 2\sigma$ in each pixel, but is systematic. If it is intrinsic, and the single-disk interpretation is correct, then this might indicate that the exponential disk is an oversimplification, and that surface mass densities near the center of high-redshift galaxies are higher than in the local Universe.

Having obtained a two-dimensional, spatially resolved fit of the central velocity field of a $z \sim 3$ LBG, it is interesting to compare this mass estimate with the estimate based on the line width of a spatially not resolved system. Most LBG mass estimates are based on line dispersions, but this might lead to underestimates of the galaxy mass (Giavalisco 2002), due to selection effects, e.g. radially declining surface brightness. Using equations 4.14 and 4.15, the observed radius $r = 3.5$ kpc, and the observed dispersion of $\sigma = 75 \pm 6$ km s $^{-1}$ yields mass estimates

$$M_{disk} = 1.3 \times 10^{10} M_{\odot} \quad \text{for a rotating disk,} \quad (8.13)$$

$$M_{bulge} = 2.3 \times 10^{10} M_{\odot} \quad \text{for a sphere.} \quad (8.14)$$

These estimates are within the range favored by the two-dimensional kinematic fit, or even exceed it, and indicate that the concerns of Giavalisco (2002) are not substantiated.

Table 3:: Emission lines in Q1422+231 D81.

line (1)	λ_0 (2)	z (3)	λ_{obs} (4)	$FWHM_{obs}$ (5)	$FWHM_{intr}$ (6)	flux (7)
[OIII]	5007	3.1041 \pm 0.00048	2.0549 \pm 0.00032	20.4 \pm 1.77	177 \pm 15	1.59 \pm 0.08
[OIII]	4959	3.1047 \pm 0.00053	2.0355 \pm 0.00035	18.2 \pm 3.84	123 \pm 26	0.54 \pm 0.047
H β	4861	3.1046 \pm 0.0008	1.9952 \pm 0.00051	25.9 \pm 10.	308 \pm 119	0.37 \pm 0.039

Table 4: (1) line ID. – (2) rest-frame wavelength in Å. – (3) observed wavelength in μ m. – (4) redshift. – (5) observed FWHM in Å. – (6) intrinsic (deconvolved) FWHM in km s $^{-1}$. – (7) integrated line flux in 10^{-19} Wm $^{-2}$.

5. The dynamics of $z \sim 3$ LBGs

5.1. Dynamical modelling and the nature of $z \sim 3$ LBGs

In a very general sense, the morphologies of high redshift galaxies are more irregular than those of galaxies at low redshift. By $z \gtrsim 2$, galaxies with regular morphologies have essentially vanished (see, e.g. van den Bergh et al. 1996, for an early account). As previously discussed, it is very straight-forward to interpret this as the outcome of mergers, but without strong additional constraints, especially from dynamical measurements, this conclusion would be very simplistic.

The previous sections have discussed individual LBGs with the aim to identify their major dynamical engines and to measure their mass. In order to obtain mass estimates more accurately than by factors of a few, it is not only necessary to set tight constraints on the inclination, but also

on the nature of the source. Clearly, if a galaxy is dominated by a rotating disk, partly extinguished or not, then its morphology will allow to constrain the inclination to some degree. If it is a pair of two individual components, then its geometry will not be a good tracer for the orientation of the orbits.

Are there robust ways to distinguish these scenarios based on simple measurements and without detailed modelling of each individual source? An approach is proposed that essentially quantifies the v/σ criterion for galaxies with the typical properties of $z \sim 3$ LBGs and specifically the exponential disk hypothesis.

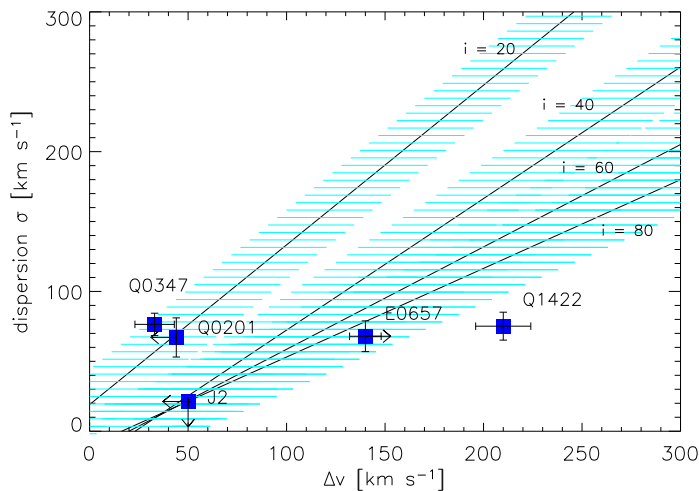


Fig. 19.— *The modelled relationship between velocity shear and dispersion for a simulated sample of “LBGs”. Black lines indicate the relationship for galaxies with varying mass and inclination, cyan shaded areas yield the typical observational uncertainties. Blue squares show the data.*

To obtain a most robust dispersion measure, the dispersion is measured from the line width in the spectrum integrated over the total source extent.

The resulting relationship is shown in Fig. 19. The black lines indicate the relationship for modeled galaxies for inclinations of 20° , 40° , 60° and 80° . The cyan shaded areas yield the typical observational uncertainty for high signal-to-noise data ($S/N \gtrsim 30$ in the integrated spectrum). Blue squares show the data.

As was found previously, Q0347-383 C5 and Q0201+113 C6 do not have dynamical properties and morphologies in good agreement with highly inclined, isolated disks, whereas 1E0657 core and Q1422+213 D81 have properties that support this hypothesis. This is also evident from Fig. 19. 1E0657 core and Q1422+213 D81 fall near the $i = 80^\circ$ line. The dispersion of Q1422+213 D81 might be somewhat lowered by a night sky line near the $[\text{OIII}]\lambda 5007$ line, which does not affect the centroids, but might somewhat lower the line width. If the $\text{H}\beta$ dispersion is used instead (which has a low signal-to-noise ratio), then $\sigma \sim 100 \text{ km s}^{-1}$, and Q1422+213 D81 falls within the $i = 80^\circ$ shaded area.

Q0347-383 C5 and Q0201+113 C6 must have very low inclinations to be well described with

A set of 77 exponential disks is modelled using DYSMAL, varying inclinations between 20° and 80° and masses between $5 \times 10^8 M_\odot$ and $5 \times 10^{11} M_\odot$. Disk scale lengths and radii are $0.3''$, matching the average radius of LBGs (Giavalisco 2002). The seeing is $0.4'' \times 0.6''$, pixel scales and spectral resolution match the SINFONI settings (see Chapter 3). These simulated data cubes are then treated like the data in this analysis: 3×3 pixel apertures are used to extract individual spectra from approximately each spatial resolution element, and the spectra are smoothed over 3 spectral bins to approximate the resolution. No noise is added.

The kinematic fields are then extracted from the data, and used to estimate the relationships between velocity dispersion and shear for different combinations of mass and inclination.

an exponential disk. In both cases, their axis ratios measured from the WFPC2 images suggest they are highly inclined systems. For Q0347-383 C5 and Q0201+113 C6, respectively, measured dispersions are 8.4σ and 3.5σ higher than expected for an exponential disk with $i \gtrsim 60^\circ$. The low mass of J2 makes the measurement difficult. However, if the line width and velocity gradient are near the resolution limit of the SINFONI data, then its kinematic properties are also in agreement with being an individual galaxy. This is not surprising, given its clearly resolved from J1.

This comparison shows that it is possible to estimate the dynamical state of LBGs with SINFONI if velocity shears and dispersions are used and if the inclination can be constrained from deep, high resolution imaging. Strictly speaking, they are only valid for the comparison with exponential disks, i.e. the dynamical model with which virialized, rotationally supported galaxies in the local Universe can appropriately be fitted.

5.2. Overall sample properties

The previous chapters have described in detail the dynamics of a small sample of $z \sim 3$ LBGs. These results will now be related to each other and discussed within the overall observational and theoretical framework. In addition, this thesis sample comprises two more LBGs, the strongly lensed gravitational arc 1E0657 arc core (Chapter 7) and the blue component J2 of SMMJ14011+0252 (Chapter 6). The latter is at a somewhat lower redshift ($z = 2.565$), corresponding to a difference in cosmic time to $z = 3$ of about 400 Myrs.

The dynamical masses of these LBGs are relatively similar, $\sim (1 - 2) \times 10^{10} M_\odot$, if the two components in the sources with two line emitting regions are taken as separate galaxies. Only J2 has a significantly smaller mass, $2 - 4 \times 10^9 M_\odot$, derived from the limit on the line width on the not resolved lines, and in agreement with the marginal velocity shear. The mass estimate of the strongly lensed arc, $M_{dyn} = (0.55 - 2.3) \times 10^9 M_\odot$, is only within the central kpc, which makes it difficult to compare it directly with the other masses. If, however, one assumes a mass profile corresponding to an exponential disk, and a typical radius $r_e = 2.5$ kpc for this source, then its mass falls within the range spanned by the other sources. In addition, the average line width within the core, $\text{FWHM} = 160 \pm 24 \text{ km s}^{-1}$, suggests a mass range of $\gtrsim 7.5 \times 10^9 M_\odot$ for a fiducial radius of $r_e = 2.5$ kpc. Hence overall, this sample appears dynamically rather homogeneous.

Less homogeneous are the star-formation rates. J2 and the arc core have $\text{H}\alpha$ -estimated, measured rates $\text{SFR} \lesssim 10 M_\odot \text{ yr}^{-1}$, whereas the other three sources have star-formation rates $\text{SFR} = 25 - 65 M_\odot \text{ yr}^{-1}$ (using the sum of the rates in Q0347-383 C5). The enclosed mass of the core out to a few kpc is probably similar to those of the other LBGs, and the fact that it is spatially resolved perpendicular to the magnification axis in the ACS image suggests that a representative part of the galaxy is magnified. Therefore, it does not seem that the dynamically measured galaxy mass regulates star-formation in an obvious way, as far as can be seen from 5 sources. Additional constraints might come into play, e.g. details of the evolutionary state, that hide such a correlation. On the other hand, this finding is in agreement with local actively star-forming galaxies (Lehnert & Heckman 1996a). Likewise, Q1422+231 D81 with its disk-like rotation pattern, has the highest observed star-formation rate in the sample, so that the presence of a companion does not seem to enhance the activity level.

Unfortunately, the available data do not allow to constrain the extinction within all sources. However, extinction were estimated from the SEDs for the 1E0657 core (see Chapter 7) J2 (see Chapter 3), and Q0201+113 C6 (Shapley et al. 2001), hence for two sources of the low-SFR sample and one from the high-SFR sample. All three sources have low extinction, indicating that the

star-formation rates will not be greatly underestimated. In addition, Shapley, Steidel, Pettini, & Adelberger (2003) find that overall in their LBG sample, extinction and star-formation rates are positively correlated. This means that the difference of star-formation rates will rather be enhanced than suppressed in the present sample. Within the limited mass range of this sample (about an order of magnitude), a simple, direct relationship between mass and star-formation rate apparently is not present, or too subtle to be traced with present-day observational accuracy. This does not mean, however, that the same is true when considering galaxies with masses varying over many orders of magnitude. Giavalisco (2002) state that star-formation is enhanced in the largest halo overdensities, and therefore essentially mass-driven. These two statements are not in contradiction to each other, because of the different mass ranges.

As a consequence, galactic winds are intimately linked to active star-formation. Following Heckman (2002) starburst galaxies with star formation rates exceeding $\rho_{SFR,min} = 0.1 \text{ M}_{\odot} \text{ yr}^{-1} \text{ kpc}^{-2}$ will inevitably drive galactic winds. $\text{H}\beta$ has been detected in 4 of the 5 LBGs presented in this chapter, so it can directly be tested whether the observed SFRs exceed this threshold. To obtain a quantitatively robust measure, and following previous definitions (see e.g. Meurer et al. 1997), the SFRs within the half-light radii r_e of the galaxies are calculated.

To be independent of the peculiar morphology of the individual target, the half-light radius is taken to be the radius of a circle with the same surface as the area within which 50% of the flux is emitted. This area is defined from the [OIII] line images, therefore it is implicitly assumed that the $\text{H}\beta$ and [OIII] line emitting regions are equivalent. Star-formation rate densities thus obtained are for Q1422+231 D81 and Q0347-383 C5 $1.4 \text{ M}_{\odot} \text{ yr}^{-1} \text{ kpc}^{-2}$ and $0.4 \text{ M}_{\odot} \text{ yr}^{-1} \text{ kpc}^{-2}$, respectively, and for E0657 core and J2 $1.43 \text{ M}_{\odot} \text{ yr}^{-1} \text{ kpc}^{-2}$ and $2.2 \text{ M}_{\odot} \text{ yr}^{-1} \text{ kpc}^{-2}$, respectively. This estimate is independent of lensing, because the magnification does not affect surface brightnesses. All four values are well above $\rho_{SFR,min}$, hence star-formation driven feedback is present, as indicated by the blue wings in some of these sources. The $\text{H}\beta$ fluxes are corrected for the Balmer decrement $\text{H}\alpha/\text{H}\beta = 2.87$, but not for extinction. Hence the intrinsic star-formation intensities are likely factors of a few higher. Because only lower limits are required for this comparison, assumptions about extinction are not necessary. It should also be noted that the typical extinction of LBGs (see the introduction to this section) is not large enough to conceal sufficient star-formation to make these galaxies “maximal starbursts”. Following definition of Meurer et al. (1997), $\rho_{SFR,min} \sim 45 \text{ M}_{\odot} \text{ yr}^{-1} \text{ kpc}^{-2}$ are needed to reach this empirical limit of star-formation rates.

If the negative correlation between age and extinction that Shapley et al. (2001) find within their sample holds also for these LBGs, then they must be comparably old. However, for the core (with an inferred age of 80 Myrs compared to 320 Myrs on average for the Shapley et al. sample), this correlation seems not to hold. Similarly, Motohara et al. (2005) find ages of 70 Myrs and 8 Myrs for their continuous and instantaneous burst model of J2, respectively. However, both galaxies have also lower stellar and dynamical masses than LBGs on average, and both sources are gravitationally lensed.

This indicates possible selection effects: SED fitting and spectral analyses are easier for sources that are comparably large and luminous, therefore the existing data might be biased – inevitably – towards the high-mass (or strongly evolved) end of the population. This finds some support from models of galaxy evolution. Nagamine (2002) obtain good agreement between the observed rest-frame optical and far-UV luminosities of LBGs and simulated evolutionary histories of galaxies in a Λ CDM universe. However, their models also predict that the observed LBGs are the most luminous members of an underlying larger population. It might be that the presence of two galaxies in this sample, that were not selected to be LBGs, but are essentially found serendipitously, have comparably low star-formation rates, and are gravitationally lensed, hints that this prediction might

be justified. A less speculative answer of course requires statistically more robust samples.

The arc core is the only source where spatially resolved kinematic data can be extracted from within the central kpc, all other sources have $\sim 3 - 4$ kpc resolution elements. Of the 5 LBGs, only the arc core and Q1422+231 D81 have velocity patterns consistent with isolated, rotating disks. Together these two sources are the first indications for rotationally supported kinematics in $z \sim 3$ galaxies, within the central kpc, and also at radii of several kpc.

The other sources have nearby companions, and their close relative projected and redshift distances suggest that these components are physically related, probably in an early stage of merging. Both scenarios can be incorporated into the hierarchical model of galaxy formation. Under the assumption that LBGs evolve quiescently, and are not triggered by mergers, star-formation will be controlled by an equilibrium between gas infall rate and cooling (Shu 2000). Resulting star-formation rates are in agreement with observation, if circular velocities are $v_{circ} \gtrsim 200 \text{ km s}^{-1}$. In an alternative scenario, LBGs are viewed as the baryon concentrations of merging dark-matter halos. Kolatt et al. (1999) find that the observed clustering of LBGs is in agreement with colliding halos of $M \sim 10^{9.8} - 10^{12.5} M_{\odot}$. They predict more galaxies than observed, but attribute this to extinction, so that these galaxies will not fulfill the LBG selection. This view has some observational support from the fact that Papovich et al. (2001) find LBGs at $z \sim 3$ and $z \sim 4$, but the distribution of evolutionary histories within their sample does not suggest that the $z \sim 4$ population evolves into $z \sim 3$ LBGs. They conclude that LBGs might undergo multiple, stochastic bursts, and are being “rejuvenated” in each new burst, as would be expected in a model of halo collision, but would be more difficult to reconcile with quiescent formation. However, recent SPITZER results (Barmby et al. 2004) do not confirm the presence of dominant old populations in $z \sim 3$ LBGs and therefore disfavor this scenario.

A study based on only 5 sources of course cannot rule out one of these scenarios. However, the co-existence of apparent early mergers and isolated sources in the sample might indicate that the $z \sim 3$ LBG population comprises both evolutionary stages, and that the merging LBGs are in a sufficiently early stage that their overall properties are still dominated by their individual evolution. This is in agreement with the simulations of Nagamine (2002), who find that many, but not all, $z \sim 3$ LBGs in their model have star-formation triggered by mergers. However, gas infall alone can also rise star-formation activity to the observed values. Estimating the relative contribution of either mode would be very interesting, but is of course impossible with a sample of 5 targets and a very diverse selection, and might be impossible without large samples with multi-waveband data.

It seems that LBGs trace their underlying dark matter halos rather closely, because of a close similarity of co-moving number density and clustering strength of observed LBGs and modelled $10^{11} M_{\odot}$ dark matter halos (Adelberger et al. 1998). For an average dynamical mass of $(1 - 2) \times 10^{10} M_{\odot}$ per LBG as found in this thesis, baryons would make up $\sim 10\%$ of the total mass. This is in broad agreement with the typical baryonic mass fractions in the local Universe. Masses of $10^{9.5} - 10^{10.5} M_{\odot}$ are also in the range predicted by Nagamine (2002). However, they are somewhat lower than masses inferred indirectly from clustering studies of LBGs, as pointed out by Giavalisco (2002). The gross agreement between the velocities inferred from the spatially-resolved velocity shear of Q1422+231 D81 and the mass estimates derived from line widths indicates that the dynamical masses within a few kpc can robustly be estimated from the line widths, if the individual galaxy is indeed a rotating disk. This does not mean, of course, that the result will also be an adequate estimate for the total galaxy mass, because only the central regions are traced by the emission line gas. This might partly explain the discrepancy between dynamical galaxy and halo masses. In addition, estimating the mass of a dark matter halo from the galaxy residing within, and the halo occupation numbers have intrinsically large uncertainties, and might also contribute to explain this difference.

5.3. Subsequent cosmic evolution of LBGs

The starburst-driven feedback observed in the LBGs will leave its imprint on the low-redshift descendants of the $z \sim 3$ LBGs. Although star-formation is not as extreme as in SMGs, they do experience large-scale feedback processes, probably with consequences similar to those observed in low redshift starburst galaxies: The gas is heated, the gas content of the galaxy reduced, and entropy increased, lowering or shutting off future star-formation. Metals pollute the IGM surrounding the LBG, for which direct evidence has been given by Adelberger et al. (2003). However, star-formation rates are rather moderate, and the gas will probably not become unbound from the dark-matter halo. LBGs seem to be forming stars over a relatively long period of time, but by $z \sim 0$ will have old populations and low gas contents. On the other hand, the feedback will probably only heat, but not unbind the gas from the dark-matter halo. Therefore, enhanced $[\alpha/\text{Fe}]$ ratios, as observed in the most massive early-type galaxies, and indicative of truncated star formation after a few $\times 10^8$ yrs, will not be preserved.

Maybe the most basic scale to identify the likely low-redshift fate of these galaxies is set by the observed sizes and dynamical masses. Surface mass densities can be calculated using the size and mass estimates in the previous sections. With the exception of SMMJ14011+0252 J2, all galaxies have mass surface densities of $2000 - 12000 M_{\odot} \text{pc}^{-2}$, similar to the central mass surface densities that Sofue et al. (2003) measured in late-type galaxies in the Virgo cluster. This hints that most of the mass near the cores of present-day galaxies was already in place by $z \sim 3$, albeit with very young stellar populations and a much higher gas fraction than today. Maybe this is the first intriguing evidence that galaxies formed inside-out obtained from galaxy dynamics. Elmegreen et al. (2005) come to similar conclusions based on photometric data, but also with relatively circumstantial arguments.

Perhaps not very surprising, this is in agreement with the masses of a few $\times 10^{10} M_{\odot}$ within radii of $\lesssim 5$ kpc, which again is very similar to large bulges and intermediate-size ellipticals at low redshift (Bender et al. 1992). In addition, the redshift distribution of LBGs approximately matches the typical ages of low redshift early type galaxies. This hints that indeed LBGs might be the forming low-redshift $\sim L^*$ bulges and intermediate-mass early-type galaxies. Additional evidence comes from the large-scale structure of LBGs. Adelberger et al. (1998); Giavalisco et al. (1998) find relatively short correlation lengths of ~ 4.2 Mpc (correcting for $H_0 = 70 \text{ km s}^{-1} \text{Mpc}^{-1}$), similar to correlation lengths of low-redshift early type galaxies and suggesting that they will preferably reside in comparably dense environments (Giavalisco 2002), possibly galaxy groups and clusters.

These results all point towards the same conclusion: Ultimately, $z \sim 3$ LBGs will become $\sim L^*$ early-type galaxies or intermediate-mass bulges. This is in agreement with their large-scale clustering, the ages of their stellar population, their dynamical masses, and the observed feedback.

Chapter 9

The powerful radio galaxy MRC1138-262: evidence for AGN feedback in the early universe

1. Introduction

One of the major challenges for the hierarchical model is not only to qualitatively describe the assembly of dark and baryonic matter in the Universe, but also to correctly predict the observed properties of structures at cosmic scales in a quantitative sense. One such property, which is tied in a very direct way to the assembly of dark matter, is the mass function, i.e. the number density of mass clumps ϕ as a function of their mass m :

$$\Phi = \int_{-\infty}^{\infty} \phi(M) dM \quad (9.1)$$

Comparing the *observed* mass function of galaxies with the *predicted* mass function of dark matter halos shows that the mass function of dark matter halos is both shallower than that of galaxies, and has an overabundance of halos at the high-mass end. Early simulations of cosmic structure formation described the built-up of mass inhomogeneities under the sole influence of gravity. However, in the simplest case, this will lead to unrestricted collapse of the most massive objects, and the “cooling catastrophe”. To not overpredict both the numbers of low and high mass galaxies, models of large scale structure and galaxy formation must therefore postulate a mechanism whereby some halos maintain a proportionally low gas content.

“Superwinds” – starburst driven galaxy scale outflows – are known from low-redshift studies to be efficient in driving out gas from the comparably shallow gravitational potentials of low mass galaxies (e.g., Lehnert & Heckman 1996a,b). As shown, e.g., in the previous chapters of this thesis, starburst-driven winds are common at high redshift. However, they are mainly energy driven, therefore susceptible to radiative losses, and they probably lack the power and efficiency to remove the necessary amount of gas from the most massive halos. If one wants to explain the discrepancies in the number densities of predicted dark matter halos and observed baryonic clumps at the high-mass end, therefore, another phenomenon must be included. The only seriously discussed candidate process is feedback from active galactic nuclei (AGN).

Energy- and momentum-driven AGN winds may reach very high energy output through radi-

ation pressure and particle ejection. They should be efficient in removing large quantities of gas and in principle are sufficient to explain the difference between dark matter halos and galaxy mass distributions even in the most massive galaxies (Springel et al., in prep.). As they slow and expand, they are able to heat rather evenly distributed gas like the ICM and IGM efficiently (e.g., Nath & Roychowdhury 2002). However, due to the clumpy nature of the ISM in galaxies, rather small working surface (the so-called “dentist drill” model Scheuer 1982), and AGN producing “light jets”, AGN driven winds are not generally thought to couple strongly with ambient ISM in their hosts (Begelman 1997).

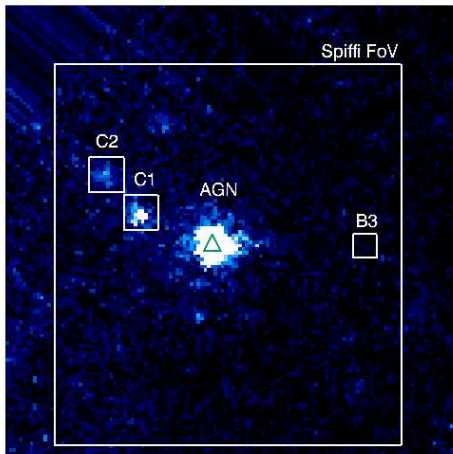


Fig. 1.— NICMOS *F160W* image of MRC1138-262 indicating the primary features.

low the tight “ $M_{BH}-\sigma$ ” relation (Ferrarese & Merritt 2000; Gebhardt et al. 2000) over a large mass range. This suggests that the black hole and the bulge growth were co-eval and perhaps self-regulated through negative feedback directly from the AGN. Thus both direct observations at high redshift and fossil evidence at low redshift require powerful and efficient feedback in the early evolution of massive galaxies.

However, no significant constraints have so far been given on the hypothesized “smoking gun” of AGN feedback that is needed to make this connection plausible. The most direct way to investigate the role of AGN feedback in the most massive galaxies is to study galaxies that are growing rapidly, are massive, and host powerful AGN. Powerful high- z Radio Galaxies (HzRGs) fit these requirements: They reside in high density environments (Venemans et al. 2002; Kurk et al. 2004; Best et al. 2003; Stevens et al. 2003). Their magnitudes, colors, and continuum morphologies are both consistent with radio galaxies having large stellar masses that from $z \approx 2 - 3$ are evolving passively (van Breugel et al. 1998). HzRGs at $z > 2 - 3$ also contain large masses of molecular gas ($10^{11} M_{\odot}$; e.g., Röttgering et al. 1997), dust ($10^{8-9} M_{\odot}$; e.g., Archibald et al. 2001; Reuland et al. 2004), and UV/optical line-emitting gas ($10^{8-9} M_{\odot}$; e.g., van Oijk et al. 1997). At the highest redshifts, they are also likely to be forming stars at prodigious rates ($100 - 1000 M_{\odot} \text{ yr}^{-1}$; e.g., Dey et al. 1997). In short, they have all the properties one might expect for the formation of a massive spheroidal galaxy.

There is an interesting convergence of these cosmological postulates with what is needed to explain the observed characteristics of massive galaxies and their black holes at low redshift. In the local Universe, the most massive galaxies, all virtually spheroidal galaxies, are “old, red, and dead”. They are metal-rich and have luminosity weighted ages consistent with high-redshift formation. The small scatter in the Fundamental Plane¹ and zero-points of its projections are in agreement with high-redshift formation and relatively similar star-formation histories. Moreover, the metal abundance ratios, especially $[\alpha/Fe]$, indicate intense star-formation truncated by strong feedback within about 1 Gyr of formation (e.g., Thomas, Greggio, & Bender 1999). Perhaps more directly, spheroidal and black hole mass are found to fol-

¹An empirical tight relationship between central velocity dispersion, surface brightness and effective radius of early-type galaxies comparable to the Tully-Fisher relation for disk galaxies.

In spite of recognizing the important role HzRGs may play in gauging the significance of AGN feedback, a lack of technology has so far limited our ability to robustly investigate its impact. All previous work by necessity used longslit spectrographs, and has focused on where the emission line gas is bright and most extended, which is along the radio jet. But this is insufficient because even the “dentist drill”, i.e., weak coupling with the ISM, predicts mechanical stirring and shock heating not only along the radio axis. Furthermore, for the feedback to satisfy the requirements of both the cosmological simulations and the detailed characteristics of massive spheroids in the local Universe, the AGN must have a significant impact on the entire ISM of the host galaxy and have a sufficiently strong coupling to remove the gas in less than few 10^8 to 10^9 yrs. The only way to test this is with integral field spectroscopy of the rest-frame optical emission line gas to obtain the overall gas dynamics and impact of mechanical heating and radiation pressure.

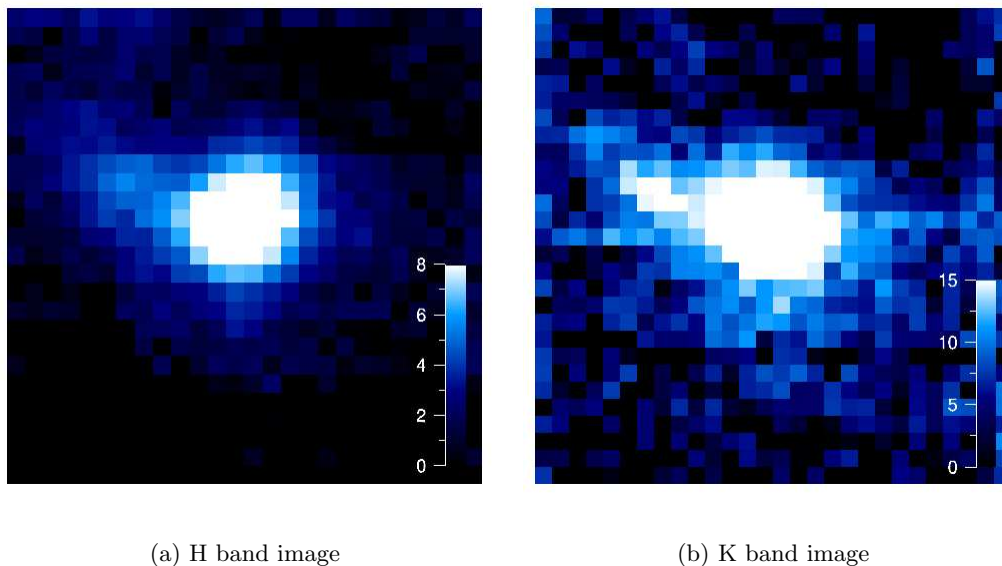


Fig. 2.— *H* (left) and *K* band (right) continuum images of MRC1138-262. All structures identified in the deeper NICMOS *F160W* image are also found here, although *C2* is only marginally detected. Colorbars indicate the flux in units of $10^{-18} \text{ W m}^{-2} \mu\text{m}^{-1} \text{ arcsec}^{-1}$.

An excellent candidate for such a study is MRC1138-262 at $z = 2.16$ ² – one of the brightest HzRGs, with magnitudes $m_K = 16.1$ mag in the *K* band and $m_H = 18.04$ mag in *H* (Pentericci 1999). Because of its brightness for a high redshift object, it is one of the best studied galaxies of this class, with observations spanning from the X-ray (keV) to the radio-range. For MRC1138-262 in particular, the emerging picture is that of a massive galaxy residing in a very inhomogeneous, clumpy environment, embedded in a giant $\text{Ly}\alpha$ ($\sim 150 \times 125$ kpc) and X-ray halo, and with two luminous, but very clumpy and irregular, radio jets (Pentericci 1999). MRC1138-262 is surrounded by an over-density of both $\text{Ly}\alpha$ and $\text{H}\alpha$ emitters (Kurk et al. 2004). Pentericci (1999) derived a (stellar) mass from *H* band photometry, suggesting $M = 5 \times 10^{11} M_\odot$. Rest-frame UV spectroscopy indicates MRC1138-262 is forming stars at rates of $40 - 70 M_\odot \text{ yr}^{-1}$. Kurk (2003) have obtained rest-frame UV spectroscopy along different lines of sight across the nebulosity, and found $\text{Ly}\alpha$, CIV, HeII and NV emission lines with widths of FWHM $\gtrsim 1000 \text{ km s}^{-1}$ and relative velocities of up to

²Using a flat $H_0 = 70 \text{ km s}^{-1}$, $\Omega_M = 0.3$, $\Omega_\Lambda = 0.7$ cosmology, size scales at $z = 2.16$ are $8.3 \text{ kpc}''$, the luminosity distance is 17070 Mpc, the angular size distance is 1710 Mpc. Cosmic age at that redshift is 3.0 Gyrs.

$\sim 1000 \text{ km s}^{-1}$.

In the SPIFFI-GI run in April 2003, data of the $z = 2.16$ powerful radio galaxy MRC1138-262 have been taken in the H and K bands, which at that redshift approximately correspond to the rest-frame V and R bands. Total exposure times were 140' in K and 75' in H, respectively. Rest-frame wavelength ranges from $4720\text{\AA} - 5630\text{\AA}$ and $6170\text{\AA} - 7500\text{\AA}$ are covered by the H and K-band observations, respectively, and several emission lines were identified, namely $H\beta$, $[\text{OIII}]\lambda\lambda 4959, 5007$, $[\text{OI}]\lambda 6300$, $[\text{NII}]\lambda\lambda 6548, 6583$, $H\alpha$, and $[\text{SII}]\lambda\lambda 6717, 6730$.

2. Integral-field portrait of a $z = 2.2$ powerful radio galaxy

2.1. Rest-frame optical morphology

The Pentecicci (1999) deep (3.6 hrs integration time) F160W (roughly H-band) HST-NICMOS image of MRC1138-262, taken from the HST archive, was reduced for this thesis. It is shown in Fig. 1 to indicate the position of several of the primary features: The AGN appears as a bright point source, which is surrounded by an $8'' \times 4''$ large, diffuse nebulosity ($\sim 50 \text{ kpc}$). Two bright knots are seen to the north-east, labeled C1 and C2. B3 indicates the position of the brightest knot in the strong (western) radio jet at about 30 kpc from the nucleus, and is also the primary $\text{Ly}\alpha$ emitter. Since this knot is very faint in the continuum, it is not detected in the F160W image.

Line-free H and K band continuum (AGN and host) images are shown in Fig. 2. Although the square-root of the flux is plotted to enhance the faint extended emission, the AGN still dominates in both the K and the H band. Significant emission was detected over an area of $\approx 6'' \times 3''$ in right ascension and declination, respectively ($\approx 50 \times 25 \text{ kpc}$ in the applied cosmology).

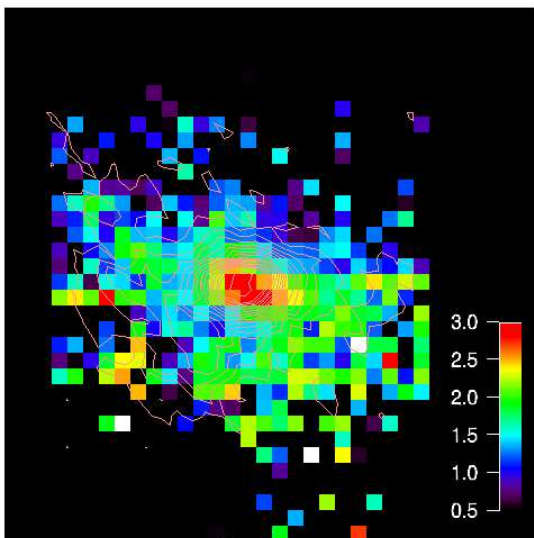


Fig. 3.— $H - K$ color image of MRC1138-262 with the contours showing the $[\text{OIII}]\lambda 5007$ line fluxes, integrated over a dynamical range of 3990 km s^{-1} .

The line-free continuum (AGN+host) image in the H band was obtained from the cube using the method outlined in Section 6 of Chapter 3. In the K band, this method cannot be used, because of the extreme width and flux of the broad $H\alpha$ line emission from the AGN (see also the next section). Therefore, the continuum redward of the $H\alpha$ line ($\gtrsim 2.15 \mu\text{m}$) is approximated by a linear fit. This fit is extrapolated over the full K band width, and averaged spectrally, to yield the line-free continuum image.

The $H - K$ color image, obtained from the line-free images, is shown in Fig. 3. The $H - K$ color was calculated for all pixels in which the continuum was detected at $S/N > 3$ in either band. Contours indicate the $[\text{OIII}]\lambda 5007$ line emission integrated over a dynamic range of 4000 km s^{-1} , which roughly equals the full width at zero intensity (FWZI) of the $[\text{OIII}]\lambda 5007$ emission line in the extended emission.

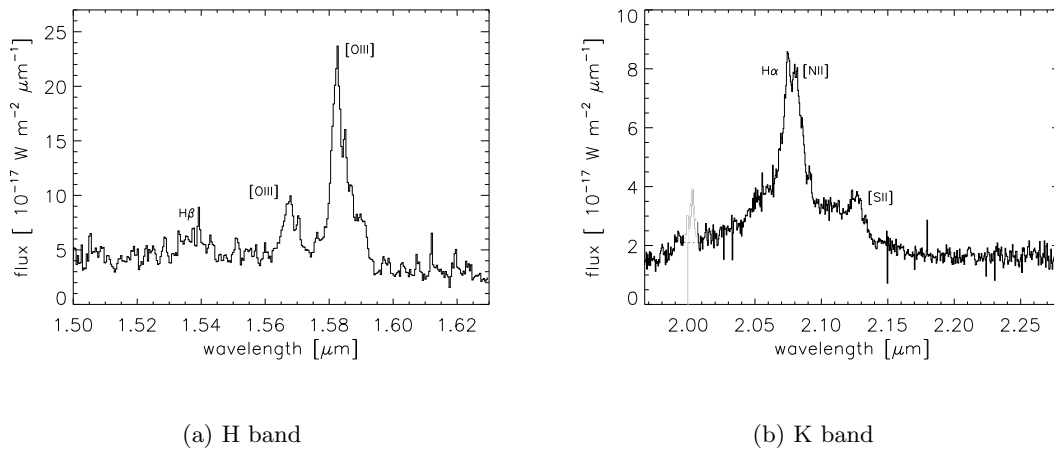


Fig. 4.— *Integrated spectra of the innermost $0.75'' \times 0.75''$ of MRC1138-262. Broad $H\alpha$ and $H\beta$ components are clearly identified. $[OIII]$ lines have very complex profiles caused by the extreme kinematics of the extended line emission. The dotted line in the K band indicates a region of strong telluric residuals which were clipped.*

The reddest feature is obviously the AGN, with $H - K \sim 3$. As will be discussed in the next section, the AGN is highly obscured, so the red color is likely explained with extinction. The AGN appears somewhat elongated, which is a result of the non-circular SPIFFI-PSF.

A region of comparably blue emission stretches north-east ($H - K \sim 1$). Two small areas of somewhat redder color are embedded into this zone (at P.A. $\sim 290^\circ$), coincident with C1 and C2. Towards south-west (P.A. $\sim 0 - 90^\circ$) $H - K$ colors are redder, with $H - K \sim 1.5 - 2$. Although poorly constrained, this area seems to roughly coincide with the position of the radio jet (as can be seen by comparison with Pentecicci 1999). Continuum emission from the $Ly\alpha$ bright B3 object is too faint to be measured.

2.2. Removal of the AGN emission

Based on rest-frame UV emission, MRC1138-262 has previously been considered a narrow-line radio galaxy. Emission lines at rest-frame UV wavelengths are found to have FWHMs of $\mathcal{O}(1300 \text{ km s}^{-1})$ and comparably low ($\sim 50 - 70 \text{ \AA}$) equivalent widths (Kurk 2003). The Balmer lines in the SPIFFI spectra, however, differ dramatically from the line emission commonly observed in narrow-line radio galaxies.

The integrated H and K band spectra of MRC1138-262 are shown in Fig. 4. Especially $H\alpha$ is surprisingly broad ($FWHM = 14300 \text{ km s}^{-1}$), which is rather extreme even compared to most broad line radio galaxies, (see Sulentic et al. 2000), and emits $\sim 60\%$ of the total K band flux, reaching an equivalent width of 1615 \AA . In H, the situation is equally complex, the $[OIII]\lambda\lambda 4959, 5007$ doublet is very luminous and obviously composed of a number of components with different widths and relative velocities. $H\beta$ is very faint, a broad $H\beta$ component can hardly be discerned, a narrow component is not observed. Using the Balmer decrement of 2.9, and applying the formalism outlined in section 1.3, the resulting extinction amounts to $A_V = 8.7$. In plain words, the nucleus of MRC1138-262 is optically thick at optical wavelengths.

Comparing the near-infrared and optical morphology of MRC1138-262, e.g. the F160W (roughly H band) image taken with NICMOS (see Fig. 1 and the FORS B-band image), give a similar impression: At longer wavelengths, MRC1138-262 shows a bright nuclear point source consistent with an AGN, which does not appear at shorter wavelengths. These findings are consistent with MRC1138-262 harboring an obscured quasar rather than being a radio-galaxy. A similar picture was obtained for the $z = 2.5$ radio-galaxy MRC2025-218 (Larkin et al. 2000), which, however, has a much different overall morphology. At present, this type of AGN is poorly understood.

The AGN obviously complicates the analysis of the extended emission. However, this can partly be overcome by the integral-field nature of the SPIFFI data, because imaging and spectroscopic data can be corrected for the AGN emission simultaneously.

In the present analysis, this was especially exploited for the K-band data cube, where the luminous broad $H\alpha$ emission line was used to directly estimate the AGN contribution on a pixel-to-pixel base. For each pixel, the continuum redward of $H\alpha$ ($\lambda > 2.15 \mu\text{m}$) was approximated by a linear fit which is extrapolated to the low-wavelength edge of the K band ($\sim 1.95 \mu\text{m}$). Scaled fractions of the spatial pixel containing the nucleus are then removed from all other pixels (in decreasing steps of 1 % of the broad line flux), until a best fit to the linear continuum is obtained. The incremental removal automatically accounts for the AGN power-law continuum of the AGN, because the entire nuclear spectrum is scaled and removed, and not just the broad-line emission. The algorithm stops when less than 1 % removal is necessary.

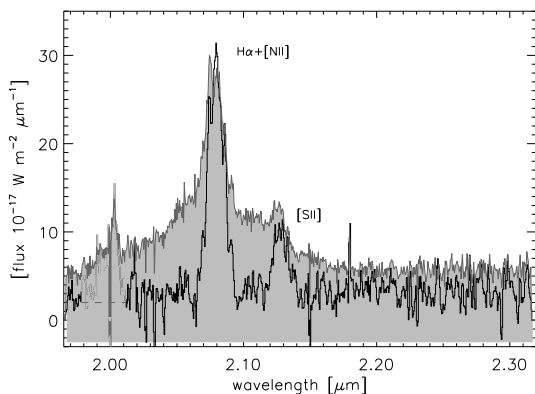


Fig. 5.— *Integrated K band spectrum after AGN removal. Gray regions show the AGN spectrum integrated over the central 3×3 pixels for comparison and is scaled arbitrarily. Strong night sky line residuals at $\lambda \approx 2 \mu\text{m}$ were clipped in the integrated spectrum.*

this procedure was found to be more precise than e.g. fitting the narrow $[\text{OIII}]\lambda 5007$ emission in the spectra or the PSF in the continuum image. As a consequence of the worse fit, the extended $[\text{OIII}]\lambda 5007$ emission was examined only where the velocity offset from the nucleus exceeds the FWHM of the nuclear part of the narrow-line regions or if the spatial offset from the nucleus is sufficiently large so that even in the K band no broad line emission was observed. Due to the large kinematic offsets, this is luckily the case for most of the line emission found in MRC1138-262.

This procedure helps removing the AGN flux efficiently, as no residuals resembling the broad $H\alpha$ line were found when integrating over several pixels in the AGN-removed data cube. In particular, this method yields better results than scaling the AGN flux according to the PSF. This might be due to the luminous extended line emission, or hint internal variations in the photoionization, scattering or attenuation of the AGN emission within the host galaxy.

Although $H\beta$ in the H band is equally broad, it is not luminous enough to be used in the same way as $H\alpha$. Therefore, the (roughly power-law) slope of the H band continuum emission is used in an analogous way as the broad $H\alpha$ line in the K band to remove the scaled nuclear spectrum from the other spatial pixels. Although this does not yield results that are as good as in K (residual broad $H\beta$ emission appears when integrating over several pixels),

2.3. Kinematics of the diffuse emission line gas within the inner ~ 20 kpc

Fig. 4 reveals the unusually rich kinematics of the extended emission of MRC1138-262. This becomes most obvious in the $[\text{OIII}]\lambda 5007$ emission line, which clearly has contributions from several components with different velocities and widths. The FWHM of the integrated line is $FWHM = 3990 \text{ km s}^{-1}$. These extreme kinematics make it impossible to use the $\text{H}\alpha$ line as dynamical tracer, because it merges with the nearby $[\text{NII}]\lambda 6583$ line ($\Delta v(\text{H}\alpha, [\text{NII}]) \approx 900 \text{ km s}^{-1}$). Accordingly, $[\text{NII}]/\text{H}\alpha$ line ratios cannot be accurately measured. Typical ratios observed in AGN range from ~ 0.7 to >3 (Osterbrock 1989), so that the ratio cannot properly be constrained by analogy with other sources. These uncertainties will also concern the kinematics, if it is based on $\text{H}\alpha$ line emission, therefore the kinematics of the diffuse gas were derived from the relative shifts of the $[\text{OIII}]\lambda 5007$ line.

The complexity of the kinematic field around MRC1138-262 clearly requires spectroscopy with integral-field devices. To be not affected from the direct AGN emission (even the NLR), the AGN-removed data cubes were used. To approximate the seeing and spectral resolution, the cubes were smoothed by 3 pixels both in spectral and the two spatial directions. The spectral smoothing will lower the resolution. Given the extreme velocities and line widths, this is negligible. Spectra were extracted and fitted separately for each spatial element within radii of ~ 25 kpc from the nucleus of MRC1138-262.

Lines were fitted with SPLOT, up to three individual kinematic components were identified in the $[\text{OIII}]\lambda 5007$ emission line of each spatial element. Subsequently, the significance of the line detection was examined for each identified component, and components detected at $<3\sigma$ were excluded from further analysis. A total of ~ 550 $[\text{OIII}]\lambda 5007$ components in 300 spatial pixels was obtained.

This method is prone to large systematic errors, especially in the line fluxes. In addition, the AGN removal in the H band is not very precise. Therefore, these spectra were only used to identify zones of rather uniform kinematics, whereas the properties of these zones, and especially line ratios, were derived from spectra integrated over these larger areas, profiting from the higher signal to noise ratio.

Relative velocities of the $[\text{OIII}]\lambda 5007$ line are shown in Fig. 6 as a function of (the apparent) radial distance from the nucleus. This figure includes all fitted line components with $>3\sigma$. The velocities fall into 4 intrinsically rather uniform groups, possibly rising or outflowing bubbles, with radii of $R_i = 1 - 2''$ (8 – 16 kpc) and spanning over the total radius of $R_{tot} \gtrsim 3''$ (25 kpc). A small number of data points cannot uniquely be assigned to a particular group, but shows some overlap. However, this concerns only a minor fraction of the total available data, and does not seriously affect the very clear kinematic distinction between the different kin-

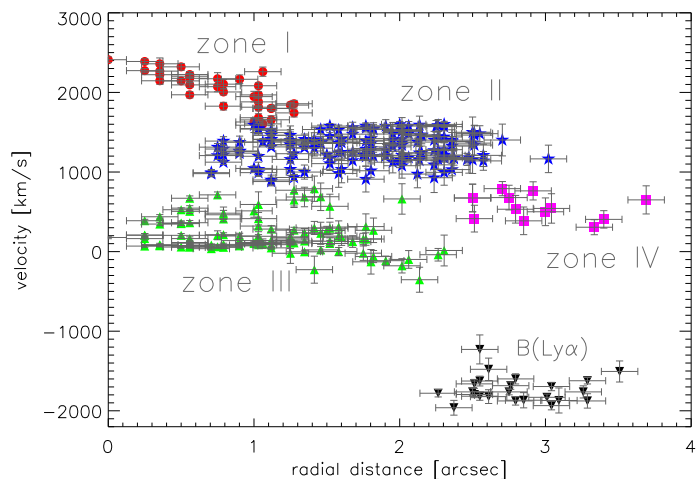


Fig. 6.— *Relative velocities in the nebulosity of MRC1138-262 as a function of projected distance from the nucleus.*

matic zones. Fig. 6 also gives the labels of the bubbles which will be used hereafter. The structure indicated by the black upside-down triangles has previously been identified as the Ly α bright radio knot B3 (Pentericci 1999). The term “bubble” should not be understood in too close analogy to the buoyantly rising low-density regions observed in low-redshift radio galaxies. In this context it refers to the clearly separated areas in velocity space, that appear rather complex internally, but comparably uniform.

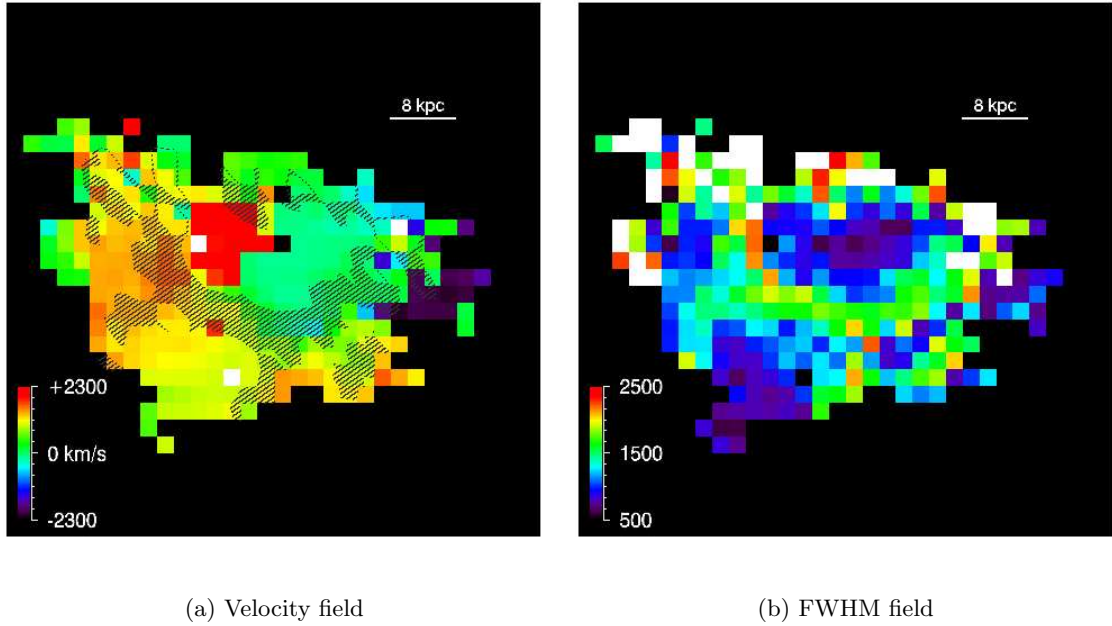


Fig. 7.— Velocities measured in each spatial pixel of the SPIFFI data cube. The hatched regions indicate the location of pixels where the maximum FWHM $> 1400 \text{ km s}^{-1}$.

To illustrate the projected spatial distribution of the different regions, and especially their dependence on position angle, which is not considered in Fig. 6, Fig. 7 shows a map of the relative velocities of the brightest [OIII] $\lambda 5007$ line component in each spatial pixel. Again, the separation into at least three distinct kinematic regions, each separated in velocity space by $\sim 1000 \text{ km s}^{-1}$, but with rather narrow intrinsic velocity spread, is evident. Velocities in region 1 decline with increasing projected distance from the nucleus, gradually approaching the values in region 2 at the eastern bound. This is in agreement with Fig. 6, which also suggests that the velocities in region 1 at its low-velocity end approach the velocities in region 2. Zone 3 has largely uniform intrinsic velocities, whereas velocities in zone 2 vary gradually with P.A. and reach a maximum at $\sim P.A. = 230$.

Minimum FWHMs found within the extended emission of MRC1138-262 are about 800 km s^{-1} . This and the extreme velocity range rule out that the observed dynamics are due to virialized gravitational motion, which would lead to a more regular kinematic field, more regular velocity gradients of a few hundred km s^{-1} , and line FWHMs of $\mathcal{O}(200-300) \text{ km s}^{-1}$. Galactic winds as a consequence of star-formation cannot yield the necessary input energy to explain these extreme kinematics, e.g. terminal wind velocities in starburst galaxies are $\sim 300 \text{ km s}^{-1}$ (Lehnert & Heckman 1996a,b). To explain the extreme kinematics in MRC1138-262, therefore a more powerful dynamical driver is required, which can only be the AGN. The physical properties of the AGN feedback and their cosmological consequences will be discussed in Section 4 and following sections.

None of the spectra extracted from the extended emission around MRC1138-262 show stellar features, although the UV-emission hints the formation of $40 - 60 M_{\odot}$ (Kurk 2003) and should lead to noticeable optical line emission. Given the extreme dynamics of the AGN-driven gas, it appears nearly impossible to isolate the more subtle (more narrow, smaller velocity range, possibly fainter) emission line signature of young stellar populations.

It might appear contradictory at first sight, that the gas dynamics are attributed to AGN-related outflows, although nearly all relative velocities are redshifted with respect to the nuclear emission. This might indicate that also the AGN narrow line region has a negative line-of-sight velocity component, as would be natural for outflows if the orientation of the AGN is near the line of sight. This is probably the case, because the luminous broad-line emission is a clear indication that sight-lines deep into the AGN exist. Alternatively, outflows can appear redshifted when the rear side of an expanding bubble appears brighter than the front side. These differences will not affect the discussion of the emission line kinematics in Section 5, because the relative velocities remain equally large, or even increase, independently of the chosen reference frame.

Maximum FWHMs in each pixel are shown in the right panel of Fig. 7. The most striking feature is a ring of broad lines ($\sim 1400 - 2500 \text{ km s}^{-1}$) around the narrower line emission ($\sim 800 \text{ km s}^{-1}$) of zones 1 and 3, which is best seen in Fig. 7, where regions with emission line widths $>1400 \text{ km s}^{-1}$ are shown as hatched areas. These extended broad-line regions might be due to overlaps between neighboring bubbles or indicate enhanced turbulence where the boundaries of the distinct gas masses interact. The coincidence is not perfect: The high-velocity emission in zone 1 is of uniform width ($\sim 2500 \text{ km s}^{-1}$), and does not show a surrounding broad-line emitting ring, whereas zone 2 appears intersected by at least three less pronounced rings of broad lines. The first might be due to different inclinations between the bubbles with the line of sight, the second might be a sign that it further separates into two distinct gas masses. Because velocities are not very distinct, however, zone 2 is not further dissected.

In the following, the three individual major bubbles will be analyzed in more detail. The complexity of the spectra makes it difficult to find a unique, well-constrained fit. The following method helps to reduce the number of free parameters: The $[\text{OIII}]\lambda 5007$ line in the H-band is fitted first, to constrain the number of components based on the best isolated and brightest line. Components are added until the fit residuals are within the noise and do not lead to artifacts in the $[\text{OIII}]\lambda 4959$ line. The ratios within the $[\text{OIII}]\lambda\lambda 4959, 5007$ and $[\text{NII}]\lambda\lambda 6548, 6583$ doublets are forced to be $R(4959/5007) = R(6548/6583) = 0.3$. Broad lines are fitted first, the residual narrow lines later. This might tendentially lead to an overestimate of the broad line emission. However, if the number of free parameters is to be minimized, then this is unavoidable.

In the H-band fits, the full data cube was used (i.e., the narrow $[\text{OIII}]$ emission from the AGN is included) before fitting the extended emission. Line emission within one FWHM of the nuclear $[\text{OIII}]\lambda\lambda 4959, 5007$ lines was individually fitted with a Gaussian and subtracted from each of the integrated H-band spectra. The position and width of the AGN $[\text{OIII}]\lambda\lambda 4959, 5007$ line were fixed to the same values in each region, so that only the line flux remained as free parameter.

Subsequently, the K-band spectra were fitted, restricting the fits to have approximately the same redshifts and line widths as found in the H-band spectra. Only the relative line strengths will then remain as free parameters. This would be a powerful way to constrain the $[\text{NII}]/\text{H}\alpha$ ratio, if off-nuclear $\text{H}\beta$ was detected at good signal-to-noise. In spite of extinction, the observed $\text{H}\beta/\text{H}\alpha$ ratio would at least set a lower limit on the expected $\text{H}\alpha$ emission. Unfortunately, the extended $\text{H}\beta$ emission is rather faint, so that $[\text{OIII}]\lambda 5007$ had to be used, which is the only line that can be reasonably well isolated within the full dynamic range of the diffuse gas.

It might not be strictly correct that the [OIII] λ 5007 fit parameters will be representative for the K-band as well, especially H α . Nonetheless, both lines are bright enough to expect that any cloud emitting [OIII] will have some H α emission, too, so that the basic dynamical properties (i.e. line width and redshift) will be rather similar, and only the relative line fluxes will change. It is difficult to give good H α flux estimates, because of the blending with [NII]. The H α luminosity will be used subsequently to give a lower limit to the power of the outflow in MRC1138-262. For consistency with this analysis, it was tried to maximize the [NII]/H α ratios in the line fits, while respecting the above constraints.

Region 1

This zone extends north-east and is directly adjacent to, but offset from, the nucleus. It has a size of $\sim 1'' \times 1.25''$ in right ascension and declination, respectively ($\sim 8 \times 10$ kpc). Taking the average of the two sides as a representative approximate diameter of this region and assuming that its intrinsic shape is approximately spherical, the occupied volume is 1.1×10^{61} m³.

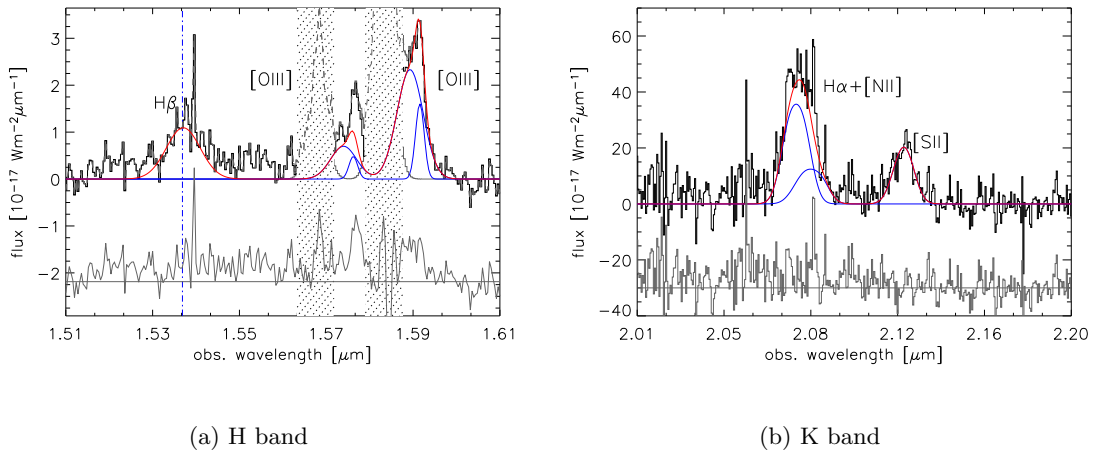


Fig. 8.— *Integrated H and K-band spectra of all pixels of zone 1 are shown as black line. For the H-band, the width of the nuclear [OIII] lines is shown as hatched regions. The overall fit is shown as red line, individual components are shown in blue. The lower grey spectra show the fit residuals.*

The highest relative velocities observed within the extended nebulosity of MRC1138-262 are reached in this zone, which are between 1600 km s^{-1} and 2400 km s^{-1} and systematically decrease with increasing distance to the AGN. This zone appears red in the velocity map shown in Fig. 16.

The integrated H and K band spectra are shown in Fig. 8. The [OIII] lines were fitted with 4 components at redshifts between 2.161 and 2.173, and FWHMs between 870 km s^{-1} and 2700 km s^{-1} . Overall line ratios can be given by integrating over all subcomponents in this region. A (for this source) rather extreme $[NII]/H\alpha = 1$ is found, and $[SII]/H\alpha = 0.22$. The $H\alpha/H\beta$ ratio is nominally 2.7, but is affected by broad H β emission from the nearby AGN, which is difficult to quantify, and which could not adequately be removed from the spectrum. It is therefore not used to derive an extinction. $[OIII]/H\beta = 5.2$, which again should be taken as a lower limit, because of the AGN contribution to H β .

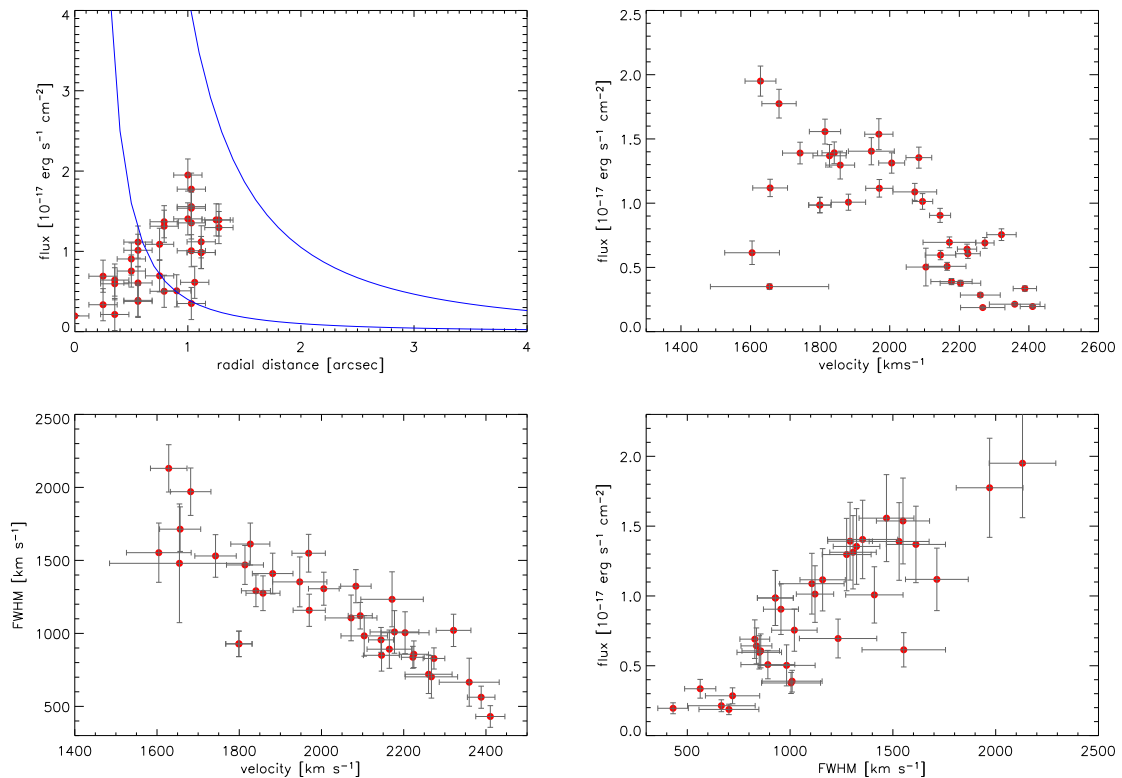


Fig. 9.— *Emission line features within zone 2 and correlations.*

To examine the spatial distribution of line emission within zone 1 in more detail, the discussion will now return to the fitted emission lines the “high resolution” data, i.e. in every spatial element. Fig. 9 shows the properties of the fitted emission lines assigned to zone 1 in each spatial bin. “Fluxes” are the integrated line fluxes within one spatial element, i.e. flux contained in the spatial pixels smoothed over boxes of $0.75'' \times 0.75''$. Hence, double-counting of pixels does occur, because all individual pixels are included if they have $S/N > 3$. If more than one [OIII] line component was detected in the same spatial element, then all components are included. The four diagrams show a few interesting correlations:

Velocity is negatively correlated with distance. Pearson’s correlation coefficient is rather low ($R = -0.15$), however, this can be explained with the rather large scatter of the data. In this case, non-parametrized correlation tests are more appropriate. Both the Spearman rank-test and Kendall’s τ yield correlation probabilities of $< 10^{-6}$ that the data are correlated. Velocity is also negatively correlated with width. Pearson’s correlation coefficient is $R = -0.84$, both non-parametrized tests yield probabilities better than 10^{-9} .

In addition, velocity is negatively correlated with flux. Although not with a very good correlation coefficient ($R = -0.67$), the correlation is more pronounced in the non-parametrized tests (both yield probabilities $< 10^{-6}$). And finally, width is positively correlated with flux, $R = 0.99$. The non-parametrized tests have significances $< 10^{-9}$.

The strong correlation between projected distance from the AGN and flux is obviously in contradiction to photoionization being the main heating process of the gas, because in this case, line fluxes should decrease with increasing radius, following an inverse square law. The expected distribution is indicated qualitatively by the two dotted grey lines in the upper left panel of Fig. 9.

The negative correlation between velocity and radius is also untypical for a classical wind, because the gas would then be accelerated as it moves away from the nucleus. Correlations of this kind have been described by Dopita & Sutherland (1995) to be the result of deceleration shocks, as the high-velocity material heated by the AGN hits against the confining higher-density ISM and is slowed down.

Table 1:: Emission lines in zone 1

zone (1)	line (2)	λ_{rest} (3)	z (4)	λ_{obs} (5)	FWHM (6)	true FWHM (7)	flux (8)
1	H α	6563	2.1730 ± 0.0004	2.0824 ± 0.0002	141 ± 6	2027 ± 82	1.72 ± 0.1
1	[NII]	6583	2.1730 ± 0.0004	2.0888 ± 0.0002	141 ± 6	2020 ± 82	1.72 ± 0.1
1	[OIII]	4959	2.1730 ± 0.0003	1.5735 ± 0.001	141 ± 28	2685 ± 540	1.26 ± 0.32
1	[OIII]	5007	2.1730 ± 0.0006	1.5887 ± 0.0003	141 ± 7	2660 ± 130	3.50 ± 0.32
1	H α	6563	2.1613 ± 0.0001	2.0748 ± 0.0001	141 ± 2	2034 ± 33	4.18 ± 0.1
1	[NII]	6583	2.1613 ± 0.0001	2.0811 ± 0.0001	141 ± 2	2028 ± 33	4.18 ± 0.1
1	[SII]	6717	2.1613 ± 0.0004	2.1234 ± 0.003	141 ± 7	1987 ± 110	1.35 ± 0.09
1	[SII]	6730	2.1613 ± 0.0003	2.1276 ± 0.0002	141 ± 5	1983 ± 67	2.09 ± 0.09
1	(H β)	4861	2.1613 ± 0.002	1.5367 ± 0.001	188 ± 24	3669 ± 466	2.19 ± 0.3
1	[OIII]	4959	2.1775 ± 0.008	1.5757 ± 0.004	47 ± 29	882 ± 553	0.289 ± 0.4
1	[OIII]	5007	2.1775 ± 0.0006	1.5910 ± 0.0031	47 ± 8	874 ± 143	0.803 ± 0.19
1	[OIII]	4959	2.1610 ± 0.0004	1.5675 ± 0.0022	94 ± 5	1793 ± 102	2.53 ± 0.19
1	[OIII]	5007	2.1610 ± 0.0001	1.5827 ± 0.0006	94 ± 2	1776 ± 34	7.01 ± 0.17

Column (1) – Location. Column (2) – Line ID. Column (3) – Observed wavelengths in μm . Column (4) – Redshift of the line. Column (5) – Full-width at half-maximum measured for H α in \AA . Column (6) – Intrinsic FWHMs corrected for instrumental resolution units of km s^{-1} . Column (7) – Line fluxes in units of $10^{-19} \text{ W m}^{-2}$.

Although it is clear that this is a zone of strong jet-cloud (or jet-ISM) interactions, the exact mechanism is more difficult to constrain. The observed relative velocities are in the range predicted for jet entrainment: As the (mildly supersonic) jet passes through the denser ISM, Kelvin-Helmholtz instabilities will occur along the boundaries and drive large turbulent vortices with line-of-sight velocities of $\sim 3000 \text{ km s}^{-1}$. The uncertain inclination of the outflow in zone 1 with the line of sight leads to correction factors of up to a few, so that the agreement between the observed velocity of $\sim 1700 \text{ km s}^{-1}$ and the expected velocity of $\sim 3000 \text{ km s}^{-1}$, and also the turbulent FWHMs in the same range, give good indications that zone 1 is the location of the strongest interaction between the jet and the ISM. This picture is also in agreement with the “shock+precursor” model derived from the line ratios.

Region 2

This area spans nearly across the northern hemisphere of the AGN, from P.A. 50° - 300° , but is not directly adjacent to the nucleus, possibly because it lies behind the two other bubbles and is partly covered if their optical depth is sufficiently high. It appears very elongated and bent, its projected surface is $\sim 9.5 \square''$, or 38 kpc^2 . With the same method as used for region 2, this corresponds to an estimated volume of $2.05 \times 10^{62} \text{ m}^3$. It should be noted that this volume approximates only the visible volume. If this regions stretches towards the nucleus, and is partially hidden, then the occupied volume would be accordingly larger.

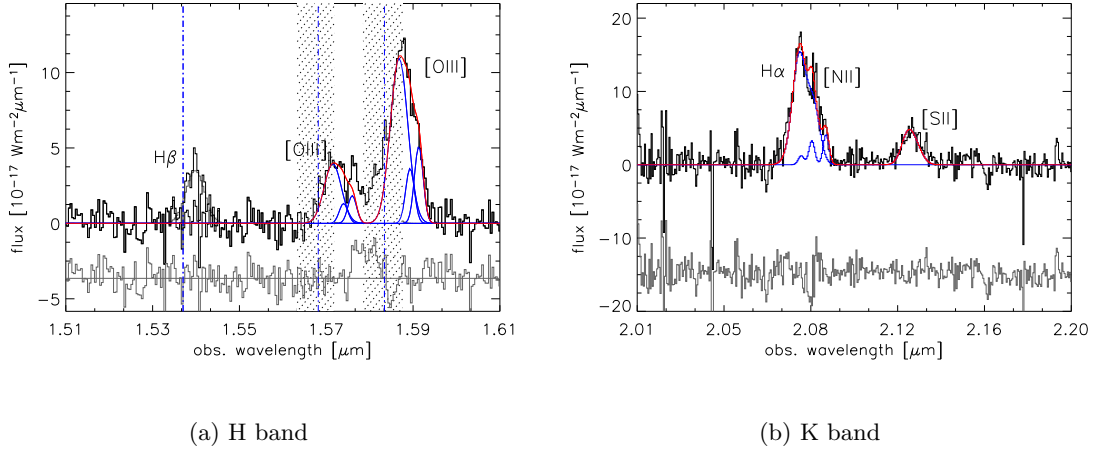


Fig. 10.— Integrated H and K -band spectra of all pixels of zone 2 are shown as black lines. For the H -band, the width of the nuclear $[OIII]$ lines is shown as hatched regions. The overall fit is shown as red line, individual components are shown in blue. The lower grey spectra show the fit residuals.

Velocities in zone 2 range from ~ 800 km s $^{-1}$ to 1500 km s $^{-1}$. This bubble is shown in blue in Fig. 7.

No clear correlations can be found within this zone. The relationship between flux and distance from the AGN (upper left panel of Fig. 11) indicate that the line fluxes approximately follow an r^{-2} -law (the two gray lines). This shows that photoionization has a large contribution to the overall gas heating. Other kinematic parameters appear mostly uncorrelated with each other and with flux, which is also a sign of photoionization dominating the gas heating.

Table 2:: Emission lines in zone 2

zone (1)	line (2)	λ_{rest} (3)	z (4)	λ_{obs} (5)	FWHM (6)	true FWHM (7)	flux (8)
2	[OIII]	4959	2.1613 ± 0.0007	1.5677 ± 0.0003	84 ± 8	1613 ± 167	0.711 ± 0.1
2	[OIII]	5007	2.1613 ± 0.0002	1.5829 ± 0.00011	84 ± 3	1597 ± 50	1.97 ± 0.08
2	[OIII]	4959	2.6800 ± 0.0001	1.8249 ± 0.00007	84 ± 1	1383 ± 25	3.56 ± 0.08
2	[OIII]	5007	2.6800 ± 0.00004	1.8426 ± 0.00002	84 ± 1	1370 ± 10	9.85 ± 0.09
2	[OIII]	4959	2.1770 ± 0.0002	1.5755 ± 0.00010	47 ± 2	882 ± 41	0.920 ± 0.06
2	[OIII]	5007	2.1770 ± 0.00007	1.5907 ± 0.00004	47 ± 1	874 ± 15	2.55 ± 0.06
2	H α	6563	2.1770 ± 0.0003	2.0851 ± 0.0014	47 ± 4	659 ± 55	1.64 ± 0.18
2	[NII]	6583	2.1770 ± 0.0002	2.0914 ± 0.0001	47 ± 3	657 ± 41	2.05 ± 0.18
2	[OIII]	4959	3.1680 ± 0.0001	1.5710 ± 0.00006	94 ± 1	1789 ± 28	3.95 ± 0.08
2	[OIII]	5007	3.1680 ± 0.00004	1.5862 ± 0.00003	94 ± 1	1772 ± 10	10.9 ± 0.09
2	H α	6563	3.1680 ± 0.00008	2.0792 ± 0.0005	103 ± 1	1485 ± 16	15.9 ± 0.22
2	[NII]	6583	3.1680 ± 0.0001	2.0855 ± 0.00009	103 ± 2	1480 ± 29	9.01 ± 0.2
2	[SII]	6717	3.1680 ± 0.0003	2.1279 ± 0.0002	103 ± 4	1450 ± 59	4.51 ± 0.24
2	[SII]	6730	3.1680 ± 0.0007	2.1321 ± 0.0005	103 ± 13	1448 ± 186	1.80 ± 0.29

Column (1) – Location. Column (2) – Line ID. Column (3) – Observed wavelengths in μm . Column (4) – Redshift of the line. Column (5) – Full-width at half-maximum measured for H α in \AA . Column (6) – Intrinsic FWHMs corrected for instrumental resolution units of km s $^{-1}$. Column (7) – Line fluxes in units of 10^{-19} W m $^{-2}$.

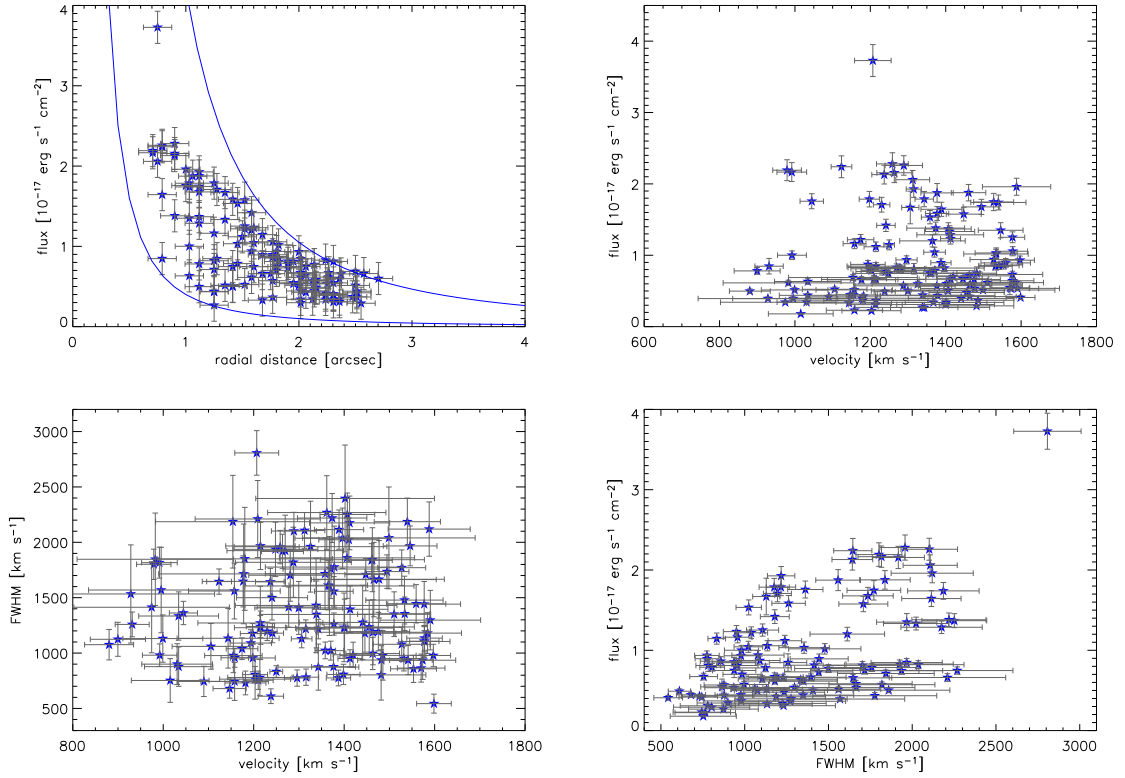


Fig. 11.— *Emission line features within zone 2 and correlations.*

Measured line ratios in this zone are $[\text{NII}]/\text{H}\alpha = 0.63$, $[\text{SII}]/\text{H}\alpha = 0.25$, $\text{H}\alpha/\text{H}\beta = 4.54$, and $[\text{OIII}]/\text{H}\beta = 6.6$. This region is comparably far away from the AGN, hence $\text{H}\beta$ is probably dominated by the extended emission. This finds strong support from the observation, that also broad $\text{H}\alpha$ emission has no major contribution to the integrated emission of this bubble, if the uncorrected cube is used. Hence, the $\text{H}\beta$ emission is taken to be extended.

Region 3

The third region of distinct gas dynamics occupies the south-western quadrant of the diffuse gas, and also comprises the nucleus. Its projected shape appears comparably spherical with a diameter of about $2.5''$ ($\sim 20 \text{ kpc}$). This yields an estimated volume of $1.2 \times 10^{62} \text{ m}^3$.

Velocities are rather moderate, ranging from systemic values to $\sim 800 \text{ km s}^{-1}$. In the velocity map it appears as the green area. Its eastern part overlaps with zone 1 (components consistent with the either of the bubbles were identified in the spectra). To the west it is confined by the bright $\text{Ly}\alpha$ emitter B, to the south by the eastern part of zone 2.

The width map (Fig. 7) reveals a comparably regular structure: An area of relatively narrow line emission ($\text{FWHM} \sim 700 \text{ km s}^{-1}$) is centered $\sim 0.75''$ (6 kpc) away from the AGN. It is surrounded almost in its entirety by a ring at similar velocity, but with substantially larger width ($\text{FWHM} \gtrsim 1400 \text{ km/s}$).

As in bubble 2, the upper left panel of Fig. 13 indicates that lines fluxes decrease with increasing radius, and roughly follow an inverse square law (indicated by the grey envelopes). Velocity and flux

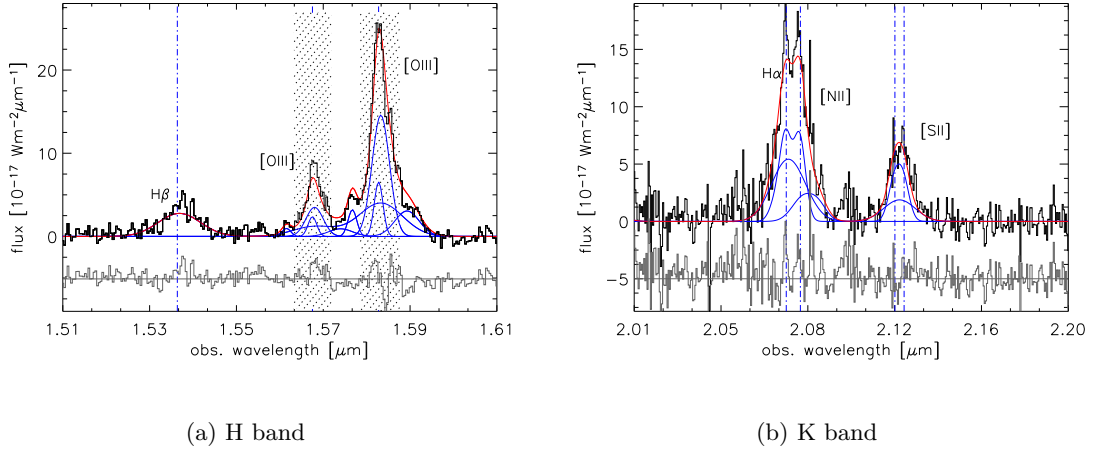


Fig. 12.— Integrated H and K -band spectra of all pixels of zone 3 are shown as black lines. For the H -band, the width of the nuclear $[OIII]$ lines is shown as hatched regions. The overall fit is shown as red line, individual components are shown in blue. The lower grey spectra show the fit residuals. The broad $H\beta$ line originates from the AGN.

however show a positive correlation (lower left panel of Fig. 13), which broadens for large values. This can be explained with an outflow being accelerated and more broadened, as the kinetic energy is dissipated. Velocities and line widths are unrelated to the flux, in agreement with assuming photoionization to be the major heating process, or again a radius-dependent density gradient.

Table 3:: Emission lines in zone 3

zone (1)	line (2)	λ_{rest} (3)	z (4)	λ_{obs} (5)	FWHM (6)	true FWHM (7)	flux (8)
3	$H\alpha$	6563	2.1728 ± 0.0005	2.0823 ± 0.0004	141 ± 9	2027 ± 131	2.46 ± 0.21
3	$[NII]$	6583	2.1728 ± 0.0005	2.0886 ± 0.0004	141 ± 9	2021 ± 131	2.46 ± 0.21
3	$[OIII]$	4959	2.1728 ± 0.0003	1.5734 ± 0.0003	131 ± 5	2506 ± 103	1.55 ± 0.08
3	$[OIII]$	5007	2.1728 ± 0.0002	1.5886 ± 0.00008	131 ± 2	2482 ± 37	4.29 ± 0.08
3	$H\alpha$	6563	2.1608 ± 0.00009	2.0744 ± 0.00006	94 ± 1	1352 ± 20	7.87 ± 0.16
3	$[NII]$	6583	2.1608 ± 0.00009	2.0807 ± 0.00006	94 ± 1	1347 ± 20	7.87 ± 0.16
3	$[SII]$	6717	2.1608 ± 0.0002	2.1231 ± 0.0002	94 ± 3	1320 ± 50	3.28 ± 0.17
3	$[SII]$	6730	2.1608 ± 0.0002	2.1272 ± 0.0001	94 ± 3	1318 ± 47	3.44 ± 0.17
3	$H\alpha$	6563	2.1608 ± 0.0003	2.0744 ± 0.0002	235 ± 5	3397 ± 72	9.01 ± 0.25
3	$[NII]$	6583	2.1608 ± 0.0006	2.0807 ± 0.0004	235 ± 9	3387 ± 137	4.92 ± 0.26
3	$[SII]$	6717	2.1608 ± 0.0002	2.1231 ± 0.001	235 ± 31	3319 ± 441	2.05 ± 0.34
3	$[SII]$	6730	2.1608 ± 0.0011	2.1272 ± 0.0007	235 ± 18	3313 ± 256	2.87 ± 0.29
3	$[OIII]$	4959	2.1610 ± 0.00010	1.5675 ± 0.00005	94 ± 1	1793 ± 22	4.20 ± 0.07
3	$[OIII]$	5007	2.1610 ± 0.0003	1.5827 ± 0.00001	94 ± 1	1776 ± 6	14.6 ± 0.07
3	$[OIII]$	4959	2.1600 ± 0.0001	1.5670 ± 0.00006	47 ± 1	887 ± 28	1.19 ± 0.16
3	$[OIII]$	5007	2.1600 ± 0.00004	1.5822 ± 0.00002	47 ± 1	879 ± 10	3.28 ± 0.05
3	$[OIII]$	4959	2.1480 ± 0.0003	1.5611 ± 0.0001	47 ± 3	891 ± 63	0.58 ± 0.05
3	$[OIII]$	5007	2.1480 ± 0.0009	1.5762 ± 0.00005	47 ± 1	882 ± 20	1.60 ± 0.05

Column (1) – Location. Column (2) – Line ID. Column (3) – Observed wavelengths in μm . Column (4) – Redshift of the line. Column (5) – Full-width at half-maximum measured for $H\alpha$ in \AA . Column (6) – Intrinsic FWHMs corrected for instrumental resolution units of km s^{-1} . Column (7) – Line fluxes in units of $10^{-19} \text{ W m}^{-2}$.

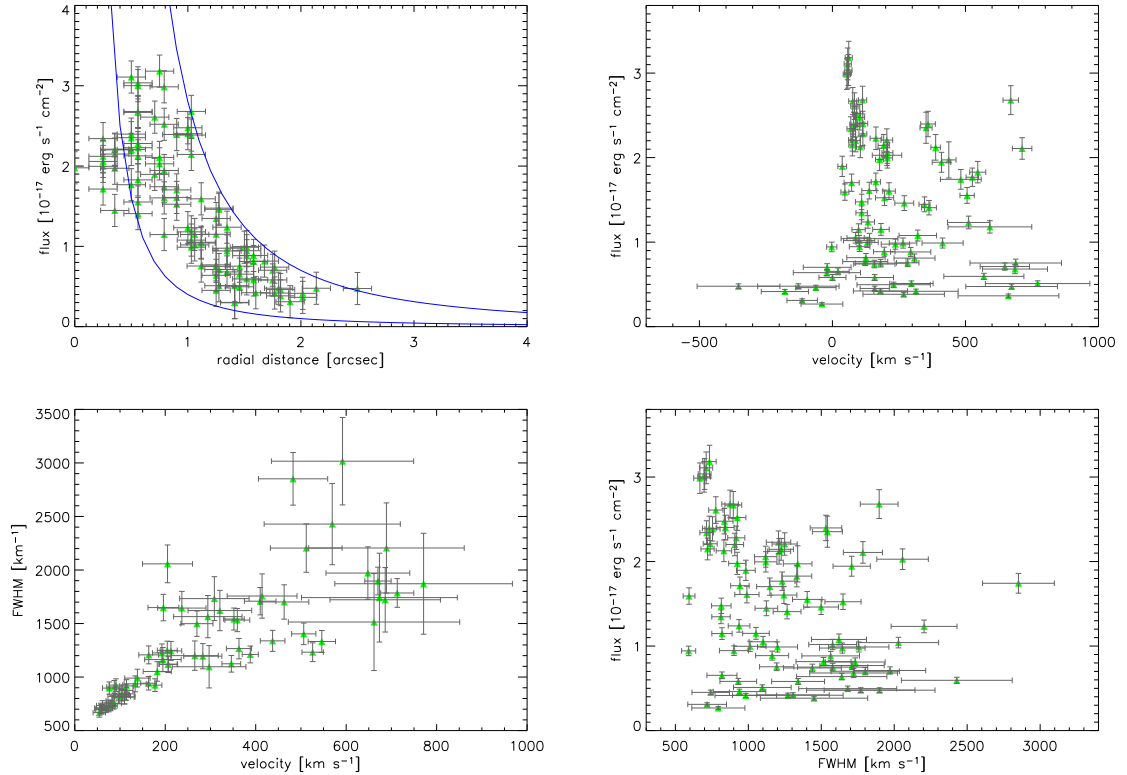


Fig. 13.— *Emission line features within zone 3 and correlations.*

Line ratios integrated over this area are $[\text{NII}]/\text{H}\alpha = 0.79$, $[\text{SII}]/\text{H}\alpha = 0.28$, $\text{H}\alpha/\text{H}\beta = 6.76$, and $[\text{OIII}]/\text{H}\beta = 8.31$. As in region 1, the exact contribution of AGN emission to the measured $\text{H}\beta$ flux are difficult to constrain precisely, even more as the velocity range within this zone is not very distinct from the nucleus. Therefore, line ratios with $\text{H}\beta$ in the denominator are treated as lower limits.

3. Individual sources surrounding MRC1138-262

3.1. Continuum knots C1 and C2

Apart from the nucleus of MRC1138-262, these two knots aligning south-east from the AGN are the brightest sources in the H and K band continuum images in Fig. 2. In the applied cosmology, the projected distances of C1 and C2 from the AGN are 145 kpc and 370 kpc, respectively.

The $H - K$ color image of the line-free continuum emission in Fig. 3 reveals that C1 is redder than the surrounding gas. In spite of the low signal-to-noise ratio, the image hints that this is also true for knot C2.

Both knots are radio-quiet, and do not show prominent $\text{Ly}\alpha$ emission. Kurk (2003) report to have found line emission spatially coincident with knot C1. However, the SPIFFI integral field data suggest a different picture: Line emission that appears roughly co-spatial with the continuum knots is very similar to the overall line emission from the surrounding gas, and does not show intensity peaks at the position of the knots. This suggests that this emission is not related with the

continuum-bright emitters, but part of the diffuse line emitting halo of MRC1138-262. The spatial resolution of both the ISAAC and SPIFFI data is too coarse to safely separate the continuum emitters from the surrounding gas, and is further degraded by the seeing disk, whose size exceeds the intrinsic size of the continuum knots. These facts together indicate that the continuum emitters are not the origin of the line emission, but are merely along the line of sight. However, their close vicinity to the AGN and rather similar colors might indicate they are physically related, possibly embedded into the gaseous halo around MRC1138-262.

Due to the absence of line emission from the knots, it is impossible to estimate dynamical masses of the knots. Their continuum emission is therefore the only available tracer to obtain a limit on their (stellar) mass.

Using STARBURST99 (Leitherer et al. 1999), and measuring the K band magnitude of the center pixel of C1 alone (to be as safe as possible from contamination of the surrounding medium) yields a stellar mass of $\sim 0.5 - 8.5 \times 10^{10} M_{\odot}$ for a stellar population over a large range of ages and assuming solar metallicity. The flux within a 3×3 pixel aperture around the center of C1 yields a stellar mass $M_{\text{stellar}} = 1.7 - 30 \times 10^{10} M_{\odot}$. As poorly constrained as these numbers are, they are all consistent with the knots being satellite galaxies of MRC1138-262, possibly in the course of a merger.

It is interesting to note that, if this interpretation is correct, then these galaxies appear rather distinct from the $z = 2.16$ strong $H\alpha$ emitters that Kurk et al. (2004) found in the field of MRC1138-262. Kurk et al. (2004) view these as parts of a galaxy cluster forming around the massive radio galaxy. The absence of strong line emission from C1 and C2 (which should manifest as local emission line maxima even if they had a projected velocity similar to that of the surrounding gas) might indicate that their gas was stripped due to interactions with the outskirts of the radio galaxy. Alternatively, Nath & Roychowdhury (2002) have argued that the energy output of powerful radio galaxies is possibly large enough to efficiently suppress star-formation within their clusters. This gives a natural explanation for the absence of strong nebular line emission in C1 and C2, if indeed they are at a redshift $z \sim 2.16$.

3.2. The Lyman α emitting knot B3

From FORS narrow-band imaging, Kurk (2003) found that the peak of the $\text{Ly}\alpha$ emission does not coincide with the nucleus of MRC1138-262, but with the bright radio peak $\sim 2.5''$ west, baptized B3.

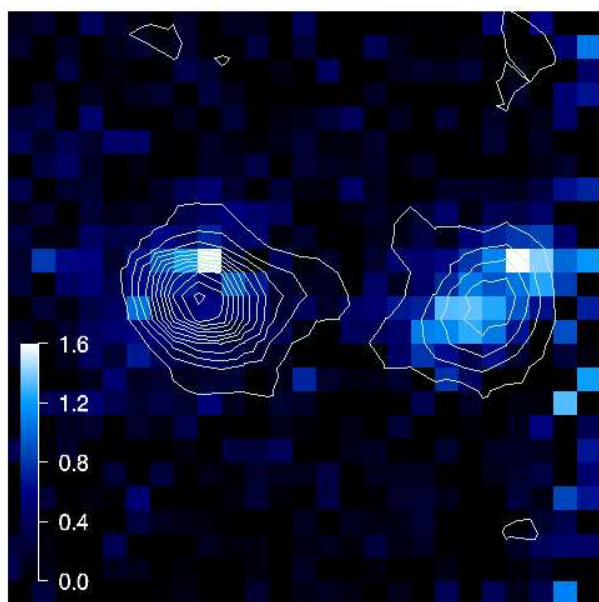


Fig. 14.— $[OIII]\lambda 5007$ line image centered on the observed wavelength at a redshift of 2.147. The colorbar yields the integrated line flux in units of $10^{-16} Wm^{-2}arcsec^{-2}$. Contours show the integrated $H\alpha$ line emission and are given for 3 to 17σ in steps of 1σ .

The rest-frame UV and optical data sets cannot directly be aligned, due to the relatively small SPIFFI field of view, and the lack of strong Ly α emission from the AGN. Therefore, the FORS Ly α image was first registered with respect to stars also observed in the FORS B band image. The B-band morphology follows more closely the K band appearance, and hence can be more easily aligned with the SPIFFI cubes. The precision of the alignment is within a SPIFFI spatial pixel (0.25").

The SPIFFI data set covers this area, although it falls near the edge of the cube. Optical line emission ([OIII] λ 5007 and H α) was found at the position of B3. A [OIII] λ 5007 continuum-subtracted line image of the Ly α emitter is shown in Fig. 14. H α emission originates from one single position, analogous to Ly α , and stretches from NE to SW. [OIII], on the contrary, has 2 peaks. Hydrogen emission peaks roughly in the middle between the two [OIII] peaks. The H and K band spectra of B3 are shown in Fig. 15. They were extracted from an area of $\sim 1\text{''}$, where [OIII] emission was detected. From [OIII] λ 5007, a redshift of $z = 2.148$ is derived for B3, equivalent to a $\sim 1650 \text{ km s}^{-1}$ blueshift with respect to the AGN. Superimposed is faint broad line emission at a redshift consistent with the extended emission of MRC1138-262 ($z \sim 2.16$).

Similar redshifts were derived from the [OIII] and also the H α emission line. A good agreement is crucial in this case, because the data quality suffers near the edge of the cubes. This is the result of imperfect sky subtraction, coverage by only parts of the individual data frames, and because strong night sky lines are projected onto the edges of adjacent slitlets in the SPIFFI raw frames. This explains why the [OIII] λ 4959 line is not observed, although it should be comparably strong

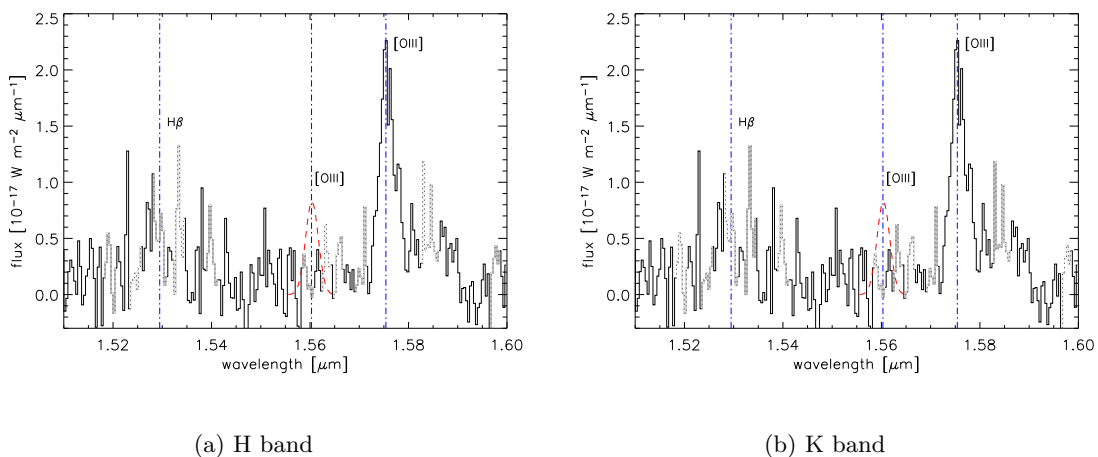


Fig. 15.— *Integrated spectra in the H (upper panel) and K (lower panel) band of the Ly α emitting radio knot B3. Dotted line indicate position of strong night sky line residuals in the two-dimensional spectrum. Blue dotted-dashed vertical lines indicate the expected position of prominent emission lines at the H α redshift. The red dashed line in the upper panel shows the expected [OIII] λ 4959 line.*

(red line in Fig. 15). [NII] λ 6583 emission is also not observed, maybe indicating very low metallicity (as would be expected if the cloud consists of rather unprocessed gas) or extremely high density (the critical density for collisional de-excitation of [NII] at a fiducial temperature of 10^4 K is $8.4 \times 10^4 \text{ cm}^{-3}$, an order of magnitude lower than than for [OIII]; Osterbrock 1989).

Individual spectra were extracted from $0.75'' \times 0.75''$ large boxes centered on the two [OIII] blobs. The two lines are shown in Fig. 16. The two blobs have slightly different redshifts, and an relative velocity shear of $\Delta v = 210 \pm 28 \text{ km s}^{-1}$, with a significance of 7.5σ .

This is the first time that the internal dynamics of a radio knot in a $z \gtrsim 2$ radio galaxy is observed directly. Its integrated luminosity derived from the $\text{H}\alpha$ flux is $\mathcal{L}_{B3} = 48.85 \times 10^{41}$ ergs, which (using the method described in Section 5.4 of Chapter 4) yields a hydrogen mass estimate of $1.5 \times 10^6 M_{\odot}$ (for a fiducial electron density of $n_e = 10^3 \text{ cm}^{-3}$). The origin of this cloud is uncertain, it might be tracing largely unprocessed gas in a subclump of the dark matter halo around MRC1138-262.

Pentericci (1999) have proposed that this region corresponds to a dense hydrogen cloud which is being disrupted by the radio jet, according to the mechanism introduced by Lonsdale & Barthel (1986) to explain double hot-spots in radio jets: As the jet enters a sufficiently massive gas cloud in the IGM, it inflates a bubble of hot plasma, and then escapes from the cloud where it is most weakly confined.

If the Lonsdale & Barthel (1986) scenario is approximately correct, then the relative velocity of $\sim 200 \text{ km s}^{-1}$ observed within the cloud would most likely also be the result of the jet disrupting the cloud. If it reflected internal motions due to self-gravity, and assuming virialized rotation along the line of sight, the required mass would be $\approx 2.2 \times 10^{10} M_{\odot}$ and likely a few times higher if inclination is taken into account. However, the lines are much too broad to be in agreement with virialized motion: $\text{FWHM}(\text{H}\alpha) = 670 \pm 135 \text{ km s}^{-1}$. This points towards cloud rupture as the cause for the velocity shear.

3.3. The nature of the extended line emission around MRC1138-262

Based on rest-frame UV longslit spectroscopy and $\text{H}\alpha$ narrow-band imaging, Kurk (2003) have proposed a number of possible mechanisms leading to the complex kinematics of MRC1138-262:

- Jet-cloud interactions
- A multiple merger of “Lyman-break-like” galaxies
- Infall of primordial gas
- A bipolar outflow,s

or, what they think is most likely, a combination of several of these processes.

The spatially resolved SPIFFI data allow to set better constraints. Most easy to rule out is the scenario where the line emission predominantly arises from a close group of Lyman-break galaxies. Rest-frame optical line emission and continuum knots do not appear spatially aligned, as no line emission was found to arise from C1 or C2, that would not resemble more widely distributed gas. As already mentioned, the extreme line widths observed everywhere within the nebulosity, and extreme [OIII]/ $\text{H}\beta$ line ratios do not support the picture that most of the emission originates from stellar photoionization. The correlations presented in Section 2.3 also suggest that the main heating mechanisms are photoionization by the AGN (as shown by the inverse-square-laws relative to the nucleus) and shocks.

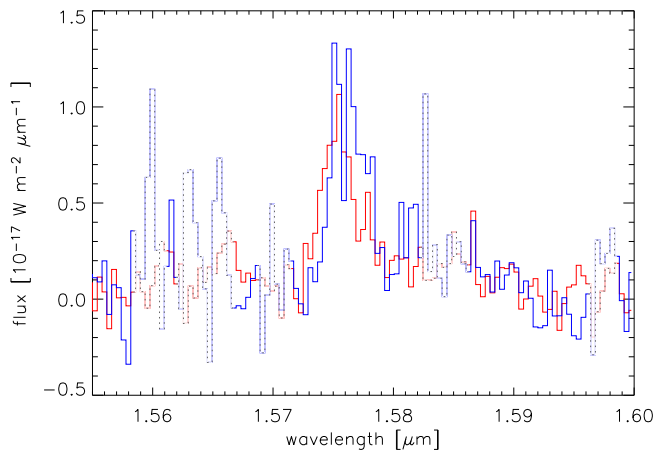


Fig. 16.— Zoom into the wavebands near the $[OIII]\lambda 5007$ line of B3. The spectra were extracted from the north western (blue line) and south eastern (red line) extremities of the $[OIII]$ line emitting region. Dotted lines indicate strong night sky lines.

tion, the gas is certainly not primordial, but appears enriched by e.g., nitrogen, oxygen and sulphur, as these lines are observed across most of the extended gas. A vague indication for infalling primordial gas clouds might come from the $Ly\alpha$ and optical line emitting radio knot B3. Only line emission from this knot was found, but no continuum.

The remaining scenario is that of jet-cloud interactions. Indeed, indications for jet-cloud interactions are found, e.g. the velocity shear in the radio knot B3, which is a strong source of $Ly\alpha$, $[OIII]$, and $H\alpha$ emission, but cannot be discerned in the continuum image. Another example are the dynamics within the comparably small “bubble 1” that was previously identified within the diffuse gas (Section 2.3), which shows indications for being due to jet entrainment. The overall extreme dynamics of the source suggests that indeed interactions between the AGN and jet are the dominating driver of the gas dynamics in the nebulosity of MRC11382-262. However, these are not localized phenomena, as jet-cloud interactions are classically pictured, but the jet-injected energy affects all the gas around the AGN. If the sphere projected on the sky is representative for the three-dimensional geometry, then the AGN feedback has nearly a $4-\pi$ geometry. In the remaining sections, the physical parameters and especially the energetics of this outflow will be discussed, and their cosmological impact estimated.

4. The physical characteristics of the outflow

The primary aim of this section is to constrain the physical properties of the outflow, such as mass, gas density (both in the ambient and the postshock medium), the shock heating rates and the total kinetic energies. Furthermore, a number of questions will be addressed, especially: Can the total recombination line surface brightness be explained by shock heating? What is the fraction of the total AGN luminous and mechanical energy that is coupled to the outflowing interstellar medium?

Subsequently, the estimates of the energetics of the extended emission line gas will be compared

A bipolar outflow would lead to a different kinematic pattern than observed: Especially, the gas seems to be grouped in 3–4 bubbles with different intrinsic and relative dynamics. The only way to bring this into agreement with a bipolar outflow would be to assume that the jet axis changes within less than a dynamical timescale of the gas (see Section 4), which is in contradiction to the observation that the dynamical time scale of the jet is similar to that of the gas.

A dominant infall of primordial gas is equally ruled out by the kinematic maps. The observed velocities are too large to be of gravitational origin in a $\sim 10^{11} M_{\odot}$ system and the energy stored in the gas likely exceeds the binding energy of the galaxy. In addition, primordial gas should be more evenly distributed and cold. This is in clear contradiction to the observations. In addition,

with an estimate of the jet power in MRC1138-262. This will lead to an estimate of the coupling efficiency between the jet and the ambient ISM of the host galaxy. Ultimately these constraints will allow to distinguish whether the luminous and mechanical energy output from the AGN is consistent with that necessary to explain both the characteristics of early type galaxies in the local Universe and what is needed in the models of galaxy formation and evolution.

4.1. Timescale and lifetimes

The emission line kinematics as revealed by the SPIFFI integral-field spectroscopy were discussed in Section 2.3. The most straightforward estimate arising from these data is the dynamical timescale of the outflow. In the simplest picture, the dynamical timescale is given by the crossing time. In an outflow with velocities as high as observed this is appropriate, because the gas likely reaches large distances from the gravitational center and might even completely escape the host potential. Under these circumstances, the observations of the kinematics of the ionized gas in MRC1138-262 can be used to estimate dynamical time scales for the emission line nebula. Explicitly, they are given by:

$$t_{dyn} = t_{crossing} \approx R/V = 9.8 \times 10^6 (R_{proj}/10kpc)(V_{proj}/1000 km s^{-1})^{-1} yrs \quad (9.2)$$

For the kinematically distinct components identified in the optical emission line gas, typical bulk motions range from 1000 to 2000 km s⁻¹. These bulk motions are observed over radii of about 25 kpc. This implies dynamical timescales of about $1 - 2.5 \times 10^7$ yrs.

Interestingly, this timescale is similar to the estimated current ages and lifetimes of powerful radio sources. Superficially, one can estimate the current age of any radio source by making the analogous argument to the one above. This can be put on more solid grounds, if an advance speed jet-head is estimated or measured. Dividing the projected size of the radio sources by the velocity estimate will then yield an age estimate. Jet-head advance speeds have been estimated to be $\sim 0.1c$ (e.g., Wellman, Daly, & Wan 1997, with ranges of about $0.01c$ to about $0.2c$). The “largest angular size” of the radio source at $\nu=1.41$ GHz in MRC1138-262 is 11.1 arcsec (Kapahi et al. 1998). In the concordance cosmology, this translates into a projected linear size of 92 kpc. With a jet-head advance speed of $0.1c$, roughly the median of the measured, typical velocity range of radio galaxies, this would imply a dynamical timescale of $\sim 3 \times 10^6 f_{proj,jet}$ yrs. The factor $f_{proj,jet}$ corrects for the true linear size due to the projection angle of the jet and the plane of the sky. Due to the uncertain projection angle, the dynamical timescale estimate can only be a lower limit, and the intrinsic value is likely a few times higher, up to a few $\times 10^7$ yrs.

Wan, Daly & Guerra (2000) have carried out a more sophisticated analysis by modelling the radio jets to explain the source sizes and radio powers, which suggests that the ages of radio sources decrease with increasing redshift. However, this might at least in parts be due to the flux limited sample they use, so that with increasing redshift, the average radio power will increase, whereas the sizes decrease. Using their relationship between radio power and redshift, and the redshift of MRC1138-262 implies an age of ~ 0.4 to 1×10^7 yrs. This is in good agreement with the estimate inferred from the largest angular jet size in MRC1138-262.

In either *ansatz*, the age of the radio source is significantly less than the crossing time of the emission line nebula. The radio jet and lobes reach a factor of ~ 2 larger radii than the (detected) high surface brightness emission line gas. Although this is in itself not sufficient to indicate that the radio jet is powering the outflow, it is however a necessary prerequisite.

4.2. Extinction

If $H\alpha$ and $H\beta$ can be measured independently, then the extinction can be derived with the method described in Section 1.1 of Chapter 4. However, for MRC1138-262 this is complicated by the faintness of broad $H\beta$ emission from the AGN, which is difficult to isolate from the extended $H\beta$ lines. The lines are faint, so that it is difficult to uniquely fit the complex profiles found in [OIII] also to the $H\beta$ lines, especially for the broad components where the line core rises only slightly above the noise level.

Because the exact contribution of $H\beta$ emission from the AGN cannot be stated precisely, the extinctions derived from the observed $H\alpha/H\beta$ ratios should be considered as lower limits. Since the $H\alpha$ luminosities will be used in the following to estimate the total hydrogen mass and constrain the energetics of the outflow, such a lower limit to the extinction will turn into a lower limit on the intrinsic luminosity and hence hydrogen mass.

To deduce meaningful $H\alpha/H\beta$ ratios, only $H\alpha$ components were used that have matching redshift and line widths as those of the $H\beta$ lines. Thus, one obtains (see Tables 1 to 3 for reference)

$$\begin{aligned} H\alpha/H\beta &= 4.1 && \text{in zone 2} \\ H\alpha/H\beta &= 5.9 && \text{in zone 3} \end{aligned} \tag{9.3}$$

In zone 1, the overlap with the AGN is particularly strong, and the measured $H\alpha/H\beta$ ratio is about the theoretically expected Balmer decrement. Hence a reasonable limit to the extinction cannot be given for this zone. In zone 2 and zone 3, $H\alpha$ emission is attenuated by factors 2.2 and 2.9, respectively.

4.3. Electron temperatures and densities

The data on MRC1138-262 do not include all required lines for any of the temperature sensitive line triplets, e.g. [OIII] λ 4363 in combination with [OIII] λ λ 4958,5007 or [NII] λ 5755 in combination with [NII] λ λ 6548,6583. However, temperature estimates will be important for some of the conclusions in the following sections. For this reason, the most likely temperature range will now be estimated from theoretical grounds and by comparison with radio galaxies with more complete data sets.

When gas is heated by either fast shocks or an AGN the electron temperatures are generally higher than in regions photoionized by massive stars (e.g., HII regions in nearby galaxies). For shock speeds faster than several hundred km s^{-1} , the optical emission line gas is primarily photoionized by the extreme ultraviolet and soft X-rays produced upstream just behind the shock, and not heated mechanically by the shock itself. In shock models which include this pre-heating, the electron temperatures are about 1 to a few $\times 10^4$ K (e.g., Binette, Dopita, & Touhy 1985). In emission line gas excited by the power-law ionizing spectrum of an AGN it is difficult to model this uniquely due to broad range of possible effects. These include, among others, the influence of metallicity or metallicity variations, collisional de-excitation altering line ratios in higher-density clouds, high pressures, mechanical energy injection, etc.

Kraemer, Ruiz, & Crenshaw (1998) discuss the detailed modelling of the narrow line region of NGC 1068 based on a wide range of emission lines throughout the UV and optical regions.

Considering the excitation of the high ionization lines and the likely possibility of collisional de-excitation of some of the forbidden lines, they conclude that the emission line nebula has a most likely temperature of 17,000 K. Without these more complex and sophisticated considerations, a higher temperature would be favored by the observed emission line ratios. Narrow line regions in other active galaxies, for which temperature estimates are based on much less information, have typically been estimated to have temperatures of about 1 to 1.5×10^4 K (Heckman & Balick 1979; Osterbrock 1989). Based on the SPIFFI-data of MRC1138-262, the electron temperature in the extended “narrow” line emitting region cannot be estimated directly from the observed emission lines, therefore $T_e=10^4$ K will be assumed in the following. For a temperature range $T_e = 1-2 \times 10^4$ K, which is most likely the case in MRC1138-262, the temperature does not factor significantly in the estimates of the physical characteristics like the total mass of the emission lines gas. The additional uncertainty due to the uncertainty in the emission line gas temperature is within a few percent, negligible for the typical uncertainties in the parameters estimated here.

Electron densities can be derived from density-sensitive emission line doublets such as [SII] $\lambda\lambda 6717, 6730$, as was outlined in Section 1.1. In spite of the luminous line emission, however, in MRC1138-262 robust estimates of the [SII] line ratios are difficult to obtain. The extreme dynamics of the extended gas smear both lines over wavelength ranges that greatly exceed the spectral distance (580 km s^{-1}) between the two lines. Due to the large line widths, this is also the case when using small apertures.

In spite of the merged lines, it was attempted to fit the two components separately where line widths are relatively narrow, keeping their theoretical wavelengths fixed and using the $H\alpha$ redshift and line width. The only remaining free parameter is then the ratio of the two [SII] components. Thus, robust fits could be found for two 3×3 pixel apertures situated in zone 2. Spectra and line fits are shown in Fig. 17, for a ratio $I(6716)/I(6730) = 1.1 \pm 0.1$ in either spectrum. Fig. 17 shows the relationship between electron density and [SII] ratio for an assumed temperature of 10^4 K (blue line). Taken at face-value, the best-fit electron density is 300 cm^{-3} . The hatched area shows an uncertainty of ± 0.1 in the line ratio, which is the fit uncertainty and translates into a density range $n_e = 240 - 570 \text{ cm}^{-3}$. This agrees with the densities of about 100 cm^{-3} in the precursors of fast radiative shocks found from radio observations (Bicknell et al. 1997).

4.4. Bolometric and $H\alpha$ luminosities

The bolometric luminosity of the AGN in MRC1138-262 is difficult to estimate robustly. Several approaches are given in the literature to estimate \mathcal{L}_{bol} from measurements in different wavebands, which will now be used and compared.

Following, e.g. Elvis et al. (1994), the X-ray luminosity can be used as an indicator of the overall bolometric luminosity of the AGN. The factor between the X-ray and the total emission is about 0.1, with a range of about a factor of $\sim 2 - 4$ (Elvis et al. 1994). From this conversion and the measured X-ray luminosity of MRC1138-262 in the 2 – 10 keV band ($\log L_{2-10\text{keV}}=45.6$ ergs s^{-1} from Carilli et al. 2002), follows a bolometric luminosity of the AGN of $\sim 10^{46.6}$ ergs s^{-1} .

Alternatively, one can apply the relationship between bolometric luminosity and rest-frame optical flux density of the AGN, which Kaspi et al. (2000) established for quasars: $L_{bol} \simeq 9 \lambda L_\lambda(5100 \text{ \AA})$. From the SPIFFI data, the flux at 5100 Å is measured to be $f_{5100\text{\AA}} = (5.5 \pm 0.53) \times 10^{-17} \text{ W } \mu\text{m}^{-1} \text{ m}^{-2}$. In the adopted cosmology, the Kaspi et al. (2000) relation translates this into $L_{bol} \simeq (1.7 \pm 0.2) \times 10^{46} \text{ ergs s}^{-1}$. This result does not take extinction and systematic uncertainties of the estimator

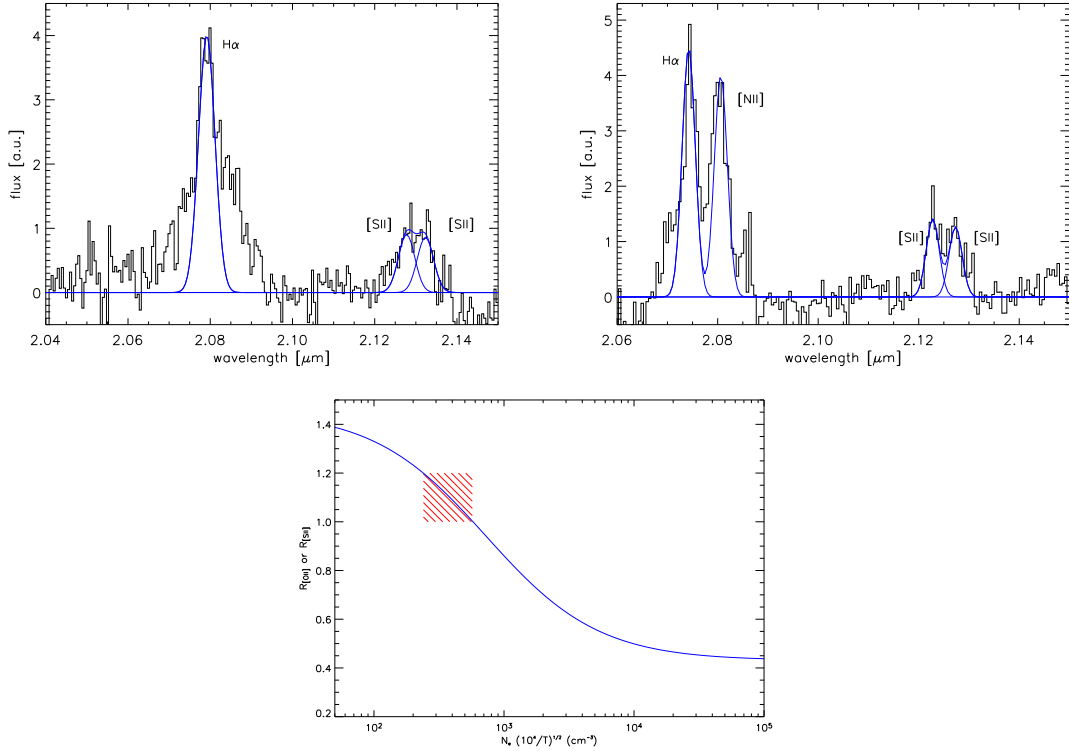


Fig. 17.— *MRC1138-262 electron density.*

into account, which will increase the flux measurement and bolometric luminosity estimate easily by factors of a few. From the ratio of the broad H α and H β emission (Section 2.2), an extinction $A_V = 8.7$ mag was calculated for the central light-days of the AGN, where the broad line emission is likely to arise. Although the extinction of the AGN continuum might be significantly less, this shows that the rest-frame optical flux estimate is a lower limit on the intrinsic bolometric luminosity, because the AGN of MRC1138-262 is highly extinguished.

Both estimates yield consistent luminosities. In the following, $\mathcal{L}_{bol} = 10^{46.6} \text{ ergs s}^{-1}$ will be adopted, to mitigate against uncertainties related to extinction.

H α fluxes are difficult to measure in MRC1138-262, because the H α lines partially blend with [NII] λ 6583. The [NII]/H α line ratios are uncertain, generally, typical values found in AGN are in the range [NII] λ 6583/H $\alpha \sim 0.7 - 3$. Section 2.3 describes how it was attempted to obtain robust H α flux estimates in spite of these uncertainties. Using the fitted H α fluxes extracted from the spectra integrated over the three zones results in integrated luminosities of

$$\mathcal{L}(1) = 2 \times 10^{43} \text{ ergs} \quad (9.4)$$

$$\mathcal{L}(2) = 6.1 \times 10^{43} \text{ ergs} \quad (9.5)$$

$$\mathcal{L}(3) = 6.7 \times 10^{43} \text{ ergs} \quad (9.6)$$

$$\mathcal{L}(tot) = 1.48 \times 10^{44} \text{ ergs} \quad (9.7)$$

$$(9.8)$$

Assuming that the noise is nearly Gaussian, relative uncertainties on the total measured flux are 8.4%. This translates into a total luminosity $\mathcal{L}(tot) = (1.48 \pm 0.12) \times 10^{44} \text{ ergs}$. This estimate of course does not take the blending of [NII] and H α into account, which yields additional uncertainties.

This is not of concern for an analysis aiming at establishing robust lower limits to the energetics of the emission line gas, if all luminosities are consequently treated as lower limits.

4.5. Mass, outflow rates, and filling factor of the emission line nebula

The mass of the emission line nebula can be estimated assuming case B recombination and using the total $H\alpha$ luminosity (Equation 4.20).

As discussed in Section 2.3 the complex dynamics of the emission line nebula blends the lines to an extent that makes it difficult to uniquely disentangle each component of the doublet. As discussed in that section, it was nonetheless tried to separate the doublet lines of [SII] in two regions with sufficiently narrow lines to make a robust estimate. Both estimates are similar, suggesting that they yield values typical for most of the line-emitting gas. Assuming simple recombination, the following elementary formula will describe the mass of hydrogen in a line emitting nebula:

$$M_H = L_{H\alpha} [h\nu_{H\alpha} \alpha_{H\alpha}^{eff}]^{-1} m_p n_e^{-1} = 9.73 \times 10^8 L_{H\alpha,43} n_{e,100}^{-1} M_\odot \quad (9.9)$$

A total $H\alpha$ luminosity of $(14.8 \pm 1.2) \times 10^{43}$ ergs s^{-1} and an electron density of $240 - 570$ cm^{-3} imply a total gas mass in the range $M_{HII} = 2.3 - 6.5 \times 10^9 M_\odot$. Taken at face value, this is about 1% of the total (stellar) mass estimated for MRC1138-262, ($M_{stellar} = 5 \times 10^{11} M_\odot$ Pentericci 1999). Because this analysis is valid on an order-of-magnitude level only, and measured uncertainties are small compared to the astrophysical uncertainties in the subsequent assumptions, in the following, $M_{HII} = 3.7 \times 10^9 M_\odot$ is adopted, corresponding to the $H\alpha$ luminosity and density at face value.

Assuming that the mass outflow rate has been constant over the dynamical time of the flow, one can estimate the acceleration rate of the outflowing material necessary to maintain the flow. This estimate can then be used for an order-of-magnitude constraint of the final amount of material that will be accelerated during the lifetime of the jet. This estimate, albeit uncertain, will later be used as basis for the cosmological significance of AGN feedback. As will be seen later, order-of-magnitude estimates are already useful for this comparison.

In the most simple scenario, the acceleration efficiency can be assumed as constant, so that the relation between the amount of material and the time necessary to reach the distances from the AGN at which the material is observed will be linear. Obviously, the relationship is only approximate and will vary during the lifetime of the jet, due to jet precession, variations in the jet energy or its mass density, or changing coupling efficiency to the ISM. In addition, the jet is not only accelerating, but also ionizing the gas, so that a simple approximation is likely to underestimate the dynamical time of the outflow and mostly serves as a lower limit.

Under the assumptions discussed previously, the mass outflow rate can be estimated by:

$$\dot{M}_{outflow} \sim M_H / t_{dyn} \approx 370 M_\odot yr^{-1} \quad (9.10)$$

With the very basic paradigm that the jet powers this outflow, it must have existed for at least as long as the crossing time of the gas at the measured velocities, and it must be able to accelerate the gas to the observed velocities.

The volume filling factor of the emission line gas can also be constrained, assuming recombination and for a given electron density and relative ionization. If the density is approximately

uniform across the line emitting regions, then the total luminosity of the H α emitting nebula will be proportional to the emissivity per unit volume times total volume necessary to explain the total luminosity. The emissivity is a simple estimate using case B recombination. The comparison to the total H α luminosity yields a “total emission volume”.

The filling factor can be estimated using the following,

$$ff_V = V_{emission}/V_{nebula} = 0.15 L_{H\alpha,43} n_{e,100}^{-2} V_{nebula,kpc^3}^{-1} \quad (9.11)$$

This estimate uses that $n_p \approx 3n_e$, which is appropriate for the “partially ionized” zone where the [SII] density sensitive lines are likely to arise.

Approximating the three-dimensional distribution of the line-emitting gas by rotating the projected area of emission about the radio axis, a crude estimate of the total volume of line-emitting gas is $\approx 10^4$ kpc³. Relating this estimate with the required emitting volume, derived from the emissivity per unit gas volume, the filling factor of emission line gas is about 1.6×10^{-6} . Main uncertainties are the three-dimensional structure, gas density, and the relative ionization. Thus, albeit in projection it appears that a large area is covered with emission, the emission line gas intrinsically only occupies a relatively small fraction of the total volume. The likely geometry of the line emitting gas is in sheets, small clouds and/or filaments all of whose surfaces are bright line emitters.

5. Driving the outflow in MRC1138-262

5.1. Energy and mechanical luminosity

Both the total energy and mechanical luminosity of the nebula are important parameters to gauge the likely impact and significance of AGN driven outflows. Namely, both parameters are indispensable for determining whether or not the AGN is the likely power source of the emission line luminosity, determining the ionization state of a gas, and driving its kinematics. The H α -derived masses and the offset velocities relative to the nucleus were both extracted from the SPIFFI data cube and can be used to estimate the energy contained in the bulk outflow E_{bulk} and in the turbulent velocities E_{turb} . The energy estimates follow then directly from the simple kinetic relationships, taking into account the unknown inclination by including a correction factor f_{proj} . This correction obviously depends on the position within MRC1138-262, which through simple geometric arguments about the likely statistical configurations of the gas is expected to lie between 1 and 3.

$$E_{bulk} = (1/2)\Sigma_i m_i v_i^2 \approx 1.9 \times 10^{58} f_{proj} \text{ ergs} \quad (9.12)$$

$$E_{turb} = (1/2)\Sigma_i m_i \sigma_i^2 \approx 2.9 \times 10^{58} f_{proj} \text{ ergs} \quad (9.13)$$

It is important to note explicitly, that these calculations only take into account the emission line gas masses and kinematics. Material in other phases, like the X-ray emitting gas or the molecular gas will also contain significant amounts of thermal and ram pressure (in the case of the X-ray emitting gas) and perhaps significant mechanical energy in the case of the neutral (HI, neutral metals like Na) or molecular gas (H₂). Hence, strictly speaking, these estimates represent a lower bound to the true total kinetic energy.

A simple assumption between the kinetic energy total and the dynamical time of the emission line gas will yield an order-of-magnitude estimate of the total energy injection rate which is needed to explain the observed kinematics of the gas. With the time estimates obtained in Section 4.1 it follows that:

$$\dot{E}_{kinetic} \approx (E_{bulk} + E_{turb})/t_{dyn} \approx 1.5 \times 10^{44} t_{10Myrs}^{-1} \text{ ergs s}^{-1} \quad (9.14)$$

Particularly interesting is the amount of power contained in the turbulence. The energy necessary to drive the turbulence can be estimated by setting,

$$\dot{E}_{turb} \simeq -(1/2) \rho v_{rms}^3 / L_d = -9 \times 10^{-21} n_{100cm^{-3}} v_{rms,1000}^3 \text{ km s}^{-1} L_{d,10} \text{ kpc} \text{ ergs cm}^{-3} \text{ s}^{-1} \quad (9.15)$$

where n_{100} is the measured electron number density in units of 100 cm^{-3} , $v_{rms,1000} \text{ km s}^{-1}$ is in units of 1000 km s^{-1} , and $L_{d,10} \text{ kpc}$ is the driving scale of the turbulence. Using $n = 390 \text{ cm}^{-3}$ and the average velocities measured in the different zones yields $\dot{E}_{turb} \simeq -6.5 \times 10^{-21} \text{ ergs cm}^{-3} \text{ s}^{-1}$.

In Equation 9.14 for the kinetic energy input rate it was specifically assumed that the turbulence is inversely proportional to the bulk crossing time. This is not appropriate for turbulence in that the energy is dissipated in a fraction of the ‘‘turn over time’’, i.e., the time necessary for the turbulent eddy to make one turn. This time scale can be estimated by,

$$\tau_d = E_{turb} / \dot{E}_{turb} \simeq L_d / v_{rms} = 9.8 v_{rms,1000}^{-1} \text{ km s}^{-1} L_{d,10} \text{ kpc} \text{ Myrs} \quad (9.16)$$

Using $v_{rms} = 800 \text{ km s}^{-1}$, this yields a turn over time of $12.3 L_{d,10} \text{ kpc} \text{ Myrs}$. Hence, about $7 \times 10^{-21} \text{ ergs cm}^{-3} \text{ s}^{-1}$ must be injected into each volume of the gas to power the turbulent flow, and this energy flow must be maintained for $\sim 12 \text{ Myrs}$.

If ultimately the turbulence is dissipated in heating and ionizing the gas, e.g. through shocks, then the resulting $H\alpha$ luminosity can be predicted using this dissipation rate.

$$L_{H\alpha} = \dot{E}_{turb} V f f_V \frac{L_{H\alpha}}{L_{tot}} = 1.2 \times 10^{40} \text{ ergs s}^{-1}, \quad (9.17)$$

where V is the volume of shocked gas, $f f_V = 1.6 \times 10^{-6}$ is the filling factor derived in Section 4.5, and $L_{H\alpha} / L_{tot}$ is the ratio of $H\alpha$ to total luminosity following Dopita & Sutherland (1996). The estimated time scales agree with the above estimates of the age of the radio source. The luminosity indicates that turbulent shocks can only have a minor contribution to the overall $H\alpha$ line emission of MRC1138-262. This is in agreement with the analysis of the spatial distribution of measured $H\alpha$ fluxes in Section 2.3, which indicate that most of the line emitting gas is in fact photoionized.

5.2. Energy and momentum injection rates necessary to accelerate the outflow

The energy and momentum injection rates needed to accelerate the clouds in the outflow can be used to roughly estimate the required minimum outflow energy. Strictly speaking, these estimates are valid only if the winds are being driven into a spherically symmetric, uniform medium. This is clearly at odds with the observed clumpiness of the ISM in MRC1138-262. Thus these can only be

“order-of-magnitude” estimates. On the other hand, averaged over the full volume and life-time of the outflow, these effects might at least partially cancel.

The density of the ambient (pre-shock) medium n_0 cannot be measured directly. It is however related to the measured density of the shocked gas, n , (Section 4.3) and the shock velocity through the adiabatic strong shock criterion, $n_0 = M_0^{-2} n$, where M_0 is the Mach number of the shock. Using $v \approx 500 \text{ km s}^{-1}$ and $c \approx 10 \text{ km s}^{-1}$ as fiducial estimate of the sound speed in the ISM, the density in the pre-shock region is $n_0 \approx 0.5 \text{ cm}^{-3}$. This number is similar to that typically estimated for the ISM of nearby spiral galaxies.

Supposing that the emission line gas is swept-up into shells as it is accelerated, the expansion speed of the shell will be directly related to the mechanical energy injection rate supplied by the AGN. Such an estimate therefore relates to the *total* energy injection rate, not the observed one, but the integrated rate necessary to accelerate the gas up to the observed velocities. For simplicity, an energy-conserving bubble expanding due to its own internal pressure is assumed. This analysis is appropriate for an explosive event of energy injection that is maintained for some time by constant energy injection. The velocity of the shell can be related to the energy content of the bubble as (e.g., Dyson & Williams 1980),

$$v_{shell} \sim 435 \dot{E}_{44}^{1/5} n_0^{1/5} t_7^{-2/5} \text{ km s}^{-1} \quad (9.18)$$

where \dot{E}_{44} is the energy injection rate in units of $10^{44} \text{ ergs s}^{-1}$, $n_0 = 0.5 \text{ cm}^{-3}$ is the ambient ISM density in cm^{-3} and t_7 is the duration of the injection (assumed to inject at a constant rate) in units of 10 Myrs. For the averaged velocity observed in the nebula, $\sim 800 \text{ km s}^{-1}$ the required energy is $\sim 4.1 \times 10^{45} \text{ ergs s}^{-1}$.

In a second method of estimating the energy injection rate, an energy conserving bubble with constant energy injection is assumed, which expands into a uniform medium with an ambient density, n_0 . The energy injection rate is then,

$$\dot{E} \approx 3 \times 10^{46} r_{10}^2 v_{1000}^3 n_0 \text{ ergs s}^{-1} \quad (9.19)$$

with the radius r_{10} given in units of 10 kpc. With the measured radius $r = 19.16 \text{ kpc}$, mean velocity $v = 800 \text{ km s}^{-1}$, and ambient density $n_0 = 0.5 \text{ cm}^{-3}$, the energy injection rate is $2.8 \times 10^{46} \text{ ergs s}^{-1}$.

Alternatively, if the bubble is momentum conserving, then the appropriate expression is

$$\dot{p} \approx 2 \times 10^{36} r_{kpc}^2 v_{1000}^2 n_0 \text{ dynes}, \quad (9.20)$$

or $2.3 \times 10^{38} \text{ dynes}$, where r_{kpc} is the bubble radius in units of kpc, v_{1000} is the shell velocity in units of 1000 km s^{-1} , and n_0 is the ambient density in units of cm^{-3} . So the jet or radiation field of the AGN in MRC1138-262 must be able to inject about $10^{46} \text{ ergs s}^{-1}$ of energy and about 10^{38} dynes of force into the ambient interstellar medium to produce the observed kinematics of the emission lines gas.

5.3. The shock heating rate

At shock speeds above a few 100 km s^{-1} , the ionization and recombination rates due to the shock are predominately determined by the “UV precursor” (the extreme ultraviolet and soft X-rays

produced upstream just behind the shock that ionizes the pre-shocked gas). Therefore the number of recombination photons emitted by each Hydrogen atom is dominated by the recombination rate in the pre-shocked gas. At lower speeds, Shull & McKee (1979) estimate that there are about 2 Balmer recombination photons per hydrogen atom for shocks of about 100 km s^{-1} . At speeds between 300 and 500 km s^{-1} , the relationship between shock speed and $H\beta$ surface brightness in Dopita & Sutherland (1996) suggests that about 2 – 3 recombinations are needed to produce one $H\alpha$ photon, declining with increasing speed.

While the exact shock speed in the nebula of MRC1138-262 is not known, it is reasonable to assume that it is somewhat higher than 500 km s^{-1} , given the line widths and bulk motions observed. Shocks with velocities higher than this are very difficult to model. This arises mainly from the dominating contribution of the UV precursor of the emission, so that line strengths and ratios become sensitive to the distribution of the pre-shocked gas. The UV precursor becomes intense enough to ionize significant amounts of gas and possibly even passes into the “matter bounded” regime where the number of ionizing photons exceeds the number of atoms available to be ionized to a significant degree. This has a strong impact on the predicted line ratios. Following this argument and the modelling of Dopita & Sutherland (1996), it is likely that the efficiency of the $H\alpha$ emission will decline significantly with increasing shock velocity.

$$\dot{M}_{shock} \approx 4.4 \times 10^4 n_{2\gamma}^{-1} \text{ per } H L_{H\alpha,43} M_{\odot} \quad (9.21)$$

About $2.5 \times 10^5 M_{\odot} \text{ yr}^{-1}$ of shocked material are needed to explain the entire $H\alpha$ luminosity. This is a lower limit because the efficiency of the emission is likely to be lower and because the fluxes cannot be adequately corrected for extinction. Over the lifetime of the radio jet, likely to be about 10^7 yrs, Section 4.1), this implies an unphysically large amount of shocked gas ($>10^{12} M_{\odot}$ or the whole of a massive galaxy).

The predicted surface brightness of a shock with a velocity of 500 km s^{-1} is about $2 \times 10^{40} \text{ ergs s}^{-1} \text{ kpc}^{-2}$ (Dopita & Sutherland 1996). The surface brightness of the emission increases dramatically with velocity ($\propto V_s^{2.4}$). The emission line nebula of MRC1138-262 has a projected area of approximately 1200 kpc^2 . If the entire nebula were shock heated, this would yield a total $H\alpha$ luminosity of $\sim 2.4 \times 10^{43} \text{ ergs s}^{-1}$. This is within $\sim 15\%$ of the observed $H\alpha$ luminosity, partly because extinction has not been accounted for. The extinction estimates presented in Section 2.3, although not very precise, indicate that the intrinsic $H\alpha$ line fluxes can only be factors of a few times higher than the measured ones, unless if the extinction differs dramatically within the extended gas, which appears unlikely due to the rather uniform $H - K$ colors. Therefore, this is another indication that fast radiative shocks are not the main source of ionization within the nebulosity of MRC1138-262, but that it is mostly photoionization from the AGN, which illuminates the turbulent material within the nebulosity.

Since the amount of shocked material necessary to power the nebula is unphysically large and the predicted surface brightness is too low, the conclusion is that shock excitation is probably not viable as the sole excitation mechanism of the emission line gas. This is consistent with the analysis of the spatially-resolved gas kinematics presented earlier in this chapter. In a later section, the contribution of the ionizing radiation from the AGN will be computed.

5.4. Jet power and coupling efficiency in MRC 1138-262

Making an accurate estimate of the total mechanical power of the jet in extragalactic radio sources is notoriously difficult. However, in order to gauge how strong the coupling to the ambient

ISM is likely to be, a rough estimate of mechanical energy is required. This can be attempted using the arguments in Wan, Daly & Guerra (2000), who empirically determined the physical parameters of radio sources in the 3CR. Based on the radio power at 178 MHz as their fiducial frequency, they give estimates of the radio source characteristics, including jet power. From the Kapahi et al. (1998) VLA measurements at 4.86 GHz of the radio flux of MRC1138-262, together with the original selection from the Molonglo Reference Catalog (MRC), namely $S_{408MHz} > 0.95$ Jy, an estimate of the radio spectral index can be derived. Kapahi et al. estimate $S_{408MHz} = 4.120$ Jy and spectral index, $\alpha = 1.34$. From these values and the redshift of MRC1138-262, the estimated total radio power in rest-frame 178 MHz is $P_{178MHz} = 6.6 \times 10^{34}$ ergs s⁻¹ Hz⁻¹ sr⁻¹. Relating this estimate with the relationship between L_{jet} and P_{178MHz} follows a jet luminosity of 1×10^{46} ergs s⁻¹. The Wan, Daly & Guerra (2000) correlation shows a scatter which allows for a range of possible kinetic luminosities within a factor of 2 or higher.

The integrated radio luminosity of MRC1138-262 in the rest-frame 0.1-1.0 GHz is 1.8×10^{45} ergs s⁻¹ (Carilli et al. 2002). Assuming that the radio luminosity is equal to 10%, $\epsilon_{10\%}$, of the total jet luminosity leads to a lower limit to the jet kinetic luminosity of $1.8 \times 10^{46} \epsilon_{10\%}$ ergs s⁻¹ – about a factor of 2 higher than the estimate of Wan, Daly & Guerra (2000) but within the scatter of their estimate. For the subsequent analysis, 10^{46} ergs s⁻¹ will be adopted as the fiducial jet kinetic luminosity.

If the jet is supersonic with respect to its internal sound speed, the thrust can be expressed in terms of jet power and jet speed. This is related as,

$$\dot{p}_{jet} \sim L_{jet}/v_{jet} = 3 \times 10^{35} L_{jet,46}/\beta_{jet} \text{ dynes} \quad (9.22)$$

where $L_{jet,46}$ is the jet power in units of 10^{46} ergs s⁻¹ and $\beta = v_{jet}/c$ where $v_{jet} = c$. If the jets are not light, but carry more mass, then of course the approximation used above to estimate the thrust is not appropriate. In such a case the entrainment of the ambient ISM might increase substantially and would be necessary in order to slow the jet significantly.

Both of these estimates are of course crude but they do suggest that the outflow efficiently couples to the ambient interstellar medium in MRC1138-262.

5.5. Comparison with the predictions of the dentist drill model

The “dentist drill model” (Scheuer 1982) is the most simple approach to explain how the jet interacts with the ambient ISM: Hot plasma originating from the innermost surroundings of the AGN gets collimated and moves out rather undisturbed, until it hits the surrounding ISM or IGM and is strongly shocked (termination shock). Small variations of the jet direction cause the jet to jitter across the working surface, and the resulting cavity will be larger than the jet diameter itself. Typical assumed values are $\sim 15^\circ$ (Begelman & Cioffi 1989). Thus in the “dentist drill” scenario, the interaction between radio jet and the surrounding medium is limited to the working surface of the jet, and the coupling efficiency is approximately the area of the working surface, divided by 4π . This can be parameterized as $\epsilon(\%) = (A_{jet}/4\pi) = 0.003\% A_{sqdegree}$, or 0.045% for 15° . From the direct measurement of MRC1138-262 follows $\epsilon_{MRC1138-262} \sim 10\%$. This difference is about two orders of magnitude. Hence the observed kinematics in MRC1138-262 cannot be explained with the dentist drill.

5.6. Radiation driven winds

The radiative luminosity of the AGN in radio galaxies can be extremely high. The intense radiation field should both heat the gas in the immediate environment due to Compton scattering (Compton heating) and accelerate the gas mainly through the dust opacity. The latter can excite an outflow, due to Coulomb coupling of charged dust grains to the ionized gas. The impact of the Compton heated/accelerated gas has been calculated and is generally not sufficient to drive large scale outflows (e.g., King 2003).

Direct observations of powerful AGN suggest that they can drive substantial outflows. For example, the blue shifted X-ray absorption lines in bright quasars suggest outflows which drive $\sim 1 M_{\odot} \text{ yr}^{-1}$ with velocities $\sim 0.1 c$ (e.g., Reeves, O'Brien, & Ward 2003). These outflows, which are likely located within a few pc of the supermassive black hole, are probably optically thick to electron scattering and are likely related to Compton heating. While the kinetic energy of these outflows is high, the amount of accelerated material is relatively small (at least 2 orders of magnitude less than what is needed in MRC1138-262) and their radii of influence are rather small, where they can accelerate the gas before cooling and dilution of the radiation field become important (e.g., King 2003). Given the mass loss rates involved, it is therefore unlikely that these are directly related to large scale outflows like that observed in MRC1138-262.

The importance of radiation pressure in driving an outflow obviously depends on the intensity of the radiation field itself, i.e., by the bolometric luminosity. The bolometric luminosity of the AGN in MRC1138-262 was previously estimated (see Section 4.4), $\mathcal{L}_{bol} = 10^{46.6} \text{ ergs s}^{-1}$.

Interestingly, this bolometric luminosity estimate agrees approximately with the estimated power of the radio jet. Hence the relative importance of each in driving the outflow is a matter of how strongly they couple to the ambient ISM. Obviously, this will depend sensitively on the opacity of the ISM in the case of radiation pressure and on the size of the working surface and the pressure if the mechanical heating is due to the jet.

There is a simple relation between the radiation pressure and acceleration for a momentum driven wind. If the gas is optically thick but not highly self-shielding, the momentum deposition rate due to the radiation pressure is simply:

$$\dot{P}_{rad} = L_{AGN}/c \approx \dot{M}_{rad} V_{\infty} \quad (9.23)$$

From this follows an estimated mass acceleration rate which can be compared with what was deduced from the recombination line emission. This yields

$$\dot{M}_{rad} \approx 1.1 \times 10^{-6} \tau_1 L_{AGN,46} V_{\infty,1500}^{-1} M_{\odot} \text{ yr}^{-1} \quad (9.24)$$

where τ_1 is for $\tau=1$, $L_{AGN,46} = L_{AGN}/10^{46} \text{ ergs s}^{-1}$, and $V_{\infty,1500} = V_{\infty}/1500 \text{ km s}^{-1}$. The scaling for V_{∞} was chosen to be the representative velocity of the outflowing gas.

Further, similar arguments can be used as presented in for example, King (2003) and Murray, Quataert, & Thompson (2005), to estimate other quantities of a momentum driven wind powered by an AGN. For an optically thick wind, the equation of motion is,

$$\dot{P}_{rad} = M_g(r) \dot{V} = -GM(r)M_g(r)/r^2 + L_{AGN}/c \quad (9.25)$$

Following Murray, Quataert, & Thompson (2005), the solution for the velocity as a function of the distance for the black hole, r , is,

$$V(r) = 2\sigma\sqrt{(L/L_M - 1)\ln(r/R_0)} \quad (9.26)$$

where in the context of the Murray, Quataert, & Thompson (2005) characterization of this problem, $L_M = 4f_g c\sigma^4/G$, where f_g is the gas fraction of the total mass, σ is the velocity dispersion of the galaxy, and G is the gravitational constant. R_0 is the radius where the acceleration begins. R_0 is the dust sublimation radius which should be a few pc from the black hole since dust at smaller radii is likely to be destroyed by the intense radiation field. L_M for a $\approx L^*$ galaxy is $L_M \simeq 3 \times 10^{46} f_{g0.1} \sigma_{200}^4 \text{ ergs s}^{-1}$.

The luminosity of the AGN in MRC1138-262 was estimated to be of-order $1 - 4 \times 10^{46} \text{ ergs s}^{-1}$, a gas fraction of 10-50% is likely reasonable, and the velocity dispersion of 250 km s^{-1} corresponds to a galaxy of similar mass to that estimated for MRC1138-262. This suggests that $L_M \simeq 10^{47}$ or well-above the bolometric luminosity of MRC1138-262. However, optimistically assuming a lower gas fraction and smaller velocity dispersion, it is possible for radiation pressure to play a role. Making the assumption that $L/L_M = \frac{4}{3}$, then the acceleration would have to have been maintained for a few $\times 10^{8-9}$ yrs in order to accelerate the line emitting mass observed in MRC1138-262 to the velocities observed. In addition, it is very unlikely that radiation pressure alone can produce these velocities over a region of a few to several 10s of kpc. Typically, this analysis would produce line velocities of about $\frac{1}{2}$ those observed (not considering the effects of projection). This is likely significantly longer than the age of the radio source. Hence, radiation driven winds are not very strong candidates to be the prime driver of the kinematics observed in the nebula.

5.7. Ionizing radiation contribution to the emission line nebula

In Section 5.6, the radiative bolometric luminosity of the AGN in MRC1138-262 was estimated to be about $4 \times 10^{46} \text{ ergs s}^{-1}$. Using the average difference between the ionizing and bolometric luminosity as given in Elvis et al. (1994), this leads to an estimated ionizing luminosity of $\sim 4 \times 10^{45} \text{ ergs s}^{-1}$. For constant density across the line emitting volume, the number of ionizing photons necessary to power the $H\alpha$ emission from the nebula is

$$Q(H^0) \approx 3.7 \times 10^{54} L_{H\alpha,43} \text{ photons s}^{-1} = 5.5 \times 10^{55} \text{ photons s}^{-1} \quad (9.27)$$

for the measured $H\alpha$ luminosity of $1.5 \times 10^{44} \text{ ergs s}^{-1}$. This provides an estimate of the number of photons needed to maintain the ionization equilibrium if the nebula is “radiation bounded”, i.e., if it absorbs all photons emitted by the AGN. The total ionizing energy depends on the average energy of each photon. The results of Elvis et al. (1994) imply that the average energy is about 3 times of the ionizing potential of Hydrogen. This results in,

$$L_{ion} = Q(H^0)h \langle \nu \rangle_{ion} \approx 3.3 \times 10^{44} L_{H\alpha,43} \text{ ergs s}^{-1}, \quad (9.28)$$

or $\approx 4.9 \times 10^{45} \text{ ergs s}^{-1}$. The estimated ionizing continuum luminosity of $6 \times 10^{45} \text{ ergs s}^{-1}$ is more than sufficient to power the emission line nebula around MRC1138-262, if the escape fraction of the radiation is less than about 90%. So the nebula could easily be “matter bounded”. However, the volume filling factor was found to be very small, only about 10^{-6} (Section 4.5). The

estimate, that the covering factor must be $\gtrsim 10\%$ in order to power the nebula implies that the gas is distributed in elongated structures with large surface area and relatively small volumes. The geometry where ratio between the surface area (1 side of the full area) and the volume is about a factor of 10^4 makes it most likely that the gas is either clumped into large numbers of small, approximately spherical clouds, long and thin “string-like” structures, or in thin, broad sheets. This must be the case for either shock or radiation excitation of the nebula.

6. The cosmological significance of AGN-driven feedback

In the previous sections, the detailed study of the dynamics of MRC1138-262 was used to give robust observational constraints on the energetics of the jet-triggered outflow in a massive radio galaxy. These results will now be used to derive estimates for the impact of AGN feedback on the evolution of the general class of very massive galaxies. Although this analysis is based on only one source, the main physical drivers are fairly fundamental, and will therefore not depend strongly on the individual galaxy provided it is massive enough and hosts an AGN. This is even more true as all estimates are given on an order-of-magnitude level only. In that sense, the results obtained in MRC1138-262 can be expected to be rather universal. The “clumpiness” of the ISM in the host might have an impact, but cloud disruption will ultimately smoothen the ISM and lower the impact of the environment in the individual host (an example for ongoing cloud disruption in MRC1138-262 is given in section 3.2). In addition, observational evidence does exist that extreme gas dynamics in the range observed in MRC1138-262 are typical for galaxies hosting powerful AGN. Examples are the distribution of radio power indicating the typical strength of the energy source, or the frequently observed large velocity dispersions of extended emission line regions (e.g. McCarthy et al. 1996).

6.1. Is MRC1138-262 unique? Comparison with longslit analyses

To estimate the cosmological impact of AGN feedback similar to MRC1138-262, this analysis should be compared to a larger sample. However, no similar integral-field data set of the rest-frame optical line emission of a HzRG has so far been obtained, as verified by a recent literature search. Therefore it must be addressed in a more indirect way whether MRC1138-262 is only the first, or possibly the only one of its kind.

Earlier studies of the kinematics in the extended emission line regions of HzRGs used longslit spectrographs. The axis of the MRC1138-262 radio jet in the SPIFFI data cube is roughly along the x coordinate (i.e. along right ascension), therefore the “longslit” spectra were extracted from 4 adjacent slitlets centered on the nucleus. Whereas it is straight-forward to simulate the spectrum of a cutout of the SPIFFI data cube corresponding to a typical $1''$ wide slit, properly estimating and accounting for slit-losses due to misalignment and uncertainties in the positioning is difficult. Therefore it can be expected that line fluxes in the simulated SPIFFI “slit” will be tendentially higher than measured with a longslit.

To investigate the effect of small errors in the positioning, additional SPIFFI “slits” were measured, which were centered on slitlets with offsets of ± 2 slitlets around the nucleus (corresponding to misalignments of $\pm 0.5''$). This leads to variations in the measured line fluxes of factors ~ 2 , which dominates the error budget, even compared to the notoriously large uncertainties of flux measurements at observed near-infrared wavelengths.

Two samples of longslit studies were used for this comparison: Iwamuro et al. (2003) obtained J and H band spectra of 15 HzRGs at $z = 2.0 - 2.6$ using the OHS spectrograph on SUBARU telescope on Mauna Kea, Evans (1998) obtained H and K band spectra of 8 HzRGs in the same redshift range, but on 2 – 4 m class telescopes with rather low signal-to-noise ratios (typically 5 – 10), and partly without flux calibration. This inhomogeneity is the reason why the number of galaxies with longslit data will vary in the comparison.

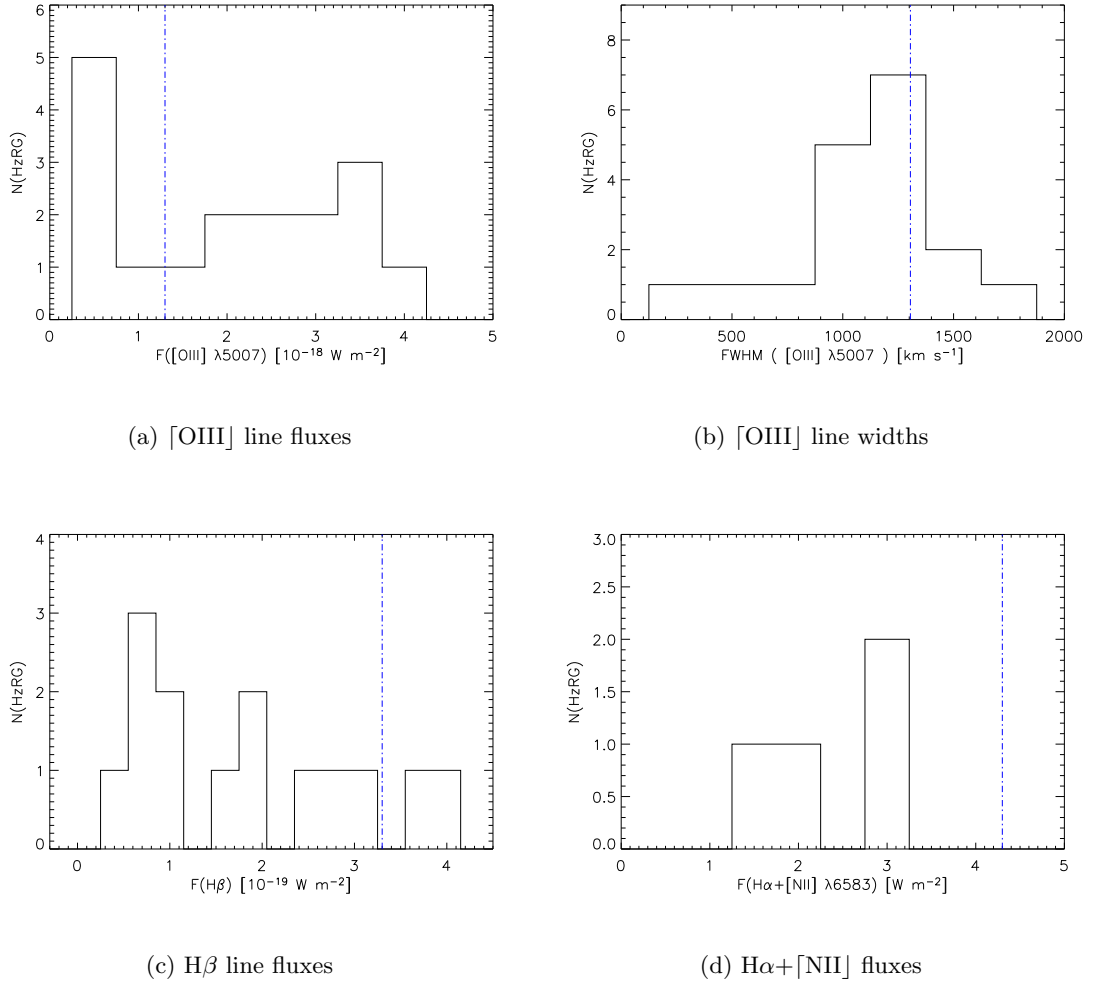


Fig. 18.— Comparison of simulated longslit data of MRC1138-262 with other longslit spectroscopic studies of HzRGs.

Fig. 18 shows how the simulated longslit data of MRC1138-262 relate to the Iwamuro et al. and Evans et al. samples. The [OIII] λ 5007 line width of MRC1138-262 measured through a 1'' wide “slit” centered on the nucleus and roughly aligned with the radio axis, is near the average of the comparison sample. Similarly, [OIII] λ 5007 and H β fluxes in MRC1138-262 have typical values.

The H α + [NII] flux of MRC1138-262, however, is about a factor 2 larger than in the comparison sample, which in this case consists only of the Evans sample (Iwamuro et al. 2003, did not take K band spectra). Given the small number of galaxies in the longslit sample, their typically low signal-to-noise ratios, uncertainties in the slit position, and varying [NII]/H α line ratios, this discrepancy is not very worrisome. In addition, the full MRC1138-262 spectrum was used for this comparison

(including the AGN, only measuring the narrow-line emission), because the AGN correction might overestimate the AGN contribution in MRC1138-262 (see Section 2.2) and a similar correction is not possible for the comparison sample.

The MRC1138-262 “longslit” line fluxes and line widths are smaller than what was obtained from the integral-field data set. Assuming that the ratios between longslit and integral-field data measured with SPIFFI are typical, it can be tried to “correct” the average values in the reference sample with this ratio to estimate the characteristics of “typical” outflows in the combined Iwamuro and Evans reference sample of 22 HzRGs. The average $H\alpha + [\text{NII}]\lambda 6583$ flux in the Evans sample is $2.7 \pm 0.9 \times 10^{-18} \text{ W m}^{-2}$, or 71% of the flux in MRC1138-262, taken at face value. The average $[\text{OIII}]\lambda 5007$ line width is $1243 \pm 360 \text{ km s}^{-1}$, or 95% of the width in MRC1138-262, and the width in MRC1138-262 is within 1σ of the mean of the distribution. The average $H\beta$ flux is $1.98 \pm 1.2 \times 10^{-19} \text{ W m}^{-2}$, 60% of the flux in MRC1138-262.

Overall, this indicates that the turbulent and bulk velocities observed in the outflow of MRC1138-262 are typical for this class of objects, but the ionized hydrogen gas masses in other galaxies might be somewhat lower, up to a factor 2. Since all estimates presented here are accurate to an order of magnitude only, and our simulated “slit” likely underestimates the true amount of slit losses, this is not a major concern for the present analysis. The outflow in MRC1138-262 appears typical with respect to the reference samples.

6.2. The significance of AGN-feedback: Simple energetic argument

In the standard picture, AGN activity is triggered by major mergers of massive galaxies. It is now fairly secure that the most massive systems observed in the local universe have experienced at least one major merger during their evolution. Therefore, and in agreement with the short lifetimes of AGN compared to a Hubble time, AGN activity can only be episodic. Whether a given galaxy experiences only one single such “duty-cycle” or a sequence of these events, is uncertain. To obtain a lower limit, therefore, it will be assumed for the following argumentation that each galaxy undergoes at most one AGN cycle. The energy output during one such cycle follows from the previous analysis:

$$E_{tot,1138} = \dot{E}\tau = 8.9 \times 10^{60} \text{ ergs.} \quad (9.29)$$

The co-moving number density of luminous AGN was calculated by e.g., Pei (1995), and is $\Phi(QSO) \approx 5 \times 10^{-7} \text{ Mpc}^{-3}$ at high redshift. Strictly speaking, this number is valid for optically selected QSOs brighter than $M_B = -26$. If the “unified model” of AGN is correct, then QSOs are a subsample of all active nuclei, where the nucleus is surrounded by an optically thick torus whose opening roughly points towards the observer. In this picture, the observed number density of QSOs will be a few times lower than the intrinsic number density of the full AGN population. It is known that the number density of powerful AGN is a strong function of redshift, therefore the limited redshift range must be taken into account. Fig. 9 of Pei (1995) indicates that 95% of all quasars shone between $z_{QSO} = 1.4 - 4.0$. This estimate was derived by digitizing and interpolating Fig. 9 of Pei (1995) and integrating the number density within the 95% percentiles about the maximum quasar density at $z \approx 2.7$. The digitized data are shown in Fig. 6.2.

This redshift range corresponds to ~ 2.94 Gyrs, or ~ 300 AGN lifetimes, if the AGN lifetime $\tau \sim 10^7$ yrs found in Section 4.1 is representative. Strictly speaking, this is the time until the AGN has reached its most luminous phase, the intrinsic lifetime might be higher if a (probably

more realistic) luminosity-evolution is accounted for. In addition, it is motivated by the observed lifetime of MRC1138-262, which is not necessarily near completion of its AGN phase. In a statistical sense, and with an accuracy limited by the rough lifetime estimate, the intrinsic number of luminous and dormant AGN will be ~ 300 times higher than that observationally found from the number counts of AGN that are observed while they shine.

In another, independent way, the correction factor f_{duty} can be estimated from comparing the correlation lengths of dark matter halos as predicted for a hierarchically collapsing Λ CDM universe with the observed correlation length of AGN. This can be done most easily using Fig. 2 of Mo & White (2002). Correlation lengths of AGN have been obtained by, e.g. Croom et al. (2002) from data of the 2dF survey. Although their median redshift, $z_{2dF} \sim 1.5$ is lower than the redshift of MRC1138-262 ($z = 2.2$) and the peak of the AGN number density shown in Fig. 6.2 ($z \sim 2.7$), inspection of Fig. 2 of Mo & White (2002) shows that the co-moving number densities will only slightly change at redshifts between $z = 1.5$ and $z = 2.7$. Inspection of Fig. 6.2 shows that also the observed number densities of AGN do not change dramatically between these redshifts, although the peak correlation length will be somewhat lower. Since these are order-of-magnitude estimates only, these differences are marginal.

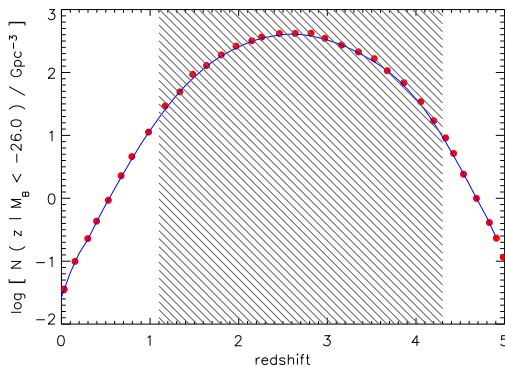


Fig. 19.— *Co-moving QSO number density for QSOs brighter than $M_B = -26.0$ as a function of redshift (Pei 1995). 95% of all QSO were active between redshifts 1.4 and 4.0 (shaded area).*

et al. (2004); Salucci et al. (1999) and (or) redshift (McLure & Dunlop 2004). Adelberger & Steidel (2005) come to a similar result from analyzing the correlation lengths of galaxies clustered around AGN, albeit with only 90% confidence. They estimate f_{duty} between 10 and 10^4 , with large uncertainties.

Following these estimates for the duty cycle and co-moving density of QSOs, the overall energy budget of powerful AGN can be gauged by,

$$\frac{dE_{AGN}}{d^3r} = \Phi_{QSO} f_{duty} E_{tot,1138}. \quad (9.30)$$

As a result, powerful AGN provide a cosmic energy density of $\gtrsim 1.3 \times 10^{57} \text{ ergs}/\text{Mpc}^{-3}$.

At $\langle z \rangle \sim 1.5$, Croom et al. (2002) measure correlation lengths in the range $s_m = 4.05 - 8.37$, corresponding to number densities of $\Phi = 0.015 - 0.0017 \text{ Mpc}^{-3}$, respectively. In the Λ CDM cosmologies, these co-moving space densities at $z \sim 1.5$ correspond to (dark matter) halo correlation lengths of $\sim 0.8 \text{ Mpc}$ and halo masses of $\mathcal{O}(10^{12}) M_\odot$. If AGN are typical evolutionary stages occurring within each massive dark-matter halo, then the length of a duty cycle will follow from comparing the total number of expected halos with the observed number of halos with AGN. Correction factors thus obtained range within $f_{duty} = 300 - 600$, i.e., they indicate AGN lifetimes of a few $\times 10^6 - 10^7$ yrs.

The total AGN lifetime might depend on the black hole mass, as pointed out by Shankar et al. (2004); Salucci et al. (1999) and (or) redshift (McLure & Dunlop 2004). Adelberger & Steidel (2005) come to a similar result from analyzing the correlation lengths of galaxies clustered around AGN, albeit with only 90% confidence. They estimate f_{duty} between 10 and 10^4 , with large uncertainties.

6.3. The significance of AGN-Feedback: local black hole mass density

Independently from the estimates in the previous section, the cosmological significance of AGN feedback can also be constrained from the total amount of accreted mass as contained in the local co-moving mass density of black holes. Yu & Tremaine (2002), using the co-moving number density of spheroids and the $M_{BH} - \sigma$ relation, estimate the local mass density of nuclear black holes of $(2.9 \pm 0.5) \times 10^5 h_{70}^2 \text{ Mpc}^{-3}$. The total kinetic luminosity can be estimated from the simple scaling:

$$\rho_{E,kin} = \epsilon_k \epsilon_{rad} \Delta M_{BH} c^2 = 4.5 \times 10^{57} \epsilon_{k,0.1} \epsilon_{rad,0.1} \text{ ergs Mpc}^{-3}, \quad (9.31)$$

where $\epsilon_{k,0.1}$ is the efficiency of the kinetic energy output relative to the radiative (bolometric) luminosity, and ϵ_{rad} is the radiative efficiency relative to the accreted rest mass energy. The radiative efficiency of massive black holes has been estimated to be roughly 10% to 30% (e.g., Yu & Tremaine 2002, and references therein), whereas there is a broad range of relative kinetic energy efficiency of 0.05 to 1 (Willott et al. 1999). Adopting this range of values suggests that the kinetic energy density is approximately 2 to $100 \times 10^{57} \text{ ergs Mpc}^{-3}$. For a fiducial $\epsilon_{k,0.1}=1$, the estimated kinetic energy density ejected is about $4.5 \times 10^{57} \text{ ergs s}^{-1} \text{ Mpc}^{-3}$ or about a factor of 4 higher than estimated from the QSO co-moving space density and duty cycle.

This estimate however implies that throughout the growth of the black hole the accreted rest-mass is converted to kinetic energy with efficiencies as high as assumed. This might be unrealistic, for example if the black hole is growing through BH-BH mergers. Essentially, this discrepancy implies that the AGN growth time might be underestimated by the timescale during which the AGN is most luminous and radio-loud. Indications for obscured AGN growth are, e.g. the type-II quasars. In addition, the estimate in the previous section assumed an AGN lifetime $\tau = 10^7 \text{ yrs}$, which might be an underestimate by factors of a few. Especially, there are no indications that MRC1138-262 is seen near the end of its duty-cycle. In the spirit of estimating strict lower limits to the AGN feedback, this result agrees with the previous estimate. At any rate, this calculation shows that no low-redshift constraints were violated on the amount of feedback from supermassive black holes.

6.4. The overall energy and mass ejection of AGN feedback

Considering the lowest upper limit on the feedback using the rest mass density of BHs in the local Universe (i.e., $\approx 2 \times 10^{57} \text{ ergs s}^{-1} \text{ Mpc}^{-3}$), both estimates of the total co-moving density of feedback energy agree. However, characterizing the amount of feedback as an energy density lacks an astrophysical context. To put this into perspective, this number is normalized by the local space density of L^* early type galaxies. This provides a rough estimate of the energy output per galaxy under the assumption that every massive galaxy had an episode of rapid, AGN driven gas ejection. This does not literally have to be the case, but is meant to give a scaling of the significance of this feedback. The local co-moving space density of L^* galaxies is $0.0020 h_{70}^3 \text{ Mpc}^{-3}$ (Bernardi et al. 2003) or $0.0022 h_{70}^3 \text{ Mpc}^{-3}$ for M^* early type galaxies (Sheth et al. 2003). Thus, per M^* early-type galaxy, the total amount of energy ejected is about $9 \times 10^{59} \text{ ergs}$. As discussed in more detail in the next section, this is approximately the binding energy of an elliptical galaxy with a total mass of $4 \times 10^{11} M_{\odot}$. Such a mass corresponds to a galaxy that is approximately one magnitude brighter than L_r^* (Bernardi et al. 2005). Based on simple energetic arguments alone, it is clear that AGN feedback could have a significant impact on the most massive galaxies, at least those greater than L^* local ellipticals.

Within this context, can the winds escape and what is their mass ejection rate if they do?

One of the conclusions of Section 4.5 was that these AGN-driven winds can be characterized by mass and energy outflow rates of $\gtrsim 400 M_{\odot} \text{ yr}^{-1}$ and $\sim 3 \times 10^{46} \text{ ergs s}^{-1}$, if MRC 1138-262 is typical of the ensemble of powerful AGN. In a lifetime of $\gtrsim 10^7$ yrs this yields a total mass ejection of $> 4 \times 10^9 M_{\odot}$ and $\sim 9 \times 10^{60}$ ergs. If the wind can escape after achieving blow out from the ambient ISM, then all of its mass and energy will escape into the IGM. The mechanical energy of the AGN is able to entrain ambient material propelling it outwards at the high velocities observed. The maximum amount of ambient material (if accelerated to escape velocity) can be approximated by an energy conservation argument as:

$$M_{ej,max} = 2 \times 10^{11} E_{outflow,60} v_{esc,500}^{-2} M_{\odot} \quad (9.32)$$

where $E_{outflow,60}$ is the energy of the outflow in units of 10^{60} ergs and $v_{esc,500}$ is the escape velocity in units of 500 km s^{-1} .

But will this material escape? That is difficult to calculate directly since the mass profiles of galaxies are not well constrained. Assuming a NFW profile, consistent with N-body simulations of galaxies (Navarro et al. 1997; Bullock et al. 2001), then there is a simple relationship between the escape velocity and the virial radius and mean density of the halo over the background dark matter density (see Bullock et al. 2001). Making the simple assumption that the ratio of dark matter to baryonic matter in MRC1138-262 is 10 (similar to the local universe), the escape velocity is about 700 km s^{-1} at the virial radius of about 120 kpc (Bullock et al. 2001). While the estimate is crude to say the least, it does suggest that, plausibly, much of the observed gas could be escaping the potential of the galaxy.

Thus, if MRC1138-262 is typical of QSOs and other radio galaxies, then AGN feedback drives out between $0.04 - 9 \times 10^{11} M_{\odot}$ of material. The value of $4 \times 10^9 M_{\odot}$ is also a strong lower limit which only includes the optical emission line gas, and extinction corrections alone will increase this amount by factors of a few. The true outflow total is likely to be an order of magnitude higher. Observations of carbon monoxide in high redshift radio galaxies suggest about $\approx 10^{10}$ to $10^{11} M_{\odot}$ of interstellar material (Papadopoulos et al. 2000; Greve et al. 2005). Since these observations are during the process of growing and fueling the black hole and stellar population of the host galaxy, it can plausibly be assumed that the total amount of expelled interstellar matter is larger than the total needed to quench future star-formation. This leads directly to the conclusion that the total amount of matter ejected by AGN feedback is sufficient to remove most, if not all of the ISM of radio galaxies and QSOs.

6.5. Influence on the IGM: metal ejection

Given that the amount of ambient ISM that the AGN mechanical energy is likely to drive out of the galaxy and perhaps out of the dark matter halo in which it resides, it is pertinent to ask, how much metals could such outflows eject. Following the same arguments in Section 6.2, the estimate of the amount of material ejected by MRC1138-262 will now be used to make the assumption that this amount is typical for all QSOs and radio galaxies, and then to estimate the total co-moving mass likely driven out of the ensemble of powerful high redshift AGN. This should only be taken as an order of magnitude estimate.

The total outflow rate of MRC1138-262 was estimated in Section 6.4, $\dot{M} = 0.04 - 9 \times 10^{11} M_{\odot}$. Given a co-moving density of QSOs and the inverse of their duty cycle, and assuming that the outflow rates determined for MRC1138-262 are typical, this suggests a density of material that has been swept out by the AGN of:

$$\rho_{ej,max} \gtrsim 2 - 40 \times 10^6 \Phi_{QSO,-6.3} f_{duty,300} M_{\odot} Mpc^{-3} \quad (9.33)$$

where $\Phi_{QSO,-6.3}$ is the co-moving space density of QSOs in units of $5 \times 10^{-6} Mpc^{-3}$ and $f_{duty,300}$ is the inverse duty cycle in units of 300. This implies that approximately $4 - 80 \times 10^9 M_{\odot}$ of material is ejected per M^* galaxy. Although the range of possible values is large, this is approximately the mass of ISM in a low redshift gas rich galaxy and also the mass of molecular material in high redshift submm sources and radio galaxies. Again, this suggests a significant impact of AGN feedback on the host galaxies and could be the mechanism for rapid gas loss necessary to explain the characteristics of nearby early type galaxies.

Although the metallicity of the ISM of high redshift radio galaxies is not well constrained, the local galaxies that likely have had an episode of strong AGN-feedback during their evolution, all have solar or super-solar metal abundances. If the ISM that is blown out is of solar abundance (and again this is in the spirit of an order of magnitude estimate), the analysis above indicates that powerful AGN feedback expels $2 - 40 \times 10^7 M_{\odot}$ of metals per M^* galaxy. A galaxy approximately one magnitude brighter than L^* early-type galaxy in the nearby Universe has a mass of approximately $3 \times 10^{11} M_{\odot}$. Such a galaxy also has a metallicity approximately 0.3 dex higher than the solar value (Tremonti et al. 2004). This suggests that the total metal content is $\approx 10^{10} M_{\odot}$. Thus, AGN feedback of the power and duration of MRC1138-262 could plausibly eject a similar amount of metals as contained in a brighter than L^* elliptical in the local Universe.

6.6. AGN feedback: solving the $[\alpha/Fe]$ puzzle?

Although it appears that nearly all massive galaxies in the local Universe host massive black holes in their centers, it is not clear how and when these black holes were fueled, what fraction reached QSO luminosities, and what the characteristics of their host galaxies were at the time of their most active phase. What is clear is that the co-moving number density of quasars is – even taking the above correction factors into account – too low to assume that every local galaxy was an AGN in earlier cosmic times. In addition, several lines of evidence indicate that only the most massive (early-type) galaxies have had powerful QSO-like nuclear activity in the past – e.g., the similar fundamental planes (Bettoni et al. 2001) and $K - z$ correlations of powerful radio galaxies and massive early type galaxies (De Breuck et al. 2002), the high $[\alpha/Fe]$ abundances in massive early type galaxies (Thomas, Greggio, & Bender 1999) compared to disk stars in the Milky Way.

The cause of the last of these, the high $[\alpha/Fe]$ observed in local massive early-type galaxies (Thomas, Greggio, & Bender 1999), has been interpreted as due to rapid cessation of all star-formation. The abundance ratio of α -elements to iron traces the relative frequency of thermonuclear and core-collapse supernovae and is a tracer of truncated star formation. To explain the enhanced $[\alpha/Fe]$ abundances within massive local early-type galaxies, Thomas, Greggio, & Bender (1999) must invoke a mechanism by which nearly all gas is efficiently removed from the host in $\lesssim (0.5 - 1) \times 10^9$ yrs. This limit can directly be compared with the dynamics of the outflow in MRC1138-262. Obviously, the findings in this chapter suggest that AGN feedback is a promising mechanism to effectively remove the gas impulsively (i.e., short compared to the dynamical time of early type galaxies). The necessary timescale and energetics implied by Thomas, Greggio, & Bender (1999) will now be explicitly compared with the characteristics of AGN-related outflows.

In Section 4.5 the mass outflow rate from the host of MRC1138-262 was calculated to be $\sim 400 M_{\odot} yr^{-1}$. The photometric mass estimate of MRC1138-262 indicates $M_{stellar} \sim 5 \times 10^{11} M_{\odot}$. If this outflow rate is approximately constant, then the host will lose 10% of its baryonic mass in

about 10^8 yrs. Assuming a gas fraction $f_{gas} \approx \text{few} \times 10\%$, the AGN can efficiently remove the full gas content from its host within $\text{few} \times 10^8$ yrs. While this does not imply that the AGN can provide enough energy to remove all gas from the host, it does show that it has the potential to accelerate sufficient amounts of gas to high enough velocities so that the gas is removed fast enough in a highly impulsive event. Since much of the gas has velocities that are likely well beyond the escape velocity of even the most massive low redshift galaxies, it is likely that this gas is unable to contribute to future episodes of star-formation, meeting the necessary conditions to be a plausible explanation for the enhanced $[\alpha/\text{Fe}]$ abundance ratio.

This is different from feedback due to massive stars, where the feedback can affect the gas in a similar time scale but lacks sufficient energy to eject the gas from the potentials of the most massive galaxies. Thus stellar driven winds are an unlikely explanation the enhanced $[\alpha/\text{Fe}]$ in the most massive early type galaxies. The outflow rate observed and total energy from the AGN in MRC1138-262 suggests that AGN feedback is a suitable mechanism by which to explain the origin of the $[\alpha/\text{Fe}]$ enhancement and other characteristics of early type galaxies in the local Universe.

7. Conclusions

A thorough study of the dynamic properties of the ISM in the $z = 2.2$ powerful radio galaxy MRC1138-262 has been presented. This is one of the first such studies for a powerful high-redshift radio galaxy. The integral-field kinematic properties of the optical nebular emission line gas were measured over radii of 20 kpc from the central AGN. Relative velocities are up to 2500 km s^{-1} , with an average $\sim 800 \text{ km s}^{-1}$, and line widths are $\text{FWHM} = 800 - 2000 \text{ km s}^{-1}$. Emission line properties indicate that the gas is ionized by shocks and photoionization from the AGN. The ionized gas has a low filling factor $\mathcal{O}(10^{-6})$ and is most likely distributed in sheets and filaments. Astrophysical uncertainties are large compared to the measurement errors (which are $\sim 10\%$), so that the analysis aims only at placing lower limits or order-of-magnitude estimates.

The AGN couples efficiently with the ISM, $\epsilon = 0.1$, about two orders of magnitude higher than expected from the dentist drill model. Simple shock models indicate that the AGN must inject about $10^{46} \text{ ergs s}^{-1}$ into the ISM to power the observed gas dynamics. With the estimated bolometric luminosity, radiation-driven winds alone can accelerate the gas only to about half the observed velocities and require acceleration time scales an order of magnitude larger than the observed age of the radio source. From the dynamical timescale and amount of ionized gas, $(2.3 - 6.5) \times 10^9 M_{\odot}$, follows an outflow rate of $400 M_{\odot} \text{ yr}^{-1}$. With an assumed lifetime of $\gtrsim 10^7$ yrs, at least 10^{61} ergs are dissipated into the host ISM, and the outflowing gas mass corresponds to a mass loss of $\sim 10\%$ of the stellar host mass in 10^8 years. During this time, about $(4 - 80) \times 10^9 M_{\odot}$ of metals are expelled into the IGM.

This detailed analysis is based on only one source, but indirect evidence exists that phenomenologically, MRC1138-262 is far from being unique. Velocities of $\sim 1000 \text{ km s}^{-1}$ are not uncommon in the extended emission line gas of powerful radio galaxies (albeit they are generally measured along the radio jet axis only, due to the limitations of longslit spectrographs). The bolometric and radio jet luminosities of MRC1138-262 are not unusual, and the source follows the $K - z$ relationship of high-redshift radio galaxies, if correcting for the luminous broad $\text{H}\alpha$ line emission.

Using the observed space density of powerful AGN at high redshift and their correlation length allows to constrain the cosmological impact of powerful radio galaxies. As a result, powerful AGN drive out $\sim 10^{57} \text{ ergs Mpc}^{-3}$, or, in a more astrophysical context, 10^{60} ergs per low-redshift L^* galaxy. This lower limit does not violate any low-redshift constraints. If the local mass function of

supermassive black holes is used instead of the AGN distribution, then the energy output increases by factors of a few. This is due to the rudimentary knowledge of the physics of supermassive black holes, their number of activity phases, obscured growth, etc., but not intrinsic to this analysis.

The analysis of the AGN feedback presented here draw a plausible scenario for the so far puzzling properties of the most massive galaxies in the local universe. Their star-formation ended 10 Gyrs ago, stellar populations are accordingly old, they have high metallicities, and are very gas poor. These require a feedback mechanism which is powerful enough to quickly remove significant gas fractions from the host. While starburst driven winds are not powerful enough to accelerate the gas beyond the escape velocities of massive galaxies, this analysis shows that AGN feedback can. In addition, the mass loss in gas is high enough to shut-off star-formation fast enough to preserve the enhanced $[\alpha/\text{Fe}]$ relative abundances observed in the most massive galaxies at low redshift.

Chapter 10

Implications for early galaxy evolution: summary

This thesis is a systematic study of high-redshift galaxies using integral-field spectroscopy in the near-infrared. The redshifts of the sources shift the optical into the near-infrared and allow us to study these galaxies at wavelengths commonly used to study nearby galaxies. Integral-field studies of high-redshift galaxies are still a novel approach. Therefore, in many respects, this thesis is a pilot study: the number of targets is small, and the galaxies are not uniformly selected, but are selected using several and popular techniques, allowing us to study a range of physical processes important for galaxy evolution. The sources span a wide redshift range, $z \sim 1 - 3$, corresponding to cosmic ages $\tau = 1.8 - 4.6$ Gyrs after big bang. Detailed analyses of the individual objects were described in the last 5 chapters, including 5 Lyman break galaxies selected on their rest-frame UV properties, at $z \sim 3$, 2 submillimeter selected galaxies at $z \sim 2.5$, a $z = 2.2$ powerful radio galaxy, and a $z \sim 1.3$ H α selected merging pair with physical properties resembling the "BM" (UV-selected galaxy) population at similar redshifts.

Several thousand galaxies have measured redshifts at $z \gtrsim 2$, but detailed analyses beyond measuring ensemble photometric properties of these populations (luminosity functions, color and redshift distributions) are still very rare. Clearly, some of the most fundamental questions regarding high-redshift galaxies cannot be answered with photometry alone, e.g., regarding their evolutionary history, mass, and the physical drivers of their mass assembly. This work also goes beyond previous studies using longslit spectrographs, because it allows to analyze the two-dimensional kinematics of high redshift galaxies and provides the galaxy morphology in both the continuum and the emission line gas. These are significant advantages. Longslit spectroscopy, the most common technique, can only provide information along the slit axis, and thus may only yield lower limits to the projected line widths and velocity offsets unless the kinematic major axis is known *a priori*.

The quality of the data sets on these sources allowed for the extraction of velocity fields of the bright emission lines (H α at $z \lesssim 2.6$, [OIII] $\lambda 5007$ at $z \gtrsim 3$). Since all data sets were flux calibrated, luminosities were calculated to estimate physical properties like ionized gas masses or star-formation rates. In the best data sets and in the most extended sources, variations of these physical quantities within a source could be investigated. Line ratios allow for estimating gas densities, metallicities, and to constrain the nature of the ionizing source (photoionization by hot stars or an AGN, shocks). Details of this were described in Chapter 4.

Theoretically, the main driver of galaxy evolution is the gravitational collapse of the under-

lying dark-matter halo and the relationship between the collapse of baryons and the dark matter. However, it has recently been recognized that a significant impact comes from feedback by both active galactic nuclei (AGN) and intense star-formation. In this thesis, the hypothesis that this feedback could be significant seems to be verified. The following paragraphs will summarize and highlight the most important findings of this work.

1. Rotation in the central kiloparsec of a $z \sim 3.2$ Lyman-break galaxy

Understanding how and at what rate galaxies were assembled is one of the main goals of observational astrophysics. In gaining this understanding, being able to make dynamical mass estimates of different galaxy types and at a range of epochs is crucial. A few studies have aimed at measuring the kinematic properties of emission line gas in high-redshift galaxies, such as velocity gradients or line widths. In virialized systems, these can serve as a tracer for the large-scale rotation and to estimate the total (luminous, non-luminous and dark) matter content. However, it remains yet to be proven whether these measurements indeed reflect rotation.

The most direct signature of virialized rotation are velocity curves with the characteristic flattening at the “turnover points”, but “turnover points” have not yet been uniquely identified in high-redshift galaxies. This is partly a problem of limited spatial resolution: a close binary system of two gravitationally bound, individually unresolved objects might be indistinguishable from a rotation curve. This is of particular concern, because the spatial resolution of seeing-limited observations is $\gtrsim 0.5''$ corresponding to a projected distance of ~ 5 kpc at $z = 2 - 3$, which is within the range of distances in close galaxy pairs or early-stage galaxy mergers. The other limitation is caused by cosmological surface brightness dimming, making it exceedingly difficult to trace the emission line gas of high-redshift galaxies out to large enough radii.

Gravitationally lensed galaxies provide a mechanism for overcoming both limitations, especially if the kinematic major axis of the high-redshift source is approximately aligned with the magnification axis of the lens. The 1E0657 arc+core galaxy studied in this thesis (Chapter 7) is such a source. [OIII] λ 5007 line emission from its brightest, and probably central region (the “core”, Mehlert et al. 2001) shows a regular, steeply rising velocity gradient of 140 km s^{-1} over ~ 500 pc with a turnover (Fig. 10 of Chapter 7), and uniform velocity dispersions of $\sim 70 \text{ km s}^{-1}$. These characteristics are consistent with a rotating galaxy. No similarly clear case of a rotation curve in the very center of a high-redshift galaxy has previously been reported.

The rotation curve implies a lower limit to the galaxy mass within radii $R \sim 500$ pc, $M_{e0657} \gtrsim 10^9 M_{\odot}$. The mass could be factors of a few larger because the intrinsic velocity could be higher due to the inclination of the galaxy and misalignment of the magnification axis of the gravitational lens with the major kinematic axis of the galaxy.

With this mass and radius follows a surface mass density of $\sim 500 - 1000 M_{\odot} \text{ pc}^{-2}$ in the inner regions of the arc+core galaxy, similar to the central surface mass densities of low-redshift early-type galaxies and bulges (e.g., Sofue et al. 2003). This strongly supports the conclusion of Steidel et al. (1996) that LBGs are the inner spheroid component of local $\sim L^*$ galaxies seen during a phase of rapid growth. This implies that most of the mass in the centers of present-day galaxies was already in place a few Gyr after big bang, although presumably not predominately in old stars as in local massive galaxies.

2. Characterizing the starburst and feedback in a $z = 2.6$ Submillimeter Galaxy

With star-formation rates of $\sim 1000 M_{\odot} \text{ yr}^{-1}$, bright Submillimeter galaxies (SMGs) are sites of spectacularly intense star-formation in the high-redshift universe. These galaxies are very dust-enshrouded and due to the high extinction are difficult to observe in the rest-frame UV and optical. Except for mm interferometry, observations at longer wavelength, where most of the bolometric luminosity originates, currently lack the sensitivity and spatial resolution to investigate the spatially-resolved properties of high-redshift galaxies over similar radial distances (i.e., $R \sim 5 - 10$ kpc).

One of the best, if not the best-studied SMG is the $z = 2.6$ SMMJ14011+0252. It has a wealth of available data sets, including high-resolution HST rest-frame UV imaging, deep ground-based rest-frame optical imaging and far-infrared/CO emission line observations. It is one of the brightest SMGs at rest-frame optical wavelengths ($m_K = 17.8$ mag). The line emitting gas is comparatively very extended ($3.5'' \times 2''$) with large ($\lesssim 150 \text{ \AA}$) rest-frame equivalent widths. SMMJ14011+0252 is moderately gravitationally lensed (magnification factor $\mathcal{M} \sim 5$) by the foreground galaxy cluster A1835 at $z = 0.25$.

By combining the publicly available data sets with deep SPIFFI observations in the J, H, and K bands, it was possible to investigate SMMJ14011+0252 in greater detail than any other SMG. The relative astrometry between the CO and rest-frame UV/optical data was improved by cross-correlating the CO and rest-frame UV/optical data sets, placing the CO peak safely within the optical counterpart, roughly in the middle between the continuum and $H\alpha$ line emission peaks. This solves a controversy in the literature. The remaining positional uncertainty ($\sim 0.3''$) and small ($< 1''$) offset between the continuum and line emission peaks, however, make it difficult to uniquely assign the CO emission to either of the two components. It is also possible that the CO gas – and hence the site of the starburst – is not assigned to any of the individual rest-frame optical components, but is intrinsically placed inbetween.

Emission line ratios indicate that the physical conditions in SMMJ14011+0252 are within the broad range observed in local ULIRGs and hint that the starburst is the major ionizing source. Line widths are $\sigma \sim 75 - 95 \text{ km s}^{-1}$, in the range expected for a massive ($10^{10} - 10^{11} M_{\odot}$) galaxy. The spatial distribution of line widths is irregular, and peaks near the maximum of the $H\alpha$ emission.

Relative velocities within the source have an overall gradient of $\sim 180 \text{ km s}^{-1}$, with a significant (4.4σ) intermediate dip $0.75''$ north of the rest-frame UV/optical continuum peak. The limited spatial resolution and signal-to-noise ratio of the data make it difficult to constrain the nature of this structure, but conservatively, one cannot rule out that the emission line gas is in a more complex configuration than a self-gravitating, isolated disk. Again, this highlights the similarity of SMGs and ULIRGs. Possible (speculative) scenarios include a co-rotating merger or a kinematically decoupled component within the galaxy.

Star-formation rates were calculated from the extinction-corrected $H\alpha$ fluxes, $SFR = 1100 M_{\odot} \text{ yr}^{-1}$, not correcting for lensing. The $H\alpha$ surface brightness varies by a factor ~ 6 across the source. $H\alpha$ equivalent widths and reddening are positively correlated in SMMJ14011+0252, indicating that most of the reddening comes from extinction (rather than age), and the dispersion in the $J - K$ colors indicate variations in the reddening. This positive correlation also suggests that the dust distribution is clumpy, so that $H\alpha$ escape fractions are relatively high at least in some parts of the galaxy.

The high star-formation rates and large spatial extent of SMMJ14011+0252 have previously led some authors to speculate that high-redshift star-formation might be more efficient in isolated

galaxies than observed at low redshift (Goldader et al. 2002). The complexity of the kinematics sheds some doubts as to whether SMMJ14011+0252 is a viable basis for such a claim. Moreover, the star-formation rate density in SMMJ14011+0252 is $57 M_{\odot} \text{ yr}^{-1} \text{ kpc}^{-2}$, similar to the “maximal starburst” surface density in low-redshift starbursts ($45 M_{\odot} \text{ yr}^{-1} \text{ kpc}^{-2}$, Meurer et al. 1997). Although the existence of such a limit is still somewhat controversial, this hints that at least on a basic level, the properties of the starburst in SMMJ14011+0252 do not greatly differ from those at low redshift and that the star-formation may be self-regulating.

The intense star-formation in SMMJ14011+0252 triggers a massive outflow similar to galactic “winds” in actively star-forming galaxies at low redshift. Conventionally, outflows at high-redshift are identified by blue asymmetries in emission lines. The large [NII] λ 6583/ $H\alpha$ ratios, especially in the northern part of the source ([NII]/ $H\alpha \sim 0.7$), indicate that a major part of the line emission is caused by shocks. The excellent, spatially-resolved data set of SMMJ14011+0252 allows to go further and use correlations between emission line widths and line ratios as a wind diagnostic, similar to low-redshift observations (Lehnert & Heckman 1996a). In SMMJ14011+252, the [NII]/ $H\alpha$ ratio correlates strongly with the FWHM of [NII] (Pearson’s correlation coefficient is $R = 0.83$). This is the expected signature of shocks with speeds of a few hundred km s^{-1} , which become more luminous with increasing speed. A similar analysis of the $H\alpha$ line emission indicates that this outflow does not influence the observed $H\alpha$ emission line kinematics, and hence cannot explain the irregular velocity and dispersion maps discussed earlier.

The SPIFFI data set includes and spectrally resolves the [OII] $\lambda\lambda$ 3726,3729 and [SII] $\lambda\lambda$ 6717,6730 emission line doublets, with ratios that are sensitive to electron densities in the line emitting regions (i.e., the partially ionized zone). The measured density of $\sim 300 \text{ cm}^{-3}$ translates into a pressure of $1.2 \times 10^{-9} \text{ dyn cm}^{-2}$, in excellent agreement with low-redshift starburst-driven winds, and indicating similar outflow mechanisms at low and at high redshift. However, comparison of the SMMJ14011+252 wind with low-redshift outflows also shows that the $H\alpha$ surface brightness in SMMJ14011+0252 is brighter by about an order of magnitude. Of course, this comparison spans a wide range of luminosities and the high surface brightness of the wind in SMMJ14011+252 may reflect more intense star-formation and extinction leading to a higher fraction of gas seen as an outflow. However, the $H\alpha$ gas is emitted from clouds that are being swept-up, ionized, and accelerated by the hot, X-ray emitting outflow, this might indicate a higher filling factor in SMMJ14011+0252, perhaps related to an intrinsically higher gas fraction compared to local starburst galaxies exhibiting winds. At any rate, it appears that starburst-driven winds may have a significant impact on SMMJ14011+0252 and SMGs in general.

3. AGN-feedback and the evolution of the most massive galaxies in the universe

Another feedback mechanism has recently been recognized by theorists (e.g. Di Matteo et al. 2005) as perhaps having a significant impact on galaxy evolution, but is observationally as yet very little studied: large-scale outflows from the host galaxy caused by the central AGN. Powerful AGN (i.e., quasars and powerful radio galaxies) have a co-moving space density which is strongly peaked around $z \sim 2$, and projected sizes of a few arcseconds, which makes them particularly suited for detailed observations with SPIFFI. They are also the likely progenitors of the most massive galaxies in the local universe, and might therefore hold the key to some of the peculiar properties of this population: At low redshift, the most massive galaxies have old stellar populations, very low gas fractions, and high metallicity. Maybe the tightest constraint is set by their overabundance of α elements relative to iron, $[\alpha/\text{Fe}]$, which indicates that the star-formation stopped within a few $\times 10^8$ yrs (Thomas, Greggio, & Bender 1999).

Powerful AGN feedback removing significant gas masses from the host galaxy at the end of a phase of rapid growth is a plausible scenario to explain these properties. To investigate whether AGN have the predicted characteristics necessary to provide a significant influence on galaxy evolution, this thesis includes a detailed analysis of the integral-field kinematics in the extended emission line region around the $z = 2.2$ powerful radio galaxy MRC1138-262 (Chapter 9). Emission lines in MRC1138-262 have widths of $\text{FWHM} = 800 - 2000 \text{ km s}^{-1}$ and relative velocities of up to 2400 km s^{-1} . Emission line properties indicate that the gas is ionized by shocks and photoionization from the AGN.

The gas does not have a smooth gradient consistent with rotation, but is grouped into at least 3 kinematically distinct regions with approximately uniform (albeit complex) internal kinematics, suggesting powerful large scale outflows, in broad agreement with what is required if AGN feedback has indeed a significant impact on the host. A detailed analysis of the properties in these regions implies a mass loss rate of $\sim 400 M_{\odot} \text{ yr}^{-1}$, enough to remove about 10% of the stellar mass of MRC1138-262 ($M_{\text{star}} \sim 5 \times 10^{11} M_{\odot}$; Pentericci 1999) in 10^8 yrs. This is within the rough timescale set by the $[\alpha/\text{Fe}]$ overabundance. The intrinsic mass loss is likely higher, because most of the outflowing material will probably emit significantly in the X-ray while only the swept-up and entrained material will be a strong emitter of optical emission line radiation.

Therefore, we had to rely on the velocity of this entrained gas to estimate the total energy of the outflowing material. To estimate the energy necessary to drive the observed outflow, an energy-conserving bubble is assumed that expands due to its own internal pressure. If MRC1138-262 has a typical AGN lifetime ($\tau \sim 10^7$; Martini 2004), then the total kinetic energy of the outflow will be of order $E_{\text{kin,tot}} = 10^{61}$ ergs, similar to the binding energy of a massive galaxy. In other words, most of the gas will probably escape from the gravitational potential of the host galaxy, suppressing subsequent star-formation.

Due to a lack of similar analyses of other high redshift radio galaxies, it is difficult to estimate whether MRC1138-262 is a unique or represents a typical (but maybe short) stage in the evolution of massive galaxies. However, a number of studies using longslit spectrographs aligned with the radio jets, previously identified similarly extreme kinematics with FWHMs and velocity gradients exceeding 1000 km s^{-1} (e.g. Tadhunter 1991; Evans 1998; Iwamuro et al. 2003). If indeed similar outflows are common in powerful AGN, then AGN-driven feedback might have a similar or even larger contribution to the total energy and mass injection from galaxies into the intergalactic medium (IGM) or intracluster medium (ICM) than feedback related to star-formation. The cosmological impact of AGN feedback can be estimated from the observed properties of MRC1138-262 and the co-moving space density of powerful AGN corrected for the ‘‘duty cycle’’ (i.e. the AGN lifetime relative to the total epoch of powerful AGN). It appears that overall, AGN-feedback ejected similar energy densities as starburst-driven winds, $\sim 10^{57} \text{ ergs Mpc}^{-3}$. Per L^* galaxy, about $\mathcal{O}(10^9 M_{\odot})$ in gas are released into the ICM/ISM, including $\mathcal{O}(10^7 M_{\odot})$ in metals (for solar metallicity). Hence the global cosmological impact of both processes could be similar. However, since the velocities and total energy in individual sources is higher in the case of AGN feedback, it is likely that AGN feedback is much more significant in the evolution of the most massive galaxies than starburst driven outflows.

4. Outlook

Substantial populations of high-redshift galaxies with spectroscopic redshifts were only found in the last decade, and thus the direct exploration of the early universe is still in its infancy.

Nonetheless, it is already providing powerful constraints on our understanding of galaxy evolution and large-scale structure, and will certainly continue to do so, especially with ever improved instrumentation and telescopes (e.g., ALMA and JWST).

Obviously, much larger galaxy samples are needed to investigate the properties of high-redshift galaxies in greater detail, and this early study of the integral-field kinematic and evolutionary properties of a small galaxy sample is only a first step. Given that the properties of individual high-redshift galaxies are still essentially unknown territory, it seemed more than appropriate to initially investigate the broad range of physical processes that can be traced with spatially-resolved kinematics, and that are important for galaxy evolution. And undoubtedly, this thesis has shown that galaxy dynamics at high-redshift are as rich and complex as in the local universe – at least.

REFERENCES

- Abuter, R. et al., "SINFONI Data Reduction Software", to be published in the Proceedings of the Workshop "IFS techniques and data reduction", 4-8 July 2005, CfAI Durham, eds. J Gerssen, J. Allington-Smith & D. Robertson, in a special edition of *New Astronomy Reviews*, Elsevier.
- Adelberger, K. L., Steidel, C. C., Giavalisco, M., Dickinson, M., Pettini, M., & Kellogg, M. 1998, *ApJ*, 505, 18
- Adelberger, K. L., Steidel, C. C., Shapley, A. E., & Pettini, M. 2003, *ApJ*, 584, 45
- Adelberger K. L., Steidel, C. C., astro-ph/05005210
- Alexander, D. M., Smail, I., Bauer, F. E., Chapman, S. C., Blain, A. W., Brandt, W. N., & Ivison, R. J. 2005, *Nature*, 434, 738
- Allende Prieto, C., Lambert, D. L., & Asplund, M. 2001, *ApJ*, 556, L63
- Almaini, O., et al. 2003, *MNRAS*, 338, 303
- Amram, P., Marcelin, M., Boulesteix, J., & Le Coarer, E. 1992, *A&A*, 266, 106
- Appenzeller, I., et al. 1998, *The Messenger*, 94, 1
- Archibald, E. N., Dunlop, J. S., Hughes, D. H., Rawlings, S., Eales, S. A., & Ivison, R. J. 2001, *MNRAS*, 323, 417
- Baker, A. et al., in preparation
- Barden, M. et al., in preparation
- Barger, A. J., Cowie, L. L., Smail, I., Ivison, R. J., Blain, A. W., & Kneib, J.-P. 1999, *AJ*, 117, 2656
- Barger, A. J., Cowie, L. L., & Richards, E. A. 2000, *AJ*, 119, 2092
- Barger, A. J., Cowie, L. L., Steffen, A. T., Hornschemeier, A. E., Brandt, W. N., & Garmire, G. P. 2001, *ApJ*, 560, L23
- Barlow, R. 1989, *The Manchester Physics Series*, New York: Wiley, 1989,
- Barmby, P., et al. 2004, *ApJS*, 154, 97
- Begelman, M. C., & Cioffi, D. F. 1989, *ApJ*, 345, L21
- Bender, R., Burstein, D., & Faber, S. M. 1992, *ApJ*, 399, 462
- Bender, R., Burstein, D., & Faber, S. M. 1993, *ApJ*, 411, 153
- Bernardi, M., et al. 2003, *AJ*, 125, 1882
- Bernardi, M., Sheth, R. K., Nichol, R. C., Schneider, D. P., & Brinkmann, J. 2005, *AJ*, 129, 61
- Berta, S., Fritz, J., Franceschini, A., Bressan, A., & Lonsdale, C. 2004, *A&A*, 418, 913
- Bertin, E. & Arnouts, S. 1996, *A&AS*, 117, 393
- Best, P. N., Lehnert, M. D., Miley, G. K., & Röttgering, H. J. A. 2003, *MNRAS*, 343, 1

- Bettoni, D., Falomo, R., Fasano, G., Govoni, F., Salvo, M., & Scarpa, R. 2001, *A&A*, 380, 471
- Bicknell, G. V., Dopita, M. A., & O'Dea, C. P. O. 1997, *ApJ*, 485, 112
- Binette, L., Dopita, M. A., & Touhy 1985, *ApJ*, 297, 476
- Binney, J., & Merrifield, M. 1998, *Galactic astronomy* / James Binney and Michael Merrifield. Princeton, NJ : Princeton University Press, 1998. (Princeton series in astrophysics) QB857 .B522 1998 (\$35.00),
- Binney, J., & Tremaine, S. 1987, Princeton, NJ, Princeton University Press, 1987, 747 p.,
- Biretta, J. et al. 2001, *WFPC2 Instrument Handbook, Version 6.0*
- Blain, A. W., Kneib, J.-P., Ivison, R. J., & Smail, I. 1999, *ApJ*, 512, L87
- Blain, A. W., Smail, I., Ivison, R. J., Kneib, J.-P., & Frayer, D. T. 2002, *Phys. Rep.*, 369, 111
- Blain, A. W., Chapman, S. C., Smail, I., & Ivison, R. 2004, *ApJ*, 611, 725
- Borys, C., et al. 2004, *MNRAS*, 352, 759
- Boselli, A., et al. 2005, *ApJ*, 623, L13
- Bremer, M. N., Jensen, J. B., Lehnert, M. D., Schreiber, N. M. F., & Douglas, L. 2004, *ApJ*, 615, L1
- Bruzual, G., & Charlot, S. 2003, *MNRAS*, 344, 1000
- Bouwens, R. J., Illingworth, G. D., Blakeslee, J. P., Broadhurst, T. J., & Franx, M. 2004, *ApJ*, 611, L1
- Bullock, J. S., Kolatt, T. S., Sigad, Y., Somerville, R. S., Kravtsov, A. V., Klypin, A. A., Primack, J. R., & Dekel, A. 2001, *MNRAS*, 321, 559
- Bundy, K., Fukugita, M., Ellis, R. S., Kodama, T., & Conselice, C. J. 2004, *ApJ*, 601, L123
- Calzetti, D. 1997, *AJ*, 113, 162
- Carilli, C. L., Harris, D. E., Pentericci, L., Röttgering, H. J. A., Miley, G. K., Kurk, J. D., & van Breugel, W. 2002, 567, 781
- Chapman, S. C., et al. 2000, *MNRAS*, 319, 318
- Chapman, S. C., Shapley, A., Steidel, C. C., Windhorst, R. 2002, *ApJ*, 572, L1
- Chapman, S. C., Blain, A. W., Ivison, R. J., & Smail, I. 2003, *Nature*, 422, 695
- Chapman, S. C., Smail, I., Blain, A. W., & Ivison, R. J. 2004, *ApJ*, 614, 671
- Chapman, S. C., Blain, A. W., Smail, I., & Ivison, R. J. 2005, *ApJ*, 622, 772
- Charlot, S. & Fall, S. M. 2000, *ApJ*, 539, 718
- Chitre, A., & Joshi, U. C. 2001, *Journal of Astrophysics and Astronomy*, 22, 155
- Colina, L., Arribas, S., & Monreal-Ibero, A. 2005, *ApJ*, 621, 725

- Conselice, C. J., Bershad, M. A., Dickinson, M., & Papovich, C. 2003, *AJ*, 126, 1183
- Croom, S. M., Boyle, B. J., Loaring, N. S., Miller, L., Outram, P. J., Shanks, T., & Smith, R. J. 2002, *MNRAS*, 335, 459
- in preparation.
- Daddi, E., et al. 2004, *ApJ*, 600, L127
- De Breuck, C., van Breugel, W., Stanford, S. A., Röttgering, H., Miley, G., & Stern, D. 2002, *AJ*, 123, 637
- Dey, A., van Breugel, W., Vacca, W. D., & Antonucci, R. 1997, *ApJ*, 490, 698
- Dickinson, M., Papovich, C., Ferguson, H. C., & Budavári, T. 2003, *ApJ*, 587, 25
- Dopita, M. A., & Sutherland, R. S. 1995, *ApJ*, 455, 468
- Dopita, M. A., & Sutherland, R. S. 1996, *ApJS*, 102, 161
- Dopita, M. A., & Sutherland, R. S. 2003, *Astrophysics of the diffuse universe*, Berlin, New York: Springer, 2003. Astronomy and astrophysics library, ISBN 3540433627,
- Downes, D. & Solomon, P. M. 2003, *ApJ*, 582, 37
- Dyson, J. E., & Williams, D. A. 1980, *The Physics of the Interstellar Medium*, (John Wiley & Sons: New York, New York)
- Eisenhauer, F., Tecza, M., Mengel, S., Thatte, N. A., Roehle, C., Bickert, K., & Schreiber, J. 2000, *Proc. SPIE*, 4008, 289
- Eisenhauer, F., et al. 2003, *Proc. SPIE*, 4841, 1548
- Ellis, R. S., Colless, M., Broadhurst, T., Heyl, J., & Glazebrook, K. 1996, *MNRAS*, 280, 235
- Ellis, R. S. 1997, *ARA&A*, 35, 389
- Ellison, S. N., Kewley, L., astro-ph/0508627
- Elmegreen, B. G. 1999, *ApJ*, 517, 103
- Elmegreen, B. G. 2005, Elmegreen, D. M., Vollbach, D. R., Foster, E. R., Ferguso, T. E., *ApJ*, in press, astro-ph/0510245
- Elvis, M., Wilkes, B. J., McDowell, J. C., Green, R. F., Bechtold, J., Willner, S. P., Oey, M. S., Polomski, E., & Curti, R. 1994, *ApJS*, 95, 1
- Erb, D. K., Shapley, A. E., Steidel, C. C., Pettini, M., Adelberger, K. L., Hunt, M. P., Moorwood, A. F. M., & Cuby, J. 2003, *ApJ*, 591, 101
- Erb, D. K., Steidel, C. C., Shapley, A. E., Pettini, M., & Adelberger, K. L. 2004, *ApJ*, 612, 122
- Evans, A. S. 1998, *ApJ*, 498, 553
- Faber, S. M., et al. 1997, *AJ*, 114, 1771
- Fabian, A. C., et al. 2000, *MNRAS*, 315, L8

Ferland, G. J. 2004, American Astronomical Society Meeting Abstracts, 205,

Ferrarese, L., & Merritt, D. 2000, ApJ, 539, L9

Ferrarese, L. 2002, ApJ, 578, 90

Fixsen, D. J., Dwek, E., Mather, J. C., Bennett, C. L., & Shafer, R. A. 1998, ApJ, 508, 123

Förster Schreiber, N. M., Genzel, R., & Lutz, D. 2003, ApJ, 599, 193

Fort, B., & Mellier, Y. 1994, A&A Rev., 5, 239

Fosbury, R. A. E., et al. 2003, ApJ, 596, 797

Freeman, K. C. 1970, ApJ, 160, 811

Franx, M., Illingworth, G. D., Kelson, D. D., van Dokkum, P. G., & Tran, K. 1997, ApJ, 486, L75

Franx, M., et al. 2003, ApJ, 587, L79

Frayer, D. T., Ivison, R. J., Scoville, N. Z., Yun, M., Evans, A. S., Smail, I., Blain, A. W., & Kneib, J.-P. 1998, ApJ, 506, L7

Frayer, D. T., et al. 1999, ApJ, 514, L13

Frayer, D. T., Armus, L., Scoville, N. Z., Blain, A. W., Reddy, N. A., Ivison, R. J., & Smail, I. 2003, AJ, 126, 73

Frayer, D. T., Reddy, N. A., Armus, L., Blain, A. W., Scoville, N. Z., & Smail, I. 2004, AJ, 127, 728

Freeman, K., & Bland-Hawthorn, J. 2002, ARA&A, 40, 487

Gebhardt et al. 2000, ApJ, 543, L5

Giavalisco, M., Steidel, C. C., & Macchetto, F. D. 1996, ApJ, 470, 189

Giavalisco, M., Steidel, C. C., Adelberger, K. L., Dickinson, M. E., Pettini, M., & Kellogg, M. 1998, ApJ, 503, 543

Giavalisco, M. 2002, ARA&A, 40, 579

Giavalisco, M., et al. 2004, ApJ, 600, L103

Glazebrook, K., et al. 2004, Nature, 430, 181

Goldader, J. D., Meurer, G., Heckman, T. M., Seibert, M., Sanders, D. B., Calzetti, D., & Steidel, C. C. 2002, ApJ, 568, 651

Greve, T. R., et al. 2005, MNRAS, 359, 1165

Hauser, M. G., et al. 1998, ApJ, 508, 25

Hawarden, T., Leggett, S., Letawsky, M., Ballantyne, D., & Casali, M. 2001, MNRAS, 325, 563

Heckman, T. M., & Balick, B. 1979, A&A, 79, 350.

Heckman, T. M., Armus, L., & Miley, G. K. 1990, ApJS, 74, 833

- Heckman, T. M., Robert, C., Leitherer, C., Garnett, D. R., & van der Rydt, F. 1998, *ApJ*, 503, 646
- Heckman, T. M., Lehnert, M. D., Strickland, D. K., & Armus, L. 2000, *ApJS*, 129, 493
- Heckman, T. M. 2002, *ASP Conf. Ser. 254: Extragalactic Gas at Low Redshift*, 254, 292
- Heckman, T. M. 2003, *Revista Mexicana de Astronomia y Astrofisica Conference Series*, 17, 47
- Hosokawa, T. 2004, *ApJ*, 606, 139
- Immeli, A., Samland, M., Westera, P., & Gerhard, O. 2004, *ApJ*, 611, 20
- Ivion, R., Smail, I., Le Borgne, J.-F., Blain, A. W., Kneib, J.-P., Bézecourt, J., Kerr, T. H., & Davies, J. K. 1998, *MNRAS*, 298, 583
- Ivion, R. J., Smail, I., Barger, A. J., Kneib, J.-P., Blain, A. W., Owen, F. N., Kerr, T. H., & Cowie, L. L. 2000, *MNRAS*, 315, 209
- Ivion, R. J., Smail, I., Frayer, D. T., Kneib, J.-P., & Blain, A. W. 2001, *ApJ*, 561, L45
- Iwamuro, F., et al. 2003, *ApJ*, 598, 178
- Kapahi, V. K., Athreya, R. M., van Breugel, W., McCarthy, P. J., & Subrahmanya, C. R. 1998, *ApJS*, 118, 275
- Kaspi, S., Smith, P. S., Netzer, H., Maoz, D., Jannuzi, B. T., & Giveon, U. 2000, *ApJ*, 533, 631
- Kauffmann, G., & Haehnelt, M. 2000, *MNRAS*, 311, 576
- Kauffmann, G., White, S. D. M., & Guiderdoni, B. 1993, *MNRAS*, 264, 201
- Kennicutt, R. C. 1998, *ARA&A*, 36, 189
- Kennicutt, R. C. 1992, *ApJS*, 79, 255
- Keres, D., Yun, M. S., & Young, J. S. 2003, *ApJ*, 582, 659
- Kewley, L. J., Dopita, M. A., Sutherland, R. S., Heisler, C. A., & Trevena, J. 2001, *ApJ*, 556, 121
- Kewley, Dopita, Evans, Groves, Sutherland, Binette, Allen, Leitherer, 2004, in prep
- King, A. 2003, *ApJ*, 596, L27
- Kinney, A. L., Calzetti, D., Bohlin, R. C., McQuade, K., Storchi-Bergmann, T., & Schmitt, H. R. 1996, *ApJ*, 467, 38
- Kobulnicky, H. A., Kennicutt, R. C., Jr., & Pizagno, J. 1998, *ApJ*, 514, 544
- Kraemer, S. B., Ruiz, J. R., & Crenshaw, D. M. 1998, *ApJ*, 508, 232
- Krist, J. E., & Hook, R. N. 1997, *The 1997 HST Calibration Workshop with a New Generation of Instruments*, p. 192, 192
- Kobulnicky, H. A. & Koo, D. C. 2000, *ApJ*, 545, 712
- Kolatt, T. S., et al. 1999, *ApJ*, 523, L109
- Kurk, J., 2003, PhD thesis

- Kurk, J. D., Pentericci, L., Röttgering, H. J. A., & Miley, G. K. 2004, *A&A*, 428, 793
- Lagache, G., Abergel, A., Boulanger, F. Désert, F.-X., & Puget, J.-L. 1999, *A&A*, 344, 322
- Larkin, J. E., et al. 2000, *ApJ*, 533, L61
- Le Fèvre, O., et al. 2000, *MNRAS*, 311, 565
- Lehnert, M. D. & Heckman, T. M. 1996a, *ApJ*, 462, 651
- Lehnert, M. D. & Heckman, T. M. 1996b, *ApJ*, 472, 546
- Lehnert, M. D., Heckman, T. M., & Weaver, K. A. 1999, *ApJ*, 523, 575
- Lehnert, M. D., Förster Schreiber, N. M., & Bremer, M. N. 2005, *ApJ*, 624, 80
- Leitherer, C., et al. 1999, *ApJS*, 123, 3
- Lemoine-Busserolle, M., Contini, T., Pelló, R., Le Borgne, J.-F., Kneib, J.-P., & Lidman, C. 2003, *A&A*, 397, 839
- Lena, P., Lebrun, F., & Mignard, F. 1998, *Observational astrophysics*. 2nd rev. and enl. ed. Edited by P. Lena, F. Lebrun, and F. Mignard. Transl. by S. Lyle. Publisher: Berlin: Springer, 1998. *Astronomy and Astrophysics Library*. ISBN: 3540634827,
- Lequeux, J. 1983, *A&A*, 125, 394
- Liu, C. T., & Kennicutt, R. C. 1995, *ApJS*, 100, 325
- Lonsdale, C. J. & Barthel, P. D. 1986, *AJ*, 92, 12
- Madau, P., Ferguson, H. C., Dickinson, M. E., Giavalisco, M., Steidel, C. C., & Fruchter, A. 1996, *MNRAS*, 283, 1388
- Magorrian, J., et al. 1998, *AJ*, 115, 2285
- Maraston, C., Kissler-Patig, M., Brodie, J., Barmby, P., & Huchra, J. 2002, *Ap&SS*, 281, 137
- Martini, P. 2004, *Coevolution of Black Holes and Galaxies*, 170
- Mas-Hesse, J. M., Kunth, D., Tenorio-Tagle, G., Leitherer, C., Terlevich, R. J. & Terlevich, E. 2004, *ApJ*, 598, 858
- Di Matteo, T., Springel, V., & Hernquist, L. 2005, *Nature*, 433, 604
- McCarthy, P. J., Baum, S. A., & Spinrad, H. 1996, *ApJS*, 106, 281
- McCarthy, P. J., et al. 1999, *ApJ*, 520, 548
- McGaugh, S. S. 1991, *ApJ*, 380, 140
- McLure, R. J., & Dunlop, J. S. 2004, *MNRAS*, 352, 1390
- Mehlert, D., et al. 2001, *A&A*, 379, 96
- Meurer, G. R., Heckman, T. M., Lehnert, M. D., Leitherer, C., & Lowenthal, J. 1997, *AJ*, 114, 54
- Mihos, J. C., & Hernquist, L. 1996, *ApJ*, 464, 641

- Mihos, J. C., & Bothun, G. D. 1997, *ApJ*, 481, 741
- Mihos, C. J., Richstone, D. O., & Bothun, G. D. 1992, *ApJ*, 400, 153
- Mirabel, I. F., & Sanders, D. B. 1989, *ApJ*, 340, L43
- Mo, H. J., Mao, S., & White, S. D. M. 1998, *MNRAS*, 295, 319
- Mo, H. J., & White, S. D. M. 2002, *MNRAS*, 336, 112
- Motohara, K., et al. 2005, *AJ*, 129, 53
- Murphy, T. W., Soifer, B. T., Matthews, K., & Armus, L. 2001, *ApJ*, 559, 201
- Murray, N., Quataert, E., & Thompson, T. A. 2005, *ApJ*, 618, 569
- Nagamine, K. 2002, *ApJ*, 564, 73
- Nandra, K., Mushotzky, R. F., Arnaud, K., Steidel, C. C., Adelberger, K. L., Gardner, J. P., Teplitz, H. I., & Windhorst, R. A. 2002, *ApJ*, 576, 625
- Nath, B. B., & Roychowdhury, S. 2002, *MNRAS*, 333, 145
- Navarro, J. F., Frenk, C. S., & White, S. D. M. 1997, *ApJ*, 490, 493
- Nelson, C. H., & Whittle, M. 1996, *ApJ*, 465, 96
- Neri, R., et al. 2003, *ApJ*, 597, L113
- Osterbrock, D. E. 1989, *Astrophysics of Gaseous Nebulae and Active Galactic Nuclei*, (University Science Books: Mill Valley, CA)
- Pagel, B. E. J. 1989, in *Evolutionary Phenomena in Galaxies*, ed. J. E. Beckman & B. E. J. Pagel (Cambridge: Cambridge University Press), 201
- Pagel, B. E. J., Edmunds, M. G., Blackwell, D. E., Chun, M. S., & Smith, G. 1979, *MNRAS*, 193, 219
- Pagel, B. E. J., Edmunds, M. G., Blackwell, D. E., Chun, M. S., & Smith, G. 1979, *MNRAS*, 189, 95
- Pahre, M. A., Djorgovski, S. G., & de Carvalho, R. R. 1998, *AJ*, 116, 1591
- Papadopoulos, P. P., Röttgering, H. J. A., van der Werf, P. P., Guilleaume, S., Omont, A., van Breugel, W. J. M., & Tilanus, R. P. J. 2000, *ApJ*, 528, 626
- Papovich, C., Dickinson, M., & Ferguson, H. C. 2001, *ApJ*, 559, 620
- Pei, Y. C. 1995, *ApJ*, 438, 623
- Pentericci, L., 1999, PhD thesis
- Pettini, M., Kellogg, M., Steidel, C. C., Dickinson, M., Adelberger, K. L., & Giavalisco, M. 1998, *ApJ*, 508, 539
- Pettini, M., Shapley, A. E., Steidel, C. C., Cuby, J., Dickinson, M., Moorwood, A. F. M., Adelberger, K. L., & Giavalisco, M. 2001, *ApJ*, 554, 981

Pettini, M. & Pagel, B. E. J. 2004, MNRAS, 348, L59

Puech, M., Flores, H., Hammer, F., et al., in prep.

Puget, J.-L., Abergel, A., Bernard, J.-P., Boulanger, F., Burton, W. B., Désert, F.-X., & Hartmann, D. 1996, A&A, 308, L5

Ravindranath, S., Ferguson, H., Giavalisco, M., Dickinson, M., Papovich, C., & GOODS 2004, American Astronomical Society Meeting Abstracts, 205,

Reeves, J. N., O'Brien, P. T., & Ward, M. J. 2003, ApJ, 593, 65

Reuland, M., Röttgering, H., van Breugel, W., & De Breuck, C. 2004, MNRAS, 353, 377

Rix, H.-W., Guhathakurta, P., Colless, M., & Img, K. 1997, MNRAS, 285, 779

Robertson, B., Yoshida, N., Springel, V., & Hernquist, L. 2004, ApJ, 606, 32

Röttgering, H. J. A., van Ojik, R., Miley, G. K., Chambers, K. C., van Breugel, W. J. M., & de Koff, S. 1997, A&A, 326, 505

Rupke, D.S., Veilleux, S., Sanders, D.B., ApJ, accepted, astro-ph/0507027

Salpeter, E. E. 1955, ApJ, 121, 161

Salucci, P., Szuszkiewicz, E., Monaco, P., & Danese, L. 1999, MNRAS, 307, 637

Sanders, D. B. & Mirabel, I. F. 1996, ARA&A, 34, 749

Diego, J. M., Protopapas, P., Sandvik, H. B., & Tegmark, M. 2005, MNRAS, 444

Schegerer, A., Diploma Thesis, unpublished

Scheuer, P. A. G. 1982, IAUS 97, 163

Searle, L. & Zinn, R. 1978, ApJ, 225, 357

Shapley, A. E., Steidel, C. C., Adelberger, K. L., Dickinson, M., Giavalisco, M., & Pettini, M. 2001, ApJ, 562, 95

Shapley, A. E., Steidel, C. C., Pettini, M., & Adelberger, K. L. 2003, ApJ, 588, 65

Shapley, A. E., Erb, D. K., Pettini, M., Steidel, C. C., & Adelberger, K. L. 2004, ApJ, 612, 108

Shankar, F., Salucci, P., Granato, G. L., De Zotti, G., & Danese, L. 2004, MNRAS, 354, 1020

Sheth, R. K., et al. 2003, ApJ, 594, 225

Shu, C. 2000, A&A, 354, 815

Shull, J. M., & McKee, C. F. 1979, 227, 131

Silk, J. 1997, ApJ, 481, 703

Steidel, C. C., Adelberger, K. L., Shapley, A. E., Pettini, M., Dickinson, M., & Giavalisco, M. 2003, ApJ, 592, 728

Steinmetz, M., & Navarro, J. F. ApJ, 513, 555

- Stevens, J. A., Ivison, R. J., Dunlop, J. S., Smail, I. R., Percival, W. J., Hughes, D. H., Röttgering, H. J. A., van Breugel, W. J. M., & Reuland, M. 2003, *Nature*, 425, 264
- Skillman, E. D. 1989, *ApJ*, 347, 883
- Smail, I., Ivison, R. J., & Blain, A. W. 1997, *ApJ*, 490, L5
- Smail, I., Ivison, R. J., Blain, A. W., & Kneib, J.-P. 1998, *ApJ*, 507, L21
- Smail, I., Ivison, R. J., Kneib, J.-P., Cowie, L. L., Blain, A. W., Barger, A. J., Owen, F. N., & Morrison, G. 1999, *MNRAS*, 308, 1061
- Smail, I., Ivison, R. J., Owen, F. N., Blain, A. W., & Kneib, J.-P. 2000, *ApJ*, 528, 612
- Smail, I., Ivison, R., Blain, A., & Kneib, J. P. 2001, *Deep Millimeter Surveys: Implications for Galaxy Formation and Evolution*, 3
- Smail, I., Ivison, R. J., Blain, A. W., & Kneib, J.-P. 2002, *MNRAS*, 331, 495
- Smail, I., Chapman, S. C., Blain, A. W., & Ivison, R. J. 2004, *ApJ*, 616, 71
- complete this one
- Sofue, Y., & Rubin, V. 2001, *ARA&A*, 39, 137
- Sofue, Y., Koda, J., Nakanishi, H., & Onodera, S. 2003, *PASJ*, 55, 59
- Solomon, P. M., Downes, D., Radford, S. J. E., & Barrett, J. W. 1997, *ApJ*, 478, 144
- Spergel, D. N., et al. 2003, *ApJS*, 148, 175
- Steidel, C. C., & Hamilton, D. 1993, *AJ*, 105, 2017
- Steidel, C. C., Giavalisco, Pettini, M., Dickinson, M., & Adelberger, K. L. 1996, *ApJ*, 462, L17
- Steidel, C. C., Adelberger, K. L., Giavalisco, M., Dickinson, M., Pettini, M. 1999, *ApJ*, 519, 1
- Steidel, C. C., Hunt, M. P., Shapley, A. E., Adelberger, K. L., Pettini, M., Dickinson, M., & Giavalisco, M. 2002, *ApJ*, 576, 653
- Steidel, C. C., Shapley, A. E., Pettini, M., Adelberger, K. L., Erb, D. K., Reddy, N. A., & Hunt, M. P. 2004, *ApJ*, 604, 534
- Sulentic, J. W., Marziani, P., & Dultzin-Hacyan, D. 2000, *ARA&A*, 38, 521
- Swinbank, A. M., Smail, I., Chapman, S. C., Blain, A. W., Ivison, R. J., & Keel, W. C. 2004, *ApJ*, 617, 64
- Swinbank, A. M., Smail, I., Bower, C., Borys, C., Chapman, S. C., Blain, A. W., Ivison R. J., Ramsay Howat, S., Keel, W. C., Bunker, A. J., 2005, *MNRAS*, accepted (astro-ph/0502096)
- Tacconi et al., in preparation.
- Tadhunter, C. N. 1991, *MNRAS*, 251, 46P
- Tecza, M., Thatte, N. A., Eisenhauer, F., Mengel, S., Röhrle, C., & Bickert, K. 2000, *Proc. SPIE*, 4008, 1344

- Tecza, M., et al. 2004, ApJ, 605, L109 (Paper I)
- Teplitz, H. I., et al. 2000, ApJ, 542, 18
- Thatte, N. A., et al. 1998, Proc. SPIE, 3533, 704
- Thomas, D.; Greggio, L.; Bender, R. 1999, MNRAS, 302, 537
- Tremonti, C., et al. 2004, ApJ, 613, 898
- Tody, D. 1993, in *Astronomical Data Analysis Software and Systems II*, ed. R. J. Hanisch, R. J. V. Brissenden, & J. Barnes (San Francisco: ASP), 173
- Tremaine, S., et al. 2002, ApJ, 574, 740
- Tucker, W., et al. 1998, ApJ, 496, L5
- van Breugel, W. J. M., Stanford, S. A., Spinrad, H., Stern, D., & Graham, J. R. 1998, ApJ, 502, 614
- van den Bergh, S., Abraham, R. G., Ellis, R. S., Tanvir, N. R., Santiago, B. X., & Glazebrook, K. G. 1996, AJ, 112, 359
- van Dokkum, P. G., & Stanford, S. A. 2003, ApJ, 585, 78
- van Dokkum, P. G., Franx, M., Kelson, D. D., & Illingworth, G. D. 2001, ApJ, 553, 39
- van Dokkum, P. G., Kriek, M., Rodgers, B., Franx, M., Puxley, P., ApJ, accepted(astro-ph/0502082)
- van Ojik, R., Roettgering, H. J. A., Miley, G. K., & Hunstead, R. W. 1997, A&A, 317, 358
- Veilleux, S., Kim, D.-C., & Sanders, D. B. 1999, ApJ, 522, 113
- Venemans, B. P., Kurk, J. D., Miley, G. K., Röttgering, H. J. A., van Breugel, W., Carilli, C. L., De Breuck, C., Ford, H., Heckman, T., McCarthy, P., & Pentericci, L. 2002, ApJ, 569, L11
- Vogt, N. P., Forbes, D. A., Phillips, A. C., Gronwall, C., Faber, S. M., Illingworth, G. D., & Koo, D. C. 1996, ApJ, 465, L15
- Vorobyov, E. I. 2003, *Astronomical and Astrophysical Transactions*, 22, 95
- Wan, L., Daly, R. A., & Guerra, E. J. 2000, ApJ, 544, 671
- Wellman, G. F., Daly, R. A., & Wan, L. 1997, ApJ, 480, 96
- Willott, C. J., Rawlings, S., Blundell, K. M., & Lacy, M. 1999, MNRAS, 309, 1017
- IMPRSS lecture given in September 2003
- Yee, H. K. C., Ellingson, E., Bechtold, J., Carlberg, R. G., & Cuillandre, J.-C. 1996, AJ, 111, 1783
- Yu, Q., & Tremaine, S. 2002, MNRAS, 335, 965
- Zibetti, S., Gavazzi, G., Scodreggio, M., Franzetti, P., & Boselli, A. 2002, ApJ, 579, 261
- Ziegler, B. L., Böhm, A., Fricke, K. J., Jäger, K., Nicklas, H., Bender, R., Drory, N., Gabasch, A., Saglia, R. P., Seitz, S., Heidt, J., Mehlert, D., Möllenhoff, C., Noll, S., & Sutorius, E. 2002, ApJ, 564, L69

Zwicky, F. 1937, ApJ, 86, 217

Zwicky, F. 1952, PASP, 64, 242

Acknowledgements

*“A Pigmy placed on the shoulders of giants
sees more than the giants themselves.”*

Marcus Annaeus Lucanus

A.D. 39-65

If science is not only about accurate measurements, but also similar wording, then how can the length of a pigmy’s legs allow him to stand on the shoulders of more than one single giant? While this might originate from imprecise translation and common practice, it is a mystery why Isaac Newton, unlike Didacus Stella, Robert Burton, and Coleridge did not avoid this issue (*“If I have seen further it is by standing on the shoulders of giants.”*, Letter to Robert Hooke, I. Newton, Feb. 5th, 1676). Let us just hope for all pigmies that Lucanus’ giants will always walk in strict unison! Neglecting these details, and as should be obvious to all, such a picture is as yet more adequate (and the arrangement definitely more efficient) than placing a giant on the shoulders of dwarfs.

Having had the pleasure to study the furthest corners of this Universe over the last three years, I am deeply indebted to a sheer infinite chain of giants who made this work possible, providing both the technical and the scientific basis for such an undertaking. More specifically, I wish to thank everybody who continuously believed in me during this period, and who helped me with their patience and by sharing their extensive insight. Matt Lehnert has been a wonderful teacher.

Special thanks to Professor Genzel who generously shared his SPIFFI-GI data with me, and to the SPIFFI commissioning team for doing their best in taking these data, which form the backbone of this thesis. The reduction scheme was provided quickly and timely by Ric Davies and proved to be a valuable basis from which I could develop my own package. Having collected the vast amount of multi-wavelength data to complement the SPIFFI data, I also wish to thank those who kindly shared their data with me, and often before they were publicly available. This especially includes Dennis Downes, Christine Forman-Jones, Roser Pello, Amy Barger, Rob Ivison, Dörte Mehlert, and Stella Seitz.

Finally, *mahalo ho’o maika’i* to the small tribe of 100Micronesians, for taking me to their sacred places, dancing around the fire, and for sharing their secret magic *kui ’o’hiu* rites.

Lebenslauf

12. Dezember 1975 Geburt in Offenbach am Main
- 1982 – 1986 Grundschule in Nidderau-Ostheim
- 1986 – 1995 Otto-Hahn-Schule in Hanau am Main
- 1995 – 2000 Physikstudium an der Johann Wolfgang Goethe-Universität
in Frankfurt am Main
- 2/1996–4/1996 Hospitanz bei der Frankfurter Allgemeinen Zeitung,
anschließend 4 Jahre regelmäßige freie Mitarbeit
- 2/1997–4/1997 Praktikum beim Sender Freies Berlin, Wissenschaftsredaktion Hörfunk
- 1996-2001 Stipendiatin der Konrad-Adenauer-Stiftung
- 6/1999 – 9/1999 Sommerstudent am CERN in Genf
- 2000 – 2001 Diplomarbeit an der Ludwig-Maximilians
Universität in München (LMU) am Lehrstuhl Schaile
15. Mai 2001 Diplom in Physik der LMU, Note 1.1
- 6/2001 – 10/2001 Volunteer am Hawai'ian Volcano Observatory auf Big Island, Hawai'i
- 10/2001 – 12/2002 Mitarbeit am Experiment ATLAS am CERN
- 01/2003–06/2006 Promotion am MPE, Garching, in der Infrarot– Arbeitsgruppe.
Titel der Dissertation: “Integral-Field Spectroscopy of High-Redshift Galaxies:
Implications for Early Galaxy Evolution
6. Juni 2006 Promotion an der LMU, magna cum laude

